HAL
open science

Fluorescence-based nanofluidic biosensor platform for real-time measurement of protein binding kinetics

Pattamon Teerapanich

To cite this version:

Pattamon Teerapanich. Fluorescence-based nanofluidic biosensor platform for real-time measurement of protein binding kinetics. Micro and nanotechnologies/Microelectronics. Université Paul Sabatier - Toulouse III, 2015. English. NNT : 2015TOU30239 . tel-01285405

HAL Id: tel-01285405

https://theses.hal.science/tel-01285405v1

Submitted on 9 Mar 2016

HAL is a multi-disciplinary open access archive for the deposit and dissemination of scientific research documents, whether they are published or not. The documents may come from teaching and research institutions in France or abroad, or from public or private research centers.

L'archive ouverte pluridisciplinaire **HAL**, est destinée au dépôt et à la diffusion de documents scientifiques de niveau recherche, publiés ou non, émanant des établissements d'enseignement et de recherche français ou étrangers, des laboratoires publics ou privés.

Université Fédérale
Toulouse Midi-Pyrénées

THÈSE

En vue de l'obtention du

DOCTORAT DE L'UNIVERSITÉ DE TOULOUSE

Délivré par :

Université Toulouse 3 Paul Sabatier (UT3 Paul Sabatier)

Présentée et soutenue par :
Pattamon TEERAPANICH

le mardi 10 novembre 2015

Titre :

Fluorescence-Based Nanofluidic Biosensor Platform for Real-Time Measurement of Protein Binding Kinetics

---

École doctorale et discipline ou spécialité :

ED GEET : Micro et Nanosystèmes

Unité de recherche :

Laboratoire d'Analyse et d'Architecture des Systèmes (UPR 8001)

Directeur/trice(s) de Thèse :

Docteur Thierry LEICHLE

Jury :

Professeur Bruno LE PIOUFLE - Rapporteur
Professeur Jonas TEGENFELDT - Rapporteur
Docteur Harry HEINZELMANN - Examinateur
Professeur Chia-Fu CHOU - Examinateur
Professeur Philippe MENINI - Président du Jury
Docteur Martine PUGNIERE - Invitée

The starting point of all achievement is desire.

Napoleon Hill

Keep your face always toward the sunshine –

and shadows will fall behind you.

Walt Whitman

Acknowledgements

First and foremost, I would like to express my deepest gratitude to Thierry, my supervisor, for giving me the great opportunity to work on this interesting project and for always helping me with his excellent guidance, encouragement and endless care at any moment of difficulty throughout these four years of my PhD. I would like to express my sincere thanks to the members of my jury for their efforts and their time devoted to review my PhD manuscript and for offering detailed evaluation. Special thanks go to Martine and Corinne for their contributions to SPR experiments and for fruitful discussions. I am very grateful to Chia-Fu and his student Yii-Lih, our friendly and competent collaborator from Academia Sinica, for exchanging valuable knowledge and their constant assistance.

This PhD would not have succeeded without the monumental contributions of people from TEAM and I2C. I would like to give many thanks to Pierre-Francois, Eric, Aurélie, Ludovic, David, Jean-Christophe, Bernard, Laurent, as well as Charline, Sandrine and Fabrice. Thank you Xavier for all your microfluidic supports made with rapidity and professionalism.

My gratitude also goes to the entire NBS group in particular Liviu for introducing me to my great supervisor and for his positive energy and encouragement. Thank you Sven, Jonathan, Florent, Florian, Adhitya, Yingning, Jean, Hélène, Aude, Raphaël, Sabrina, Cécile and Maxime for their friendship and for providing me great moments of joy during coffee breaks. I wish to express my appreciation to N2Is group in particular Aurélien, Pierre, Hubert, Vincent, Sébastien, Joris, Marc, Antoine, Rémi who have closely helped me to overcome difficulties in the world of microfluidic along with their warm and friendly working styles.

Of course, I cannot forget to thank special friends, Aliki, Didi, Laurène and Valentina for sharing marvelous moments as well as crazy adventures during the past four years.

I would like to also thank my parents and my big family for their long-distance moral support and unconditional love. Thank you Pornpanit and Jamie Langford for your revision.

And last, but not least, I want to thank the most important person, Denis, who has been a constant source of love and support standing by my side throughout this important step of my life. Thank you for spending every moment together during my good and bad times.

The financial supports from the Agence Nationale de la Recherche (ANR-13-IS10-0001) and the Ministère des Affaires Etrangères (MAE) are gratefully acknowledged.

Table of Contents

INTRODUCTION **1**

Chapter 1 Kinetic study of biomolecular interactions

1.1 Importance of kinetic studies of biomolecular interactions…… 5
1.2 Protein-protein interaction…… 7
1.2.1 Structures of proteins and interaction forces…… 7
1.2.2 Measuring protein interactions – solution vs surface…… 10
1.2.3 Affinity and kinetic determination with surface-based assays…… 11
1.2.3.1 Equilibrium analysis…… 12
1.2.3.2 Kinetic analysis…… 14
1.2.3.3 Deviation from Langmuir binding…… 16
1.3 Current tools for real-time monitoring of protein binding kinetics…… 17
1.3.1 Classical methods (solution-based assays)…… 17
1.3.2 Alternative technologies (surface-based assays)…… 19
1.3.2.1 Biosensors – affinity-based sensors…… 19
1.3.2.2 Label-free technologies…… 20
1.3.2.3 Fluorescence-based methods…… 25
1.3.2.4 Fluoresce-enhanced label-free sensors…… 27
1.4 Challenges in affinity-based biosensor development and the need for alternative answers. 30
1.5 Conclusion…… 31
Bibliography…… 32

Chapter 2 Nanofluidics: Miniaturized systems as an alternative answer for kinetic study

2.1 Introduction to nanofluidics…… 39
2.1.1 What is nanofluidics?…… 39
2.1.2 Extended nanospace – a new gap between nano-and microdevices…… 42
2.1.3 Main applications of nanofluidics…… 43
2.1.3.1 Biomolecule separation and sieving…… 43
2.1.3.2 Pre-concentration of biomolecules…… 45
2.1.3.3 Single-molecule analysis – the benefits of nanoconfinement…… 47
2.2 Biosensing with nanofluidics…… 49
2.2.1 Current nanofluidic-based biosensors…… 49

2.2.2 Kinetics of biomolecular interactions in nanofluidics…… 52
2.3 Issues related to nanofluidic sensing …… 55
2.3.1 Integration of biofunctional layers…… 55
2.3.2 Sealing process…… 56
2.3.3 Detectability and response time …… 57
2.3.4 Fluid handling…… 59
2.4 Concept and contributions of our approach …… 60
2.5 Diffusion, convection and reactions in surface-based biosensors …… 64
2.5.1 Model system description …… 65
2.5.2 Dimensionless number …… 65
2.5.2.1 The Reynolds number…… 65
2.5.2.2 The Peclet number …… 66
2.5.2.3 The Damköhler number – interplay of mass transport and reactions…… 66
2.5.3 Phase diagram of mass transport…… 67
2.6 Conclusion…… 70
Bibliography…… 71

Chapter 3 Fabrication and implementation of the nanofluidic biosensor platform

3.1 Device design and conception…… 77
3.2 Fabrication process …… 80
3.2.1 Nano- and microchannel fabrication…… 81
3.2.2 Thermal oxidation and gold deposition…… 82
3.2.3 Lamination and inlet/outlet hole opening…… 82
3.3 Biointerface …… 84
3.3.1 Biological model …… 85
3.3.2 Surface chemistry…… 86
3.3.3 Open-top surface functionalization…… 88
3.4 Chip encapsulation…… 92
3.5 Device assembly and fluidic configuration…… 95
3.6 Experimental setup…… 97
3.7 Flow calibration…… 98
3.7.1 Materials and methods …… 98
3.7.2 Results and discussion …… 99
3.8 Conclusion…… 102
Bibliography …… 103

Chapter 4 Real-time fluorescence detection of protein binding kinetics in nanofluidic biosensors

4.1 Real-time kinetic measurement …… 105
4.1.1 Streptavidin-biotin binding model…… 105

4.1.1.1 Assessment of bio-functionalization 105
4.1.1.2 Kinetic assay 107
4.1.2 Mouse IgG/anti-mouse IgG interaction model 110
4.1.2.1 Post-sealing surface modification 110
4.1.2.2 Kinetic assay 111
4.2 Fluorescence data analysis 113
4.3 Kinetic constant quantification 114
4.3.1 Finite element method (FEM) 114
4.3.1.1 Model construction 114
4.3.1.2 Simulation parameters 117
4.3.2 Analytical solution (well-mixed model) 120
4.3.3 BIAevaluation software package 121
4.3.4 Results and discussion 122
4.3.4.1 Streptavidin-biotin binding model 122
4.3.4.2 Mouse IgG/anti-mouse IgG interaction model 123
4.4 SPR benchmarking 126
4.4.1 SPR principle 126
4.4.2 Kinetic measurement 127
4.4.3 Binding kinetics at varying probe grafting density 130
4.4.4 Effect of fluorescence labeling on protein binding kinetics 132
4.5 Comparison of our sensor performances with the literature and SPR setup 135
4.6 Range of operation and detection limit 137
4.7 Repeatability assay 139
4.8 Conclusion 141
Bibliography 142

Chapter 5 One-shot kinetic assay in nanofluidic sensors with integrated concentration gradient generator

5.1 Introduction 145
5.2 Principle of transport phenomena in microfluidic gradient dilutors 148
5.2.1 Navier-Stokes equation 148
5.2.2 Hydraulic analogy of Ohm's law 149
5.2.3 Convective-diffusive transport 149
5.2.4 Mixing length in gradient generators 151
5.3 Gradient generator achievements up-to-date 152
5.3.1 Diffusion-based gradient generators 154
5.3.2 Laminar flow-based gradient generators 155
5.3.3 Gradient generators for kinetic analysis 159
5.4 Requirement of microfluidic gradient generator-incorporated nanoslit system for kinetic study 160
5.5 Device concept and design validation 161

5.5.1 Chip design 161
5.5.2 Design validation with finite element simulations 163
5.6 Device fabrication 167
5.7 Experimental validation of the concentration gradient generator 168
5.7.1 Fluorescence calibration 168
5.7.2 Concentration gradient visualization 169
5.8 One-shot parallel kinetic measurements 173
5.9 Conclusion 177
Bibliography 178

GENERAL CONCLUSION **181**
Abbreviations 184
Appendix 186
A Device fabrication process 186
B Materials and reagents 188
C Validation of the full functionalization protocol using quartz crystal microbalance (QCM) apparatus 189
D Compositions and preparation of h-PDMS mixtures 192
E Sensor preparation and receptor immobilization with BIACORE setup 193

Introduction

Living beings are made of cells, the fundamental biological units that carry out all specific tasks to maintain the well-being of living organisms. Proteins are the workhorse macromolecules of the cells. They play a significant role in virtually all cellular functions, are diverse in structures and have different roles. To perform a particular biological function, proteins naturally associate and dissociate with other molecules (*e.g.*, ligands). In cellular sensing and responses, involving signal transduction cascades, protein-protein interactions are responsible for conveying the extracellular signaling stimuli to the cell's interior, activating intracellular receptors, and terminating the signal-transduction pathway. The failure or disruption of any signaling process can lead to uncontrollable or inappropriate cell growth, and eventually stimulating cancers or other disease states, such as hypertension, heart diseases, and diabetes. Therefore, information of the interaction dynamics or kinetics of protein-protein interactions is central not only to understand the underlying mechanisms of biochemical cascades and other cellular processes, but also to allow the discovery and development of potential treatments for combating diseases. For instance, kinetic profiling is an important element in drug optimization, which reveals drug's efficiency and toxicity. A drug which possesses a long dissociation time may offer clinical benefits and increase patient compliance but at the same time may induce side-effects to the patients.

Affinity-based biosensors have been recognized as dominant tools for characterizing protein-protein interactions in real-time, hence enabling the quantification of kinetic parameters of these interactions. They rely on the affinity recognition between the target analyte in solution and immobilized biomolecules on the transducer surface. Among affinity-based biosensors, surface plasmon resonance (SPR) is currently a standard and mature technology routinely used in the field of pharmaceutical and life science research to study protein binding kinetics. While this technique offers a label-free detection, it still has limitations in terms of sensitivity when analyzing small molecules, such as hormones or drug-fragments. Furthermore, the observed kinetic rates of extremely fast reactions (high association rate) are not accurate due to inherent mass transport limitations. More importantly, SPR necessitates expensive and specialized instruments and high-skilled personnel to accomplish the measurements, thus restricting its accessibility to the classical chemical and biological laboratories.

In this PhD work, we present a simple alternative biosensor platform which facilitates real-time monitoring of protein-protein interaction in a cost-effective manner. Our approach involves the use of biofunctionalized uniaxial confined nanofluidic slit (nanoslit) in combination with a conventional fluorescence microscope and a charge-coupled device (CCD) camera system. This miniaturized system undeniably offers great promises for high device performances in terms of sensitivity, assay-time, and allows low-volume sample handling and increases sample throughput. Similar to SPR

technique, our approach allows the quantification of individual kinetic parameters, but with additional advantages of simplicity, enhanced binding efficiency, and optimized response times, with no analyte mass dependence. To demonstrate our device capability, we study the reaction kinetics of two dedicated biological models with different binding affinities, streptavidin-biotin and IgG/anti-IgG interactions. The kinetic parameters associated with these interactions are extracted by means of three different fitting methods, including finite element model, analytical model, and a commercial software package. In order to validate our device performances, we compare the estimated kinetic parameters with those obtained from the SPR setup and the values found in the literature. Additionally, we propose to incorporate a concentration gradient generator to the biofunctional nanoslits. This novel approach allows one-shot parallel kinetic studies to be realized, which could potentially be applied for high-throughput drug screening and other biologically relevant reactions.

The dissertation consists of 5 chapters.

Chapter 1 first discusses the importance of kinetic studies of biomolecular interactions. Protein structures and forces involved in protein-protein interactions are then presented. After introducing the methods used to characterize protein-protein interactions including homogeneous and heterogeneous formats, we explain how to determine the kinetic parameters with surface-based assays. In addition, we review the tools that are currently available for protein kinetic studies with a particular focus on affinity-based biosensors. Finally, challenges related to affinity-based biosensor development are discussed.

Chapter 2 provides an introduction to nanofluidic technology along with its leading applications. The literature on biosensing and kinetic studies using nanofluidics is discussed together with associated issues. Then, we present the concept of our approach, based on nanofluidic biosensors in combination with fluorescence detection, and their unique features that give rise to real-time monitoring of protein binding kinetics. Finally, we provide a general description of mass transport and reaction phenomena involved in surface-based biosensors and the key dimensionless numbers useful for device design and understanding.

Chapter 3 deals with the implementation of our cost-effective sensing platform. It includes the device design and the microfabrication process used to manufacture our nanofluidic devices. We present the biointerface that consists of two representative models of protein-ligand pairs and we describe the surface functionalization protocols used to graft the bioreceptors within the nanoslits. The chip encapsulation and packaging are presented as well as the experimental setup used to carry out the kinetic studies.

Chapter 4 concerns the experimental validation of our fabricated devices through kinetic studies of two dedicated biological models with different binding affinities: streptavidin-biotin and mouse IgG/anti-mouse IgG interactions. We then validate the output measurements of our biosensor platform with the well-established SPR technology as well as literature values. The range of operation, detection limit, and repeatability of our devices for the detection of IgG are also discussed.

Chapter 5 describes our intention of providing an effective and high-throughput means to achieve one-shot kinetic measurements in a parallel manner. We incorporate an on-chip microfluidic concentration gradient network to our validated nanofluidic-based biosensor device. In this manner, simultaneous interrogations of multiple binding events of up to 10 different analyte concentrations are achieved in a single-experiment, thus minimizing the assay time with a minimum of sample handling.

Finally, a general conclusion is provided at the end of this dissertation.

Chapter 1

Kinetic study of biomolecular interactions

In this chapter, we firstly discuss the importance of kinetic studies of biomolecular interactions, particularly in drug discovery process. Then, we give an introduction to protein-protein interactions including protein structures and forces involved in their interactions. The methods to measure protein-protein interactions including solution-based and surface-based approaches are presented. In addition, we provide the fundamental methodology relying on equilibrium and kinetic analysis for determination of the affinity and kinetic parameters using surface-based assays. Special attention is put on a literature review of current tools used for real-time monitoring of protein binding kinetics. Finally, we intend to discuss challenges related to affinity-based biosensor development which clearly drive advancements of this field toward alternative bioanalytical systems.

1.1 Importance of kinetic studies of biomolecular interactions

Knowledge of the binding affinity of interacting biomolecules is of paramount importance in facilitating the study of cellular functions and underlying biological events responsible for heath symptoms of hereditary diseases, such as cancers and amyloidosis-related diseases (*e.g.*, Alzheimer's, Parkinson's diseases). This basic comprehension regarding the cellular functions has led to the exploration and the engineering of complex biological processes, including cell adhesion and viral infection, as well as the development of novel clinical therapeutic drugs to combat life-threatening maladies [1, 2]. Besides, kinetic studies offer insight information concerning the relationships between structure and biochemical activities as well as the mechanism of complex formation, hence improving our understanding of life at the cellular level. Since biomolecular interactions are dynamic processes, deliberating distinctive association and dissociation rates of these interactions provides clues that might be concealed in the conventional equilibrium analysis [3].

Kinetic analysis of biomolecular interactions has found prevalent applications in various domains, including drug discovery and development (Figure 1.1), kinetic profiling of immunotherapeutic, and life science research. Biomolecular affinity is solely not an ideal parameter because different compounds having comparable affinities can possess on-off kinetic rates that can span several orders of magnitude. In drug screening, knowing the kinetic profile is pivotal for pharmaceutical industries to fish out the potential drug candidates, based on their efficacy, stability and durability, which produce a desired therapeutic response [4].

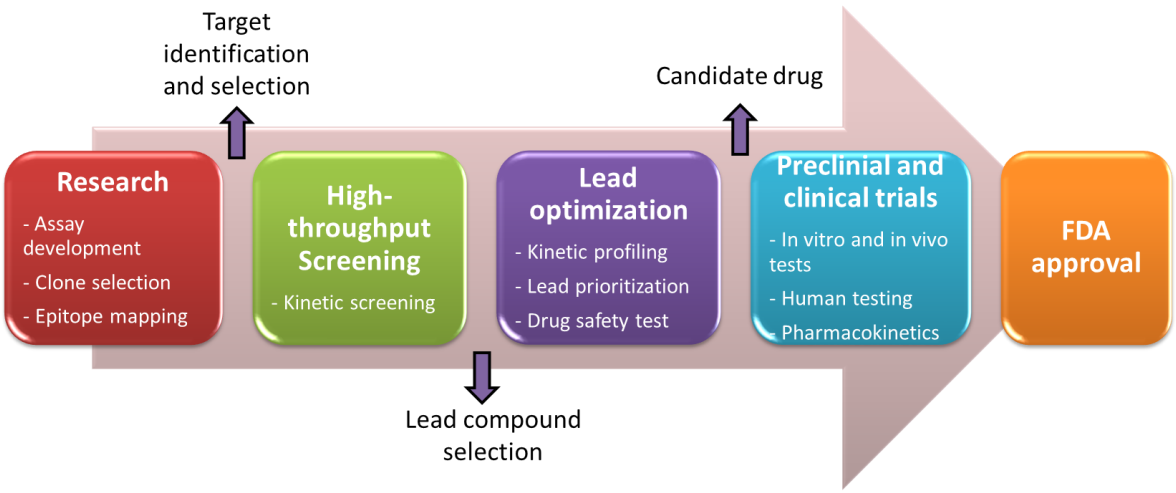

Figure 1.1 Drug discovery procedures (adapted from [5]).

Resolving kinetic features of drug-ligand interactions offers benefits to medical optimization of potential lead compounds [6]. According to drug-receptor theory, the drug action is accomplished only when a drug is bound to its target receptor [7]. A splendid balance between efficient drug transport and sequestration is a prime for drug action against diseases [8]. In fact, the efficient transport requires moderate drug affinity (*i.e.*, rapid association and dissociation rates), providing a safe profile of the drug. On the one hand, if the association rate is slow, a great quantity of the drug is necessary to facilitate drug-target binding, thus boosting the risk of side effects to the patients. On the other hand, if the dissociation rate is too low, the drug is potentially sequestered in the body and thereby suppresses the interaction with its target receptor. Accordingly, kinetic considerations have important therapeutic implications for the identification of clinical drug reagents with optimal *in vivo* efficacy and minimal toxicity [9].

A drug residence time (the time a drug remains bound to its target), dictated by its dissociation rate constant (k_d), has been recognized to play a major role in clinical success of drug design and development. Knowing this parameter, ineffective or dangerous candidates can be isolated earlier in the drug discovery procedures, thus reducing drug attrition rates and costs [10, 11]. The quantitative binding kinetics of drug/disease-related receptor interactions also reveals the source of drug resistance developed by the patients, which triggers failures of the therapy [12]. In addition, kinetic analysis has positive impact on the pharmacokinetic studies of patient sera during clinical trials [13]. Once the drug candidate is approved, kinetic profiles are very useful for quality inspection of the manufactured biotherapeutic proteins and vaccines [14].

Apart from the applications in clinical arena, kinetic evaluations can be used to select monoclonal antibodies (mAb) for specific uses. The association and dissociation rates are considered to be the prime indicators for evaluating their performances, and indicating a decent antibody candidate for an immunopurification procedure [15]. For instance, the best mAb choice for an affinity support is the one that possesses high association and dissociation rates because it allows the use of high flow rates and mild elution conditions.

The abovementioned examples, thereby, demonstrate the importance of kinetic studies of biomolecular interactions taking place in virtually every biological process in a living cell. There are numerous varieties of biomolecular interactions, including protein-protein, protein-DNA, ligand-receptor, cell-antibody interactions, etc. The main focus of our study concerns protein-protein/ligand interactions.

1.2 Protein-protein interaction

1.2.1 Structures of proteins and interaction forces

Proteins are very important biological macromolecules consisting of long chains of amino acid residues. They have a particular three-dimensional shape that modulates their biological activities. Linderstrom-Lang *et al.* [16] named different levels of protein structures, comprising the primary structure or amino acid sequences, the secondary structure (alpha helix and beta sheets), and the tertiary structure (protein folding into a globular shape). Moreover, some proteins containing more than one polypeptide chain exhibit quaternary structure, which involves the spatial arrangement of subunits. These proteins include hemoglobin and DNA polymerase [17] (Figure 1.2).

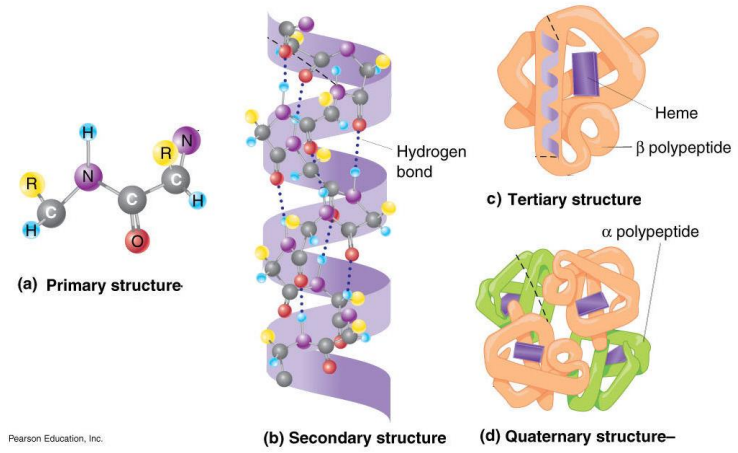

Figure 1.2 Levels of protein structures (from [18]).

Proteins maintain the structural and functional integrity within our cells: examples of their roles include the regulation of enzymes and hormones in the metabolic pathways, defensive functions against the foreign invaders, signal transduction and gene expression, to name a few. Protein malfunction can lead to the development of neurological disorders, such as Creutzfeld-Jacob and Alzheimer's disease [19]. Studies of protein-protein interaction are thus central for understanding how they interact with each other or with other molecules (referred as ligands) in order to perform physiological functions and for unraveling the molecular machinery within cells [20].

Protein-protein/ligand interactions are regulated by a variety of weak noncovalent interactions (since the biological reaction requires reversibility), *i.e.*, van der Waals attractions, hydrogen bonds, electrostatic forces, and hydrophobic interactions [21]. Protein binding usually displays an extraordinary specificity in which a protein binds to only a certain molecule among an abundance of other substances it confronts. This ability is achieved thanks to the simultaneous formation of those weak bonds, giving that the ligand must fit precisely into the protein binding sites. These binding sites are cavities located on the protein surface containing specific arrangement of amino acids, which are created upon protein folding (Figure 1.3). Upon interactions, proteins may undergo conformation changes in such a way that their chemical reactivity is enriched, which is known as induced-fit effects [22].

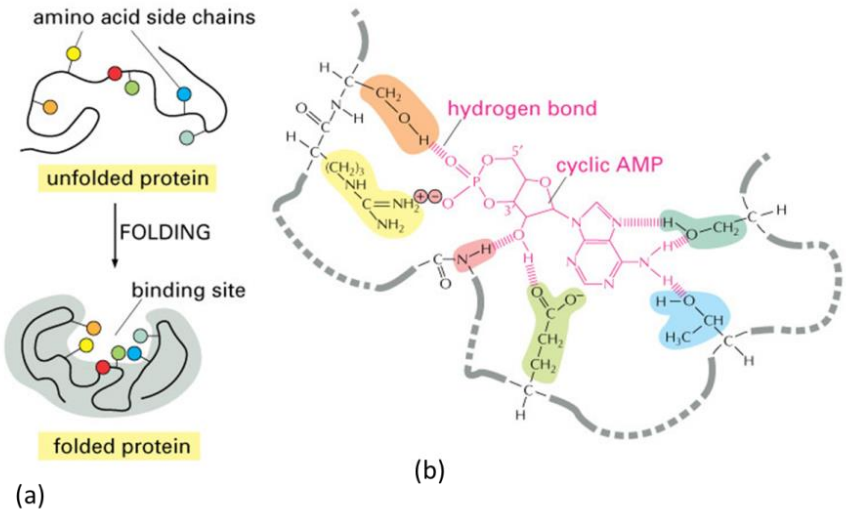

Figure 1.3 (a) The folding of polypeptide chain results in the creation of a cavity or a binding site on the protein surface. The binding site contains a specific arrangement of amino acid chains in a way that the protein can recognize only certain incoming ligands. (b) A zoom in of the binding site depicting hydrogen and ionic bonds formed between a protein and its ligand (cyclic AMP) (from [23]).

Antibodies or immunoglobulins are one class of proteins that are responsible in the immune system for tagging or neutralizing the foreign objects. With no doubt, all living organisms need to defend themselves against infection by harmful invaders or pathogens, such as bacteria or viruses [24]. Antibodies are typically secreted from the lymphosites, called B cells, in response to these foreign molecules. It is Y-shaped and possesses two identical binding sites (one on each arm of the Y) for specific recognition of its target, called an antigen, via the variable domain.

The antibody structural unit is composed of four polypeptide chains; two identical heavy chains and two identical light chains linked together by disulfide bonds [25], forming an antibody structure with a molecular weight of about 150 kDa . Heavy chains define different types of antibody isotopes (IgA, IgD, IgE, IgG and IgM). The antibody binding site (paratope) interacts with a particular complementary region or an antigenic determinant (epitope) located on the antigen surface. The unique specificity of the antibody for binding a certain antigen epitope is modulated by the loop of polypeptide chain (carrying specific amino acid sequences) at the tip of the antibody structure, referred as the complementary-determining regions or CDRs [26] (Figure 1.4).

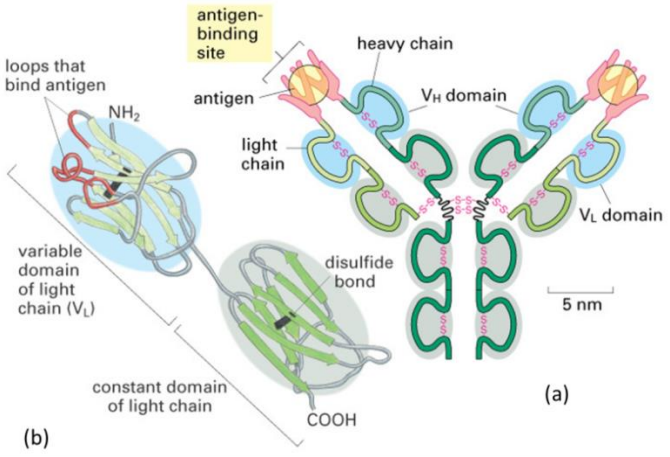

Figure 1.4 (a) An antibody molecule consisting of two light chains and two heavy chains. (b) The variable domain of light chain with finger-like loop involved in antigen binding (from [27]).

Antibodies can be produced either as monoclonal or polyclonal antibodies. Monoclonal antibodies are made from the same immune cell thus they are identical and bind to the same epitope. Polyclonal antibodies, on the other hand, are generated from different cell clones, resulting in the mixture of antibodies with the different affinity properties, each recognizing a different epitope. Despite the fact that monoclonal antibodies are expensive to produce, therapeutic mAB antibodies are now very important in clinical use for the treatment of human diseases such as breast cancer, asthma, arthritis, and leukaemia.

1.2.2 Measuring protein interactions – solution vs surface

The characterization of protein interactions is prerequisite to unraveling cellular metabolism. A variety of biophysical methodologies have been employed for measuring protein-protein interactions, which can be categorized into two main approaches: **solution (homogeneous)** and **surface-based (heterogeneous)** assays (Figure 1.5). The former involves the measurement of protein binding while both partners are freely diffusing in the solution whereas the latter deals with the interaction of a protein in solution phase (**analyte**) with a surface-immobilized protein partner (**receptor or ligand**). Both sensing formats concomitantly display advantages and drawbacks and, they do both represent real situations of protein interactions occurring in nature, for example, enzymatic reactions in blood or cytoplasm [28] or receptor-ligand interactions at the cell membranes [29, 30].

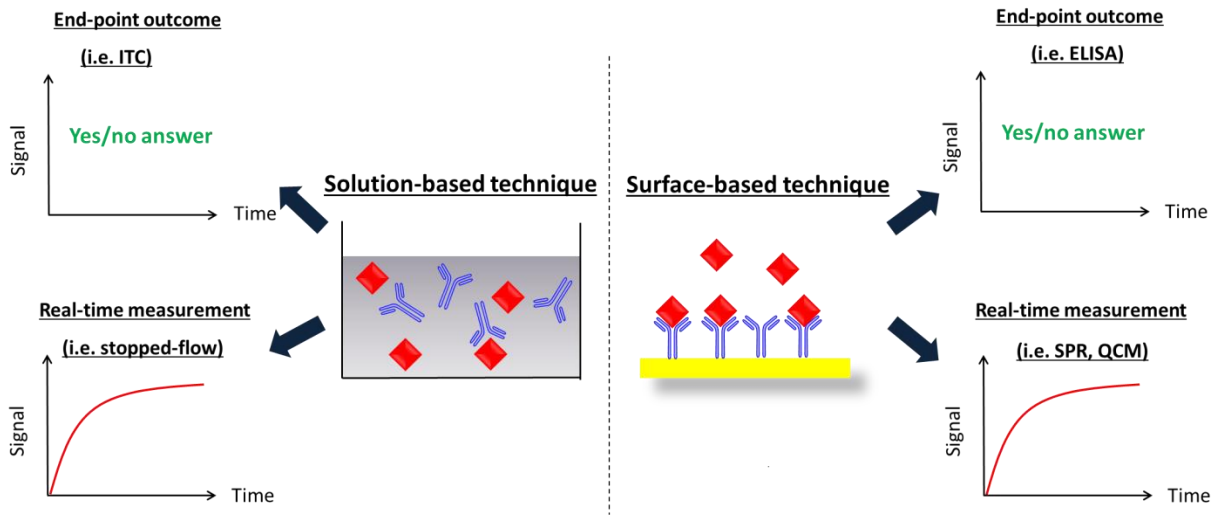

Figure 1.5 Schematic diagrams depicting two different approaches for protein interaction measurements including solution- and surface-based techniques.

Solution-based assays benefit from the well-defined three dimensional protein structure and translational and rotational diffusion properties as well as homogeneous microenvironments of the binding sites [31]. Despites these benefits, interactions in solution-based assays are unlikely to represent many biological interactions that occur *in vivo*. Surface-based assays have become an important new tool for probing protein interactions taking place on the surface in recent years, owing to their versatility and simplicity. Numerous types of transducer technologies, typically based on optical, mechanical and electrical principles, are currently available to probe the binding events. The sensor surface itself permits the discrimination between bound complexes and free analytes.

Contrary to solution-based techniques, the surface-based format offers the possibility to integrate parallel sensors for high-throughput analysis and perform multiple reagent injections and rinsing. As a result, the binding and dissociation of protein targets can be investigated using the same receptor surface.

However, the immobilization of proteins onto a surface can cause potential measurement artifacts and thus can complicate the interpretation of the experimental data. Indeed, first, surface grafting can lead to conformational changes or even denaturation of proteins. Moreover, the protein orientation and binding site accessibility associated with the steric hindrance have substantial impact on the binding properties [32, 33]. Secondly, non-specific adsorption constitutes an important problem with real-world samples wherein a low concentration of the analyte has to be detected in the presence of a higher concentration of other macromolecules. These factors therefore need to be considered when designing the surface-based technique for protein analysis. It has been demonstrated that when the surface-based techniques is performed with care, the equilibrium, thermodynamic and kinetic constants match those conducted in solution-based methods [34].

Both sensing formats either rely on end-point detection wherein the detection is carried out when the reaction reaches equilibrium, or real-time monitoring of both binding and debinding events. While end-point analysis allows qualitative analysis (presence/absence of a target specie or calculation of unknown concentrations) and provides knowledge concerning thermodynamic properties of an interaction, real-time detection yields more detailed dynamic information underlying protein complex formation owing to its possibility to extract kinetic parameters of a given interaction. Therefore, the choice of protein sensing format depends directly on the initial aim of the measurement whether one requires a yes/no outcome or detailed kinetic information of the interactions.

As mentioned above each sensing method has its own pros and cons, we chose to work with surface-based techniques owing to their versatility and wider applicability. Addition to resource-saving benefits, this technique conveniently enables high-throughput sensing formats for probing multiple binding events in a parallel manner. In the following section, we will explain the methodology to obtain affinity and kinetic information of an interaction with surface-based assays.

1.2.3 Affinity and kinetic determination with surface-based assays

The strength of an interaction between proteins is termed as the **protein affinity**, which is translated into the physio-chemical property, called the **equilibrium dissociation constant (K_D)**. For a reversible reaction assuming a simple 1:1 stoichiometry interaction, we can write:

$$C_0 + B \overset{k_a, k_d}{\longleftrightarrow} C_s \tag{1.1}$$

C_0 denotes the concentration of free proteins in solution (analyte), B denotes the concentration of free surface-immobilized protein partner (receptor), and C_s denotes the concentration of the bound complex (product) (Figure 1.6). B and C_s are two-dimensional analogs of concentration (surface density) and are expressed in units such as mol/cm^2. k_a and k_d are the forward and reverse reaction rate constants, respectively.

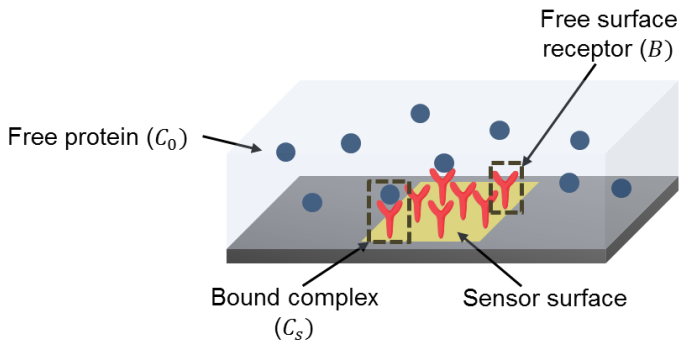

Figure 1.6 Schematic representation of the interaction between free proteins in solution and surface-immobilized receptor partners.

K_D is defined at equilibrium (when the rate of complex formation is equal to the rate of complex dissociation) as the ratio between the reactants and the bound complex as follows:

$$K_D = \frac{k_d}{k_a} = \frac{C_0 B}{C_s} \tag{1.2}$$

In fact, the lower the value of K_D, the stronger the interaction, and thus the more complex is formed. The equilibrium dissociation constant can be determined either from the **equilibrium analysis** (measuring the degree of reactions), in which the concentration of bound complex is measured as a function of free analyte concentration when the reactions equilibrate; or from the **kinetic approach** (how fast the reactions occur).

1.2.3.1 Equilibrium analysis

As the reactions occur on the surface, it is convenient to define the term: $b_m = B + C_s$; the surface density of total immobilized receptors. From this relationship, equation 1.2 can be transformed into the Langmuir binding equation [35] as:

$$Fraction\ saturation = \frac{C_s}{b_m} = \frac{C_0}{C_0 + K_D} \tag{1.3}$$

A plot between the fraction saturation and the analyte concentration performed at a constant temperature is termed as the Langmuir binding isotherm (Figure 1.7a). This rectangular-hyperbola isotherm shows distinctive regions: when $0 < C_0 \leq 0.1K_D$, only a fraction of receptors are bound to analyte molecules at equilibrium ($\leq$ 9% fraction occupancy), half-saturation of receptors is obtained at $C_0 = K_D$, and most receptor molecules are occupied when $C_0 \geq 10K_D$($\geq$ 91% fraction occupancy). Since there is a fixed amount of receptors on the surface, the maximum concentration of bound complex is thus equal to b_m, which is the total concentration of receptors on the surface.

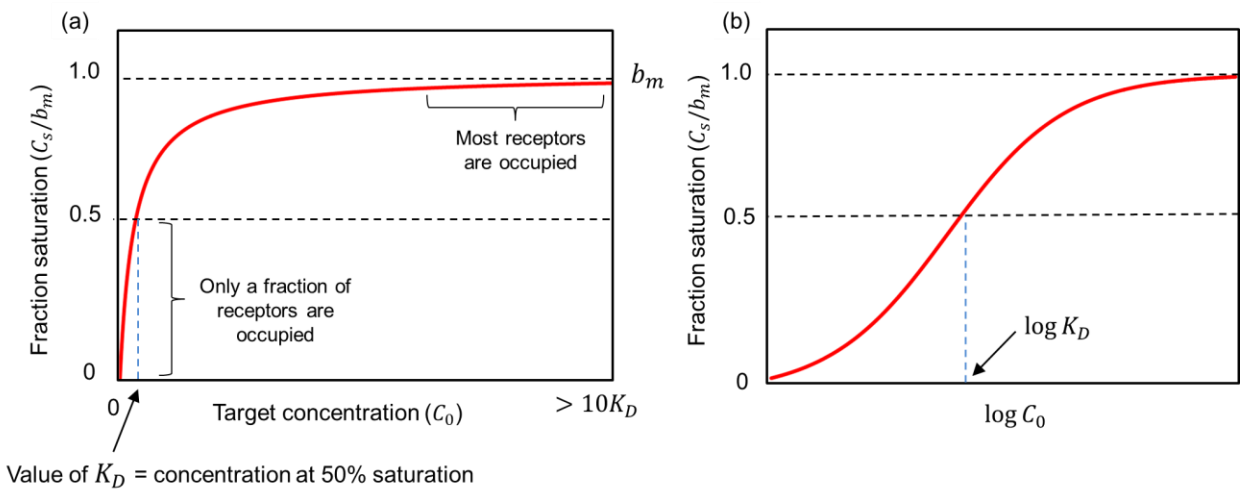

Figure 1.7 (a) A plot of fractional saturation as a function of target concentration, referred as hyperbolic binding isotherm. (b) A binding isotherm replotted with logarithm of the target concentration (x-axis), displaying a characteristic sigmoidal curve.

The equilibrium dissociation constant (K_D) is most commonly used by biochemists to describe the affinity of protein interactions rather than its inversed form: the equilibrium association constant (K_A). This is simply due to its unity in molarity (M) which can be directly equated to the concentration of the analyte at which half of receptor binding sites are occupied at steady-state. For typical binding isotherm analysis, the target concentration should span a wide range from less than K_D where target binding barely occurs to high enough for saturating virtually all surface receptors [36]. This range typically covers more than two orders of magnitude around K_D [37].

However, it is often difficult to estimate the value of K_D by visual inspection from the hyperbola binding curve because all the informative data points are gathered close to the left side of the curve where the concentrations are very low. As a result, the fraction saturation is usually plotted as a function of the logarithm of the target concentration. This plot yields a sigmoidal curve (Figure 1.7b)

which would allow more convenient read out for the value of K_D. This curve is nearly linear between 0.1-fold and 10-fold K_D. Important biological interactions have K_D ranging from mM-μM for the weak interactions (*e.g.*, protein kinase-ATP complex, signaling protein binding to a target) to nM-pM for the stronger interactions (*e.g.*, small molecule inhibitors (drugs) binding to their target proteins) [38].

1.2.3.2 Kinetic analysis

Kinetic analyses yield dynamic characteristics of the reversible interactions, which are associated with two individual parameters; the association rate constant (k_a, $M^{-1}s^{-1}$) and the dissociation rate constant (k_d, s^{-1}). The former determines how fast the complex is formed whereas the latter defines the stability of the complex or the rate of complex dissociation. The basic concept of kinetic analysis is to follow the rates of forward and reverse reactions under transient state by varying the concentration of free analytes in solution while keeping the amount of immobilized partners comparatively low. In this manner, there is a negligible change in the concentration of free analytes in a solution, and thus the association reaction proceeds with pseudo-first order kinetics.

Figure 1.8 depicts a typical kinetic sensorgram that shows the change of response signal versus time. When the analyte is injected, the binding of analyte to the immobilized receptor leads to an increase in the signal corresponding to the association phase. The signal reaches a plateau when the equilibrium is established. The analyte injection is replaced by a continuous flow of the buffer solution and a decrease of sensor signal is observed, indicating the dissociation of analyte from the surface-bound complex. The kinetic rate constants can be derived from the association and dissociation phases of this real-time sensorgram by fitting it to an appropriate model. To perform the next cycle of kinetic measurement, the surface is regenerated to remove the remaining bound analyte without damaging the immobilized receptor.

For a simple biomolecular reaction (equation 1.1), the rate of complex formation is equal to the difference between the association rate and the dissociation rate as:

$$\frac{dC_s}{dt} = k_a C_0 B - k_d C_s \tag{1.4}$$

B is defined as the concentration of free receptors at the surface and can be written as $B = b_m - C_s$. Substituting B into equation 1.4 gives:

$$\frac{dC_s}{dt} = k_a C_0 (b_m - C_s) - k_d C_s \tag{1.5}$$

The amount of complex formation at time t is commonly obtained by integrating this differential equation, resulting in a single exponential behavior as:

$$C_s = \frac{k_a b_m C_0 \left(1 - e^{-(k_a C_0 + k_d)t}\right)}{k_a C_0 + k_d} \tag{1.6}$$

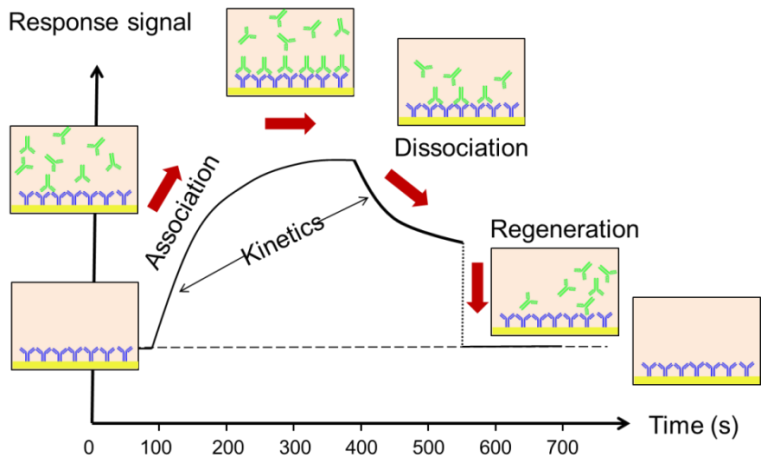

Figure 1.8 A typical kinetic sensorgram.

A new parameter associated with the exponential term K_{app} or the apparent time constant is defined as $K_{app} = k_a C_0 + k_d$. K_{app} can be determined by fitting the association phase of the binding curve to equation 1.6 using the nonlinear-squares best fit. In practice, kinetic measurement of the association process is carried out for a series of analyte concentrations. Reliable kinetic analysis requires data from 4-6 analyte concentrations, spanning in the range of 0.1-fold to 10-fold K_D [39]. For each analyte concentration, the value of K_{app} is obtained. A replot of K_{app} as a function of analyte concentration yields a linear fit whose slope equals to k_a and y-intercept equals to k_d (Figure 1.9). This fitting concept was employed to extract the kinetic constants in Chapter 4. However, k_d determined in this manner can be erroneous, particularly for low k_d values [40]. In practice, k_d is preferably derived from the dissociation phase of the sensorgram via an exponential decay fit as:

$$Dissociation: -\frac{dC_s}{dt} = k_d C_s \tag{1.7}$$

$$C_s = C_{s,eq} e^{-k_d t} \tag{1.8}$$

$C_{s,eq}$ is the concentration of complex at equilibrium which is equal to the concentration of the initial complex concentration prior to dissociation. k_d is independent on the analyte concentration and as a result its variations are indicative of other artifacts. The determination of both association and dissociation rate constants leads to the calculation of the equilibrium dissociation constant via $K_D = k_d/k_a$. Hence, knowing two of these constants gives rise to the determination of the third parameter.

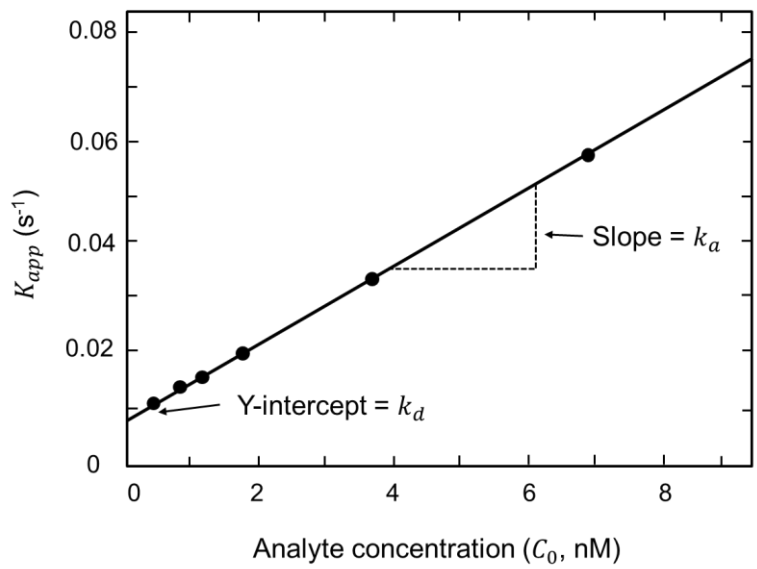

Figure 1.9 The plot between the apparent time constant (K_{app}) and the analyte concentration (C_0), showing a linear fit. The association and dissociation rate constants can be deduced from its slope and y-intercept, respectively.

The kinetic rate constants can also be calculated by means of numerical integration curve fit (global fitting), which allows the analysis of more complex interactions. However, it should be highlighted that the raw data must be of high quality for global fitting routines to be fruitful. The detailed information concerning global fitting method is described in Chapter 4.

The verification of the determined kinetic rate constants can be achieved by several means. For instance, it is advisable to calculate k_a and k_d using different fitting models and also compare the value of K_D derived from kinetic analyses with that obtained from the equilibrium binding experiment [41]. Furthermore, it is always revealing to compare the results from surface-based techniques with those performed in solution or with alternative methods (*e.g.*, calorimetry, light scattering), which utilize different principles to elucidate biomolecular interactions.

1.2.3.3 Deviation from Langmuir binding

In practice, the kinetic sensorgrams are not always accurately described by the expected simple 1:1 Langmuir model. These deviations may stem from several contributing factors including physical effects, such as mass transport limitation, non-specific binding, and steric hindrance [42, 43], or they may arise from the presence of a more complex interaction between the interaction partners.

Mass transport limitation relies on the fact that the rate at which the analyte in solution reaches the sensor surface, via convection/diffusion transport, is slower than the binding rate of the analyte to the receptor. This gives rise to a local depletion zone of analyte concentrations in the vicinity of the sensor surface. The resulting concentration gradient can cause a miss-interpretation of the

binding data using pseudo-first order reactions which often underestimates the association rate constant. Mass transport effects are usually accompanied by a sigmoidal association profile [44] instead of a standard exponential isotherm. Analogously, during the dissociation under mass transfer limit, the analyte concentration over the sensor does not completely fall to zero due to rebinding of the analyte to the free receptors, thus decelerating the dissociation rate.

There are two ways to mitigate mass transfer limitations. The first solution is to increase the flow rate in order to increase the analyte flux to the sensor surface, but more reagents are consumed. Another preferable answer is to decrease the surface capacity or levels of the immobilized receptors which in turn reduces the demand for the analyte and minimizes the concentration gradients within the flow channel [45]. When the mass transport is unavoidable by properly experimental design, it can be eventually modeled in data analysis.

Non-specific binding is one of the problematic issues responsible for the deviation from the simple model. Several successful approaches have been exploited to create anti-biofouling surfaces using hydrophilic and bioinert polymers, suppressing non-specific protein adsorption [46]. On the other hand, the problem of steric hindrance can be overcome by employing a low capacity surface or by optimizing immobilization strategies for better orientation of the surface receptors.

1.3 Current tools for real-time monitoring of protein binding kinetics

As mentioned earlier, there have been a variety of biophysical methods exploited to characterize protein interactions. All cannot be discussed in this study; however, special attention has been paid to the current techniques specifically developed to probe protein-binding kinetics in a real-time manner, since these techniques offer more specific information on molecular interactions. After presenting the **classical methods** currently used in biological laboratories, we will then present the **alternative tools** that have been lately developed based on new technologies.

1.3.1 Classical methods (solution-based assays)

The most simple and straightforward way to measure the rate of interactions involves mixing two reagent solutions and observing the subsequent changes. This bench top operation is typically carried out manually by mixing various concentrations of one reagent with a fixed concentration of its binding partner in the different cuvettes (observation cells). The detection is subsequently made by following the spectrophotometric changes (*e.g.*, absorbance, light scattering, fluorescence polarization, nuclear spin relaxation and chemical shifts, electron spin resonance or x-ray diffraction [47]). For fast reactions, the speed of mixing and the observation rate are the key limitations because it is difficult to precisely measure the initial stage of the reactions [48], due to the time wasted for replacing cuvettes in and out from the detector.

To tackle this issue, Hartridge and Roughton developed the **continuous flow apparatus** in 1923, which was suited for kinetic studies of rapid reactions in real-time with a millisecond time resolution [49]. The principle of this early method is based on rapid mixing of two sample solutions in a mixing chamber and then the mixture flows continuously through an observation tube. The progress of the reaction is monitored (*e.g.*, by adsorption or fluorescence photometry) at a fixed observation point in the observation tube. However, this procedure is laborious and it requires copious amounts of materials.

Later, the continuous flow was replaced by the **stopped-flow technique** which appeared to be more versatile and economical. In the stop-flow configuration, the solutions are delivered to a mixing chamber via two syringes that are driven by a pneumatic or stepper-motors. The solutions are rapidly mixed and directed to an observation cell. The flow can be abruptly stopped for a desired period of time when a stopping syringe is filled and it hits the stopping block, generating a back pressure (Figure 1.10).

After the reagents are mixed, numerous real-time observation techniques can be implemented to monitor the rate of reactions including absorbance (UV/IR), fluorescence spectroscopy [50, 51], nuclear magnetic resonance (NMR) [52], and electron paramagnetic resonance (EPR) [53]. Stopped-flow method has been effectively employed for elucidating the reaction kinetics of biochemical processes, such as enzymatic reactions [54], protein folding [55], and ligand binding [56, 57]. A number of stopped-flow instruments have now been commercialized, including Bio-Logic-Science Instruments SA (Claix, France) and Hi-tech Scientific (Salisbury, UK), to name a few.

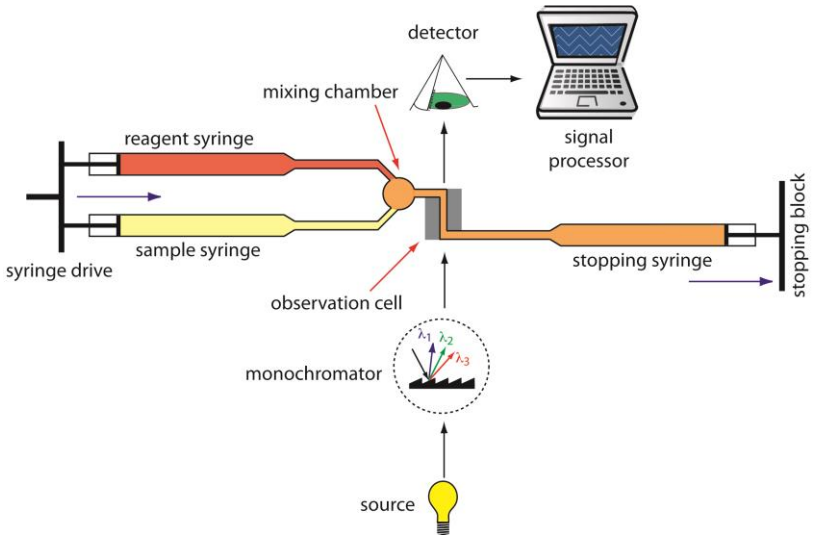

Figure 1.10 Schematic diagram of a basic stopped-flow apparatus (from [58]).

While the stopped-flow technique can be coupled with a wide range of the detection methods, a few hundred microliters of the sample volume are generally consumed to fill the observation cell. This is a main shortcoming for bioanalysis of the samples that are limited in volume and expensive to obtain, particularly in proteomics research. Therefore, a strong need for cost-benefit alternative technologies, which provide the real-time kinetic monitoring capability while minimizing sample consumption, is essential.

1.3.2 Alternative technologies (surface-based assays)

1.3.2.1 Biosensors – affinity-based sensors

A biosensor is a surface-based analytical device that integrates a biological sensing element (*e.g.*, enzymes, aptamers, or antibodies) onto a physical transducer (*e.g.*, optical, mechanical, or electrochemical). The transducer converts the molecular recognition events into a measurable electrical signal, which correlates the presence or the amount of biological substances, such as proteins, deposited on the sensing layer (Figure 1.11). Biosensor technologies have gained enormous attention in recent years to compete or even surpass the classical analytical methods in terms of analysis time, cost, and sensitivity. Other advantages of biosensors over the conventional methods include low reagent consumption, high-throughput [59], and multiplexing capability [60].

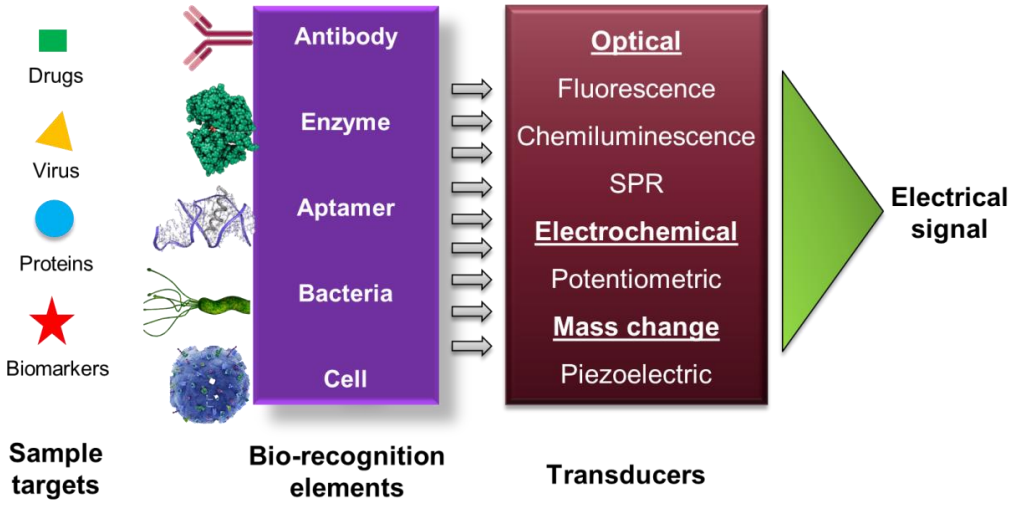

Figure 1.11 A general schematic representation of a biosensor.

Applications of biosensors have been tremendously extended along with the advancements in biosensor development, for example, to clinical diagnosis and biomedicine, environmental monitoring, and defense against bioterrorism [61, 62]. For kinetic analysis, biosensors offer a user-

friendly and effective technological platform for real-time observations of the binding events of protein-protein interactions [63]. Recent advances in micro- and nanotechnologies (*e.g.*, incorporation of microfluidics or nanomaterials to biosensors) have led to the development of biosensors for *in vitro* diagnostics and *in vivo* studies [64]. This new frontier of a multidisciplinary approach offers great promise in translating standardized laboratory routines to point-of-care clinical applications or a "bench-to-bedside" in the near future.

Biosensors are usually differentiated and categorized according to their bio-recognition elements (catalytic and affinity-based) or according to their transduction scheme. Over the last few decades, the **affinity-based biosensors**, exploiting the specific recognition of a free target analyte by an immobilized receptor on a solid surface, have been a key solution in characterizing biological interactions *in vitro*. These methods reveal the affinity and kinetic information of protein-ligand interactions [65]. The affinity biosensor solid-state device which couples immunochemical reactions (antigen-antibody complex) to a transducer is termed as an **immunosensor**.

As far as the sensing strategies are concerned, the immunosensors can be broadly classified into **label-free** and **labeled-based** methods. To be more explicit, in our context we simply define the label-free configuration as when the native protein targets are used without labeling intervention whereas if the target molecule is tagged with *e.g.*, a fluorescent molecule (fluorophore), it is referred as fluorescence-based. In the following section, we present up-to-date label-free and fluorescence-based techniques that are available for real-time detection of protein binding kinetics along with their strengths and weaknesses. In this context, we focus on fluorescence-based methods rather than other label-based techniques (*e.g.*, radioactivity or chemiluminescence) because fluorescence labeling has been a common method extensively used in proteomics applications over the last decades owing to its sensitivity and versatility.

1.3.2.2 Label-free technologies

The surface plasmon resonance (SPR) is currently a standard commercialized technology routinely used in the field of pharmaceutical and life sciences. SPR has come to the forefront of optical sensing to quantify protein binding kinetics in real-time without label requirement [66, 67]. It detects a change in refractive index when the biosensing molecules (*e.g.*, antibodies) immobilized on the transducer (thin metal film) bind with their specific targets. Details of SPR principle are provided in Chapter 4. SPR devices have addressed the demand for protein array-based sensing with the advent of the SPR imaging (SPRi) technology (Figure 1.12), permitting multiple assay spots to be screened simultaneously via a CCD camera [68, 69].

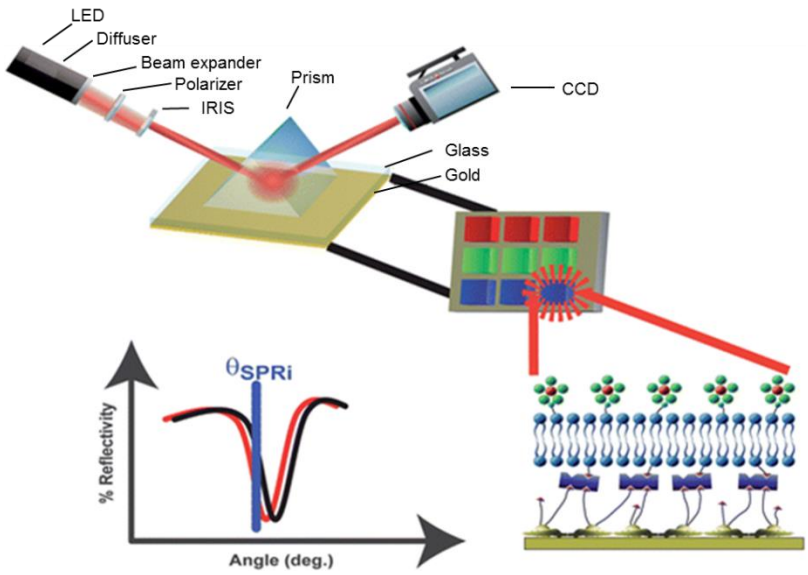

Figure 1.12 Schematic representation of an SPR imaging apparatus (adapted from [70]).

In practice, measuring the interactions of low-molecular weight analytes, such as hormones, antibiotics, and chemical drug-fragments, with the SPR instrument is limited in terms of sensitivity. Furthermore, if the reaction is too fast (*i.e.*, with high association rate), the obtained kinetic information is not reliable due to the strong effects of mass transfer [71]. So far, SPR has merely been accessible through the use of high-cost dedicated sensor surfaces and specialized instrumentation with sophisticated optical components, which in turn increases overall running and maintenance costs and also restricts its application.

There have been several attempts to reduce the instrumental costs through the development of inexpensive sensor chips and portable SPR systems [72], but little success has been met [61]. Until now, typical users, however, prefer using high-end machines which offer more benefits in terms of well-optimized fluidic handling and the user-friendly commercialized software for data analysis. Other examples of label-free optical biosensors, including optical waveguide lightmode spectroscopy (OWLS) [73, 74], nanoplasmonic sensors [75, 76], and surface enhanced Raman spectroscopy (SERS) [77], have been extensively utilized for real-time monitoring of molecular interactions with the bioactive surfaces.

OWLS is a new sensing technology relying on the use of the evanescent field of guided light to probe the binding reactions in the vicinity of the waveguide layer (Figure 1.13a). The advantage of optical waveguides over SPR technology is the freedom in sensor design aimed at increasing the penetration depth of the guided waves into the sample volume to detect relatively large biomolecules [78]. This property is limited for SPR system exhibiting a shorter propagation length because the penetration depth is merely controlled by the material properties [79]. In addition, more information

can be gathered using OWLS since both the thickness and the refractive index of the adsorbed layer can be simultaneously determined [73]. The main drawback of OWLS setup arises from its rotating sensor configuration which therefore hampers the sensor miniaturization.

Nanoplasmonic biosensors (*e.g.*, nanohole arrays) operating with a simple collinear transmission or reflection illumination geometry [80], necessitate neither bulky prism-coupling instruments nor sensor moving parts which in turn open up the opportunities for sensor miniaturization and low-cost production. They improve the sensor signal-to-noise ratio through engineered nanostructures such that biomolecular interactions occur in a region of high field strength. The combination of plasmonic sensing and fluid transport has led to the miniaturized biosensor system with the possibility to exploit the flow-through sensing format to improve the sensor response time as compared to the traditional flow-over method (Figure 1.13b) [75]. However, the chip fabrication of nanoplasmonic sensors are expensive and burdensome due to the need of nanopatterning techniques [81].

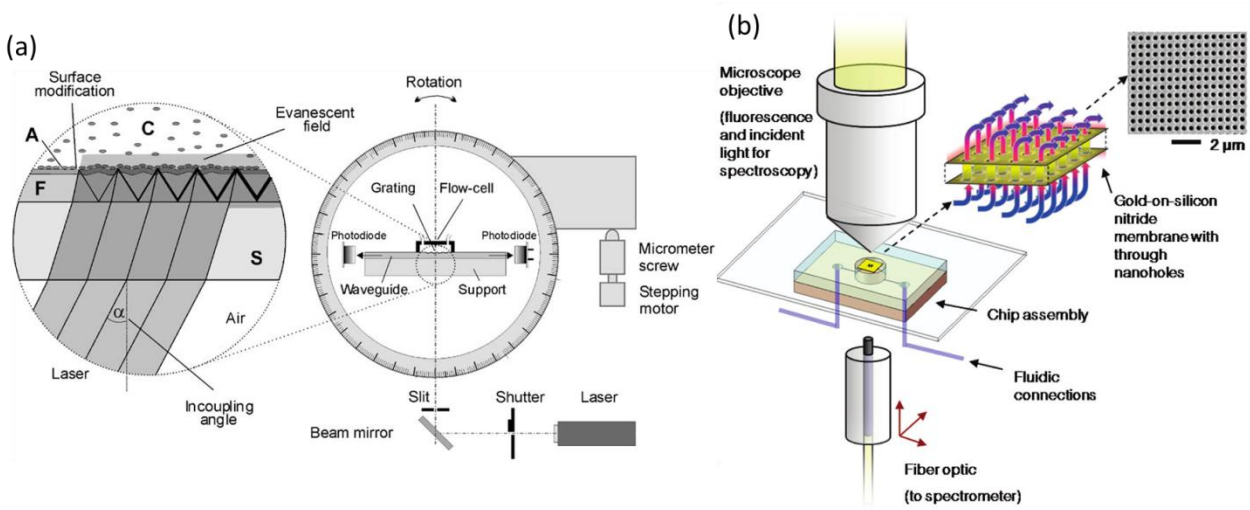

Figure 1.13 (a) Optical setup of an OWLS instrument (from [73]). (b) Flow-through nanoplasmonic sensing (adapted from [75]).

Another ultrasensitive optical method with minimal background interference is SERS. This technique provides limit of detection down to single molecule level by taking advantage of electromagnetic enhancement induced by the localized surface plasmon resonance (LSPR) on noble metal nanostructures and the chemical enhancement [82]. Apart from its intrinsic sensitivity, SERS allows structural and conformational studies of biological components and it is ideal for multiplexed detection and discrimination of target molecules. However, the utility of this powerful technique has been impaired due to the fact that most SERS substrates are expensive and complex to prepare. In

addition, the signal amplified specific locations, or hotspots, are randomly dispersed on the substrate, hence reproducibility and reliable detection are often difficult to achieve [83].

In the last decade, there has been growing interest in emerging electrochemical assays for protein detection due to their low-cost, simplicity, and sensitivity as compared to the optical based instrumentation [84]. In principle, the surface-bound affinity complex is associated with a change in the electrical properties (*e.g.*, current, potential or conductivity) of the reactive layer immobilized on the electrode surface. Label-free electrochemical impedance detection provides possibility to examine binding kinetics of molecules between electrolytes and the electrode surface; for example, small molecules binding to their target proteins (kinases Abl1 and p38-α) [85]. Lately, nanoparticles and carbon nanotubes (CNTs) have been introduced in electrochemical biosensor devices to improve the electrochemical responses [86, 87].

While being sensitive with a label-free operation capability, the electrochemical-based assays rely on electron transfer reactions with electroactive species whereas most clinically relevant biological compounds are not electrochemically active. As a result, a combination of enzymatic reactions to generate an electroactive product is highly needed [88]. Furthermore, the biospecifically bound complex on the electrochemical transducer that shields the surface can cause the interference in electron transfer, resulting in diminished electrical signals [89].

Among semiconductor-based biosensors, ion-sensitive field-effect transistor (IS-FET) and nanowire based field-effect transistor (NW-FET) have attracted much attention in scientific community as new effective and high-throughput approaches in electrical biosensing technology. Due to their extreme miniaturization capability, they are very well-suited for use in micro-total-analysis-systems (μ-TAS). Their sensing principle is based on the change in the drain-source current upon binding of the analyte to the gate electrode modified with biological receptors. Many studies on IS-FET and NW-FET for real-time detection of various kinds of biological entities, such as DNA, proteins, enzymes, and cells, have been previously reported [90-94].

When applying FET-type biosensors for clinical diagnosis, presence of the Debye screening length is of importance since the biomolecular recognitions takes place within this distance (Figure 1.14). As a result, to improve the FET sensitivity, sample desalting is often required prior to analyte detection. Realizing the sensing events under physiological conditions (at high ionic strength) typically decreases the sensing performances, which in turn limits their universal applicability [95, 96].

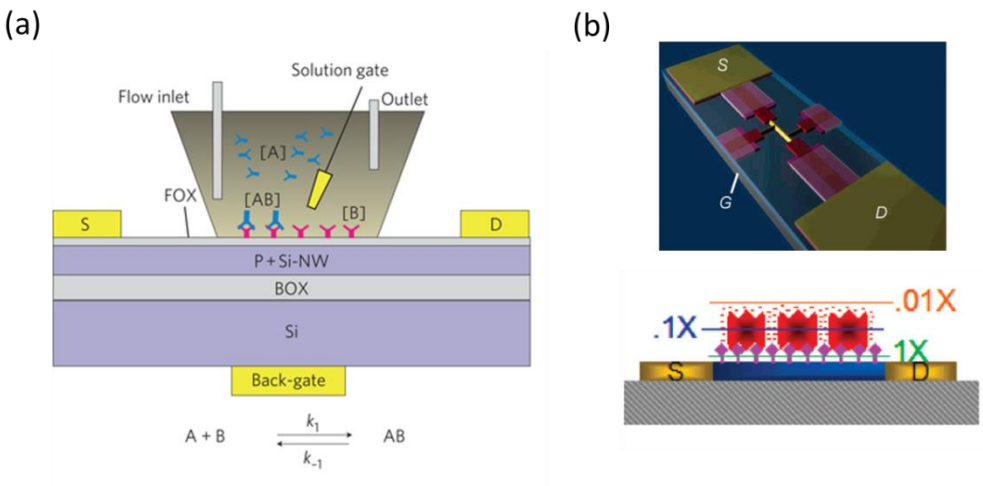

Figure 1.14 (a) Schematic of the Si-NW FET biosensor setup used for kinetic analysis of protein interactions (from [90]). (b) Schematic depicting the impact of Debye screening length (λ_D) on the biomolecular sensing. Increasing the ionic strength of the buffer solution leads to the reduction of the λ_D, thus minimizing device sensitivity (from [96]).

Other promising candidates for label-free detection are mechanical biosensors, owing to their high sensitivity, fast response, and high dynamic range [97]. Quartz crystal microbalance (QCM) is a mass sensor widely employed to characterize biological interactions by continuously measuring changes in the mass adsorbed on the oscillating crystal surface. While QCM measurement is applicable in liquid environments with sensitivity in the nanogram range [98], it requires large sample volumes and is not suitable for high-throughput assays. Other prominent mechanical biosensors are microelectromechanical systems (MEMS). Analyte binding to a microcantilever is detected by measuring the bending of the cantilever induced by the surface stress (static mode) or by measuring the change in mechanical resonant frequency due to the additional mass on the cantilever (dynamic mode) (Figure 1.15). MEMS affinity biosensors have been demonstrated for reliable real-time monitoring of biomolecular interactions of C reactive protein (CRP) antigen-antibody complexes [99], and immunoassay of prostate-specific antigen (PSA) [100].

While MEMS biosensors have enabled real-time analyte monitoring with fast analysis time, the damping effects in liquid environment, causing a low quality factor and thus lowering the sensitivity, are the major caveat in the dynamic-mode operation [101]. Dip-and-dry technique has been practically employed to measure bound target molecules on the cantilever surface. This method however does not allow real-time measurements and thus limits gaining insights into the actual kinetics of biochemical reactions in physiological fluid media [102]. Consequently, real-time biomolecular sensing with liquid-phase measurement using MEMS devices has been barely reported. One way to circumvent the damping problem of the resonators in liquid was proposed by the

Manalis group [103] by integrating the suspended fluidic system within hollow cantilevers while leaving the channel exterior in a gas phase or vacuum.

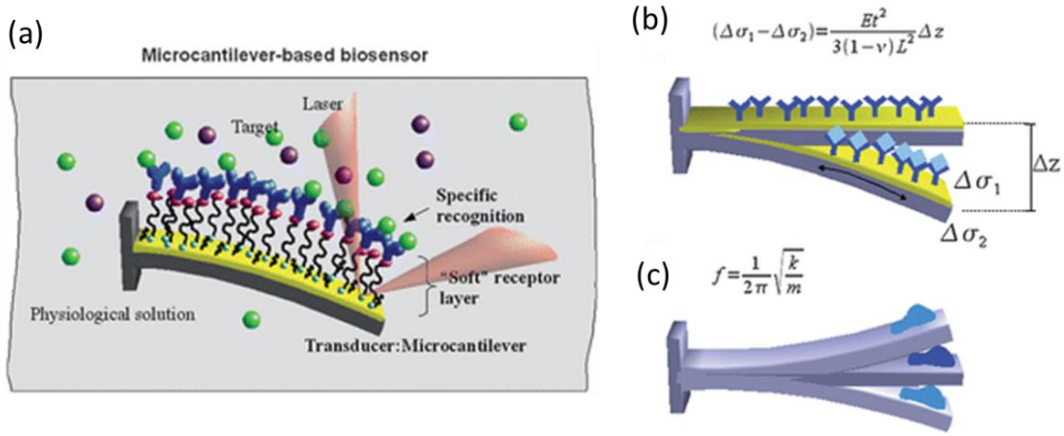

Figure 1.15 Schematic representation of the microcantilever-based biosensor (a) and its operation modes: static (b) and dynamic (c) modes (from [104]).

Although the aforementioned techniques have revolutionizing impacts on the large-scale studies of protein-protein interactions with label-free sensing capability, each technique has its own advantages and drawbacks. As a result, none of them are fully satisfactory. Another approach to study protein binding kinetics lies on fluorescence-based methods thanks to their high sensitivity and versatility.

1.3.2.3 Fluorescence-based methods

Fluorescence-based biophysical technologies are robust and common methods extensively used in proteomics to characterize protein interactions [105]. They appear to be well-suited to complex matrix analyses, such as serum, plasma, or tissues. This is owing to their capability to specifically recognize only the analyte, which is fluorescently-tagged, without interference by highly nonspecific binding from the background. These techniques enable quantitative and semi-quantitative detection by relating the generated signal to the amount of the analyte captured. As opposed to the label-free SPR detection, the analytical methods merging a labelling technique are independent on the molecular weight of the analyte and, thereby, offer considerably higher sensitivity, down to single molecule identification [106]. Regarding clinical applications, labels such as radioactive isotopes and fluorophores have already been widely employed in immunoassays [107].

Concerning new developments, the total-internal-reflection fluorescence (TIRF) microscopy is a powerful analytical tool capable of real-time visualization of reversible interactions of fluorescent

species on the surface with single-fluorophore sensitivity. TIRF imaging confines the illuminated volume to excite the fluorophores in an aqueous environment very close to a solid surface (within 100 nm), thus minimizing the background fluorescence and in turn improving the signal-to-noise ratio [108, 109].

The surface-selective illumination feature of TIRF has been often employed in combination with fluorescence polarization (FP) and fluorescence correlation spectroscopy (FCS) to measure the affinities and reveal the binding kinetics of ligand-receptor interactions; for instance, fluorescently labeled IgG association with mouse receptor FcgammaRII, and human estrogen receptors interaction with their specific ligands [110, 111]. Furthermore, the extraction of kinetic parameters of fluorescently labeled cell-membrane-derived liposomes upon binding to the surface-immobilized antibody fragments has been successfully demonstrated using TIRF setup [112]. The conjugation of TIRF fluorescence microscopy with protein microarrays and a CCD camera also provides a potential means of recording an abundance of binding kinetics in parallel with spatially resolved fluorescence images [113], facilitating the growth of handheld device development (Figure 1.16).

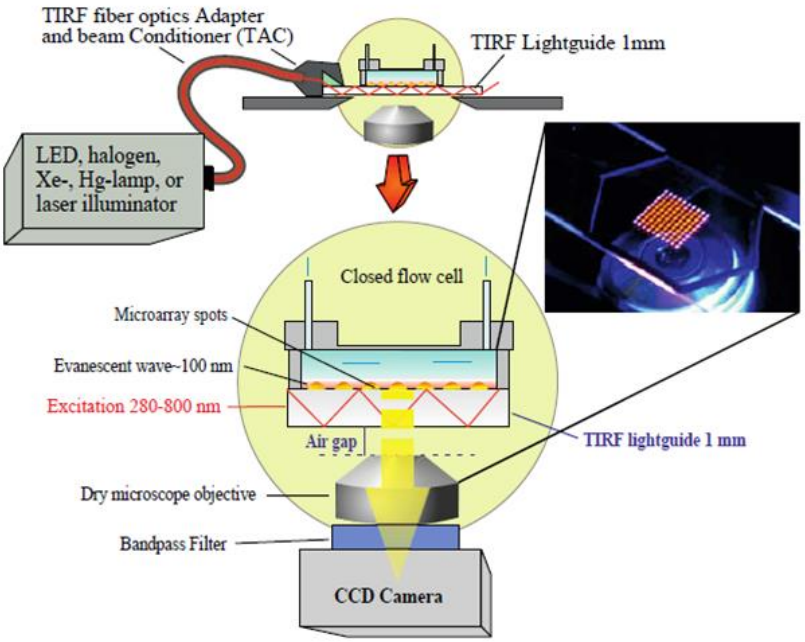

Figure 1.16 A TIRF setup mounted on an inverted microscope and coupled with the light source amenable to produce the evanescent wave needed for TIRF (from [113]). A microarray slide is placed above the microscope objective and multiple binding reactions can be simultaneously monitored via an EM-CCD camera.

Another fluorescence-based technique enabling real-time measurement of biomolecular recognition events is Förster resonance energy transfer (FRET). FRET provides not only kinetic information of the binding partners but also on the conformation changes within complexes. The FRET process involves the energy transfer from an excited fluorescent donor to an adjacent fluorescent receptor molecule via an induced dipole-dipole interaction. The ability of FRET-based approach was noticeable in the work of Li *et al.* [114], in which the binding kinetics of proteins with SNARE complex was determined with a single-molecule resolution. In addition, measuring protein interactions in living cells with high spatial resolution assays using FRET measurements has been demonstrated [115].

These single-molecule fluorescence-based techniques, however, pose several challenges. Firstly, the concentration of fluorescent species should be low enough to maintain low background fluorescence. The highest tolerable concentration is in the range of 10 nM, which becomes a hurdle for single-molecule kinetic study of many biomolecular interactions which occur at higher concentrations [116]. Secondly, the resulting signal is often small due to low excitation intensities of these techniques. Therefore, careful control experiments should be carried out for achieving reliable interpretation of the binding results [117]. To address these issues, a nanostructured device, the zero-mode waveguide, has been developed by H. Craighead and W.W. Webb to enable single-molecule analysis in FCS at high fluorophore concentrations [118].

1.3.2.4 Fluorescence-enhanced label-free sensors

One of the interesting advantages of fluorescence technologies is to increase the binding signal inherently produced from the label-free based biosensors. For instance, fluorescence detection coupled with fiber-optic biosensors (Figure 1.17) is one of most prominent technologies for quantitative measurement of the biomolecular interactions, whereby the bound fluorophore-labeled target adjacent to the fiber surface is excited by the localized evanescence wave. In contrast, the background signal of the unbound fluorescence-labeled molecule outside the evanescence field does not significantly contribute to the total measured fluorescence signal. It has been shown that this method was capable of real-time kinetic measurement of antibody-antigen interactions, such as IgG/anti-mouse IgG and PSA/anti-PSA [119, 120].

Additionally, biosensor sensitivity can be enriched by several orders of magnitude through the emergence of the highly sensitive surface plasmon-enhanced fluorescence spectroscopy (SPFS) [121], allowing the analysis of samples carrying tremendously low analyte concentration. This concept generally offers a way to amplify the signal. Figure 1.18 depicts an optical set-up of surface plasmon resonance biosensor (SPR) combined with fluorescence spectroscopy detection (SPFS). The fluorophores are chosen in such a way that their adsorption bands match the excitation wavelength of the laser. The fluorescence signal emitted from the sensor surface is measured in real-time by a photomultiplier or a CCD camera.

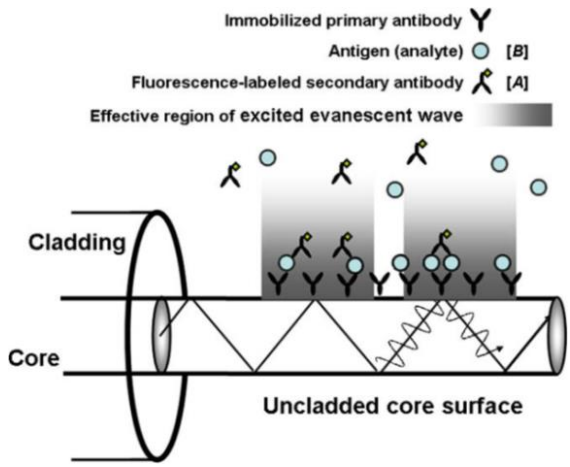

Figure 1.17 Illustration of sandwich immunoassays using fluorescence detection coupled fiber-optic biosensor (from [119]).

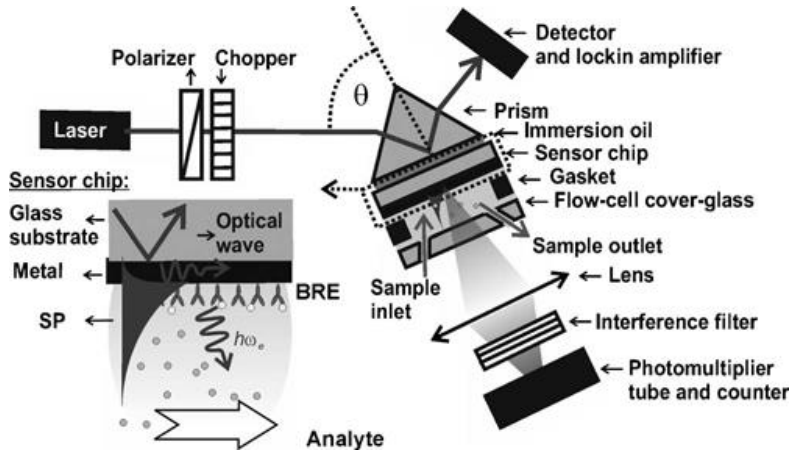

Figure 1.18 An optical biosensor set-up for the combination of angular modulation of surface plasmon resonance (SPR) and surface plasmon fluorescence spectroscopy (SPFS) (from [121]).

The enhanced intensity of the electromagnetic field associated with the coupling to surface plasmons leads to an efficient excitation of surface-confined fluorophore molecules, which is directly translated into a stronger fluorescence signal related to the interfacial binding events. Comparing with TIRF, the enhanced evanescent field displays a profoundly increased signal intensity [122]. Although the fluorescence quenching near the metal surface may pose complications to the SPFS-fluorescence signal [123], this can be overcome by using well-defined dielectric films.

SPFS have found numerous applications in kinetic analysis of binding events between the antibody and its surface-anchored antigen [124, 125].

Furthermore, Episentec has newly developed an add-on tool, called the label-enhanced SPR technology, breaking the performance barriers of the conventional SPR. This new technology aims to enhance the sensitivity and selectivity together with the capability to analyze small molecules and fast kinetic reactions by using Episentec™ dye labels [126]. This concept essentially erases the limitations of both label-free and labeled-based methods in terms of the sensitivity by taking advantage of strongly absorbing dyes, and the capability to probe preceding immobilization steps and obtain a full shape of kinetic sensorgrams.

Since labeling can possibly alter the binding behaviors of the investigated species, care must be taken to validate and select appropriate labels in any particular application [127]. The pitfalls of the necessity of labeling (*i.e.*, cost, laboriousness, and possibly changed biological activities) are therefore compensated by the high sensitivity, thus achieving low limit of detection, when fluorescence is incorporated. These aforementioned examples have clearly proved that the label-based techniques are still up-to-date and readily applicable for investigating binding kinetics of ligand-receptor interactions in complement with the label-free techniques to bring on the biologically meaningful information.

As mentioned above, numerous techniques have been successfully employed to characterize the interactions of proteins that express in soluble form or "soluble proteins". On the other hand, "membrane proteins", proteins that interact with biological membranes, are far more challenging to characterize than soluble proteins due to their hydrophobic nature and the difficulties in purifying these proteins for analysis [128]. For detailed biochemical investigation of membrane proteins, it is essential to incorporate the purified proteins into a lipid bilayer, known as reconstitution, in order to retain their native structure and activity which results in "proteoliposomes" [129]. It was reported that the proteoliposomes could be captured to the designed specific BIAcore chips and their binding kinetics were investigated *in vitro* using conventional surface plasmon resonance platforms [130]. Several groups have attempted to develop newer SPR technologies which allow membrane proteins to be presented in their native or near-native environments. This includes nanopore SPR sensors wherein membrane proteins can be integrated in free-standing lipid bilayers [131]. This approach enables the study of ligand binding to membrane proteins on both sides of the bilayer. Recently, surface plasmon resonance microscopy (SPRM) has been demonstrated for the measurement of binding kinetics of membrane proteins in single living cells [132].

1.4 Challenges in affinity-based biosensor development and the need for alternative answers

Affinity-based biosensors have been rapidly expanding in the field of research through the development of novel methodologies and efficient means of signal transduction (*i.e.*, optical, electrochemical, and mass sensitive methods) to investigate a variety of biomolecular interactions. They have found particular utility in monitoring diseases, proteomics, drug discovery and diagnosis. In clinical applications, end-users are in need for reliable, robust and fully integrated biosensor systems for analyzing complex clinical or biological specimens (such as bloods, urines, tissues). Ultimate affinity-based biosensors should offer highly desired characteristics including ease of use (for non-technical personnel), rapidity, and high throughput at an affordable cost.

Rapid continuous monitoring of biological entities using robust and highly miniaturized signal transducer elements has been an essential driving force toward point-of-care applications. Real-time bioaffinity monitors unquestionably provide detailed information about the biomolecular interactions regarding their affinity and kinetics as opposed to end-point affinity assays. This feature is well-suited for drug development industry especially in pharmacokinetics evaluation, and for assessment of drug efficiency for patients with personalized medicine [133], thus promoting optimal clinical outcomes and public health. In addition, it can be particularly useful for rapid on-site monitoring of infectious diseases and their progression in order to treat them more quickly and efficiently [134]. This is particular important for critical care at the emergency room where accurate and rapid results are required. Despite clinical needs, transforming biosensors from centralized laboratories to clinical applications at the bedside has remained a critical bottleneck in biosensor development. This is mostly caused by persistent challenges in sample preparation associated with the matrix effects as well as system integration [135]. Despite numerous attempts over the past decades, no obvious success has been realized through commercialization of affinity-based biosensors for specific applications in the biomedical market.

Traditional affinity-based biosensors have harnessed labels or label-free methods to meet the requirements of a particular application. Each method has its individual strengths and weaknesses. An SPR-based affinity biosensor is rapidly becoming the method of choice to study a broad range of biomolecule interactions in real-time without the need of labeling. However, this technique is mainly used in research laboratories due to bulky and sophisticated optical instrumentations as well as high cost of the operation and maintenance, which have limited this prevailing technology to few facilities. There is thus the clear need for alternative platform with improved sensor performances in terms of robustness, portability, and cost-effectiveness for use in point-of-care locations or home-based testing. This alternative technology is expected to increase the likelihood of translating highly standardized laboratories toward decentralized and resource-poor settings.

1.5 Conclusion

In this chapter, we have highlighted that kinetic studies of biomolecular interactions, particularly protein-protein recognitions, are central to understanding their cellular functions, offering the possibility to develop new and efficient therapies to treat protein-based diseases (*e.g.*, Alzheimer's disease and cancers). We have detailed the basic protein structures and forces involved in their interactions. A number of analytical methods have been harnessed to elucidate specific protein-protein interactions, which can be classified into solution-based (homogeneous) and surface-based (heterogeneous) approaches. In addition, we have described the methodology to determine affinity and kinetic constants of protein-protein interactions with surface-based assays, which encompasses equilibrium and kinetic analyses.

Particular attention has been placed on the current tools that have been employed to probe protein binding kinetics in real-time. Classical methods relying on solution-based assays have long been used to study rapid protein reactions. However, high reagent consumption has rendered this technology less convenient for the analysis of rare biological samples with limited volume. We have presented the alternative tools which have been newly developed, based on affinity biosensor technology. A variety of biosensing modalities, including label-free, fluorescence-based, and fluorescence-enhanced label-free technologies, have been utilized to probe biorecognition events and allow the extraction of kinetic parameters. Despite a great number of available techniques, the selection of a proper analytical tool depends on the requirements of a given application.

Affinity-based biosensors have found important utility in clinical arena, such as diseases monitoring, drug discovery and personalized medicine. In order to fulfill the clinical needs, considerable efforts should be directed toward the development of cheap, robust, and integrated affinity biosensor systems, ideally suited for point-of-care settings. Biosensors with fast continuous monitoring of biologically important species have been a key to clinical success by providing viable solutions to the patients in a rapid and efficient way. Among numerous prevailing affinity-based biosensors, SPR is a highly mature technology and its main hallmark lies on the capability to probe kinetic reactions of biomolecular interactions in real-time. However, the requirement of expensive and sophisticated optical apparatus inherent to this technique has limited its versatility and accessibility especially for field use, thus illustrating the need for an alternative biosensor platform.

In this PhD framework, we propose fluorescence-based nanofluidic biosensors as a promising alternative to conventional SPR technique. The key objective of this study is to keep the merit of SPR biosensing (real-time detection with kinetic constant extraction), while providing additional benefits such as low-cost, device miniaturization, high sensitivity regardless of analyte mass, and high-throughout. It is anticipated that this alternative tool will open up the opportunity for the development of point-of-care diagnostic devices with true clinical outcomes. The basic introduction of nanofluidics and our innovative platform will be provided in the following chapter.

Bibliography

1. Fabrizi, F., et al., *Kinetics of hepatitis C virus load during hemodialysis: novel perspectives.* J Nephrol, 2003. **16**(4): p. 467-75.
2. Zhou, S., et al., *Therapeutic drugs that behave as mechanism-based inhibitors of cytochrome P450 3A4.* Curr Drug Metab, 2004. **5**(5): p. 415-42.
3. Katsamba, P.S., S. Park, and I.A. Laird-Offringa, *Kinetic studies of RNA-protein interactions using surface plasmon resonance.* Methods, 2002. **26**(2): p. 95-104.
4. Swinney, D.C., *The role of binding kinetics in therapeutically useful drug action.* Curr Opin Drug Discov Devel, 2009. **12**(1): p. 31-9.
5. Hughes, J.P., et al., *Principles of early drug discovery.* British Journal of Pharmacology, 2011. **162**(6): p. 1239-1249.
6. Cimitan, S., et al., *Early Absorption and Distribution Analysis of Antitumor and Anti-AIDS Drugs: Lipid Membrane and Plasma Protein Interactions.* Journal of Medicinal Chemistry, 2005. **48**(10): p. 3536-3546.
7. Langley, J.N., *On the reaction of cells and of nerve-endings to certain poisons, chiefly as regards the reaction of striated muscle to nicotine and to curari.* The Journal of Physiology, 1905. **33**(4-5): p. 374-413.
8. Gustafsson, S.S., et al., *Quantification of interactions between drug leads and serum proteins by use of "binding efficiency".* Anal Biochem, 2011. **409**(2): p. 163-75.
9. Núñez, S., J. Venhorst, and C.G. Kruse, *Target–drug interactions: first principles and their application to drug discovery.* Drug Discovery Today, 2012. **17**(1–2): p. 10-22.
10. Lu, H. and P.J. Tonge, *Drug-Target Residence Time: Critical Information for Lead Optimization.* Current opinion in chemical biology, 2010. **14**(4): p. 467-474.
11. Pan, A.C., et al., *Molecular determinants of drug–receptor binding kinetics.* Drug Discovery Today, 2013. **18**(13–14): p. 667-673.
12. Wang, W., et al., *In situ drug-receptor binding kinetics in single cells: a quantitative label-free study of anti-tumor drug resistance.* Sci. Rep., 2014. **4**.
13. Vugmeyster, Y., et al., *Pharmacokinetics and toxicology of therapeutic proteins: Advances and challenges.* World Journal of Biological Chemistry, 2012. **3**(4): p. 73-92.
14. *Introducing BLItz™ - label-free protein assays in a drop*. FORTEBIO [cited 2015 June]; Available from: http://www.mscience.co.nz/view/proteomics/fortebio.
15. Regnault, V., et al., *Immunopurification of human β2-glycoprotein I with a monoclonal antibody selected for its binding kinetics using a surface plasmon resonance biosensor.* Journal of Immunological Methods, 1998. **211**(1–2): p. 191-197.
16. Linderstrom-Lang, K.U., Schellman, J.A., *Protein structure and enzyme activity*, in *In the Enzymes*. 1959, Academic Press: New York.
17. Berg, J.M., Tymoczko, J.L., Stryer, L., *Section 3.5 Quaternary structure: polypeptide chains can assemble into multisubunit structures*, in *Biochemistry*. 2002, W.H. Freeman: New York.
18. Carr, S.M. *Four levels of protein structure*. 2014 [cited 2015 June]; Available from: http://www.mun.ca/biology/scarr/iGen3_06-04.html.
19. Chiti, F. and C.M. Dobson, *Protein misfolding, functional amyloid, and human disease.* Annu Rev Biochem, 2006. **75**: p. 333-66.

20. De Las Rivas, J. and C. Fontanillo, *Protein-protein interaction networks: unraveling the wiring of molecular machines within the cell.* Brief Funct Genomics, 2012. **11**(6): p. 489-96.
21. Archakov, A.I., et al., *Protein-protein interactions as a target for drugs in proteomics.* Proteomics, 2003. **3**(4): p. 380-91.
22. Betts, M.J. and M.J.E. Sternberg, *An analysis of conformational changes on protein–protein association: implications for predictive docking.* Protein Engineering, 1999. **12**(4): p. 271-283.
23. Alberts, B., Johnson, A. Lewis, J. et al., *Protein function*, in *Molecular biology of the cell.* 2002, Garland Science: New York.
24. Alberts, B., Johnson, A. Lewis, J. et al., *The adaptive immune system*, in *Molecular biology of the cell.* 2002, Garland Science: New York.
25. Woof, J.M. and D.R. Burton, *Human antibody-Fc receptor interactions illuminated by crystal structures.* Nat Rev Immunol, 2004. **4**(2): p. 89-99.
26. Kumagai, I. and K. Tsumoto, *Antigen–Antibody Binding*, in *eLS*. 2001, John Wiley & Sons, Ltd.
27. Bruce, A., Dennis, B. et al. , *Essential cell biology*. 2th ed. 2004, New York: Garland Science.
28. Moore, G., Knight, G., Blann, A., *Haematology*. 2010: OUP Oxford.
29. Goldstein, B. and M. Dembo, *Approximating the effects of diffusion on reversible reactions at the cell surface: ligand-receptor kinetics.* Biophys J, 1995. **68**(4): p. 1222-30.
30. Hoffman, T.L., et al., *A biosensor assay for studying ligand-membrane receptor interactions: Binding of antibodies and HIV-1 Env to chemokine receptors.* Proceedings of the National Academy of Sciences of the United States of America, 2000. **97**(21): p. 11215-11220.
31. Schreiber, G., *Protein-protein interactions*, in *Biomolecular sensors*. 2002, CRC press.
32. Firestone, M.A., et al., *Film Architecture in Biomolecular Assemblies. Effect of Linker on the Orientation of Genetically Engineered Surface-Bound Proteins.* Journal of the American Chemical Society, 1996. **118**(38): p. 9033-9041.
33. Vijayendran, R.A. and D.E. Leckband, *A Quantitative Assessment of Heterogeneity for Surface-Immobilized Proteins.* Analytical Chemistry, 2001. **73**(3): p. 471-480.
34. Day, Y.S.N., et al., *Direct comparison of binding equilibrium, thermodynamic, and rate constants determined by surface- and solution-based biophysical methods.* Protein Science, 2002. **11**(5): p. 1017-1025.
35. Pollard, T.D., *A guide to simple and informative binding assays.* Mol Biol Cell, 2010. **21**(23): p. 4061-7.
36. Cooper, M.A., *Label free biosensors: techniques and applications*. 2009: Cambridge University Press.
37. Hulme, E.C. and M.A. Trevethick, *Ligand binding assays at equilibrium: validation and interpretation.* Br J Pharmacol, 2010. **161**(6): p. 1219-37.
38. Kuriyan, J., Konforti, B., Wemmer, D., *The Molecular of Life: Physical and Chemical Principles*. 2013: Garland Science.
39. Jason-Moller, L., M. Murphy, and J. Bruno, *Overview of Biacore systems and their applications.* Curr Protoc Protein Sci, 2006. **19**(19).
40. Chaiken, I., S. Rose, and R. Karlsson, *Analysis of macromolecular interactions using immobilized ligands.* Anal Biochem, 1992. **201**(2): p. 197-210.
41. Nice, E.C. and B. Catimel, *Instrumental biosensors: new perspectives for the analysis of biomolecular interactions.* Bioessays, 1999. **21**(4): p. 339-52.
42. Fagerstam, L.G., et al., *Biospecific interaction analysis using surface plasmon resonance detection applied to kinetic, binding site and concentration analysis.* J Chromatogr, 1992. **597**(1-2): p. 397-410.
43. Edwards, P.R., et al., *Kinetics of protein-protein interactions at the surface of an optical biosensor.* Anal Biochem, 1995. **231**(1): p. 210-7.

44. Edwards, P.R., P.A. Lowe, and R.J. Leatherbarrow, *Ligand loading at the surface of an optical biosensor and its effect upon the kinetics of protein-protein interactions.* J Mol Recognit, 1997. **10**(3): p. 128-34.
45. Rich, R.L. and D.G. Myszka, *Advances in surface plasmon resonance biosensor analysis.* Current Opinion in Biotechnology, 2000. **11**(1): p. 54-61.
46. Yu, Q., et al., *Anti-fouling bioactive surfaces.* Acta Biomater, 2011. **7**(4): p. 1550-7.
47. Wachsstock, D.H. and T.D. Pollard, *Transient state kinetics tutorial using the kinetics simulation program, KINSIM.* Biophys J, 1994. **67**(3): p. 1260-73.
48. Hartwell, S.K. and K. Grudpan, *Flow-Based Systems for Rapid and High-Precision Enzyme Kinetics Studies.* Journal of Analytical Methods in Chemistry, 2012. **2012**: p. 10.
49. Hartridge, H. and F.J.W. Roughton, *A Method of Measuring the Velocity of Very Rapid Chemical Reactions.* Proceedings of the Royal Society of London A: Mathematical, Physical and Engineering Sciences, 1923. **104**(726): p. 376-394.
50. Jia, Y., A. Kumar, and S.S. Patel, *Equilibrium and stopped-flow kinetic studies of interaction between T7 RNA polymerase and its promoters measured by protein and 2-aminopurine fluorescence changes.* J Biol Chem, 1996. **271**(48): p. 30451-8.
51. Wallis, R., et al., *Protein-Protein Interactions in Colicin E9 DNase-Immunity Protein Complexes. 1. Diffusion-Controlled Association and Femtomolar Binding for the Cognate Complex.* Biochemistry, 1995. **34**(42): p. 13743-13750.
52. Christianson, M.D., E.H.P. Tan, and C.R. Landis, *Stopped-Flow NMR: Determining the Kinetics of [rac-(C2H4(1-indenyl)2)ZrMe][MeB(C6F5)3]-Catalyzed Polymerization of 1-Hexene by Direct Observation.* Journal of the American Chemical Society, 2010. **132**(33): p. 11461-11463.
53. Qu, K., et al., *Kinetics and motional dynamics of spin-labeled yeast iso-1-cytochrome c: 1. Stopped-flow electron paramagnetic resonance as a probe for protein folding/unfolding of the C-terminal helix spin-labeled at cysteine 102.* Biochemistry, 1997. **36**(10): p. 2884-97.
54. Coles, B., et al., *The spontaneous and enzymatic reaction of N-acetyl-p-benzoquinonimine with glutathione: a stopped-flow kinetic study.* Arch Biochem Biophys, 1988. **264**(1): p. 253-60.
55. Roder, H., et al., *Rapid mixing methods for exploring the kinetics of protein folding.* Methods, 2004. **34**(1): p. 15-27.
56. Olsen, K., B. Svensson, and U. Christensen, *Stopped-flow fluorescence and steady-state kinetic studies of ligand-binding reactions of glucoamylase from Aspergillus niger.* Eur J Biochem, 1992. **209**(2): p. 777-84.
57. Hargrove, M.S., *Ligand binding with stopped-flow rapid mixing.* Methods Mol Biol, 2005. **305**: p. 323-42.
58. Harvey, D. *13B: Chemical Kinetics.* [cited 2015 June]; Available from: http://chemwiki.ucdavis.edu/Analytical_Chemistry/Analytical_Chemistry_2.0/13_Kinetic_Methods/13B%3A_Chemical_Kinetics.
59. Boozer, C., et al., *Looking towards label-free biomolecular interaction analysis in a high-throughput format: a review of new surface plasmon resonance technologies.* Curr Opin Biotechnol, 2006. **17**(4): p. 400-5.
60. Kingsmore, S.F., *Multiplexed protein measurement: technologies and applications of protein and antibody arrays.* Nature reviews. Drug discovery, 2006. **5**(4): p. 310-320.
61. Turner, A.P., *Biosensors: sense and sensibility.* Chem Soc Rev, 2013. **42**(8): p. 3184-96.
62. Kirsch, J., et al., *Biosensor technology: recent advances in threat agent detection and medicine.* Chem Soc Rev, 2013. **42**(22): p. 8733-68.
63. Abdiche, Y., et al., *Determining kinetics and affinities of protein interactions using a parallel real-time label-free biosensor, the Octet.* Anal Biochem, 2008. **377**(2): p. 209-17.

64. Zhang, X., Q. Guo, and D. Cui, *Recent Advances in Nanotechnology Applied to Biosensors.* Sensors (Basel, Switzerland), 2009. **9**(2): p. 1033-1053.
65. Malmqvist, M. and R. Karlsson, *Biomolecular interaction analysis: affinity biosensor technologies for functional analysis of proteins.* Curr. Opin. Chem. Biol., 1997. **1**(3): p. 378-83.
66. Myszka, D.G. and R.L. Rich, *Implementing surface plasmon resonance biosensors in drug discovery.* Pharm. Sci. Technol. To., 2000. **3**(9): p. 310-317.
67. Speight, R.E. and M.A. Cooper, *A survey of the 2010 quartz crystal microbalance literature.* J Mol Recognit, 2012. **25**(9): p. 451-73.
68. Jung, S.O., et al., *Surface plasmon resonance imaging-based protein arrays for high-throughput screening of protein-protein interaction inhibitors.* Proteomics, 2005. **5**(17): p. 4427-31.
69. Nand, A., et al., *In situ protein microarrays capable of real-time kinetics analysis based on surface plasmon resonance imaging.* Analytical Biochemistry, 2014. **464**(0): p. 30-35.
70. Linman, M.J., A. Abbas, and Q. Cheng, *Interface design and multiplexed analysis with surface plasmon resonance (SPR) spectroscopy and SPR imaging.* Analyst, 2010. **135**(11): p. 2759-2767.
71. Nguyen, B., F.A. Tanious, and W.D. Wilson, *Biosensor-surface plasmon resonance: quantitative analysis of small molecule-nucleic acid interactions.* Methods, 2007. **42**(2): p. 150-61.
72. Chinowsky, T.M., et al., *Portable 24-analyte surface plasmon resonance instruments for rapid, versatile biodetection.* Biosensors and Bioelectronics, 2007. **22**(9–10): p. 2268-2275.
73. Vörös, J., et al., *Optical grating coupler biosensors.* Biomaterials, 2002. **23**(17): p. 3699-3710.
74. Höök, F., et al., *A comparative study of protein adsorption on titanium oxide surfaces using in situ ellipsometry, optical waveguide lightmode spectroscopy, and quartz crystal microbalance/dissipation.* Colloids and Surfaces B: Biointerfaces, 2002. **24**(2): p. 155-170.
75. Eftekhari, F., et al., *Nanoholes As Nanochannels: Flow-through Plasmonic Sensing.* Analytical Chemistry, 2009. **81**(11): p. 4308-4311.
76. Jonsson, M.P., et al., *Locally Functionalized Short-Range Ordered Nanoplasmonic Pores for Bioanalytical Sensing.* Analytical Chemistry, 2010. **82**(5): p. 2087-2094.
77. Li, T., L. Guo, and Z. Wang, *Gold nanoparticle-based surface enhanced Raman scattering spectroscopic assay for the detection of protein-protein interactions.* Anal Sci, 2008. **24**(7): p. 907-10.
78. Horváth, R., et al., *Optical waveguide sensor for on-line monitoring of bacteria.* Optics Letters, 2003. **28**(14): p. 1233-1235.
79. Lukosz, W., *Principles and sensitivities of integrated optical and surface plasmon sensors for direct affinity sensing and immunosensing.* Biosensors and Bioelectronics, 1991. **6**(3): p. 215-225.
80. Brolo, A.G., *Plasmonics for future biosensors.* Nat Photon, 2012. **6**(11): p. 709-713.
81. Dahlin, A.B., et al., *Promises and Challenges of Nanoplasmonic Devices for Refractometric Biosensing.* Nanophotonics, 2013. **2**(2): p. 83-101.
82. Kneipp, K., et al., *Ultrasensitive chemical analysis by Raman spectroscopy.* Chem Rev, 1999. **99**(10): p. 2957-76.
83. Liberman, V., et al., *A Nanoparticle Convective Directed Assembly Process for the Fabrication of Periodic Surface Enhanced Raman Spectroscopy Substrates.* Advanced Materials, 2010. **22**(38): p. 4298-4302.
84. Herzog, G. and D.W. Arrigan, *Electrochemical strategies for the label-free detection of amino acids, peptides and proteins.* Analyst, 2007. **132**(7): p. 615-32.
85. Liang, W., et al., *Measurement of Small Molecule Binding Kinetics on a Protein Microarray by Plasmonic-Based Electrochemical Impedance Imaging.* Analytical Chemistry, 2014. **86**(19): p. 9860-9865.
86. Zhang, J., B.P. Ting, and J.Y. Ying, *Theoretical assessment of binding and mass-transport effects in electrochemical affinity biosensors that utilize nanoparticle labels for signal amplification.* Chemistry, 2012. **18**(47): p. 15167-77.

87. Wang, J. and Y. Lin, *Functionalized carbon nanotubes and nanofibers for biosensing applications.* Trends Analyt Chem, 2008. **27**(7): p. 619-626.
88. Michael, A.C., L.M. Borland, *Electrochemical Methods for Neuroscience*. 2007: CRC Press.
89. Laschi, S., S. Centi, and M. Mascini, *Electrochemical arrays coupled with magnetic separators for immunochemistry.* Bioanalytical Reviews, 2011. **3**(1): p. 11-25.
90. Duan, X., et al., *Quantification of the affinities and kinetics of protein interactions using silicon nanowire biosensors.* Nat Nano, 2012. **7**(6): p. 401-407.
91. Stern, E., A. Vacic, and M.A. Reed, *Semiconducting Nanowire Field-Effect Transistor Biomolecular Sensors.* Electron Devices, IEEE Transactions on, 2008. **55**(11): p. 3119-3130.
92. Chen, K.-I., B.-R. Li, and Y.-T. Chen, *Silicon nanowire field-effect transistor-based biosensors for biomedical diagnosis and cellular recording investigation.* Nano Today, 2011. **6**(2): p. 131-154.
93. Estrela, P., et al., *Field effect detection of biomolecular interactions.* Electrochimica Acta, 2005. **50**(25–26): p. 4995-5000.
94. Yeung, C.K., et al., *Validation of the use of field effect transistors for extracellular signal recording in pharmacological bioassays.* J Pharmacol Toxicol Methods, 2001. **45**(3): p. 207-14.
95. Balasubramanian, K., *Challenges in the use of 1D nanostructures for on-chip biosensing and diagnostics: a review.* Biosens Bioelectron, 2010. **26**(4): p. 1195-204.
96. Stern, E., et al., *Importance of the Debye Screening Length on Nanowire Field Effect Transistor Sensors.* Nano Letters, 2007. **7**(11): p. 3405-3409.
97. Arlett, J.L., E.B. Myers, and M.L. Roukes, *Comparative advantages of mechanical biosensors.* Nat Nano, 2011. **6**(4): p. 203-215.
98. Kim, N., D.-K. Kim, and Y.-J. Cho, *Development of indirect-competitive quartz crystal microbalance immunosensor for C-reactive protein.* Sensors and Actuators B: Chemical, 2009. **143**(1): p. 444-448.
99. Kwon, T.Y., et al., *In situ real-time monitoring of biomolecular interactions based on resonating microcantilevers immersed in a viscous fluid.* Applied Physics Letters, 2007. **90**(22): p. 223903.
100. Wu, G., et al., *Bioassay of prostate-specific antigen (PSA) using microcantilevers.* Nat Biotechnol, 2001. **19**(9): p. 856-60.
101. Hansen, K.M. and T. Thundat, *Microcantilever biosensors.* Methods, 2005. **37**(1): p. 57-64.
102. Kwon, T., et al., *Micromechanical observation of the kinetics of biomolecular interactions.* Applied Physics Letters, 2008. **93**(17): p. -.
103. Burg, T.P., et al., *Weighing of biomolecules, single cells and single nanoparticles in fluid.* Nature, 2007. **446**(7139): p. 1066-1069.
104. Alvarez, M. and L.M. Lechuga, *Microcantilever-based platforms as biosensing tools.* Analyst, 2010. **135**(5): p. 827-836.
105. Yan, Y. and G. Marriott, *Analysis of protein interactions using fluorescence technologies.* Curr Opin Chem Biol, 2003. **7**(5): p. 635-40.
106. Weiss, S., *Fluorescence Spectroscopy of Single Biomolecules.* Science, 1999. **283**(5408): p. 1676-1683.
107. Luppa, P.B., L.J. Sokoll, and D.W. Chan, *Immunosensors—principles and applications to clinical chemistry.* Clinica Chimica Acta, 2001. **314**(1–2): p. 1-26.
108. Schneckenburger, H., *Total internal reflection fluorescence microscopy: technical innovations and novel applications.* Curr. Opin. Biotechnol., 2005. **16**(1): p. 13-8.
109. Lakowicz, J.R., *Principles of Fluorescence Spectroscopy*. 3rd ed. 2006, New York: Springer.
110. Kwok, K.C. and N.H. Cheung, *Measuring binding kinetics of ligands with tethered receptors by fluorescence polarization and total internal reflection fluorescence.* Anal. Chem., 2010. **82**(9): p. 3819-25.
111. Lieto, A.M., R.C. Cush, and N.L. Thompson, *Ligand-receptor kinetics measured by total internal reflection with fluorescence correlation spectroscopy.* Biophys. J., 2003. **85**(5): p. 3294-302.
112. Gunnarsson, A., et al., *Kinetics of Ligand Binding to Membrane Receptors from Equilibrium Fluctuation Analysis of Single Binding Events.* J. Am. Chem. Soc., 2011. **133**(38): p. 14852-14855.

113. Asanov, A., A. Zepeda, and L. Vaca, *A platform for combined DNA and protein microarrays based on total internal reflection fluorescence.* Sensors, 2012. **12**(2): p. 1800-15.
114. Li, Y., G.J. Augustine, and K. Weninger, *Kinetics of complexin binding to the SNARE complex: correcting single molecule FRET measurements for hidden events.* Biophys J, 2007. **93**(6): p. 2178-87.
115. Day, R.N. and M.W. Davidson, *Fluorescent proteins for FRET microscopy: monitoring protein interactions in living cells.* BioEssays : news and reviews in molecular, cellular and developmental biology, 2012. **34**(5): p. 341-350.
116. van Oijen, A.M., *Single-molecule approaches to characterizing kinetics of biomolecular interactions.* Curr Opin Biotechnol, 2011. **22**(1): p. 75-80.
117. Piston, D.W. and G.-J. Kremers, *Fluorescent protein FRET: the good, the bad and the ugly.* Trends in Biochemical Sciences, 2007. **32**(9): p. 407-414.
118. Levene, M.J., et al., *Zero-mode waveguides for single-molecule analysis at high concentrations.* Science, 2003. **299**(5607): p. 682-6.
119. Lin, C.H., et al., *Quantitative measurement of binding kinetics in sandwich assay using a fluorescence detection fiber-optic biosensor.* Anal Biochem, 2009. **385**(2): p. 224-8.
120. Su, L.-C., et al., *Binding Kinetics of Biomolecule Interaction at Ultralow Concentrations Based on Gold Nanoparticle Enhancement.* Analytical Chemistry, 2011. **83**(9): p. 3290-3296.
121. Dostálek, J. and W. Knoll, *Biosensors based on surface plasmon-enhanced fluorescence spectroscopy (Review).* Biointerphases, 2008. **3**(3): p. FD12-FD22.
122. Liebermann, T. and W. Knoll, *Surface-plasmon field-enhanced fluorescence spectroscopy.* Colloids and Surfaces A: Physicochemical and Engineering Aspects, 2000. **171**(1–3): p. 115-130.
123. Ekgasit, S., F. Yu, and W. Knoll, *Fluorescence intensity in surface-plasmon field-enhanced fluorescence spectroscopy.* Sensors and Actuators B: Chemical, 2005. **104**(2): p. 294-301.
124. Yu, F., D. Yao, and W. Knoll, *Surface Plasmon Field-Enhanced Fluorescence Spectroscopy Studies of the Interaction between an Antibody and Its Surface-Coupled Antigen.* Analytical Chemistry, 2003. **75**(11): p. 2610-2617.
125. Knoll, W., et al., *Supramolecular interfacial architectures for optical biosensing with surface plasmons.* Surface Science, 2004. **570**(1–2): p. 30-42.
126. Granqvist, N., et al., *Label-Enhanced Surface Plasmon Resonance: A New Concept for Improved Performance in Optical Biosensor Analysis.* Sensors, 2013. **13**(11): p. 15348-15363.
127. Yin, L., et al., *How does fluorescent labeling affect the binding kinetics of proteins with intact cells?* Biosens Bioelectron, 2015. **66**: p. 412-6.
128. Daley, D.O., *The assembly of membrane proteins into complexes.* Curr Opin Struct Biol, 2008. **18**(4): p. 420-4.
129. Rigaud, J.L. and D. Levy, *Reconstitution of membrane proteins into liposomes.* Methods Enzymol, 2003. **372**: p. 65-86.
130. Maynard, J.A., et al., *Next generation SPR technology of membrane-bound proteins for ligand screening and biomarker discovery.* Biotechnology Journal, 2009. **4**(11): p. 1542-1558.
131. Im, H., et al., *Membrane protein biosensing with plasmonic nanopore arrays and pore-spanning lipid membranes.* Chemical science (Royal Society of Chemistry : 2010), 2010. **1**(6): p. 688-696.
132. Wang, W., et al., *Label-free measuring and mapping of binding kinetics of membrane proteins in single living cells.* Nat Chem, 2012. **4**(10): p. 846-853.
133. Gross, A.S., *Best practice in therapeutic drug monitoring.* British Journal of Clinical Pharmacology, 1998. **46**(2): p. 95-99.
134. Pejcic, B., R.D. Marco, and G. Parkinson, *The role of biosensors in the detection of emerging infectious diseases.* Analyst, 2006. **131**(10): p. 1079-1090.
135. Sin, M.L., et al., *Advances and challenges in biosensor-based diagnosis of infectious diseases.* Expert Rev Mol Diagn, 2014. **14**(2): p. 225-44.

Chapter 2

Nanofluidic: Miniaturized systems as an alternative answer for kinetic study

This chapter gives an introduction to the field of nanofluidics, the technology used throughout this work as an alternative tool for kinetic studies. We introduce the concept of the extended nanospace - a new dimension that bridges the gap between current nano- and microtechnologies, followed by the leading applications of nanofluidic systems, such as bioseperation, pre-concentration, and single-molecule analysis. We present current achievements of biosensing and kinetic studies using nanofluidic devices and some issues related to the realization and the use of nanofluidic biosensors. In addition, particular emphasis is placed on the concept and unique features of our approach to accomplish real-time kinetic studies. Finally, the interplay of mass transport and surface reaction in surface-based biosensors are described along with specific dimensionless numbers used as figures of merit, which are crucial indicators to define the operational regime of our biosensor system.

2.1 Introduction to nanofluidics

2.1.1 What is nanofluidics?

Over the last decades, there has been growing desire to use miniaturized systems in order to tackle fundamental physical and biological questions. Inspired from the great success of commercial integrated microelectronic circuits in the 1960s, **microfluidic** technology has emerged in the early 1980s as part of the development of biochips and microelectro-mechanical systems (MEMS) [1]. Microfluidics allows the control and manipulation of fluids on a small scale with operational lengths in the 1-100 μm range. It has recently attracted significant attention due to its unique features with a "sample-in", "answer-out" capability [2]. The striking qualities of microfluidics include small device footprint, reduced sample and reagent volume, enhanced analytical performances as compared to macroscale systems, facile integration and automation, and high throughput analysis. These features have led to tremendous applications offered by microfluidics ranging from biomedical arena, such as drug delivery, chemical and biochemical sensors, micromixers and microseparators, to non-biomedical applications, such as water purification and design of batteries and fuel cells.

On the other hand, **nanofluidics** is generally defined as the study and application of fluid flows in nanometer-sized systems with a length scale of 1-100 nm in at least one dimension [3]. The typical length scales of micro- and nanofluidics are shown in Figure 2.1. Nanofluidics has appeared not as an extension or advancement of the existing microfluidic systems, but rather as an unprecedented route for discovering a new range of phenomena that do not exist at the microscale [4].

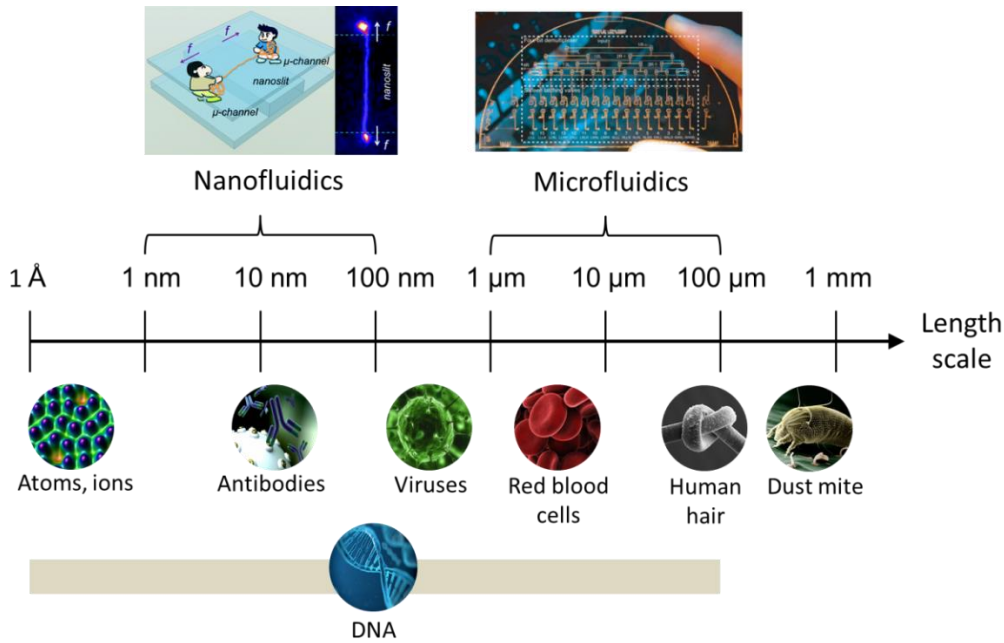

Figure 2.1 Length scales of microfluidics, nanofluidics, and relevant biological objects (adapted from [5-7]).

Indeed, nanofluidics is a highly motivating area but it is not entirely a new field of research. It has already been addressed in the past. For example, natural nanoporous materials (*e.g.*, zeolite), membranes or gels have been used as porous catalysts in petroleum industries [8] and mimic natural molecular filters [9], such as renal filtration system in our body [10]. However, uncontrollable structure geometries and sizes of such classical nanopores/membranes have limited our understanding of these systems.

Recent advances in micro- and nanotechnologies have made possible the fabrication of well-defined, deterministic networks of nanochannels/pores whose dimensions are close to the biological objects, such as DNA strands or antibodies [11]. The captivating effects inherent to nanofluidic devices have opened a new window not only to explore and identify fundamental phenomena of biological systems which have been previously inaccessible, but also for practical chemical and biological analysis. At this length scale, the enhanced electric fields obtained at low voltages can be applied to concentrate molecules, separate biological components, as well as enable DNA sequencing and single biomolecule detection. Due to the enormous potential of nanofluidics for a wide range of applications, it has been noticeable as a remarkable tool for biophysicists.

Nanofluidic devices can be classified according to their degree of confinement (*i.e.*, the number of dimensions that are not confined to the nanometer scale). For example, 1D channel has one dimension in micro/macro scale while the other two dimensions in the nanoscale. As a result, the aspect ratio (AR) between the height and the width of the cross-section is a figure of merit of

nanochannels (Figure 2.2). A large number of technological choices, mainly based on top-down approaches, are now available for nanochannel fabrication, depending on the device geometries and desired applications [12]. **Square or circular nanochannels** (**1D**), offering ultimate confinement in two dimensions, usually have near-unity AR and are complicated and expensive to fabricate since they necessitate the use of dedicated tools, such as nanopatterning techniques (*e.g.*, electron beam lithography (EBL), focused ion beam (FIB)). However, 1D nanochannels can also simply be obtained through the realization of porous membranes using alternative fabrication techniques such as anodization [13]. On the other hand, low aspect ratio **planar nanochannels** that offer nanometer-scale confinement in only one dimension (channel height) and often referred as **2D nanoslits**, are easy to fabricate using standard lithography tools. Finally, the fabrication of high aspect ratio (HAR) 2D vertical nanochannels with nanometer-sized width is more delicate since it is usually carried out by deep reactive ion etching and deposition approach or edge lithography, and spacer technique [14, 15]. HAR nanochannels are commonly made in an array format which leads to a high level of integration and a high throughput [16].

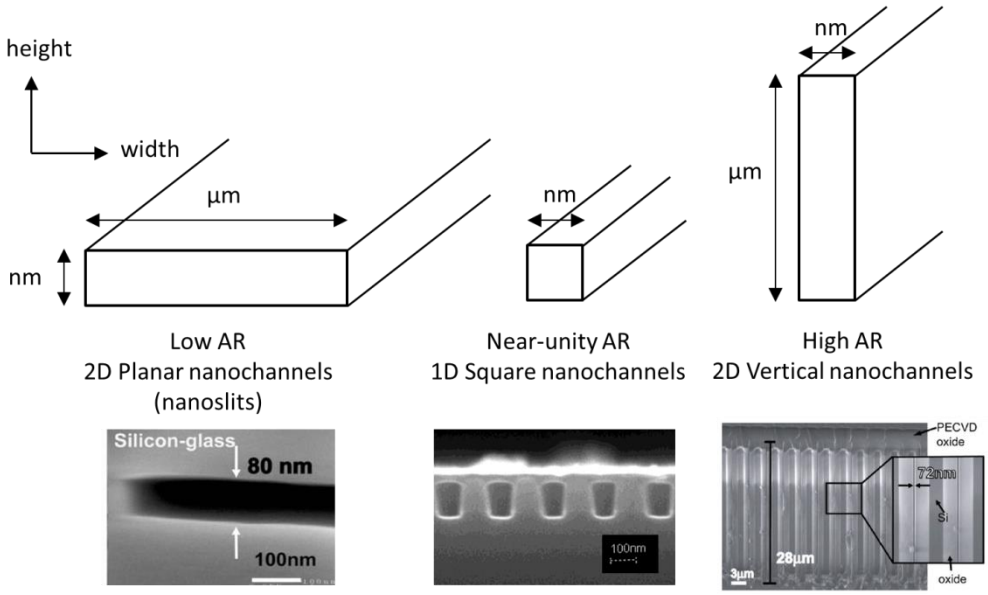

Figure 2.2 Different classes of nanochannel geometries according to their aspect ratios between the height and the width of the cross-section (adapted from [11, 16-18]).

Due to the multidisciplinary approach of the nanofluidic realm, there are many other disciplines involved in the realization, the understanding and the use of nanofluidic devices (Figure 2.3). Throughout this work, we have used scientific and engineering approaches and disciplines, such as surface chemistry, physics of fluids, and micro/nanoengineering, to achieve the goal of our study.

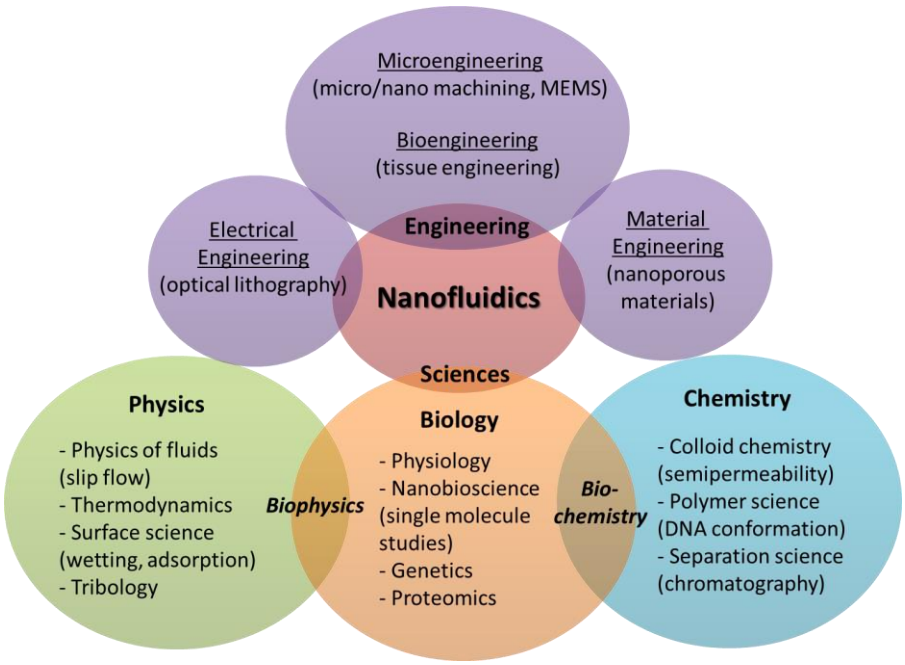

Figure 2.3 Classical disciplines of science and engineering related to nanofluidics (adapted from [19]).

2.1.2 Extended nanospace – a new gap between nano-and microdevices

The 10^1-10^3 nm length scale, referred as the "**extended nanospace**", bridges the gap between conventional nano-objects (1-10 nm, *e.g.*, carbon nanotubes) and microfluidic devices (1-1000 μm) (Figure 2.4). The fluidic properties and chemical reactions in such transient space have not been well explored due to the lack of fundamental research tools.

Kitamori's group proposed and developed the methodologies, relying on nanofabrication, fluidic control, surface modification, and detection methods, to study unique phenomena (*e.g.*, related to liquid properties) occurring in the extended nanospace [20]. They demonstrated novel applications of the extended nanofluidic systems which are unachievable using microfluidics [21]. While microfluidics accommodates the sub-nanoliter to nanoliter-scale volume within the analytical space, the smaller analytical volume and unique characteristics of the extended nanochannel are desirable for the analysis of ultra-low-volume samples (*e.g.*, individual cells) in a range of attoliter to femtoliter [22].

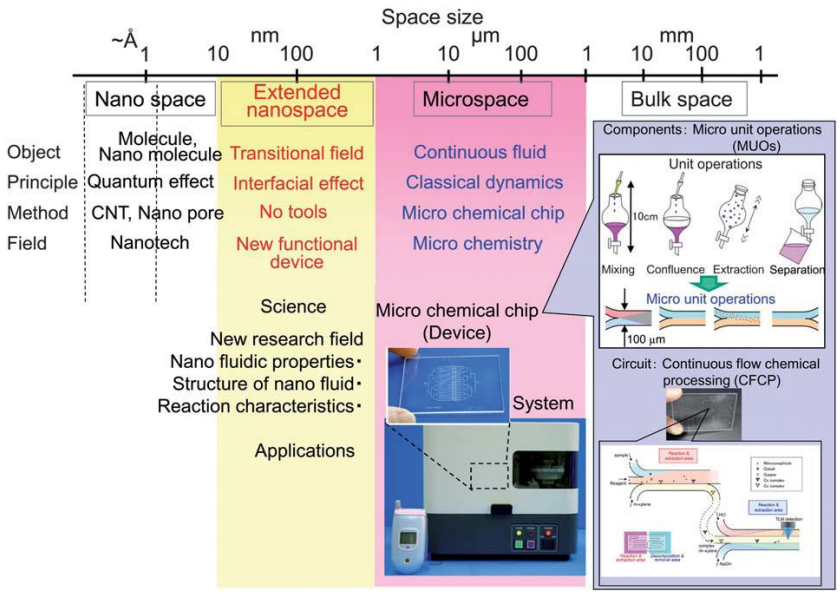

Figure 2.4 The extended nanospace bridging the gap between the nano- and microtechnologies (from[23]).

2.1.3 Main applications of nanofluidics

2.1.3.1 Biomolecule separation and sieving

Bionanotechnology - the emerging field of biological manipulation at the nanoscale, is one of the most inspiring areas in life sciences nowadays as it has found important applications in bioengineering, biotechnology, and medicine. One of the promising applications of chip-based nanofluidic systems is **biomolecule separation**.

In the last decade, various innovative nanofluidic sieves and filters have been developed to accomplish more efficient bioseparation as compared to the traditional gel separation, in terms of separation speed and resolution [24, 25]. With recent advances in micro- and nanofabrication technologies, the development of patterned regular sieving and filtering nanostructures with diverse well-defined pore sizes and tailored surface functionality becomes feasible. This allows researchers to elucidate the detailed biophysical phenomena of molecular dynamics in a controllable fashion, as opposed to their counterparts (*i.e.*, gel electrophoresis) wherein disordered porous gel media is present as molecular sieving matrixes.

Fu and coworkers [26] demonstrated that physiologically relevant macromolecules (*e.g.*, protein, DNA) could be separated in a nanofluidic filter array system under continuous-flow conditions via different sieving regimes, including **Ogston sieving, entropic trapping, and electrostatic sieving** (Figure 2.5). Briefly, the device consisted of a periodic array of deep passages and shallow nanoslits,

of which the molecule traveled through upon an application of diagonal electric field. The molecules jumped from a deep channel to another through the nanoslits at different rates, depending on their molecular properties and sieving regimes. Interestingly, this continuous-flow permits to collect purified biomolecules for downstream biosensing and detection, thus being suitable for an integrated bioanalytical system [27].

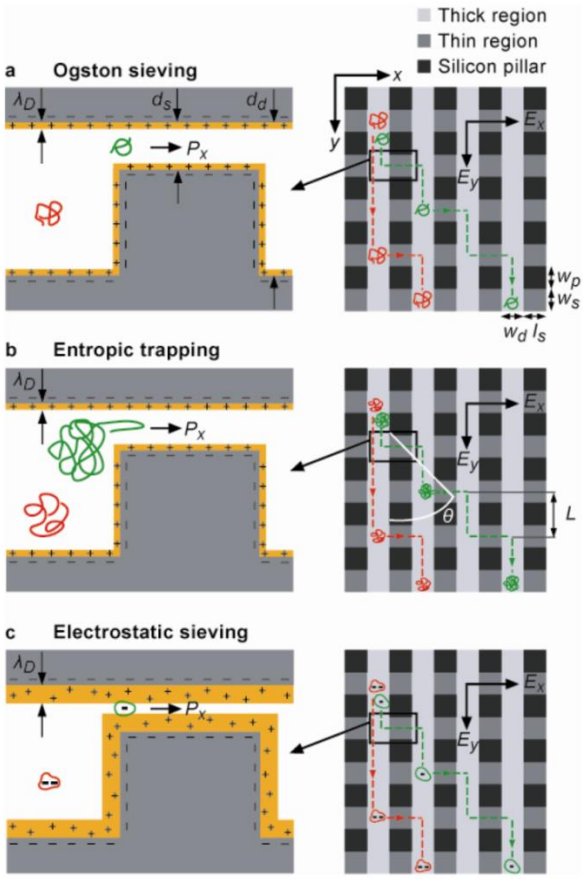

Figure 2.5 Three different sieving mechanisms in nanofluidic separation devices (from [26]).

Ogston sieving and entropic tapping separate the biomolecules based on their size. Ogston sieving relies on the process in which the biomolecules are smaller than the size of the channels and the sieving process occurs via steric repulsion by the walls of the nanofluidic channels. On the other hand, when the size of the nanochannel gap is smaller than the radius of gyration of a flexible biomolecule being separated, there is a developed entropic barrier which induces molecular trapping at the entrance of the nanochannel, referred as entropy trapping. A longer DNA has a higher overall mobility or escape probability from the confined channel, leading to a shorter trapping time [28].

Electrostatic sieving separates the biomolecules based on their charge. At low ionic strengths, when the Debye length within the charged nanochannel becomes comparable to the channel depth [29], electrostatic interactions of the molecule and the electrical double layer (EDL) become dominant, and the nanochannel is **perm-selective** (preferentially allowing transport of ions with one polarity over another) [22]. This means that the separation of biomolecules can be based on their charge density (or pI values) and pH conditions of the buffer. For instance, co-ions (negatively charged proteins) are prohibited from entering the negatively charged nanochannel due to electrostatic repulsions while permitting counter-ions to pass through [30].

2.1.3.2 Pre-concentration of biomolecules

The major problem in proteomics concerns the complexity of the biomolecule samples, such as saliva or blood serum, which contain diversities of proteins of various concentration ranges [31]. This issue is recognized as a key bottleneck in early diagnosis from the detection of trace amounts (nM-pM range) of proteins, such as biomarkers, present in body fluids [32]. To address this problem, one should concentrate these low-abundance molecules, particularly when their levels are much below the detection limit of biosensors. However, there is no equivalent amplification technique, such as polymerase chain reaction (PCR), available for proteins and peptides.

Nanofluidic concentrators have gained a significant place in scientific communities as an effective protein pre-concentration tool. Several pre-concentration schemes are currently available using such devices. One of the outstanding mechanisms is **electrokinetic trapping**. Wang *et al.* [33] have used a nanofilter (~40 nm in thickness) as an ion-selective membrane to concentrate proteins, based on electrokinetic trapping and nonlinear electroosmotic flow near a microchannel-nanochannel junction. When applying an electric field across the nanochannel, an unbalanced ionic transport between counter-ions and co-ions induces **ion concentration polarization** (ICP) [34]. This causes the depletion of ions at the anodic side because charged biomolecules are repelled from the nanochannel whereas ions are enriched at the cathode side [35] (Figure 2.6a). Such anodic repulsion force can be balanced with the electroosmotic flow through the microchannel in order to continuously trap biomolecules coming from the reservoir at the vicinity of the depletion region (Figure 2.6b). Based on this approach, a pre-concentration factor of more than a million fold has been achieved, nearly identical to the PCR technique used for nucleic acid amplification.

In addition, Liao and Chou [36] have proposed an alternative pre-concentration method, based on molecular traps and dams, for protein enrichment in nanofluidic channels using electrodeless dielectrophoresis (DEP) in physiological conditions. The underlying principle lies in the use of nano-sized constrictions to enhance the electric field and associated field gradients which results in a highly efficient protein pre-concentration at the constriction region, more than 10^5 fold faster than the trapping effects described previously.

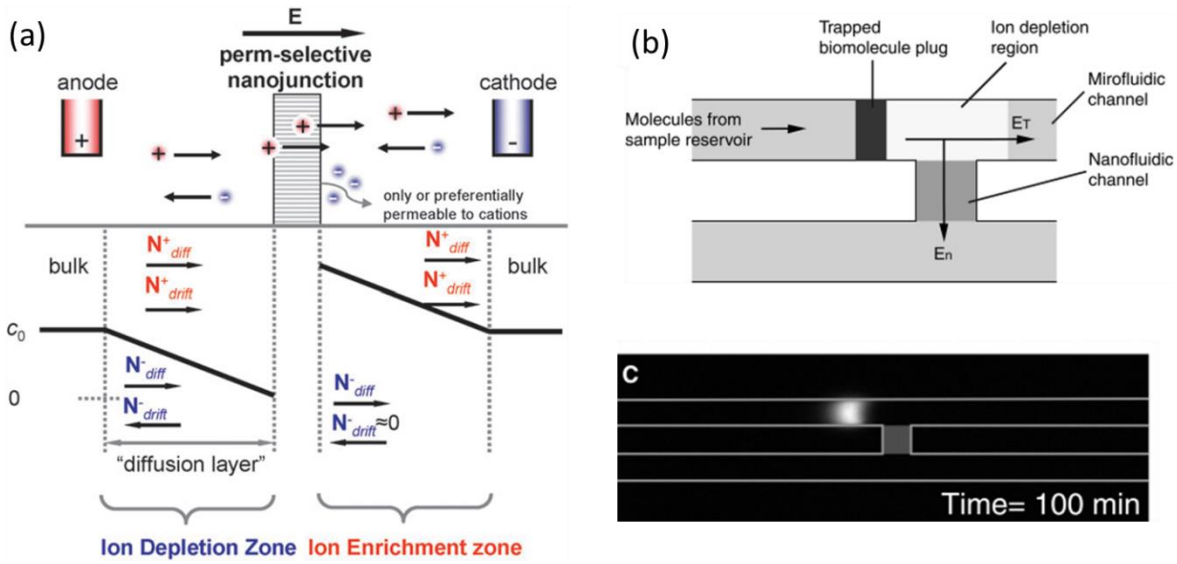

Figure 2.6 (a) A schematic diagram showing ion concentration distributions when an electric field is applied across a perm-selective nanostructure, creating ion depletion zone at the anodic side and ion enrichment zone at the cathode side (from [37]). A nanofluidic protein pre-concentration device developed by Wang *et al.* based on ion concentration polarization effects (from [33]): (b) Schematic and mechanisms of biomolecule pre-concentration near the microchannel-nanochannel junction; (c) A fluorescence image of trapped proteins after applying the electric field for 100 min.

The binding kinetics of immunoreactions is inherently controlled by several factors, such as the target concentration, the affinity (K_D) of antigen-antibody pairs, and the quality of antibodies used. When the concentration of target molecules falls below the K_D (which is the case of common disease biomarkers), the binding kinetics is limited by the diffusion and is thus extremely slow: this results in noisy signal. To tackle this issue and enhance the dynamic range and sensitivity of immunosensors, nanofluidic pre-concentration devices can be conveniently and directly associated to a biosensor within microfluidic channels [38]. Wang and Han [39] demonstrated the utility of the nanofluidic pre-concentrator to effectively enhance the binding events in a bead-based immunoassay by increasing the local concentration of the sample prior to binding, thus improving the sensitivity and reaction kinetics (Figure 2.7).

Aside from their potential use to enhance protein binding kinetics, nanofluidic-based pre-concentrators have been used to increase enzyme activities in low-level enzyme assays [40]. Furthermore, Swami *et al.* [41] have used dielectric constriction-based DEP and a nanostructured edge sensor embedded at the bottom of the constriction with immobilized DNA capture probes to simultaneously carry out DNA pre-concentration, hybridization, and real-time sensing. They demonstrated a 10 fold enhancement of DNA hybridization kinetics due to a localized amplification of DNA concentration at high field-focusing nanoconstrictions.

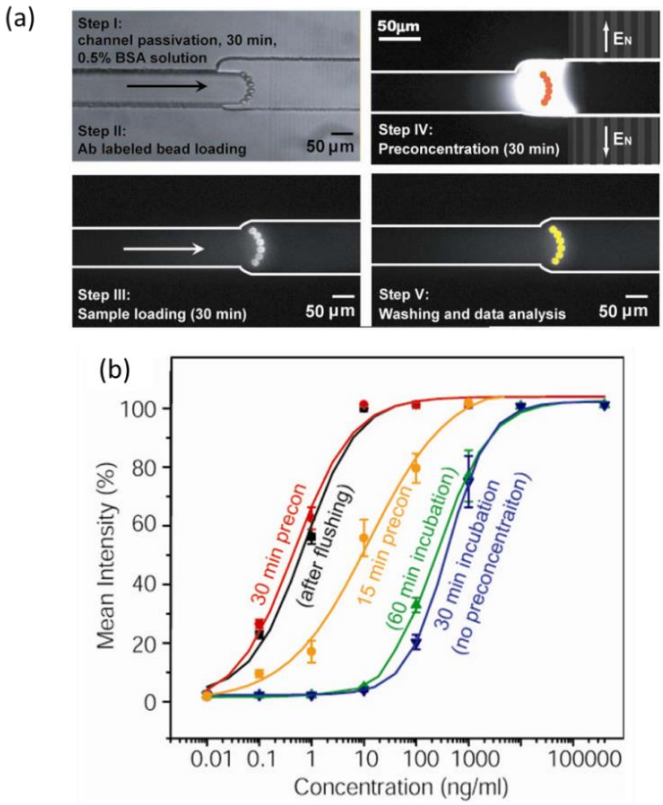

Figure 2.7 Integration of a nanofluidic pre-concentrator with bead-based assays (from [39]). (a) Procedures of bead loading, pre-concentration, and sensing. The samples were concentrated on the antibody-coated beads located in front of the nanochannels, enhancing the binding events. (b) Binding curves of the bead-based immunoassay with and without pre-concentration. After 30 min on-site pre-concentration, the detection limit was lessen from 50 pM to 100 fM range (~500 fold).

2.1.3.3 Single-molecule analysis – the benefits of nanoconfinement

As the channel dimensions are scaled down, fewer molecules are present inside the volume given by the nanofabricated fluid-filled channels. Smaller illumination probe volume improves the spatial resolution and signal-to-noise ratios of the sensing schemes [42, 43]. Similar to TIRF or two-photon excited fluorescence, confining the molecules in a nanochannel is a simple way to decrease the observation volume. Confinement of molecules in nano- and submicrometer (a height less than 1 µm) channels have allowed fundamental studies, such as molecular dynamics and transport [44-46], as well as high-resolution visualization and analysis of biopolymers (*e.g.*, DNA molecules) at a single-molecule level [47, 48]. These studies reveal the properties of the individual molecule as opposed to the classical ensemble experiments, thus giving a deeper insight into the biophysical mechanisms.

When the dimensions of the channel are comparable with the radius of gyration of an enclosed macromolecule, the physio-chemical properties of the molecule is significantly altered due to the **confinement effect**. This arises from the prohibited conformation changes within a confined channel, which are not observed for a free molecule in solution [44]. When a DNA molecule is confined to a one-dimensional nanochannel, DNA elongation is energetically more favorable than its naturally coiled configuration [17]. Uniform stretching of a DNA molecule in the nanochannel leads to enormous biological implications.

Tegenfeldt and colleagues [49] exploited a direct optical imaging approach to measure the contour length (end-to-end distance) of a single-molecule genomic DNA (>1 million bp) confined in 100-nm wide channels (Figure 2.8). They demonstrated that the measurement of the polymer extension was in accordance with the de Gennes's theory, wherein DNA extension in the nanochannel scaled linearly with the contour length. The authors also showed that the measurement of DNA extension with a standard deviation of 130 nm was achieved by means of statistical analysis. Using similar one-dimensional nanochannels, the same group was able to localize bound proteins on a DNA molecule elongated in a nanochannel [50]. These studies pave a new road for single-molecule studies of protein-DNA interactions and relevant biochemical reactions within confined spaces.

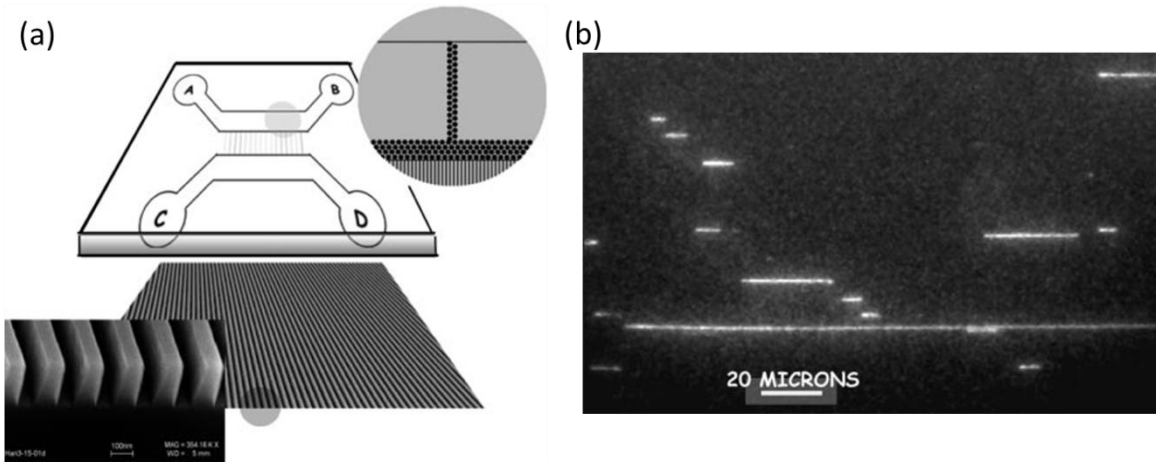

Figure 2.8 (a) Schematic illustration of a micro/nanofluidic device used for single-molecule analysis. The nanochannel arrays with 100 nm in width and 200 nm in depth were imprinted on fused silica wafers. DNA molecules were guided into the nanochannels by electrophoresis. (b) A captured digital image showing the λ-ladder DNA molecules elongated in the imprinted nanochannel array (from [49]).

DNA linearization offered by nanoconfinement has also emerged as a groundbreaking tool for physical genome mapping [51, 52] - the process of which the relative positions of genes along a chromosome are identified without sequencing the entire chromosome. Since the genetic information is stored in a linear fashion along the DNA strand, it is therefore difficult to analyze such information using the native folded structure of DNA. Nanoconfinement offers an access to this genetic information which reveals genome variation, genetic mutations, and replication dynamics [53].

2.2 Biosensing with nanofluidics

As highlighted above, the potential of nanofluidic domain has led to a wide variety of applications, enabling biomolecular separation and concentration, DNA manipulation, and single molecule analysis. Herein, we present another possibility offered from nanofluidics as an extraordinary tool for biosensing applications. This section covers some of the current achievements related to nanofluidic-based biosensors, as well as kinetic studies of biomolecular interaction with nanofluidics.

2.2.1 Current nanofluidic-based biosensors

Performances of miniaturized biosensors are often limited by inefficient analyte transport to the bioactive layer due to the presence of the surface diffusion layer [54]. This poses the difficulty for low-abundant analyte detection. The development of chip-based nanofluidic systems for biomolecule detection has recently received intense interest in the biosensor community. Downsizing the fluidic channel to nanoscale considerably accelerates the diffusion-controlled reactions and dramatically increases the signal-to-noise ratio for optical signals [55]. Once again, this is attributed to unique features offered by nanometer-scale channels, such as the molecular confinement effect and extremely large surface-to-volume ratios. Miniaturization of biochemical reactions into the nanospace benefits from faster reactions, higher binding efficiency, and further reduced amount of reagents as compared to conventional microchips and standard ELISA wells.

For biomolecular sensing, there are currently two main detection schemes integrated in nanofluidic systems: electrical and optical detections (*e.g.*, fluorescence). While electrical detection is inexpensive and compatible with miniaturized systems, optical methods are more straightforward and they provide direct visual evidence. Both sensing schemes have been evolved to complement each other for the detection of a wide range of biomolecular species in nanofluidic systems.

A number of studies have proven the capability of solid-state nanopores as a sensitive biomolecular sensor, owing to their ability to probe single molecules within tunable pore size as opposed to biological (α-hemolysis) protein nanopores [56, 57]. Various receptors can be specifically anchored inside the nanopore for electrical sensing of proteins and long biopolymers, such as His-tagged proteins [58] (Figure 2.9a) and single-stranded DNA (ssDNA) [59]. In principle, when ions and macromolecules translocate through a nanoscopic opening, the **ionic current blockages** are observed [60], producing transient changes of the ionic current. On a similar concept, Saleh *et al.* [61] developed an on-chip artificial nanopore to detect the interaction of antibody-antigen pairs

using functionalized synthetic colloids and resistive pulse technique (Figure 2.9b). Although this approach relied on end-point analysis, it appeared to be more rapid and inexpensive compared to the SPR technique.

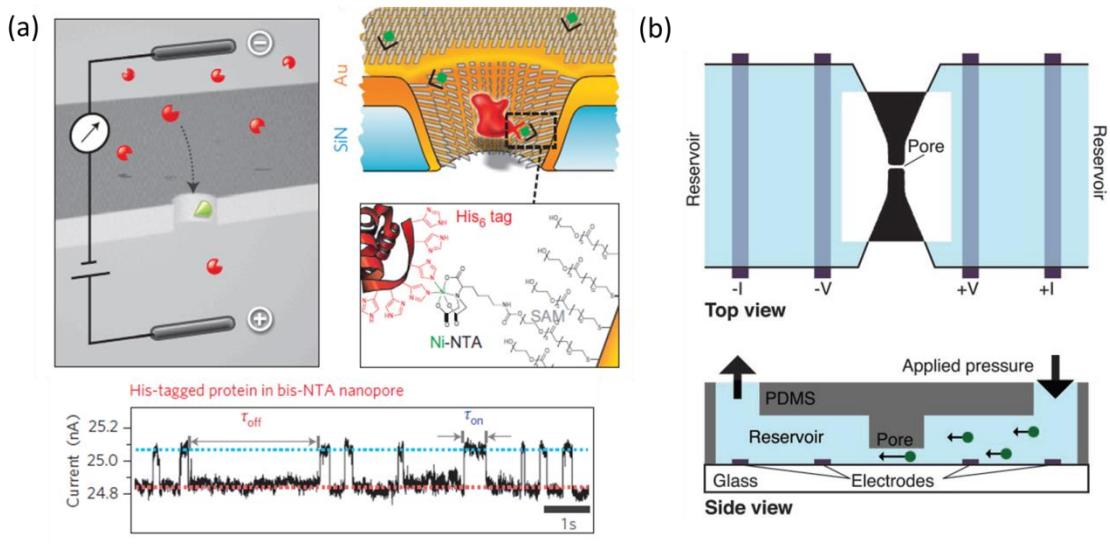

Figure 2.9 Nanopore-based single-molecule detection. (a) Gold-coated solid-state (SiN) nanopores functionalized with NTA receptor (green) thiols for stochastic sensing of His-tagged proteins (red) (from [58]). Charged analyte molecules were electrokinetically driven through the pore and being detected by transient blockades in the ion current. (b) On-chip artificial pore integrated-PDMS microfluidic device for detection of antigen-antibody binding (from [61]). Pressure was used to drive the particles through the pore and the current was measured using a four-point technique.

Apart from measuring the transient changes of ionic current when a single molecule passes through a nanoscopic opening, causing a partial or complete occlusion of a pore (**steric influence**), the binding of analyte to the nanopore wall also induces the modification of the surface charge (**electrostatic influence**), leading to current modulations across the channel [62]. Due to the proximity between the nanochannel dimension and the Debye length, surface charges play a significant role in controlling ionic concentrations inside the channel to maintain electroneutrality, especially in a low electrolyte concentration regime. Under these conditions, nanochannel conductance is proportional to the surface charge density while insensitive to the bulk ionic concentration and channel height [63]. Therefore, any adsorption of biomolecules with different surface functionalities on the channel surfaces can modulate its surface charge, and thus the nanochannel conductance. On the contrary, as the electrolyte concentration increases, the nanochannel conductance is governed by the change of channel geometry induced by the occupation of the macromolecule. Karnik *et al.* [64] demonstrated that both regimes were of

importance for probing biological reactions and surface modifications within the confined channel (Figure 2.10). They coated the entire nanochannel surface (30 nm thick) with biotin, and measured subsequent binding of the charged streptavidin partner by reading the change of nanochannel conductivity.

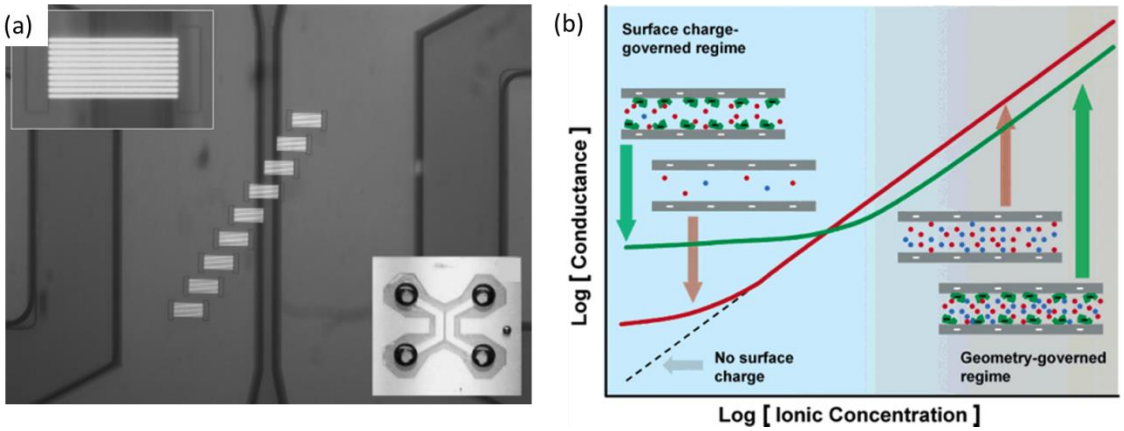

Figure 2.10 (a) An optical image of a nanochannel device with 120 μm long, 3.5 μm wide and 30 nm thick nanochannels that enabled conductance measurements. (b) A diagram depicting the effect of biomolecule modifications on the nanochannel conductance for two different regimes: surface charge-governed and geometry-governed regimes. Immobilization of biomolecules caused an increase in conductance at low ionic concentrations while a decrease in conductance was observed at high ionic concentrations due to the modified channel geometry upon molecule binding (from [64]).

Nanochannel structures have also offered numerous advantages in fluorescence microscopy thanks to the confinement of the measurement volume. High sensitivity single-molecule detection was achieved in submicrometer-sized fluidic channels, with a significant reduction of the observation volumes (two orders of magnitude) as compared to the conventional optical method [42, 65]. This leads to increased signal-to-noise ratios for single-molecule sensing at higher target concentration.

Among other inspiring optical detection modalities used for nanofluidic devices, there has been significant progress in emerging surface enhanced Raman spectroscopy (SERS) in nanofluidic biosensors. Chou *et al.* [66] presented a novel nanofluidic biosensor using SERS to detect β-amyloid peptide (Aβ), a biomarker for Alzheimer's diseases. The device consisted of a microchannel and a nanochannel (40 nm deep) in the middle (Figure 2.11a). This method notably improved the sensitivity of SERS by localizing nanoparticles (60 nm in diameter) and simultaneously concentrating the target analyte near the entrance of the nanochannel. Using the similar approach, Choi *et al.* [67] detected and structural probed Aβ aggregates at ultra-low concentration (10 fM) (Figure 2.11b). This

study is potentially useful to understand the molecular mechanism behind Alzheimer's diseases at the early stages.

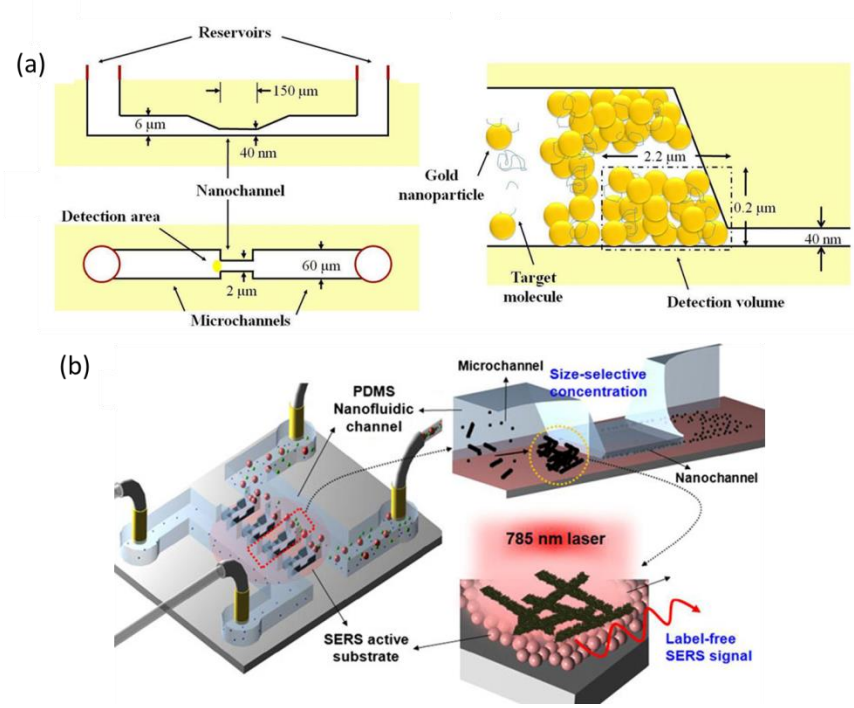

Figure 2.11 Schematic diagrams of the nanofluidic biosensor-based SERS used for β-amyloid peptide detection. (a) Gold nanoparticles were trapped at the micro/nanofluidic junction and the target molecules were concurrently concentrated (from [66]). (b) Aβ aggregates concentrated near the SERS-active surface where gold nanoparticles were initially immobilized (from [67]).

2.2.2 Kinetics of biomolecular interactions in nanofluidics

Another interesting potential of nanofluidic systems arising from nanoconfinement effect is the study of reaction kinetics. Herein, we particularly focus on nanofluidic biosensor platforms (excluding the measurements carried out in free solution) that serve as an analytical means for kinetic analysis of biomolecular interactions.

As mentioned earlier, the performance of miniaturized biosensor systems (*e.g.*, microarrays) are often restricted by diffusion transport of the target analytes to the sensing elements, thus limiting binding kinetics and increasing the time required to reach equilibrium. Several microfluidic-based techniques have been demonstrated to overcome the diffusion-limited mass transport of typical biological reactions, such as the use of high convective flow [68], flow confinement [69], mixing [70], electrothermal stirring [71], flow-through format using nanoporous membranes [72], and magnetic particle-enhanced target delivery [73]. However, the simplest and an efficient way to enhance the

binding assay is to further shrink the channel height, giving that the convective flow is applied. **Nanometer-sized channels can force target molecules to be extremely close to their binding partner on the surface. Consequently, the analyte diffusive transport is dramatically boosted over such a short distance and the binding reactions occur very efficiently in nano-confined channels.**

For instance, Schoch *et al.* [74] utilized 50 nm deep nanofluidic channels, whose internal surfaces were coated with specific binding partners, to study surface binding reactions (Figure 2.12). Low analyte concentrations were driven through the nanochannel by means of pressure-driven flow and the reactions were electrically monitored. They demonstrated that by confining the target molecules within nanochannels under continuous-flow conditions, the binding kinetics could be prominently enhanced and thus the response time to detect specific target molecules could be reduced by a factor of ~ 54, as compared to previously reported pure diffusion-limited reactions [64]. Indeed, due to the small height of the nanochannels, the diffusion of molecules to the channel walls became very efficient even at the relatively high flow speed (~23 mm/s). Consequently, all the molecules that entered the channel became bound to the binding partners. They reported the response time of approximately 1-2 h at 1 nM analyte concentration.

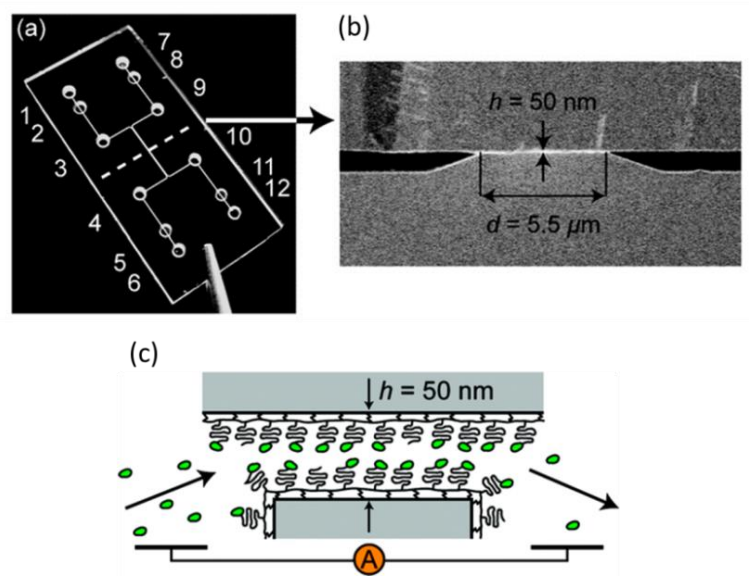

Figure 2.12 (a) A photograph of the chip (12 × 25 mm), consisting of two microchannels connected by nanochannels, used in reaction kinetic studies. (b) An SEM image depicting two microchannels and nanochannels (50 nm deep, 5.5 μm long). (c) A cartoon drawing of the channel coated with specific binding partners and the binding of target molecules can be sensed by the change in nanochannel conductance (adapted from [74]).

Another example showing significant nanoconfinement effects on reaction kinetics was demonstrated in a recent work by Wang *et al* [75]. Briefly, they investigated enzyme kinetic reactions under continuous-flow conditions using size-tunable nanofluidic devices in combination with electrochemical sensing (Figure 2.13). They proposed an efficient way to covalently immobilize glucose oxidase enzymes (GOx) on polycarbonate-based nanochannels with the depth ranging from 50 to 140 nm. Glucose substrates were electrokinetically introduced through the channel, and hydrogen peroxide products were detected by the change in steady-state electrochemical current responses. As compared with bulk-solution systems, the specific enzyme activity increased by a factor of 4. Moreover, the catalytic constant (k_{cat}) increased with decreasing the channel height, providing that the flow rate was kept the same. This suggested that faster reaction rates, hence higher conversion efficiencies could be expected in the smaller nanochannels. This was due to the fact that the substrate required shorter diffusion times to reach the immobilized enzyme in a smaller nanochannel space. These studies provide important insight in biological reactions occurring in confined spaces such as membranes, or in the crowded cellular milieu, which may be different from those occurred in bulk solutions.

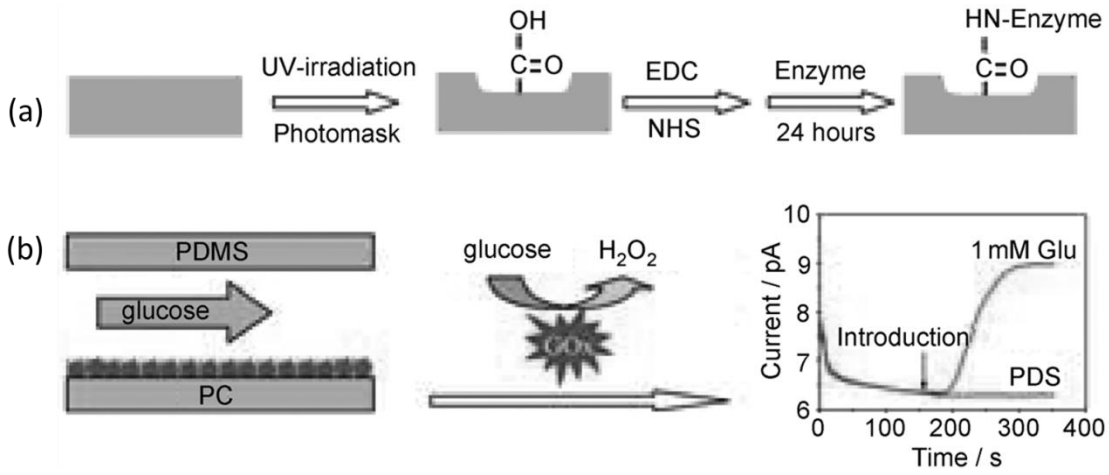

Figure 2.13 (a) Schematic diagram depicting the nanochannel fabrication and covalent attachment of enzyme on the nanochannel surface. (b) The concept of the nanofluidic device coupled with electrochemical sensing for enzyme reaction kinetic studies (from [75]).

2.3 Issues related to nanofluidic sensing

While nanofluidic systems have led to significant advances in biomolecule separation/pre-concentration and biophysical studies of single molecules, surprisingly there have been a few studies that exploited nanochannels as biosensing systems, especially for ultra-fast real-time kinetic studies of protein interactions. This is due to several challenges that need to be overcome when combining biological requirements (*e.g.*, preservation of the biological activity and localized surface modification) with the constraints imposed by manufacturing technology at the nanoscale (*e.g.*, chip assembly). In this section, we intend to provide some issues faced by researchers in this field along with conceivable solutions, which ultimately would allow one to fully benefit from the merit of nanofluidics as an effective sensing system.

2.3.1 Integration of biofunctional layers

When combining biosensors with nanofluidics, several aspects have to be taken into account. One of them concerns the integration of the biosensitive layer into nanofluidic channels. Here, we focus on the nanochannels that are fabricated by top-down approach and the assembly of nanofluidic device is achieved by sealing with another substrate. Traditional biosensors involve grafting of one interacting partner (receptor) onto the active sensor which is usually achieved in an open-top manner, by immersing the entire open substrate into a specific solution containing biomolecules of interest. Nevertheless, once dealing with enclosed fluidic systems, immobilization inside the channels becomes a technical hurdle due to inaccessibility from the outside world. From a practical point of view, there are two strategies to integrate biosensing elements in the nanochannels: **pre-bonding** and **post-bonding functionalization** [76].

In-situ or **post-bonding functionalization** relies on the biomolecule grafting after the nanochannels are sealed. This process is carried out by sequential delivery of biomolecules carrying specific functional groups which interact with the channel surface [74]. However, one of the main restrictions inherent to this approach is the inability to localize probe molecules on a specific region of the channel walls, and more importantly it does not allow grafting multiple types of biomolecules in the same channel, thereby preventing the use of nanofluidic devices as multiplexed biosensors. Although several methods can be exploited for local surface modifications in enclosed fluidic channels (*e.g.*, electron beam induced graft-polymerization [77], photochemical reaction [78, 79], diffusion-limited patterning (DLP) [80]), the fact that they require multiple reagent exchanges and washing steps make these procedures burdensome and time-consuming. This is inherently attributed to very small flows imposed by high-resistance nanofluidic channels.

Pre-bonding functionalization approach seems to be more desired to locally immobilize one or more interacting partners inside previously etched nanofluidic channels with the possibility of batch processing. In this case, several available open-top surface patterning techniques [81], such as spotting and dip-pen lithography [82], can be applied. However, the presence of biomolecules in the channels precludes the ordinary sealing techniques, such as thermal-fusion bonding and anodic

bonding, to be performed. This is due to irreversible denaturation of the biomolecules upon heat treatment, UV/plasma exposure, or harsh chemical treatment, required during system assembly. Therefore, mild sealing methods dedicated to nanofluidic channels, which preserve the bioactivity of the sensing layer and concomitantly give reasonably high bonding strengths, are central for fruitful advancements of nanofluidic biosensors.

2.3.2 Sealing process

Low temperature bonding technology is considered to be very beneficial for nanofluidic channels, which would make possible the integration of biosensing elements prior to sealing without the use of high temperatures or a vacuum. Xu *et al.* [83] proposed a low-temperature (200 ºC) direct bonding of fused-silica glass nanofluidic chips via a two-step plasma surface activation. The process consisted of an oxygen plasma treatment followed by a nitrogen microwave radical activation on two substrates bearing nanochannels and microchannels, respectively. Another strategy to address the technical challenge in nanofluidic bonding is the use of one-step plasma treatment through the surface activation process by O_2/CF_4 gas mixtures [84]. This process permitted the bonding of fused-silica glass at room temperature (Figure 2.14). While both methods enable nanofluidic channel bonding at low temperature, exposure to plasma could potentially damage pre-immobilized molecules, such as antibodies or chemical groups, on the surfaces.

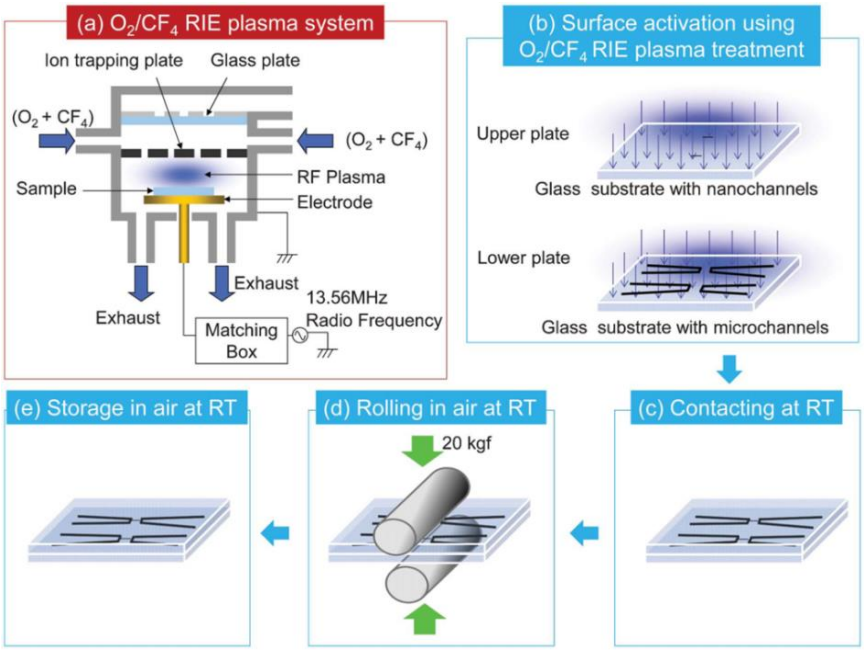

Figure 2.14 Schematic diagrams of the room-temperature bonding process of fused-silica glass nanofluidic chips based on a one-step surface activation using an O_2/CF_4 plasma treatment (from [84]).

Lately, Shirai *et al.* [21] developed another low-temperature bonding procedure for glass-glass sealing at 100 ºC. They utilized a vacuum ultraviolet (VUV) light to partially pattern functional groups on a plain substrate through a photomask for subsequent in-situ protein immobilization. At the same time, UV light rendered the surface activated for bonding with another plasma-activated substrate bearing nanofluidic networks. With this technique, they were able to pattern antibody on the inner surface of the nanochannel by pressure-driven flow and demonstrate selective molecular capture using nanofluidic-based immunoassay.

Apart from glass-glass bonding, PDMS-sealing, relying on the activation of the surface chemical group, is very popular in the microfluidic realm. However, so far it has not been employed to seal pre-biofunctionalized nanochannels due to elastomeric deformation of the PDMS. Recent work reported a novel bonding method applicable for nanometer-sized channels using polysilsesquioxane (PSQ) as an adhesive polymer layer combined with an asymmetric oxygen plasma treatment [85]. In this way, a selective surface functionalization could be accomplished prior to chip encapsulation as only the PSQ-coated substrate was activated but not the pre-functionalized nanochannel surface. Therefore, the biofunctionality of the grafted molecules could be fully preserved. The assembly procedure of our nanofluidic biosensor device was also based on a similar sealing approach.

2.3.3 Detectability and response time

As highlighted earlier, miniaturization of the analytical space into the nanoscale offers tremendous advantages for chemical and biochemical processes, such as shorter analysis time and decreased sample volume. Conversely, detection becomes challenging when low sample concentrations are present within such small detection volumes. Considering the detection volume with the dimensions of 100 ×100 ×100 nm^3, less than a single molecule is present at a sample concentration of 1 μM. This means that the sophisticated detection technology with single molecule sensitivity is compulsory.

Optical detection modality is considered as a non-invasive, sensitive technique enabling in-situ single molecule detection. Several promising optical detection schemes include laser-induced fluorescence (LIF) [86], confocal fluorescence microscopy [87] and total internal reflection fluorescence microscopy (TIRFM) [88]. While highly sensitive detection techniques are essential for probing molecules within nanofluidic channels, the absolute detection efficiency (the number of detected molecules over the total number of introduced molecules) can be expected inside the nanospace which is unattainable in microfluidic chips. This unique detection property is proven by LIF technique because a typical spot size of the laser beam (1 μm in diameter) is much bigger than the size of the nanochannel [23]. Consequently, all molecules occupying the nanochannel volume can be sensed (Figure 2.15).

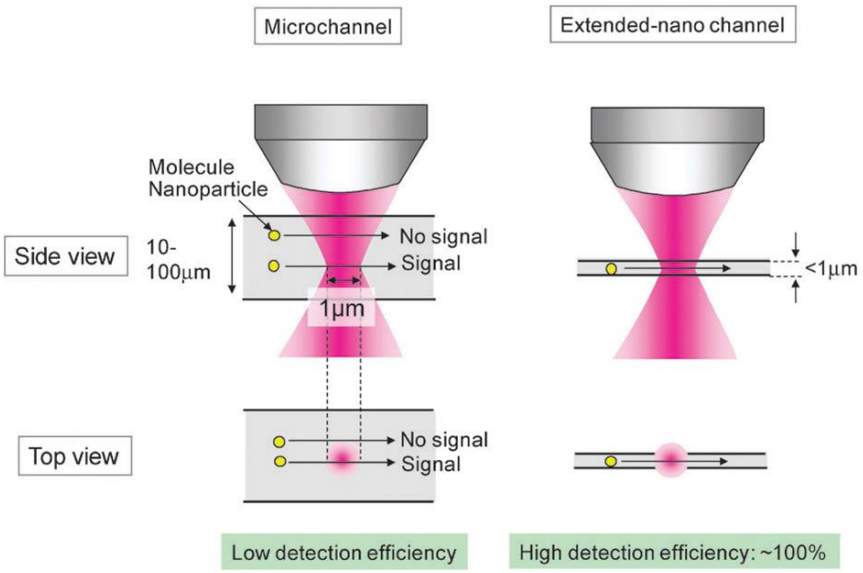

Figure 2.15 Improved detection efficiency in analytical nanospace (from [20]).

Another issue related to biosensing in nanofluidic channels lies on sensor response times. This problem seems to be contradictory to the goal of nanofluidic approach as an ultra-fast biosensor. As a direct proof, we underline the work reported by Schoch [74], where the total response time of about 1-2 h was established for the reactions in nanofluidic channels. Indeed, they grafted the entire nanochannel walls with specific probe molecules and the sensor response was made by integrating over a relatively large surface area (the whole channel length), thus they did not take full advantage of a locally enhanced reaction rate.

In fact, the binding rates on a single large sensing surface at low target concentrations tend to be restricted by mass transport of the target molecules to the sensor surface as seen in the case of typical SPR biosensors, which in turn has a direct impact on the total response time of the sensor. This is because most of target molecules are captured near the entrance of the flow channel and the concentration of target molecules is depleted downstream. As a result, the target capture at downstream regions is delayed, thus slowing down the overall capture rate of the whole sensor, especially when the whole sensor surface is integrated for detection. It was reported that arrays of spaced smaller sensors (*i.e.*, microarray spots [89]) led to a higher fractional occupancy of the immobilized probes and faster equilibrium times as compared to a single large sensor with the same overall sensing surface area [90]. Therefore, the localized selective surface modification is envisaged as an effective way to realize fast-response nanofluidic sensors.

On the other hand, the response time can be limited by other factors, such as non-specific binding effects on the channel wall outside the analysis region due to an extremely high surface-to-volume-ratio, especially when shrinking down the channel size. Hence, a proper channel surface passivation (*e.g.*, surface pretreatment with bovine serum albumin (BSA)) is recommended to prevent sample loss.

2.3.4 Fluid handling

Frequently used fluid handling systems in nanofluidic devices are electrokinetic method, capillary filling and pressure-driven flow [91]. Electrokinetic methods, such as electroosmotic pump, are favorable to drive the fluid flow in nanofluidic channels because the external electric field required to generate flows does not depend on the channel height. However, there are still some limitations inherent to an electroosmotic pump for general analytical applications because it is highly sensitive to the surface charges and any contaminants. While capillary filling is another simple way to introduce liquid into the nanochannels [92], it poses a great difficulty when it comes to a more complex fluid manipulation where multiple steps of reagent exchange (*e.g.*, sample injection, rinsing) are required.

With all these constraints, pressure-driven flow remains a key solution which allows a precise fluidic handling beneficial for widespread uses in analytical and chemical applications. However, as the flow resistance dramatically increases in nanofluidic channels, pumping of fluid in nanochannels using pressure-driven flow becomes impractical due to a huge pressure drop. In fact, the flow velocity induced by pressure-driven flow in such a narrow channel is slow; giving that the flow velocity is directly proportional to the square of the channel height.

To tackle the issue raised by pressure-driven flow in nanofluidic systems, Tsukahara *et al.* [93] developed a novel air-pressure-based nanofluidic control system, which consisted of a Y-shaped extended nanochannel and U-shaped microchannels on a fused-silica substrate (Figure 2.16). The liquid flow and mixing of different aqueous solutions could be precisely controlled by applying an air pressure into a sample solution. While fluidic handling presents a bottleneck if the chip contains only a single nanochannel due to tedious washing cycles, the flanking U-shaped microchannels integrated in this chip design facilitate rapid interchange of different reagents. This liquid handling interface noticeably shows a great potential for effective biosensing in the nanospace.

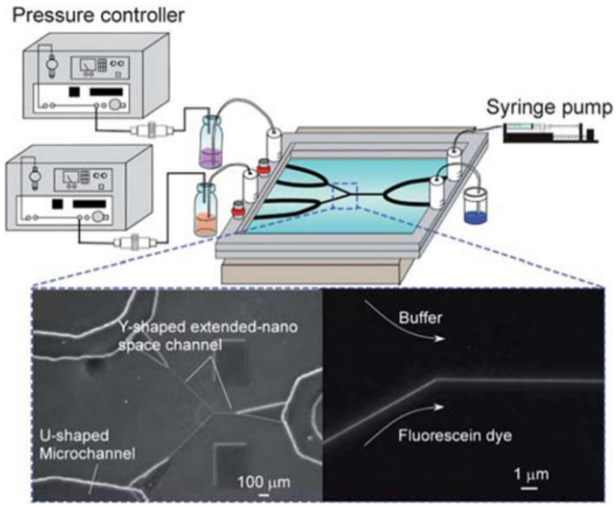

Figure 2.16 A pressure-driven nanofluidic control system (from [94]).

2.4 Concept and contributions of our approach

In this study, we utilized nanofluidic systems as a novel and cost-effective biosensor platform which enabled monitoring of reaction kinetics associated with biomolecule interactions with spatial time-resolved resolution. Our approach relied on the combination of **biofunctionalized uniaxial-confined planar nanochannels**, or **nanoslits**, and fluorescence microscopy to elucidate protein-protein interactions in physiological media. By confining the reaction volume into sub-μm thick channels with localized sensing elements, fluorescence conjugated biomolecules could be rapidly detected in real-time without cumbersome washing steps using a conventional fluorescence microscope, thus increasing the accessibility for classical biochemical or life science research laboratories where sophisticated and expensive analytical tools (*e.g.*, SPR, QCM, TIRF) are limited.

Figure 2.17 depicts the schematic diagram of our fluorescence-based nanofluidic biosensors used for kinetic studies. We locally immobilized probe biomolecules on the gold patch located at the bottom of the nanochannels prior to chip encapsulation. Such local surface modification consequently allowed us to benefit from inherently locally enhanced reaction kinetics. The biofunctionalized nanofluidic chip was sealed with a cover glass coated with a transparent adhesive material via asymmetric plasma treatment at room temperature, hence allowing the optical visualization and at the same time preserving the bio-functionality of the preceding grafted biomolecules. Once the chip was sealed, we passivated the remaining channel bottom area and roof with the protein-resistant functionalities. The fluorescently-labeled analytes were driven though the nanoslits by means of pressure-driven flow and the signals associated with analyte adsorption and desorption on/from the sensor surface were detected in real-time under a fluorescence microscope coupled with a CCD camera.

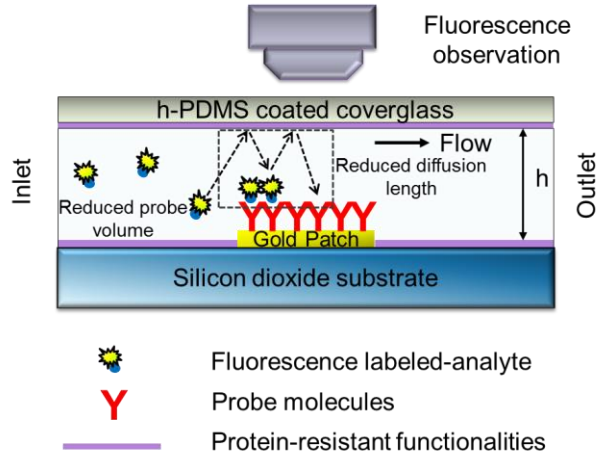

Figure 2.17 A schematic diagram of our fluorescence-based nanoslit biosensor concept.

Our proposed method permits enhancement of immuno-reaction kinetics with a maximized binding efficiency (virtually 100%) on a seconds time scale thanks to the well-known molecular confinement between the flowing target molecules and the surface-immobilized receptors. This is attributed to a dramatically decrease in the diffusion length for the molecule to travel across the channel in the vertical direction, thereby boosting the collision frequency between the analyte molecules and the sensing element located at the bottom of the channel. Therefore, conducting immunoassays in a confined-nanospace enhances the binding rates and reduces the time required for equilibrium to be reached. Furthermore, drastic reduction of the diffusion length drives the transport toward reaction-limited regime, being ideal conditions for kinetic analysis.

From a molecular point of view, if we compare the depth of the nanoslits being 450 nm with the diffusion distance of the target molecule when traveling over a 50 μm long sensing layer, the traveling time, t, required for a molecule to pass by the sensing layer can be calculated as 0.25 s, giving a linear flow velocity being 200 μm/s. The length over which the molecule has to travel as it diffuses to the probe-immobilized region during such time scale, L, can be calculated to be 2.2 μm, by equation $L = \sqrt{Dt}$, where the diffusion coefficient (D) of an IgG is 10 $\mu m^2/s$. The calculated diffusion length is significantly higher (~ 5x) than the depth of the nanoslits. **This implies that all molecules entering the nanochannel will certainly be captured by their interacting partners grafted on the sensor surface without loss**, as opposed to the typical microfluidic immunoassays wherein a relatively high fraction of the analytes just passes over the sensor without being captured and thus lost for detection. In our case, the target molecules in the sample volume are exploited more efficiently.

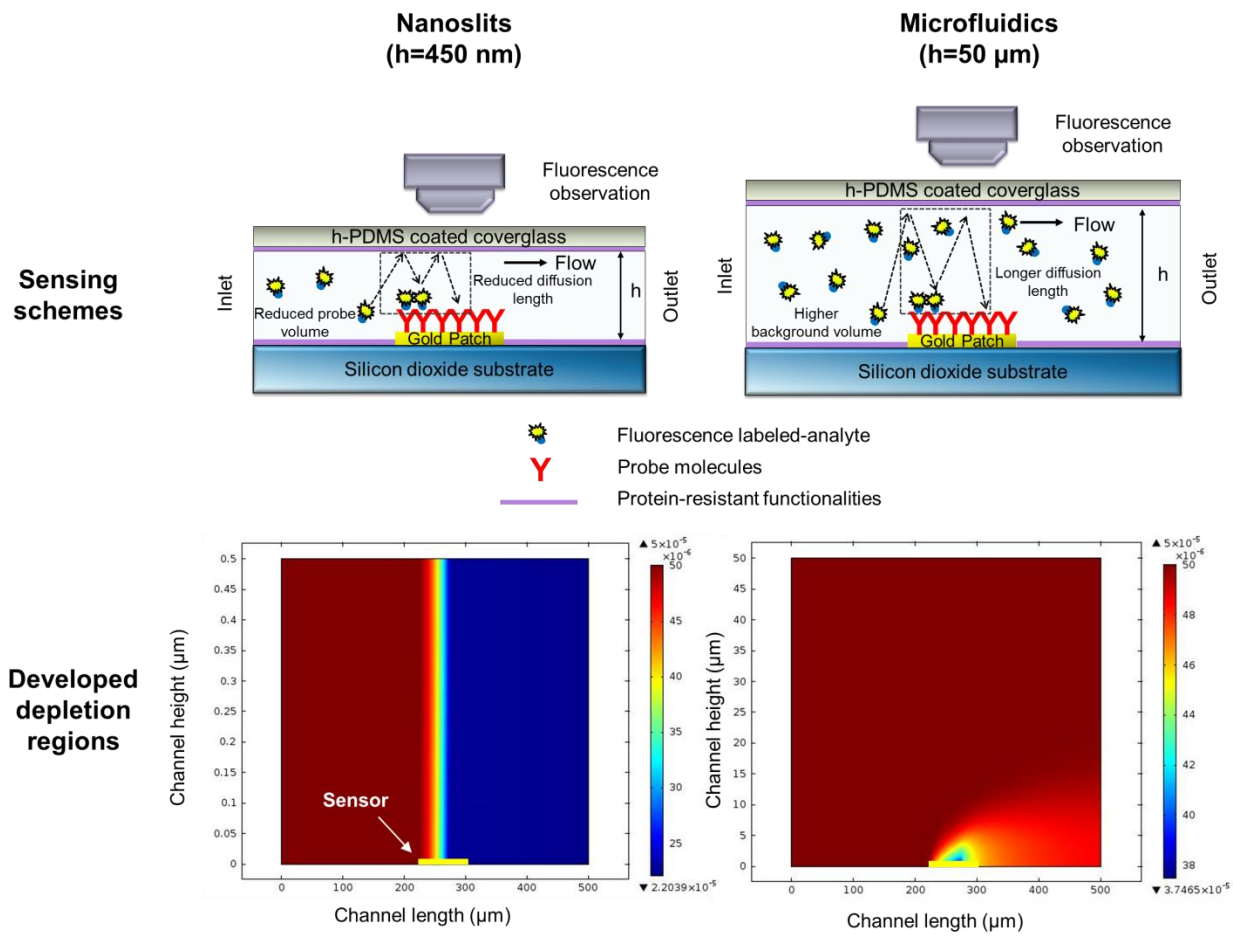

Figure 2.18 Comparisons between nanoslit and microfluidic sensing schemes (not to scale) and the depletion regions formed upon binding reactions between the flowing target analytes and the probe-immobilized sensor located at the bottom of the channel. The color map presents the concentration of the target analyte from high (red) to low concentrations (blue).

As can be seen from Figure 2.18, when the target analytes react with the sensor, the depletion region (the concentration gradient layer) expands across the entire channel height of the nanoslits, contrary to the reaction in microfluidic chips with the same sensor size wherein the depletion zone forms very close to the sensing layer. Accordingly, with an optimized flow velocity, and sensor length, our device can operate in a **full collection regime** (which will be explained in details in the following section), hence eventually suitable for ultrafast molecular filtering based on molecular affinity [95]. However, it is worth mentioning here that the analyzed sensing area in our case should be smaller than the diffusion length in order to obtain accurate kinetic data. The typical sample volume in nanoslits is in the pL range, *i.e.*, 4 orders of magnitude smaller than the sample volume of conventional microfluidic biosensor formats [96]. From the two advantages: high capture efficiency

and reduced volume, our platform is particularly suitable to the analysis of ultra-small and low-volume samples, *e.g.*, the contents of a few cells.

In addition, real-time fluorescence detection of the conjugated biomolecule interaction with the capture region within nanoslits offers the ability to extract kinetic constants. This is attributed to a considerable reduction of the sample volume during observation, leading to negligible levels of fluorescence background. This characteristic inherent to our device allows us to directly probe the sensing surface by correlating the binding fluorescence signal directly to the amount of bound targets, without the need of reagent wash and without using complicated and expensive setups, such as SPR, TIRFM, or QCM. Fluorescence microscopy also offers the possibility to carry out spatially resolved measurements where each camera pixel represents an independent measurement of the reaction kinetics. Hence, in addition to the high sensitivity with no analyte mass dependence inherent to this detection technique, a large sampling area over a number of pixels ensures reduced statistical errors [97]. On the other hand, because the fluorescent background level is proportional to the channel height, sub-micrometer channels offer signal-to-noise ratios of at least 100 on a large scale of dissociation constants K_D, from the pM to the sub-μM range, that concerns most molecules of interests.

In contrast to the reaction volume (μm scale) in conventional microfluidic formats exhibiting a high level of fluorescence background, a greatly reduced analytical space of the extended-nanochannel (nm scale) with a comparatively lower fluorescence background leads to another golden feature of our platform. This involves the capability to carry out full kinetic assays generating full kinetic sensorgrams (association and dissociation curves) in one single-experiment through reversed-buffer flow operations. This procedure is literally impractical in typical microfluidic formats because we need to pause the experiment after completion of the association phase in order to load a fresh buffer solution in the same inlet and then reset the experiment for the dissociation process. These procedures in turn prevent continuous monitoring of association and dissociation processes in a single-experiment.

Indeed, in contrast to microfluidic formats, our device operates with an absolute molecular interaction, and as a result there is a clear boundary between the regions where the analyte concentration drops from maximum to zero (the depleted region). Hence, the liquid downstream the sensor is virtually analyte free and the dissociation study can be performed directly after completion of the association phase by reversing the fluid flow within the nanochannel instead of injecting a new buffer solution at the inlet. As opposed to microfluidic chips where a large number of target molecules still remains in the detection volume, our device does not necessitate washing steps to remove the background fluorescence signal, which results in a simplified protocol and reduced total analysis times.

The advantages and unique features of our biofunctionalized nanoslit can be summarized as follows:

- cost-effective and simple operation with ultra-low reagent consumption
- compatible with any conventional fluorescence microscope, thus suitable for use in classical biochemical laboratories
- enhance the reactions kinetics with high capture efficiency and optimized response time due to a drastically reduced diffusion length
- operate in a full collection regime without sample loss, thus beneficial for analysis of low-volume and rare/expensive samples
- enable real-time monitoring of biomolecule interactions with kinetic constant extraction, similar to SPR and QCM setups, and provide the possibility to study protein interactions with a wide range of binding affinities, regardless of the analyte mass
- allow localized sensing with a high spatial resolution and reduced statistical errors (high precision) via a CCD-based fluorescence imaging system
- increase the signal-to-noise ratio of optical signals due to a significantly reduced detection volume as compared to microfluidic chip formats
- achieve full kinetic sensorgrams (association and dissociation curves) in a single-experiment using a simplified reversed-flow protocol, which is not attainable in conventional microfluidic immunoassays

2.5 Diffusion, convection and reactions in surface-based biosensors

To explore sensor binding kinetics and understand how our system behaves, it is desirable to know the physics of mass transport and surface reactions that come into play in surface-based biosensors embedded in micro/nanofluidic systems. In many situations, surface-based biosensors rely on mass transport of target molecules to the receptor on the sensor surface. Hence, there are multiple competing physical processes that need to be considered in order to reveal the operational regime of a given biosensor system. In general, target molecules are transported with convective flows and they are randomly diffused in the solution. Free target molecules have the possibility to bind to their interacting partners on the surface and the bound molecules may unbind from the surface and return to solution. As different biosensor systems exhibit diverse characteristic parameters, Squires and coworkers [98] developed elegant and intuitive rules of thumb for one to qualitatively determine the behavioral regime of a system wherein convection, diffusion and surface reactions all simultaneously take place.

2.5.1 Model system description

The biosensor model described here involves a two-dimensional channel of height H and width W (Figure 2.19). Solution containing target molecules with concentration C_0, and diffusion coefficient D, is introduced through the channel with a volumetric flow rate Q. At the bottom of the channel, a sensor of width W_s and length L_s is functionalized with receptors of a density b_m. Target molecules only bind specifically to the receptor on the surface with typical binding constants k_a and k_d, but do not bind to the channel surface outside the sensing area. As the channel width is much larger than the height, the target concentration is assumed to be uniform across the channel (in H direction).

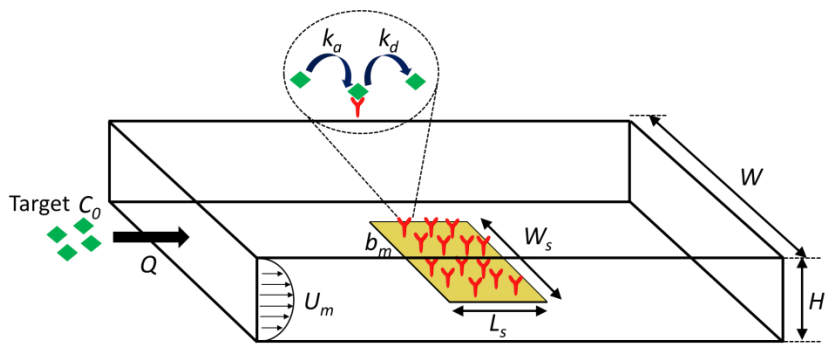

Figure 2.19 A schematic cartoon of the model biosensor system used to describe analyte transport and surface reactions.

2.5.2 Dimensionless numbers

Fluid physics of a typical surface-based biosensor system, operating under continuous-flow conditions, are governed by a competition between wide varieties of physical phenomena as mentioned above. Dimensionless numbers indicate the relative importance of such competing effects, and they can be simply determined without complex computations. Their values are very useful to identify in which regime a system operates (*e.g.*, absolute collection versus rapid collection or transport-limited versus reaction-limited regimes).

2.5.2.1 The Reynolds number

Fluid flows through a micro-/nanofluidic channel can be characterized by the dimensionless Reynolds number which is conventionally defined as the ratio of inertial forces to viscous forces as:

$$Re = \frac{inertia\ force}{viscous\ force} = \frac{\rho U_m l}{\mu}, \tag{2.1}$$

where ρ is the fluid density (kg.m^{-3}), μ is the fluid viscosity (Pa.s) and U_m is the average velocity of the flow (m.s^{-1}). l is the relevant length scale (m) which is equal to $4A/P$, where A is the cross sectional area of the channel and P is the wetted perimeter of the channel. It is well known that the laminar flow occurs at low Reynolds number (Re <2000) [99] where viscous forces are dominant whereas the turbulence flow occurs at higher Reynolds number.

2.5.2.2 The Peclet number

The transport regime of target molecules to the sensor is determined by both diffusive transport – the random movement of target molecules within the channel, and convective transport – the movement of target molecules in the direction of the fluid flow. The Peclet number represents the rate ratio of the convective transport to the diffusive transport as [100]:

$$Pe_H = \frac{convention\ rate}{diffusion\ rate} = \frac{U_m H}{D} \qquad (2.2.)$$

In other words, the Peclet number compares the rate at which a molecule diffuses across the channel with the rate at which it is conveyed downstream past the sensor with the same distance. **When $Pe_H \ll 1$, diffusion is the dominant mass transport**. This implies that convection is slow enough that all molecules have sufficient time to diffuse to the surface and being grabbed by the sensor. This occurs under extremely slow flows or small channel heights. On the other hand, **when $Pe_H \gg 1$, the convective transport wins**. Under these considerably high flows or high fluidic channels, the molecules do not have enough time to diffuse to the sensor. Consequently, merely a small fraction of target molecules very close to the sensor has chance to react to the bioactive surface while the rest of the molecules are practically swept downstream due to the reduced residence time. Therefore, the biosensor loses its sensing efficiency. This is the case of typical microfluidic formats like SPR. From a practical point of view, the Peclet number for optimal biosensors should not be neither too high that the molecules do not have adequate residence time to bind to the sensor which in turn requires a larger amount of target to reach detectable levels, nor too low that it slows down the binding process, leading to long response times [101].

2.5.2.3 The Damköhler number – interplay of mass transport and reactions

When combining surface chemical reactions with mass transport, the Damköhler number is another dimensionless parameter which expresses the relative importance of these two phenomena as:

$$D_a = \frac{reaction\ rate}{diffusion\ rate} = \frac{k_a b_m H}{D} \qquad (2.3)$$

The effects of analyte diffusive transport and reaction rates dictate the binding kinetic regimes of a system. When the rate of target diffusion to the sensor surface is much slower than the intrinsic reaction rate on the surface, **$D_a \gg 1$, then mass transport is rate limiting**. Conversely, when the reaction rate is much slower than the transport rate, **$D_a \ll 1$, binding kinetics are reaction-**

limited. Consequently, the time required for a sensor to reach equilibrium is strongly dependent on the dimensionless number D_a. Under mass transport-limited conditions, the concentration of the bound complex grows linearly in time and the sensor exhibits long equilibrium times, demanding large amounts of target sample [102]. Furthermore, the measurement becomes problematic for the determination of kinetic parameters because the estimated kinetic constants will be the rates at which analytes are transported to the sensor surface, rather than the real intrinsic reaction rate constants of the binding reactions. On the other hand, if the system falls into reaction-limited regime, the analyte concentration above the sensor is nearly identical to the bulk concentration and the bound complex concentration reaches equilibrium with an exponential growth. Under these conditions, the reaction kinetics can be solved analytically in Langmuir model. To push the reactions toward reaction-limited regimes, the channel height and grafting density of the receptor can be simply modified whereas the on-rate and diffusivity are inherent to given antigen-antibody pairs.

2.5.3 Phase diagram of mass transport

Now we consider mass transport scenario in the model system described above, assuming that the sensor acts as an **ideal perfect collector**. This means that any molecule that diffuses to the sensor will bind instantaneously upon confronting the surface receptor. As the target molecules are collected by the sensor embedded on the channel floor, the diffusion layer with a concentration gradient forms above the reactive surface. The Peclet number and the sensor length, $\lambda = L_s/H$, are the key parameters that characterize mass transport behaviors and the concentration profiles in the flow channel.

In the case where there is no bulk fluid flow, the diffusion region grows indefinitely into the channel with a size $\delta \sim \sqrt{Dt}$. When applying extremely small fluid flows, $Pe_H \ll 1, Q \ll DW$, the sensor collects all target molecules delivered by the flow and the depletion zone expands across the channel height ($\delta \gg H$) until the convention balances its progression. At a steady state where the target convective flux $J_c = C_0 Q$ is equal to the target diffusive flux $J_D = DC_0HW/\delta$, this equilibrium gives the depletion zone with a thickness $\delta \sim DHW/Q$. On the other hand, if the diffusive transport cannot compete the target delivery by convection, a thin depletion zone forms above the sensor surface. In this case, the depletion zone has a thickness $\delta \sim \left(\frac{L}{Pe_s}\right)^{1/3}$, where Pe_s is the shear Peclet number related to the sensor length, $Pe_s = 6\lambda^2 Pe_H$. Pe_s describes whether the depletion region is thicker ($Pe_s \ll 1$) or thinner ($Pe_s \gg 1$) than the sensor.

The **analyte retention** or the fraction of the analytes that are collected by the sensor for a variety of Pe_H and λ is shown in Figure 2.20a. We can observe that for a sufficiently low Pe_H, and large enough sensor λ, the incoming target molecules are completely collected. This corresponds to the **full collection regime** in region (i) in the mass transport phase diagram of the model biosensor system (Figure 2.20b). We designed the nanoslit biosensors used throughout this study to follow this full collection regime according to the values of experimental parameters. More details of dimensionless number computations for our biosensor system will be described in Chapter 4. Figure

2.20c-i show the steady state concentration profiles for different values of Pe_H and λ, corresponding to the stars in the phase diagram. In full collection regime, it can be observed that the depletion zone forms across the channel height (c,d,f). On the other hand, in region (ii) where both Pe_H and λ are sufficiently high, the developed depletion layer is thin relative to both the sensor length and the channel height (e,g,i). In the case of small sensors, $L \ll H$ (*e.g.*, nanowires), the depletion zone is thinner than the channel height but it is thicker than the sensor itself (h), corresponding to region (iii). Finally, region (iv) has not yet been studied.

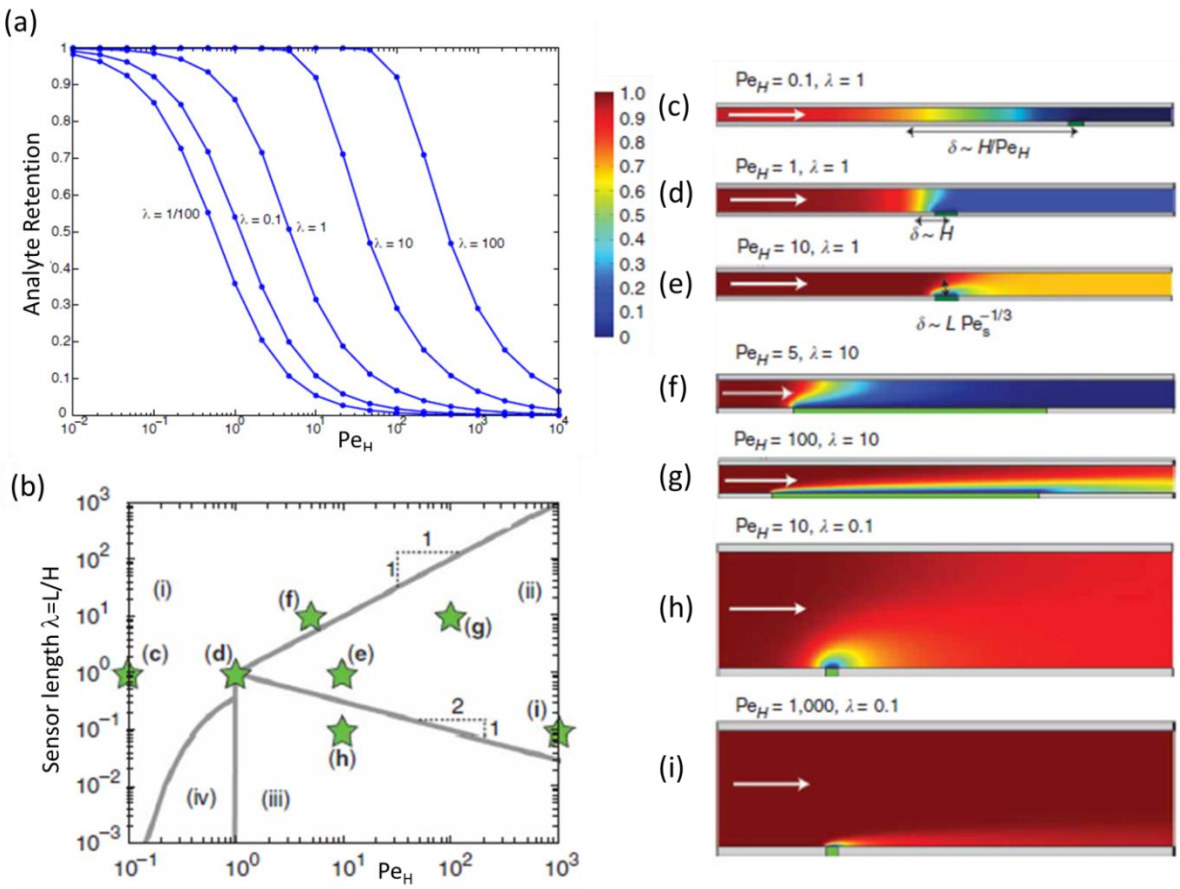

Figure 2.20 (a) Retention or collected fraction of the target analyte by the sensor for a variety of sensor lengths and the Peclet numbers, under convection-diffusion transports (b) A mass transport phase diagram of the model biosensor system. The embedded sensor is assumed to be a perfect collector in which the target molecules instantaneously bind to the surface upon encountering it. (c-i) Steady state concentration profiles in the flow channels, corresponding to the stars in different regions of the phase diagram. The color bar represents the concentration of the target analyte and the white arrow represents the direction of the fluid flow (adapted from [98]).

Computation of these dimensionless numbers is central to determine mass transport behaviors and kinetic regimes of our biosensor system. It thus provides a better understanding of how our device behaves under given experimental assay parameters. Furthermore, this analysis allows us to devise the biosensor design in order to aim for specific applications by considering numerous constraints from real-world assay conditions, such as the sample volume availability, signal-to-noise ratios of the sensing system, and total analysis times [103]. For example, high capture efficiency is desirable for finite sample volumes (*e.g.*, individual cells, small-plug samples) and when a fast assay is less important because a reasonably slow flow velocity should be used to elevate diffusive transports. On the other hand, if the sample availability is not the main constraint (*e.g.*, urine samples), a higher flow rate is applicable in order to speed up the reactions at the expense of inefficient analyte capture and lower signal.

2.6 Conclusion

In this chapter, we have introduced the field of nanofluidics which has been used throughout this PhD work as an alternative analytical tool for kinetic studies. Nanofluidics, in essence, has opened new research avenues to discover and elucidate a variety of biophysical phenomena which have not been previously accessible at the microscale. This is attributed to the unique characteristics inherent to the nanoconfined space, including molecular confinement effects and extremely high surface-to-volume ratios. Furthermore, we have introduced the extended nanospace – the 10^1-10^3 nm length scale that has bridged the gap between conventional nano- and microtechnologies. The main applications of nanofluidics including biomolecule separation, pre-concentration, and single-molecule analysis have been presented, which have highlighted the real potential of the nanofluidic realm.

A literature review related to biosensing in nanofluidics, primarily based on electrical and optical detection schemes, has been provided. Particular emphasis has been placed on kinetic studies of biomolecular interactions in the nanofluidic system. The molecular confinement offered by nanofluidic channels renders these devices extremely promising to direct the transport of target molecules toward the immobilized receptors on the surface, which in turn enhances the reaction kinetics and speeds up the time taken to reach equilibrium. In addition, we have assessed different issues related to nanofluidic biosensing which have impeded researchers in this field to fully benefit from the potential of nanofluidics as an effective biosensor. To address these challenges, we have introduced our alternative concept relying on a combination of biofunctionalized extended nanoslits and a conventional fluorescence microscope, enabling real-time kinetic monitoring of protein-protein interactions. The underlying principles of our device and its unique features have been highlighted, which have guaranteed the versatility of our cost-effective platform to carry out kinetic experiments with advantages of simplicity and optimized sensor performances in terms of the target capture efficiency and response times.

Finally, the interplay of target molecule transport and surface reaction involved in surface-based biosensors has been introduced along with the important dimensionless numbers. The Peclet number and Damköhler number are the key indicators that define mass transport behaviors and surface reaction occurring in the nanoslits, and their values are of importance to determine in which regime our biosensor system operates (*e.g.*, full target collection, reaction-limited regime). In order to validate our device concept stated above, we have fabricated nanofluidic biosensor devices and will be presented in the following chapter.

Bibliography

1. Tabeling, P., *Introduction to microfluidics*. 2005, New York: Oxford University Press.
2. Easley, C.J., et al., *A fully integrated microfluidic genetic analysis system with sample-in-answer-out capability*. Proc Natl Acad Sci U S A, 2006. **103**(51): p. 19272-7.
3. Whitesides, G.M., *What Comes Next?* Lab on a Chip, 2011. **11**(2): p. 191-193.
4. Edel, J.B., deMello, A.J., *Nanofluidics: nanoscience and nanotechnology*. 2009, Cambridge, UK: The Royal Society of Chemistry.
5. Yeh, J.-W., et al., *Entropy-Driven Single Molecule Tug-of-War of DNA at Micro−Nanofluidic Interfaces*. Nano Letters, 2012. **12**(3): p. 1597-1602.
6. Rivet, C., et al., *Microfluidics for medical diagnostics and biosensors*. Chemical Engineering Science, 2011. **66**(7): p. 1490-1507.
7. Tegenfeldt, J.O., et al., *Micro- and nanofluidics for DNA analysis*. Anal Bioanal Chem, 2004. **378**(7): p. 1678-92.
8. Rolando, M.A., Malherbe, R., *Adsorption and diffusion in nanoporous materials*. 2007: CRC Press.
9. Adiga, S.P., et al., *Nanoporous membranes for medical and biological applications*. Wiley interdisciplinary reviews. Nanomedicine and nanobiotechnology, 2009. **1**(5): p. 568-581.
10. Fissell, W.H., et al., *Development of continuous implantable renal replacement: past and future*. Translational Research, 2007. **150**(6): p. 327-336.
11. Abgrall, P. and N.T. Nguyen, *Nanofluidic Devices and Their Applications*. Analytical Chemistry, 2008. **80**(7): p. 2326-2341.
12. Mijatovic, D., J.C.T. Eijkel, and A. van den Berg, *Technologies for nanofluidic systems: top-down vs. bottom-up-a review*. Lab on a Chip, 2005. **5**(5): p. 492-500.
13. Leichle, T. and D. Bourrier, *Integration of lateral porous silicon membranes into planar microfluidics*. Lab on a Chip, 2015. **15**(3): p. 833-838.
14. Duan, C., W. Wang, and Q. Xie, *Review article: Fabrication of nanofluidic devices*. Biomicrofluidics, 2013. **7**(2): p. 026501.
15. Xie, Q., et al., *Wafer-scale fabrication of high-aspect ratio nanochannels based on edge-lithography technique*. Biomicrofluidics, 2012. **6**(1): p. 16502-165028.
16. Mao, P. and J. Han, *Massively-Parallel Ultra-High-Aspect-Ratio Nanochannels as Mesoporous Membranes*. Lab on a Chip, 2009. **9**(4): p. 586-591.
17. Guo, L.J., X. Cheng, and C.-F. Chou, *Fabrication of Size-Controllable Nanofluidic Channels by Nanoimprinting and Its Application for DNA Stretching*. Nano Letters, 2004. **4**(1): p. 69-73.
18. Mao, P. and J. Han, *Fabrication and characterization of 20 nm planar nanofluidic channels by glass-glass and glass-silicon bonding*. Lab Chip, 2005. **5**(8): p. 837-44.
19. Eijkel, J.T. and A. Berg, *Nanofluidics: what is it and what can we expect from it?* Microfluidics and Nanofluidics, 2005. **1**(3): p. 249-267.
20. Tsukahara, T., K. Mawatari, and T. Kitamori, *Integrated extended-nano chemical systems on a chip*. Chemical Society Reviews, 2010. **39**(3): p. 1000-1013.
21. Shirai, K., K. Mawatari, and T. Kitamori, *Extended nanofluidic immunochemical reaction with femtoliter sample volumes*. Small, 2014. **10**(8): p. 1514-22.

22. Napoli, M., J.C.T. Eijkel, and S. Pennathur, *Nanofluidic technology for biomolecule applications: a critical review*. Lab on a Chip, 2010. **10**(8): p. 957-985.
23. Mawatari, K., T. Tsukahara, and T. Kitamori, *Extended nanospace chemical systems on a chip for new analytical technology*. Analyst, 2011. **136**(15): p. 3051-9.
24. Han, J., J. Fu, and R.B. Schoch, *Molecular Sieving Using Nanofilters: Past, Present and Future*. Lab on a Chip, 2008. **8**(1): p. 23-33.
25. Fu, J., P. Mao, and J. Han, *Artificial molecular sieves and filters: a new paradigm for biomolecule separation*. Trends Biotechnol, 2008. **26**(6): p. 311-20.
26. Fu, J., et al., *A patterned anisotropic nanofluidic sieving structure for continuous-flow separation of DNA and proteins*. Nat Nano, 2007. **2**(2): p. 121-128.
27. Eijkel, J.C. and A. van den Berg, *Nanotechnology for membranes, filters and sieves. A series of mini-reviews covering new trends in fundamental and applied research, and potential applications of miniaturised technologies*. Lab Chip, 2006. **6**(1): p. 19-23.
28. Han, J., S.W. Turner, and H.G. Craighead, *Entropic Trapping and Escape of Long DNA Molecules at Submicron Size Constriction*. Physical Review Letters, 1999. **83**(8): p. 1688-1691.
29. Schoch, R.B., J. Han, and P. Renaud, *Transport phenomena in nanofluidics*. Reviews of Modern Physics, 2008. **80**(3): p. 839-883.
30. Levy, S.L. and H.G. Craighead, *DNA manipulation, sorting, and mapping in nanofluidic systems*. Chemical Society Reviews, 2010. **39**(3): p. 1133-1152.
31. Anderson, N.L. and N.G. Anderson, *The human plasma proteome: history, character, and diagnostic prospects*. Mol Cell Proteomics, 2002. **1**(11): p. 845-67.
32. Liotta, L.A., M. Ferrari, and E. Petricoin, *Clinical proteomics: Written in blood*. Nature, 2003. **425**(6961): p. 905-905.
33. Wang, Y.-C., A.L. Stevens, and J. Han, *Million-fold Preconcentration of Proteins and Peptides by Nanofluidic Filter*. Analytical Chemistry, 2005. **77**(14): p. 4293-4299.
34. Kim, S.J., et al., *Concentration Polarization and Nonlinear Electrokinetic Flow near a Nanofluidic Channel*. Physical Review Letters, 2007. **99**(4): p. 044501.
35. Pu, Q., et al., *Ion-Enrichment and Ion-Depletion Effect of Nanochannel Structures*. Nano Letters, 2004. **4**(6): p. 1099-1103.
36. Liao, K.-T. and C.-F. Chou, *Nanoscale Molecular Traps and Dams for Ultrafast Protein Enrichment in High-Conductivity Buffers*. Journal of the American Chemical Society, 2012. **134**(21): p. 8742-8745.
37. Kim, S.J., Y.A. Song, and J. Han, *Nanofluidic concentration devices for biomolecules utilizing ion concentration polarization: theory, fabrication, and applications*. Chem Soc Rev, 2010. **39**(3): p. 912-22.
38. Herr, A.E., et al., *Microfluidic immunoassays as rapid saliva-based clinical diagnostics*. Proceedings of the National Academy of Sciences, 2007. **104**(13): p. 5268-5273.
39. Wang, Y.C. and J. Han, *Pre-binding dynamic range and sensitivity enhancement for immuno-sensors using nanofluidic preconcentrator*. Lab Chip, 2008. **8**(3): p. 392-4.
40. Lee, J.H., et al., *Increase of Reaction Rate and Sensitivity of Low-Abundance Enzyme Assay Using Micro/Nanofluidic Preconcentration Chip*. Analytical Chemistry, 2008. **80**(9): p. 3198-3204.
41. Swami, N., et al., *Enhancing DNA hybridization kinetics through constriction-based dielectrophoresis*. Lab Chip, 2009. **9**(22): p. 3212-20.
42. Foquet, M., et al., *Focal Volume Confinement by Submicrometer-Sized Fluidic Channels*. Analytical Chemistry, 2004. **76**(6): p. 1618-1626.
43. Mannion, J.T. and H.G. Craighead, *Nanofluidic structures for single biomolecule fluorescent detection*. Biopolymers, 2007. **85**(2): p. 131-143.

44. Turner, S.W.P., M. Cabodi, and H.G. Craighead, *Confinement-Induced Entropic Recoil of Single DNA Molecules in a Nanofluidic Structure.* Physical Review Letters, 2002. **88**(12): p. 128103.
45. Bakajin, O.B., et al., *Electrohydrodynamic Stretching of DNA in Confined Environments.* Physical Review Letters, 1998. **80**(12): p. 2737-2740.
46. Reisner, W., et al., *Statics and Dynamics of Single DNA Molecules Confined in Nanochannels.* Physical Review Letters, 2005. **94**(19): p. 196101.
47. Tegenfeldt, J.O., et al., *Near-Field Scanner for Moving Molecules.* Physical Review Letters, 2001. **86**(7): p. 1378-1381.
48. Reisner, W., et al., *Nanoconfinement-Enhanced Conformational Response of Single DNA Molecules to Changes in Ionic Environment.* Physical Review Letters, 2007. **99**(5): p. 058302.
49. Tegenfeldt, J.O., et al., *The dynamics of genomic-length DNA molecules in 100-nm channels.* Proceedings of the National Academy of Sciences of the United States of America, 2004. **101**(30): p. 10979-10983.
50. Wang, Y.M., et al., *Single-molecule studies of repressor–DNA interactions show long-range interactions.* Proceedings of the National Academy of Sciences of the United States of America, 2005. **102**(28): p. 9796-9801.
51. Reisner, W., et al., *Single-molecule denaturation mapping of DNA in nanofluidic channels.* Proceedings of the National Academy of Sciences, 2010. **107**(30): p. 13294-13299.
52. Lam, E.T., et al., *Genome mapping on nanochannel arrays for structural variation analysis and sequence assembly.* Nature biotechnology, 2012. **30**(8): p. 10.1038/nbt.2303.
53. Douville, N., D. Huh, and S. Takayama, *DNA linearization through confinement in nanofluidic channels.* Anal Bioanal Chem, 2008. **391**(7): p. 2395-409.
54. Nair, P.R. and M.A. Alam, *Performance limits of nanobiosensors.* Applied Physics Letters, 2006. **88**(23): p. 233120.
55. Liu, C., et al., *Recent advances in single-molecule detection on micro- and nano-fluidic devices.* Electrophoresis, 2011. **32**(23): p. 3308-3318.
56. Bahrami, A., et al., *Solid-state nanopores for biosensing with submolecular resolution.* Biochem Soc Trans, 2012. **40**(4): p. 624-8.
57. Osaki, T., et al., *Multichannel Simultaneous Measurements of Single-Molecule Translocation in a-Hemolysin Nanopore Array.* Analytical Chemistry, 2009. **81**(24): p. 9866-9870.
58. Wei, R., et al., *Stochastic sensing of proteins with receptor-modified solid-state nanopores.* Nat Nano, 2012. **7**(4): p. 257-263.
59. Iqbal, S.M., D. Akin, and R. Bashir, *Solid-state nanopore channels with DNA selectivity.* Nat Nano, 2007. **2**(4): p. 243-248.
60. Smeets, R.M.M., et al., *Salt Dependence of Ion Transport and DNA Translocation through Solid-State Nanopores.* Nano Letters, 2006. **6**(1): p. 89-95.
61. Saleh, O.A. and L.L. Sohn, *Direct detection of antibody–antigen binding using an on-chip artificial pore.* Proceedings of the National Academy of Sciences, 2003. **100**(3): p. 820-824.
62. Vlassiouk, I., T.R. Kozel, and Z.S. Siwy, *Biosensing with Nanofluidic Diodes.* Journal of the American Chemical Society, 2009. **131**(23): p. 8211-8220.
63. Stein, D., M. Kruithof, and C. Dekker, *Surface-Charge-Governed Ion Transport in Nanofluidic Channels.* Physical Review Letters, 2004. **93**(3): p. 035901.
64. Karnik, R., et al., *Effects of biological reactions and modifications on conductance of nanofluidic channels.* Nano Lett, 2005. **5**(9): p. 1638-42.
65. Lyon, W.A. and S. Nie, *Confinement and Detection of Single Molecules in Submicrometer Channels.* Analytical Chemistry, 1997. **69**(16): p. 3400-3405.
66. Chou, I.H., et al., *Nanofluidic Biosensing for β-Amyloid Detection Using Surface Enhanced Raman Spectroscopy.* Nano Letters, 2008. **8**(6): p. 1729-1735.

67. Choi, I., Y. Huh, and D. Erickson, *Ultra-sensitive, label-free probing of the conformational characteristics of amyloid beta aggregates with a SERS active nanofluidic device.* Microfluidics and Nanofluidics, 2012. **12**(1-4): p. 663-669.
68. Pappaert, K., et al., *Enhancement of DNA micro-array analysis using a shear-driven micro-channel flow system.* Journal of Chromatography A, 2003. **1014**(1–2): p. 1-9.
69. Hofmann, O., et al., *Three-Dimensional Microfluidic Confinement for Efficient Sample Delivery to Biosensor Surfaces. Application to Immunoassays on Planar Optical Waveguides.* Analytical Chemistry, 2002. **74**(20): p. 5243-5250.
70. Vijayendran, R.A., et al., *Evaluation of a Three-Dimensional Micromixer in a Surface-Based Biosensor†.* Langmuir, 2003. **19**(5): p. 1824-1828.
71. Sigurdson, M., D. Wang, and C.D. Meinhart, *Electrothermal stirring for heterogeneous immunoassays.* Lab Chip, 2005. **5**(12): p. 1366-73.
72. Escobedo, C., et al., *Flow-Through vs Flow-Over: Analysis of Transport and Binding in Nanohole Array Plasmonic Biosensors.* Analytical Chemistry, 2010. **82**(24): p. 10015-10020.
73. Wang, Y., J. Dostalek, and W. Knoll, *Magnetic nanoparticle-enhanced biosensor based on grating-coupled surface plasmon resonance.* Anal Chem, 2011. **83**(16): p. 6202-7.
74. Schoch, R.B., L.F. Cheow, and J. Han, *Electrical Detection of Fast Reaction Kinetics in Nanochannels with an Induced Flow.* Nano Letters, 2007. **7**(12): p. 3895-3900.
75. Wang, C., et al., *Nanoconfinement effects: glucose oxidase reaction kinetics in nanofluidics.* Chemphyschem, 2012. **13**(3): p. 762-8.
76. Mross, S., et al., *Microfluidic enzymatic biosensing systems: A review.* Biosens Bioelectron, 2015. **70**: p. 376-91.
77. Idota, N., et al., *The use of electron beam lithographic graft-polymerization on thermoresponsive polymers for regulating the directionality of cell attachment and detachment.* Biomaterials, 2009. **30**(11): p. 2095-101.
78. Balakirev, M.Y., et al., *Photochemical Patterning of Biological Molecules Inside a Glass Capillary.* Analytical Chemistry, 2005. **77**(17): p. 5474-5479.
79. Renberg, B., et al., *Serial DNA immobilization in micro- and extended nanospace channels.* Lab on a Chip, 2009. **9**(11): p. 1517-1523.
80. Karnik, R., et al., *Diffusion-Limited Patterning of Molecules in Nanofluidic Channels.* Nano Letters, 2006. **6**(8): p. 1735-1740.
81. Nicu, L. and T. Leïchlé, *Biosensors and tools for surface functionalization from the macro- to the nanoscale: The way forward.* Journal of Applied Physics, 2008. **104**(11): p. 111101.
82. Demers, L.M., et al., *Direct patterning of modified oligonucleotides on metals and insulators by dip-pen nanolithography.* Science, 2002. **296**(5574): p. 1836-8.
83. Xu, Y., et al., *Low-temperature direct bonding of glass nanofluidic chips using a two-step plasma surface activation process.* Analytical and Bioanalytical Chemistry, 2012. **402**(3): p. 1011-1018.
84. Xu, Y., et al., *Bonding of glass nanofluidic chips at room temperature by a one-step surface activation using an O2/CF4 plasma treatment.* Lab on a Chip, 2013. **13**(6): p. 1048-1052.
85. Leichlé, T., et al., *Biosensor-compatible encapsulation for pre-functionalized nanofluidic channels using asymmetric plasma treatment.* Sensors and Actuators B: Chemical, 2012. **161**(1): p. 805-810.
86. Lee, Y.-H., et al., *Laser-Induced Fluorescence Detection of a Single Molecule in a Capillary.* Analytical Chemistry, 1994. **66**(23): p. 4142-4149.
87. Nie, S., D.T. Chiu, and R.N. Zare, *Probing individual molecules with confocal fluorescence microscopy.* Science, 1994. **266**(5187): p. 1018-21.
88. Wazawa, T. and M. Ueda, *Total Internal Reflection Fluorescence Microscopy in Single Molecule Nanobioscience*, in *Microscopy Techniques*, J. Rietdorf, Editor. 2005, Springer Berlin Heidelberg. p. 77-106.

89. Ekins, R.P., *Ligand assays: from electrophoresis to miniaturized microarrays.* Clin Chem, 1998. **44**(9): p. 2015-30.
90. Dezfooli, M.A.B., *Biosensor arrays for molecular source identification in mass-transport systems*, in *Electrical and computer engineering.* 2013, The University of British Columbia: Vancouver.
91. Qiao, R. and N.R. Aluru, *Ion concentrations and velocity profiles in nanochannel electroosmotic flows.* The Journal of Chemical Physics, 2003. **118**(10): p. 4692-4701.
92. Haneveld, J., et al., *Capillary filling of sub-10nm nanochannels.* Journal of Applied Physics, 2008. **104**(1): p. 014309.
93. Tsukahara, T., et al., *Development of a pressure-driven nanofluidic control system and its application to an enzymatic reaction.* Anal Bioanal Chem, 2008. **391**(8): p. 2745-52.
94. Mawatari, K., et al., *Extended-nano fluidic systems for analytical and chemical technologies.* Nanoscale, 2010. **2**(9): p. 1588-1595.
95. Wang, Y.Y., P. Cheng, and D.W. Chan, *A simple affinity spin tube filter method for removing high-abundant common proteins or enriching low-abundant biomarkers for serum proteomic analysis.* Proteomics, 2003. **3**(3): p. 243-248.
96. Darain, F., K.L. Gan, and S.C. Tjin, *Antibody immobilization on to polystyrene substrate--on-chip immunoassay for horse IgG based on fluorescence.* Biomed. Microdevices, 2009. **11**(3): p. 653-61.
97. Leïchlé, T. and C.-F. Chou, *Biofunctionalized nanoslits for wash-free and spatially resolved real-time sensing with full target capture.* Biomicrofluidics, 2015. **9**(3): p. 034103.
98. Squires, T.M., R.J. Messinger, and S.R. Manalis, *Making it stick: convection, reaction and diffusion in surface-based biosensors.* Nat Biotech, 2008. **26**(4): p. 417-426.
99. Junemo, K. and K. Clement, *Liquid flow in microchannels: experimental observations and computational analyses of microfluidics effects.* Journal of Micromechanics and Microengineering, 2003. **13**(5): p. 568.
100. Kim, J.H.-S., et al., *Characterization of DNA hybridization kinetics in a microfluidic flow channel.* Sensors and Actuators B: Chemical, 2006. **113**(1): p. 281-289.
101. Prakash, S., M. Pinti, and B. Bhushan, *Theory, fabrication and applications of microfluidic and nanofluidic biosensors.* Philos Trans A Math Phys Eng Sci, 2012. **370**(1967): p. 2269-303.
102. Murthy, C. and A. Armani, *Mass transport effects in suspended waveguide biosensors integrated in microfluidic channels.* Sensors, 2012. **12**(11): p. 14327.
103. Parsa, H., et al., *Effect of volume- and time-based constraints on capture of analytes in microfluidic heterogeneous immunoassays.* Lab Chip, 2008. **8**(12): p. 2062-70.

Chapter 3

Fabrication and implementation of the nanofluidic biosensor platform

The aim of this chapter is to present the nanofluidic biosensor platform including its design and implementation, from the fabrication of the chip to its biofunctionalization and packaging. After introducing design considerations and after detailing the microfabrication process used to realize the silicon-based nanofluidic chip, we describe the surface modification protocol carried out on the open nanofluidic device for the construction of the biorecognition element. The chip encapsulation and device assembly/packaging are then presented as well as the experimental setups for fluorescence observations and pressure-driven flow control. Finally, we calibrate the fluid flow within the nanochannels by correlating the applied pressure with the flow velocity through analysis of fluorescent bead displacement, a step necessary for subsequent kinetic assays.

3.1 Device design and conception

The nanofluidic biosensor platform developed through this work aims to provide a tool for the binding kinetics studies of biomolecular interactions while offering the well-known advantages of reduced sample volume and enhanced speed of analysis inherent to miniaturized systems. Proper device design is of critical importance for robust and high performance biosensors. Different criteria are guided by the initial requirements: for instance, ease of fabrication, facile fluidic manipulation and compatibility with optical fluorescence detection. Importantly, in order to simplify and optimize the biofunctionalization process that leads to the grafting of probe molecules onto the nanochannel surfaces, part of this process is carried out in open chip configuration and the nanochannel encapsulation thus needs to be compatible with the presence of active biomolecules. The major characteristics of our devices are described below.

- **Hybrid silicon/ hard-PDMS coated cover glass**

The choice of the materials constituting the sensor is important in the device design. It depends on the operating conditions and the targeted application. Silicon was chosen as a candidate material for the device substrate. Contrary to polymer-based fluidic systems, silicon allows the fabrication of well-defined nanochannels with a wider range of aspect ratios and without the risk of deformation [1]. What is more, the compatibility of silicon-based microfabrication processes with the deposition and patterning of metal layers [2] makes silicon an advisable choice for biosensing applications, particularly for further selective grafting of biomolecules via gold-thiol surface chemistry. However, silicon is not optically transparent, and thus may pose a complication for nanofluidic applications with optical observation.

To obtain optically transparent devices, the silicon substrate baring micro- nanochannels were encapsulated with a cover glass (Figure 3.1). In order to create a permanent seal between the silicon chip and the cover glass, we used a polymer as an adhesive. Hard-Polydimethylsiloxane (h-PDMS) was chosen for its chemical composition and properties close to the ones of PDMS (a material of choice for microfluidic applications) but with a relatively higher Young's modulus, thus preventing the risk of collapse for nanofluidic devices [3].

This hybrid silicon-polymer coated glass system not only offers the possibility to observe the biomolecular interactions inside the nanochannels through a cover glass using a bench-top fluorescence microscope, but it is also compatible with the chip pre-encapsulation biofunctionalization since only a mild asymmetric plasma-activation is required for the encapsulation process, which will be described in detail in the chip encapsulation section.

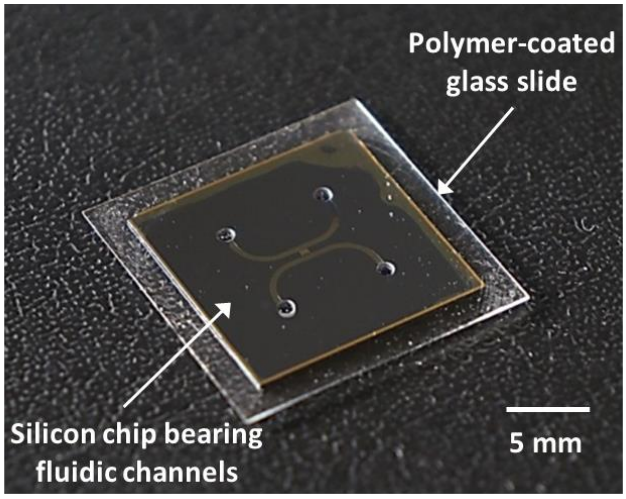

Figure 3.1 Photograph of the fabricated nanofluidic device.

- ## Device footprint and geometrical considerations

We have chosen a device footprint of 16 mm × 16 mm that resulted in 16 fabricated fluidic chips per 100 mm wafer (Figure 3.2). We found that this was a good compromise between the size and the fragility of the device during fabrication and the fluidic manipulation. The channel geometry was determined by the desired applications: in the scope of this work, we decided to fabricate a two-dimensional nanochannel (or nanoslit), where only one dimension (the channel depth) is confined to the nanoscale to offer reduction of the diffusion length with a sensor patterned within the nanochannel and to simplify the fabrication process (since we could use standard photolithography to define the channel width and length).

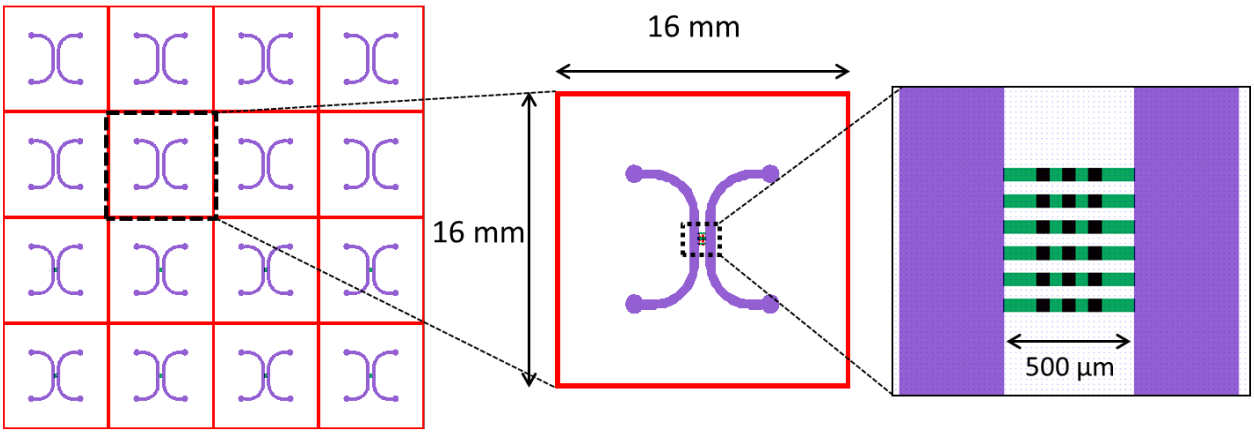

Figure 3.2 Design of the fluidic device with a footprint of 16 mm × 16 mm, corresponding to the density of 16 chips per wafer. A chip consists of a set of 6 parallel 450 nm deep, 500 µm long and 50 µm wide nanochannels (green) bridging two 5 µm deep, 400 µm wide microchannels (purple). Three 100 nm thick square gold patches with the dimensions of 50 µm × 50 µm (black) are located at the bottom of each nanochannel for localized probe grafting.

Concerning the depth of the nanoslits, we wanted to create channels as thin as possible to take advantage of the nanoconfinement effect for biomolecular sensing with reduced fluorescence background and minimized reagent consumption but also deep enough to allow the use of positive pressure with precise flow control by means of a pressure microcontroller. Importantly, we needed to achieve a flow velocity appropriate for kinetic study, and for this aim we had to decrease the fluidic resistance of the system. It is known that as the height of a channel decreases, it is troublesome to move the liquid using pressure gradients. Since the flow velocity is highly controlled by the total resistance of the nanochannels, we decided to connect small channels for analysis with larger channels for bulk transport [4].

The device consisted of 6 parallel nanochannels with 450 nm in depth, 500 µm in length and 50 µm in width with the inter-distance of 50 µm. We designed the nanochannel length and width to fit the field of view of a CCD camera upon fluorescence observation with the use of a 20X objective. The aspect ratio (height over width) being limited by the collapsing risk of the channels during chip bonding was chosen to be in the range of 1/100. These nanochannels were connected to two 5 µm deep, 400 µm wide microchannels. Both microchannels served for analyte transportation and facile reagent exchange during in-situ surface functionalization as well as for reversed-buffer flow operation upon complex dissociation process. At the bottom of each nanochannel, three gold patches (50 µm wide, 50 µm long and 100 nm thick) were locally deposited and served as the sensor surface for kinetic study of protein-protein interactions.

3.2 Fabrication process

The core fabrication of the nanofluidic chips is based on bulk machining and consists of several standard photolithography steps, thermal oxidation and metal deposition, as summarized in the fabrication chart (Table 3.1). The details of each process step are provided in the following part.

Table 3.1 Process chart for nanofluidic device fabrication

Fabrication process of the nanofluidic device on a silicon substrate		
Step	**Process**	**Remarks**
1	Substrate preparation	100 mm p-type silicon wafer 525 μm thick
2	**Nanochannel fabrication:** 2.1) First photolithography 2.2) RIE etching	 Define the nanochannel layout Create the nanochannels (550 nm)
3	**Microchannel fabrication:** 3.1) Second photolithography 3.2) RIE etching	 Define the microchannel patterns on the same substrate Create the microchannels (5 μm)
4	Thermal oxidation	200 nm thin oxide layer
5	Gold deposition	Evaporation Cr/Au (5/100 nm)
6	Lamination	Front side wafer protection
7	Inlet/outlet drilling	Sandblasting machine
8	Dicing	16 individual chips

3.2.1 Nano- and microchannel fabrication

The device was fabricated on a 100 mm P-type 525 μm thick silicon wafer (BT Electronics, France) using a standard photolithography to define the nano/microchannel structures. First, the silicon wafer was immersed in a piranha solution (H_2SO_4/H_2O_2; 1:1 v/v) for 2 min, followed by a 5% HF solution for 30 s to remove the native oxide layer carrying all impurities. The wafer was again cleaned in the piranha solution for 2 min, thoroughly rinsed with deionized water before dehydration in a 200 ºC oven for 10 min.

Before deposition of the photoresist, the silicon wafer was treated with an adhesion promoter (hexamethyldisilazane, HMDS) through vapor deposition to ensure good adhesion of the photoresist to the silicon wafer. The HMDS-activated wafer was spin-coated with the positive ECI 3012 photoresist (AZ Electronic materials) and soft-baked to remove excess solvents and activate the photo-initiators in the resist, resulting in a 2.6 μm thick resist layer. In order to define the nanochannel patterns, the wafer was exposed to ultraviolet light (12.5 s at 20 mW/cm^2) through a nanochannel-defined chromium mask using a vacuum contact mode (MA 150, Karl Suss Inc.), and then developed.

Using the patterned photoresist as a mask, the 550 ± 20 nm deep nanochannels were created on the silicon substrate using a reactive ion etching (RIE) technique, producing controllable anisotropic vertical profiles with a smooth bottom surface of the trenches. We used a profilometer (KLA-Tencor) to measure the channel depth.

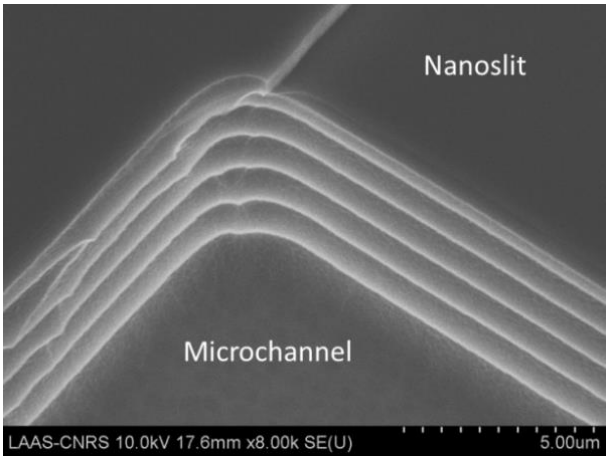

Figure 3.3 An SEM image of a microchannel connected to a nanoslit fabricated on a silicon substrate using a reactive ion etching technique.

After the photoresist dissolution, similar photolithography and etching steps were repeated to create microchannels on the same silicon wafer. However, instead of using a RIE technique, a deep reactive ion etching (DRIE) or Bosch process was employed to excavate deeper channels, which were 5± 0.4 μm deep microchannels in our case. This resulted in anisotropic sidewalls that exhibit scalloping or ripple (Figure 3.3).

3.2.2 Thermal oxidation and gold deposition

To facilitate chip encapsulation and aqueous liquid filling, we performed thermal oxidation on the etched silicon wafer to render the chip surface hydrophilic by the formation of a thin oxide layer (200 nm). The obtained silicon dioxide thickness was controlled using an ellipsometer. The roughness of the bottom of the nanochannl after thermal oxidation was measured by contact mode atomic force microscopy to be approximately 1.3 nm. **The smoothness of the bottom surface and channel sidewalls was crucial for our application since any surface defects could induce undesirable non-specific adsorption of biomolecules and non-uniform flow, thus diminishing the device performances.**

After the thermal oxidation, gold patches were patterned at the bottom of the nanochannel by means of a photolithography process. Briefly, a negative resist (AZ-NLOF 2035, MicroChemicals) was spun onto the thermally-oxidized silicon wafer, UV-insolated (MA150, 7.5 s at 20 mW/cm^2) and developed to create the gold patch structures. A 5 nm layer of chromium (Cr) and a 100 nm layer of gold (Au) were deposited using both standard thermal evaporation and lift-off techniques.

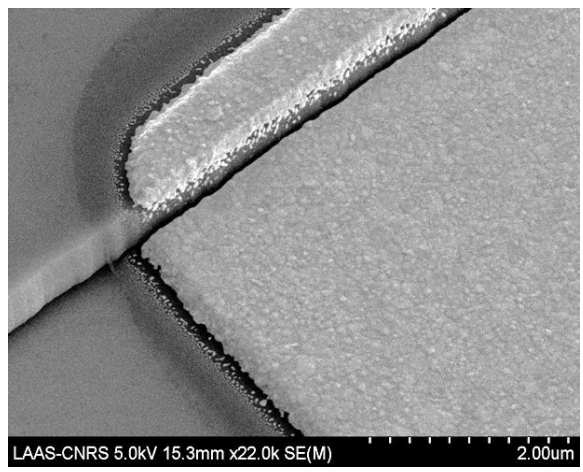

Figure 3.4 An SEM image of a 100 nm thick gold film deposited at the bottom of the nanoslit.

The metal film was allowed to recrystallize by thermal annealing at 250 °C under an N_2H_2 atmosphere for 20 min in order to reduce the stress built up at the metal-substrate interface and improve the metal adhesion on the underlying layer. The roughness of the gold surface after piranha cleaning was measured to be 1.2 nm. **The gold roughness has a substantial influence on the surface modification of the biosensing element, thus on the sensing properties of the sensor.** The SEM image of deposited gold layer at the bottom of the nanoslit is shown in Figure 3.4.

3.2.3 Lamination and inlet/outlet hole opening

To facilitate liquid injection into the fluidic chips, it was necessary to drill millimeter diameter holes on the silicon substrate, which served as inlet/outlet ports for the devices. Prior to drilling, a dry photoresist (PH2050) was laminated on the silicon substrate using a Shipley laminator (The Rohm and Haas Electronic Material, Italy) at room temperature followed by lamination at 110 ºC. The purpose of this lamination step was to protect the wafer during inlet/outlet hole opening. The holes were drilled using a sandblasting machine (Micro Blaster, Comco Inc.) equipped with aluminum oxide particles. The dry photoresist was stripped out by immersing the wafer in an acetone bath with the aid of sonication.

The wafer was then protected with the photoresist and finally diced into individual chips. The cleanroom fabrication process and the SEM picture of nanoslits are illustrated in Figure 3.5 and Figure 3.6, respectively. The detailed experimental conditions of the fabrication processes are provided in the **Appendix A**.

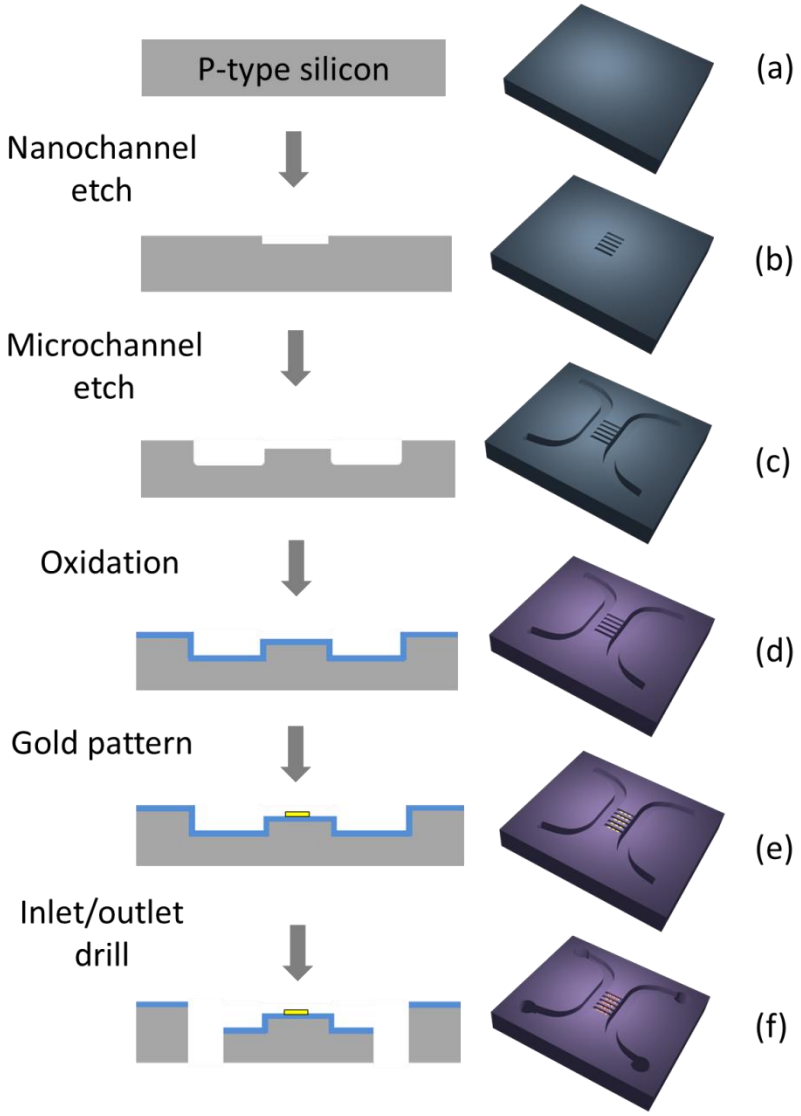

Figure 3.5 Fabrication procedure of the nanofluidic devices. (a) A 100 mm p-type silicon wafer was used as a device substrate. (b) The nanochannels were etched on a silicon wafer using RIE technique. (c) The microchannels were created on the same wafer by DRIE technique. (d) Thermal oxidation was employed to form a thin oxide layer on the silicon wafer. (e) A 5/100 nm Cr/Au layer was patterned at the bottom of the nanochannels using photolithography and lift-off processes. (f) Inlet/outlet holes (1 mm in diameter) were drilled using a sandblaster.

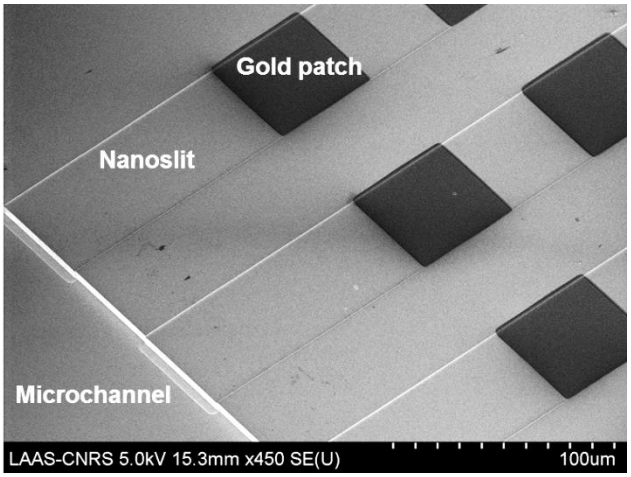

Figure 3.6 SEM image of the device having a series of parallel nanoslits linked to a microchannel.

3.3 Biointerface

Construction of a biointerface is a key ingredient in designing surface-based biosensors and has a compelling influence on the biosensor performances, in particular, sensitivity, specificity and selectivity of detection. To study kinetics of protein-protein interactions, one requires the immobilization of the receptor probes onto a suitable sensor surface. **During this immobilization process, the receptors need to retain their binding activity and they should be stable over the course of the assay.** The main characteristics of desirable biosensing elements are listed below.

1) The surface coverage should be optimum. On the one hand, the surface grafting density of the receptors should be sufficient to ensure the signal strength and thus the sensor sensitivity. On the other hand, too high a probe density induces steric hindrance upon analyte binding, leading to deviations from the Langmuir-like binding behavior, which is not advisable for kinetic studies [5, 6].
2) The orientation of the biomolecules should favor the accessibility of the analyte from the solution phase with sufficient binding sites [7].
3) Non-specific adsorption should be minimized to avoid false positive-signals and a misleading interpretation of the results [8].
4) Importantly, the surface functionalization method should be compatible with the nano/microfluidic device materials and fabrication steps (for example, chip encapsulation). In our case, we also wanted the surface functionalization scheme to be applicable to SPR setup in order to conduct kinetics experiments with this standard tool for comparison means.

Currently, various immobilization methods including physical adsorption, covalent coupling, and self-assembled monolayer have been established for the immobilization of biomolecules (receptors) onto the transducing surfaces [9]. The choice of surface chemistry strategies is governed by numerous factors such as stability and functionality of biomolecules, assay format, analyte of interest, detection scheme, and application.

The aim of the study discussed in this section was to implement surface grafting of protein receptors on the nanofluidic device for kinetic studies of protein-protein interactions. The functionalization protocol used to graft the probe molecules onto the gold sensors embedded in the nanofluidic channels was carried out partially on the open-top devices prior to chip encapsulation and in-situ bio-functionalization after chip sealing (see Chapter 4). Practically, the devices need to be dried before sealing and as a result the biorecognition elements immobilized on the sensor surface should sustain such bonding condition as part of the device fabrication.

3.3.1 Biological model

Two representative protein-receptor pairs of different affinities, streptavidin-biotin (high affinity) and mouse IgG/anti-mouse IgG (moderate affinity), were chosen to demonstrate the capability of our devices to determine kinetic parameters.

Biotin is a small water-soluble vitamin (244 Da) also known as vitamin H. Streptavidin is a 60 kDa tetrameric glycoprotein purified from the bacterium *Streptomyces avidinii*. Streptavidin-biotin binding is one of the strongest non-covalent bonds known with a dissociation constant (K_D) in the range of 10^{-14} - 10^{-16} M [10, 11]. Due to this very strong interaction, streptavidin-biotin shows a very high resistance to denaturation induced by changes in pH, temperature or exposure to denaturing agents [12]. Binding kinetics of streptavidin-biotin interaction was investigated in our study since monitoring this high affinity recognition with the standard SPR method has not yet been addressed. Figure 3.7a depicts a 3D molecular structure of the tetrameric streptavidin-biotin complex.

On the other hand, an IgG/anti-IgG pair was chosen as a generic candidate model for other varieties of protein-ligand interactions. Immunoglobulin G (IgG) is a type of antibody with a 150 kDa molecular weight, created and released by plasma B cells. Figure 3.7b illustrates a 3D structure of a monoclonal immunoglobulin. Biotinylated anti-IgG are commercially available and can be simply linked to the sensor surface via a streptavidin-biotin bridge. The dissociation constant (K_D) of anti-IgG/IgG binding is in the range of 10^{-9} M [13, 14].

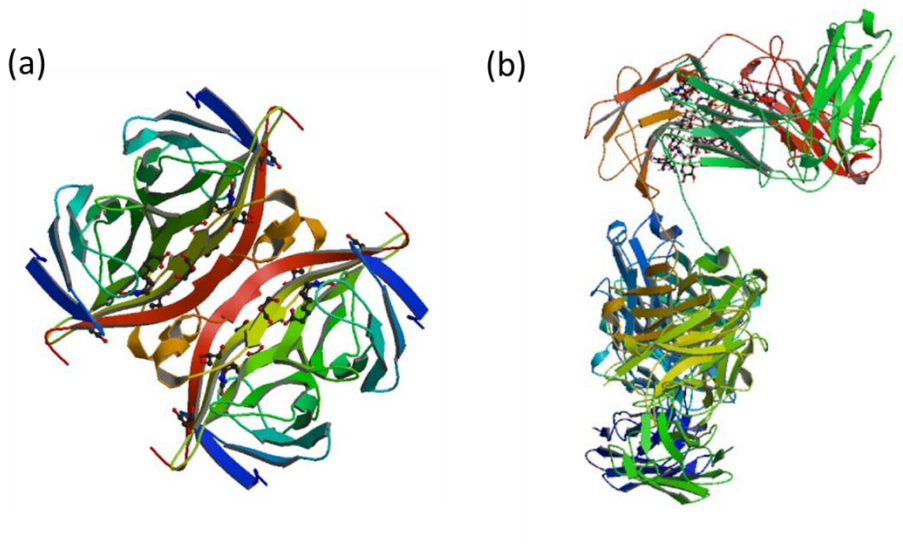

Figure 3.7 3D molecular structures of the tetrameric streptavidin-biotin complex (a) and of a monoclonal immunoglobulin (IgG) (b) (from RCSB Protein Data Bank).

3.3.2 Surface chemistry

We selected gold as a sensor surface for the immobilization of probe receptors. The first advantage of using a gold surface in this study is mainly to permit the same grafting protocol to be implemented onto our nanofluidic biosensor platform as well as on the SPR platform to conduct kinetics studies with both techniques for comparison purposes; gold is the main read-out format in SPR assay [15]. The popularity of using gold in the field of biosensors arises from its inert nature, and its compatibility with semiconductor manufacturing processes. It can be deposited onto the silicon substrate by evaporation which is applicable to our device fabrication. The most ordinary feature of gold is to allow facile and reproducible immobilization of thiol-containing biomolecules using a self-assembled monolayer via strong gold-sulfur linkage [16].

Concerning a choice of surface chemistry protocol, a self-assembled monolayer (SAM) of thiol molecules was employed for receptor immobilization on the gold sensor. SAM offers several advantages in biosensor applications due to its tremendous flexibility to design the headgroup of SAM with various functional groups. Accordingly, hydrophobic/hydrophilic surfaces can be achieved depending on specific requirements [17]. Attachment of antibodies on the sensor via SAM chemistry also prevents direct contact of proteins with the surface and provides well-oriented immobilized antibodies, which in turn ameliorates the binding efficiency toward target analytes, owing to enhanced accessibility of the binding sites [18].

In this study, SAMs were composed of two thiol species, 1) hydroxyl-terminated thiol or a spacer and 2) biotinylated thiol. The first thiol compound reduced the surface density of functional groups, and thus minimized steric hindrance and suppressed non-specific adsorption of unappealing

proteins. The second thiol species contained biotin functional headgroups used for kinetic study of streptavidin-biotin interaction as well as for subsequent immobilization of biotinylated receptor molecules through streptavidin-biotin linkage [19].

Optimization of the mixing ratio between these two compounds allows better control of immobilized surface probe densities on the sensor surface [20], which is a requisite parameter for kinetic studies. For the streptavidin-biotin interaction model, 1% of biotinylated thiol (BAT) was used to obtain an optimum surface density of immobilized biotin and to avoid the problem of steric hindrance upon binding which could change their kinetic binding behaviors. On the other hand, 10% biotinylated thiol was employed in the second model of mouse IgG/anti-mouse IgG interaction, providing the maximum density of immobilized streptavidin molecules for subsequent anchoring of the biotinylated anti-mouse IgG receptor [21, 22] (Figure 3.8). This immobilization step, based on SAM formation, was carried out prior to chip encapsulation since it required several hours of incubation (~12 h), and due to the fact that the immobilized biotin molecules could retain their functionality upon chip dehydration prior to encapsulation.

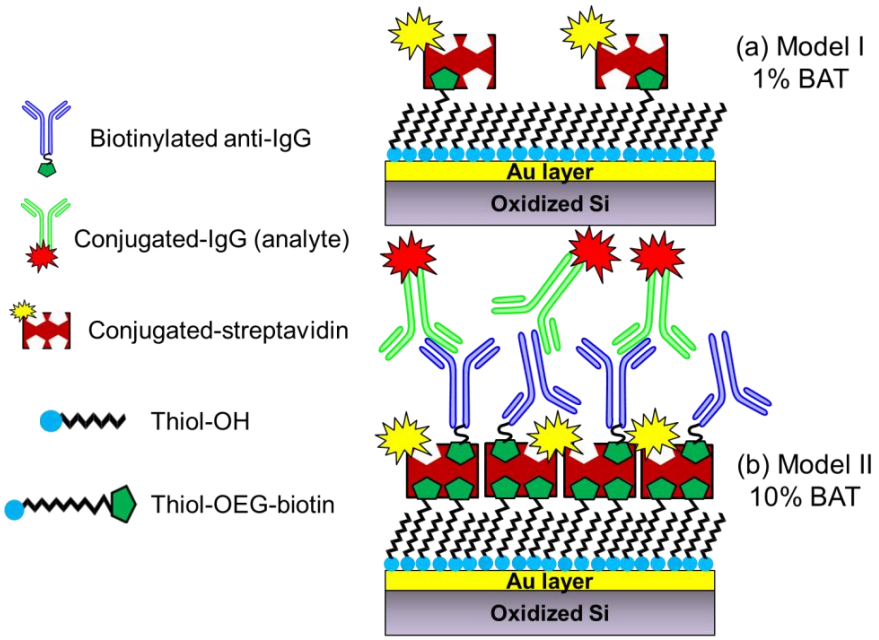

Figure 3.8 Schematic illustrations (not to scale) of two surface functionalization architectures on gold sensors used for protein kinetic study in nanoslits. (a) Model I streptavidin-biotin interaction on 1% biotinylated thiol modified surface; (b) Model II mouse anti-rabbit IgG/anti-mouse IgG interaction via biotin-streptavidin linkage on 10% biotinylated thiol modified surface. Hydroxyl-terminated thiol compound acts as a spacer to reduce non-specific adsorption of proteins on gold surfaces.

After biotin is bound to the gold surface through alkyl chain of thiol molecules, it still possesses the binding affinity toward streptavidin, allowing highly rigid and well-ordered streptavidin immobilization [20]. We used fluorescently labeled streptavidin in our study to monitor its kinetic reaction with surface immobilized biotin in the first model as well as to offer the first fluorescence detection point, revealing successful streptavidin immobilization for further modification in the second model.

Since streptavidin has four biotin-binding sites located on two opposite sides of is tetrameric structure, another layer of any biotinylated protein can thus be built on top of it. In our case, biotinylated anti-IgG was chosen as the receptor layer for the detection of fluorescent IgG molecules. The aforementioned surface functionalization steps (*i.e.*, streptavidin and biotinylated anti-IgG) were performed in a flow manner once the fluidic chip was sealed. For fluorescence imaging purposes, two different dyes with non-overlapping emission spectra were employed in order to distinguish between the immobilization of streptavidin and the subsequent binding study between the non-fluorescent immobilized receptors and the fluorescently labeled IgG analytes. In this case, streptavidin was conjugated with a green fluorescence dye (Alexa Fluor 488) while the IgG target analyte was conjugated with a far-red fluorescent dye (Alexa Fluor 647).

This surface chemistry concept not only offers widespread use of biotinylated proteins as receptors for targeting other specific analytes, but also leads to minimized non-specific adsorption while preserving bio-functionality of biomolecules with well-oriented receptors on the surface, beneficial for optimal target-probe interaction.

3.3.3 Open-top surface functionalization

Prior to implementing the surface functionalization protocol into the closed-nanofluidic devices, where the fluidic-like environment could complicate the functionality of the sensor and the device manipulation, we decided to assess the modification protocol using the **open-top chip fashion and fluorescence imaging**.

To this end, we utilized the unclosed silicon chip with embedded gold sensors as a device substrate for surface functionalization verification. Since the device consisted of both gold surfaces for selective patterning of biomolecules (receptors) and silicon dioxide surfaces on the remaining areas (Figure 3.9), it was compulsory to passivate the silicon dioxide surface with protein-blocking reagents to circumvent potential non-specific adsorption of other biomolecules, which could reduce the device sensitivity.

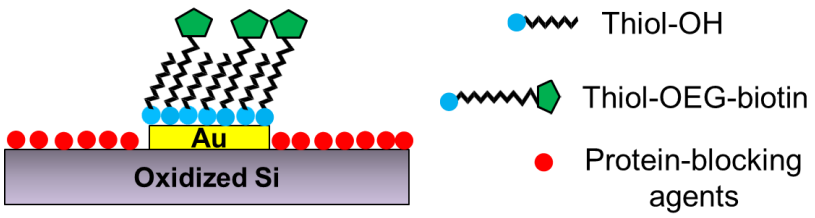

Figure 3.9 Simplified cartoon schematic depicting the device surfaces, consisting of the gold patch and silicon dioxide surface used in this experiment. The gold patch acts as the sensing layer for biomolecule immobilization via gold-thiol chemistry. The remaining silicon dioxide areas of the chip were passivated with blocking agents.

The role of blocking agents is mainly to reduce nonspecific adsorption of protein on the silicon dioxide areas, thus reducing interference background and improving signal-to-noise ratio without altering or obscuring the analyte binding onto the surface-immobilized receptors. Many blocking strategies have been reported to suppress non-specific adsorption on various surfaces. For instance, covalent attachment of poly(ethylene glycol) (PEG) creates non-fouling hydrophilic surfaces, resisting non-specific adsorption [23]. This method has also been implemented in microchannels [24].

In contrast to covalent modification, the adsorption strategy is one of the promising approaches relying solely on intermolecular interactions (van der Waals forces, hydrophobic interaction etc.) between the coating agents and the substrate surface [25]. The most commonly used coating agent is bovine serum albumin (BSA). BSA is a small protein which tends to bind to all surfaces including hydrophobic and hydrophilic surfaces [26], contributing to its widespread use in biosensor applications [27, 28]. BSA has been demonstrated to reduce background due to non-specific adsorption on PDMS microchannels in ELISA assay [29]. **In this study, BSA was used to passivate the device surface (silicon dioxide) for open-top functionalization experiment as well as to passivate the h-PDMS roof of the enclosed fluidic devices (this will be discussed in the next section).**

In all experimental conditions, the BSA passivation step was accomplished after the formation of the SAM layer on gold surfaces. Three different modified gold surfaces were studied; (1) bare gold surface, (2) 100% hydroxyl-terminated modified (MUOH) surface, and (3) 10% biotin-modified (BAT) surface. For each surface modification scheme, the silicon dioxide surface of each chip was subsequently either BSA-passivated or not. As a result, there were six different samples for functionalization investigation in this experiment. The materials used throughout these experiments are given in the **Appendix B**.

Briefly, piranha cleaned substrates were immersed in different solutions of thiols (0.5 mM in ethanol) for > 12 h to form SAMs on the gold surfaces. For the passivation step, a 2 mg/ml BSA solution was dropped onto the substrates and the surfaces were incubated for 30 min. The chips were afterwards rinsed with DI water and dried. A 100 nM Alexa Fluor 488 streptavidin solution prepared in PBS buffer was drop-casted onto the substrates to allow the interaction between streptavidin in the solution and the surface immobilized biotins for 30 min. The substrates were kept in the dark at room temperature throughout the experiment. The chips were rinsed with PBS buffer to remove any excess streptavidin molecules and they were observed under the fluorescence microscope using the same imaging parameters for all substrates (Table 3.2).

Table 3.2 Fluorescence images of the chips after different surface treatments

Modified surfaces	With BSA	Without BSA
Bare gold		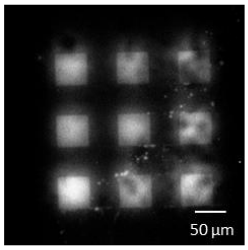
100% MUOH		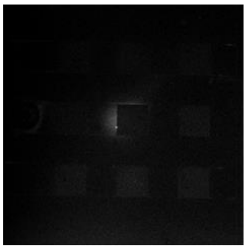
10% BAT	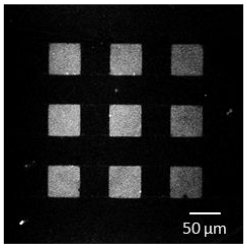	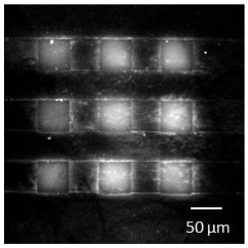

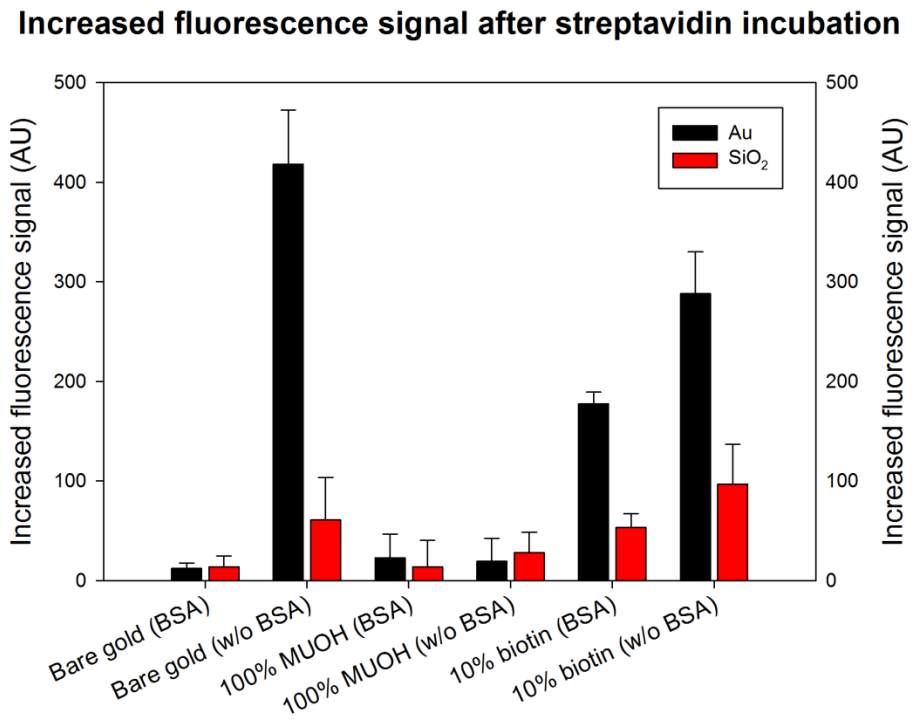

Figure 3.10 Plot of increased fluorescence intensities after streptavidin immobilization on gold sensor and silicon dioxide (areas outside sensor) of different treated gold surfaces.

From Figure 3.10, some conclusions could be drawn regarding the passivation approach and the functionality of the surface modification protocol on the various treated-surfaces as listed below.

- Streptavidin mostly non-specifically adsorbed on the bare gold surface and some adsorbed on the silicon dioxide surface. Pre-treated BSA surfaces effectively prevented these non-specific adsorptions.
- There was no significant non-specific adsorption of streptavidin on hydroxyl-thiol modified gold surfaces for both cases: the BSA treated surface and non-BSA treated surface. This was attributed to the ability of the hydrophilic hydroxyl group located on the gold surface to block undesirable adsorption.
- Streptavidin specifically bound to the 10% biotin treated gold surface. However, it was observed that streptavidin could bind more on the 10% biotin treated surface without BSA passivation. This suggested that some BSA molecules also adsorbed on the gold area which partially blocked further binding of streptavidin molecules.

Although, use of BSA passivation could partially block the binding sites on the biotinylated surface for subsequent streptavidin immobilization, adequate streptavidin binding signal on the gold sensor over background signal on the silicon dioxide surface was achieved, which is suitable for highly sensitive bio-analysis in nanochannels.

These results obtained from open-top functionalization format partly validated our bio-functionalization protocol. The validation of the full functionalization protocol was carried out using quartz crystal microbalance apparatus **(see the Appendix C)**.

3.4 Chip encapsulation

Once the gold sensors at the bottom of the nanochannels were modified with biotinylated thiols in the open-top manner, the chip was encapsulated with an optically transparent substrate, enabling the fabrication of enclosed nanofluidic systems. The essential requirement of the chip encapsulation process is primarily its compatibility with low high-aspect ratio (1/100) nanochannels, without risk of collapse. Secondly, the bioactivity of the pre-immobilized receptors should be preserved. Lastly, the bonding method should ensure appropriate bonding strength and uniformity, suitable for pressure-driven injection (applied positive pressure in the range of 0-200 mbar).

The most widely used bonding techniques for nanofluidic fabrication includes fusion bonding and anodic bonding [30]. Nevertheless, involved heat treatment induces irreversible denaturation of pre-immobilized receptors on sensor surfaces. PDMS elastomer is commonly used to fabricate chip-based microfluidic devices using lithography and replica molding. This is due to its desirable properties, including bio-compatibility and optical transparency, suitable to be used as a capping layer in microfluidic devices [31]. Replica molded PDMS can be irreversibly sealed on the glass substrates by oxygen plasma treatment and can withstand 30-50 psi of air pressure [32]. However, PDMS is impractical for the fabrication of nanofluidic devices with typical channel heights below one micron due to its deformability, leading to well-known roof collapse [33, 34].

A hard-PDMS, having similar properties and functionality to PDMS but harder (more cross-linked polymer), is an alternative material which offers 4.5 times the Young's modulus than that of standard PDMS [35]. The h-PDMS sealing approach has already been developed to fabricate nanofluidic channels [3, 36]. **Due to its hardness, pressure-induced deformation in h-PDMS can be dramatically reduced, leading to successful chip encapsulation, particularly in nanoscale devices.**

Therefore, an h-PDMS coated cover glass slide was employed in place of a regular PDMS to avoid channel collapse upon device sealing in this study. The lowest aspect ratio giving successful device sealing with h-PDMS was found to be 5×10^{-4} (500 nm deep and 1 mm wide channels).

The detailed compositions for h-PDMS preparation are provided in the **Appendix D**. Briefly, the unreticulated h-PDMS mixture was spin-coated at 3000 rpm for 30 s onto a piranha-cleaned cover glass (0.13-1.16 mm thick, Menzel-Glaser) followed by 2 hours curing in an oven at 60 ºC, resulting in a 6 µm thick deposited polymer layer (Figure 3.11). This curing temperature was adapted from previous work [36] in order to reduce the surface roughness formed on h-PDMS coated cover glass upon baking. The surface roughness was very problematic in our case because of the high degree of non-specific adsorption of biomolecules onto the rough surfaces.

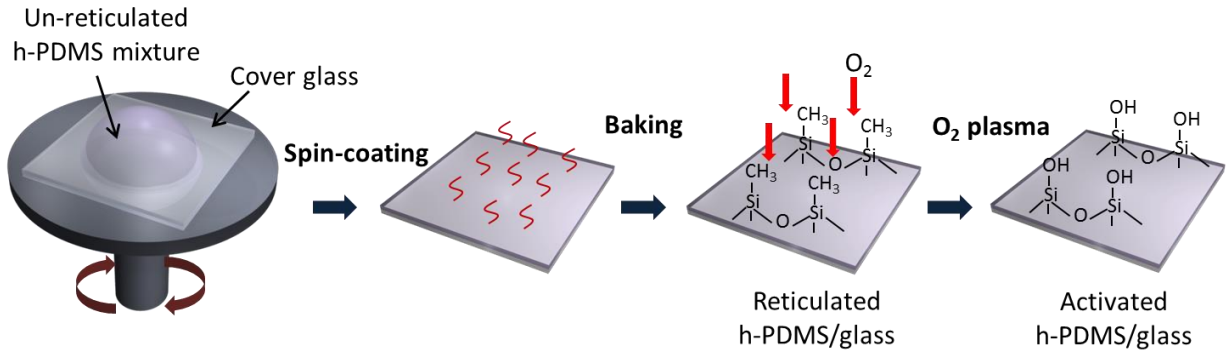

Figure 3.11 Sketch of preparation procedures for the h-PDMS coated cover glass.

Unlike ordinary polymer sealing procedure wherein both surfaces (glass and polymer-coated substrate) are activated with oxygen plasma treatment to render them hydrophilic before bonding, our sealing approach relies on the activation of only h-PDMS coated cover glass but not the pre-immobilized fluidic chip [37]. This process was performed under room temperature, thus keeping the bio-functionality of the pre-immobilized probes.

To this end, the h-PDMS cover glass was activated by oxygen plasma (120 s, 35 W, 0.5 mbar O_2, PICO Plasma Cleaner, Electronic Diener) and immediately placed in contact with the biotin-modified nanoslit chip to achieve a covalent bond (Figure 3.12). The chip was quickly baked in a 65 ºC oven for 5 min to ensure good bonding.

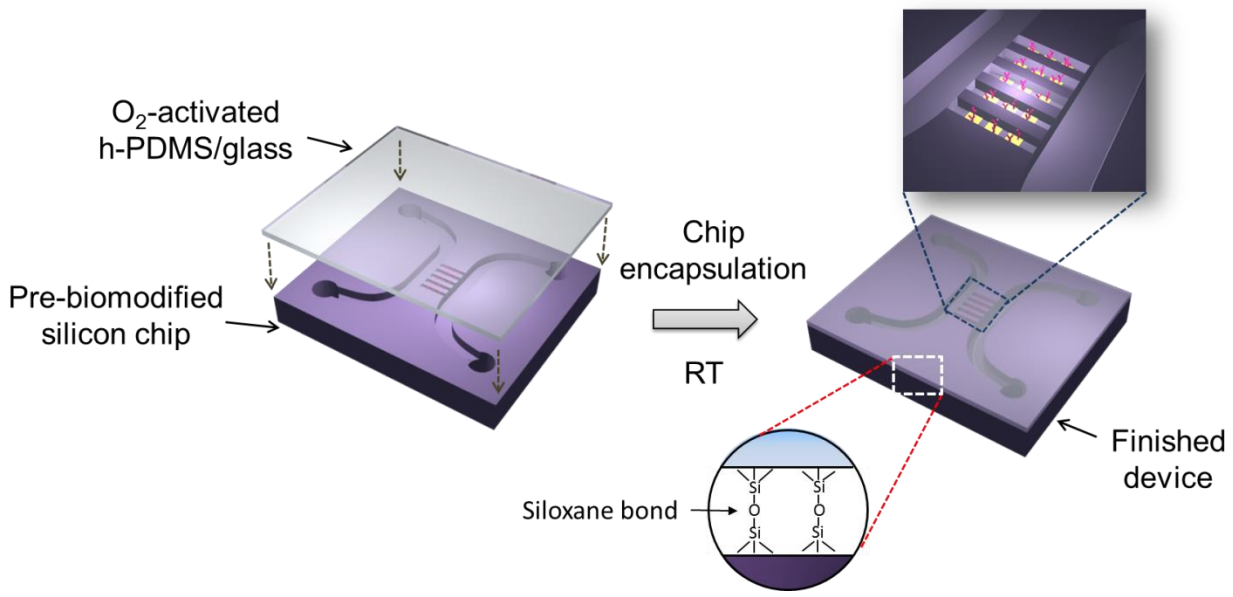

Figure 3.12 Illustration of chip encapsulation process performed at room temperature. A h-PDMS coated cover glass was activated by means of oxygen plasma exposure and then brought into contact with a receptor pre-modified silicon chip to form a finished fluidic device.

A surface molecular mechanism of SiO_2/h-PDMS bonding is considered similar to glass-PDMS bonding. Surface activation via oxygen plasma treatment alters the methyl moieties ($Si\text{-}CH_3$) at the h-PDMS surface to a hydrophilic silanol (Si-OH) surface structure. The measured water contact angle after plasma activation was less than 5 ºC, which was required for obtaining high bond strength [32]. It is well-known that oxidized PDMS based materials can recover their hydrophobicity upon exposure to air in a few hours or less. Therefore, as soon as the polymer surface was activated, the h-PDMS coated cover glass was immediately brought into conformal contact with the pre-biofunctionalized chip. The reaction of silanol moieties on both surfaces creates a strong covalent siloxane (Si-O-Si) bond through a condensation process. The device encapsulation was preferably performed in a clean-room environment to avoid any dust or other contaminants, which would result in bonding failure.

After the encapsulation step, the chips were filled with a blocking solution (1% BSA in 10 mM PBS buffer with 0.02% Tween-20, pH 7.4) by capillary forces to prevent non-specific adsorption of proteins on the channel walls (h-PDMS roof surface and silicon dioxide bottom surface). It is noted that the BSA-filled nanofluidic devices could be stored in the dark at 4 ºC in which the sensor still remained active and stable for several weeks. A detergent such as Tween-20 is commonly added to the buffer or blocking solution to minimize background caused by nonspecifically bound materials in the assay [38].

3.5 Device assembly and fluidic configuration

Fluid transport is a crucial issue in nanofluidic devices. In the scope of this work, positive pressure generated by a pressure controller (Fluigent) system was utilized throughout our experiments to pump the liquid or biological samples into the nanoslits. The pressure driven-flow method allows precise flow control and easy fluid handling, which is indispensable for immunoassay. Moreover, it is simple to implement and it is insensitive to surface contaminants, ionic strength and pH in contrast to electrokinetic flow.

In order to connect the nanofluidic device to the macro world for sample loading and injection, we have designed and constructed a dedicated fluidic interface. For the assembled devices to allow the bioanalysis to be performed in a controllable manner, several criteria were taken into account.

- The chip holder should be compatible with a bench-top fluorescence microscope stage for optical observation on one side while permitting fluidic control on the other side.

- Secondly, the disclosed fluidic assembly should be robust and perfectly sealed to sustain the application of the positive pressure, preventing the chip delamination and in consequence fluid leakage during manipulation and liquid injection.

- Last but not least, it should allow the reversed buffer flow operation by switching from analyte to buffer solution without removing the fluidic setup for reagent exchange. In this way, both association and dissociation kinetics of protein interactions can be assessed in one single experiment and without an extra buffer loading step.

With this aim, a homemade dedicated fluidic support was created in the mechanical workshop at LAAS (Figure 3.13a). Three distinct parts were employed in the sample holder: a bottom support made of aluminum and bearing a defined-dimension gasket to host the fluidic chip (and to enable microscopy observations), a part bearing the reservoirs made of Teflon directly placed on top of the chip, and the fluidic connector in Teflon mounted on top of the reservoirs to close the entire system. O-rings and Teflon screws were employed at each interface to ensure a perfect sealing. The fluidic chip was placed upside-down in the gasket support.

The benefit of this fluidic setup is the significantly reduced dead-volume of expensive biological reagents, thus minimizing the sample consumption, as compared to the conventional microfluidic setup with lengthy tubing. **Minimum reagent volume of less than 10 µL (which could be even less with an optimized setup) can be loaded into the dedicated reservoirs of our setup while hundreds of microliters are needed for a typical microfluidic device.**

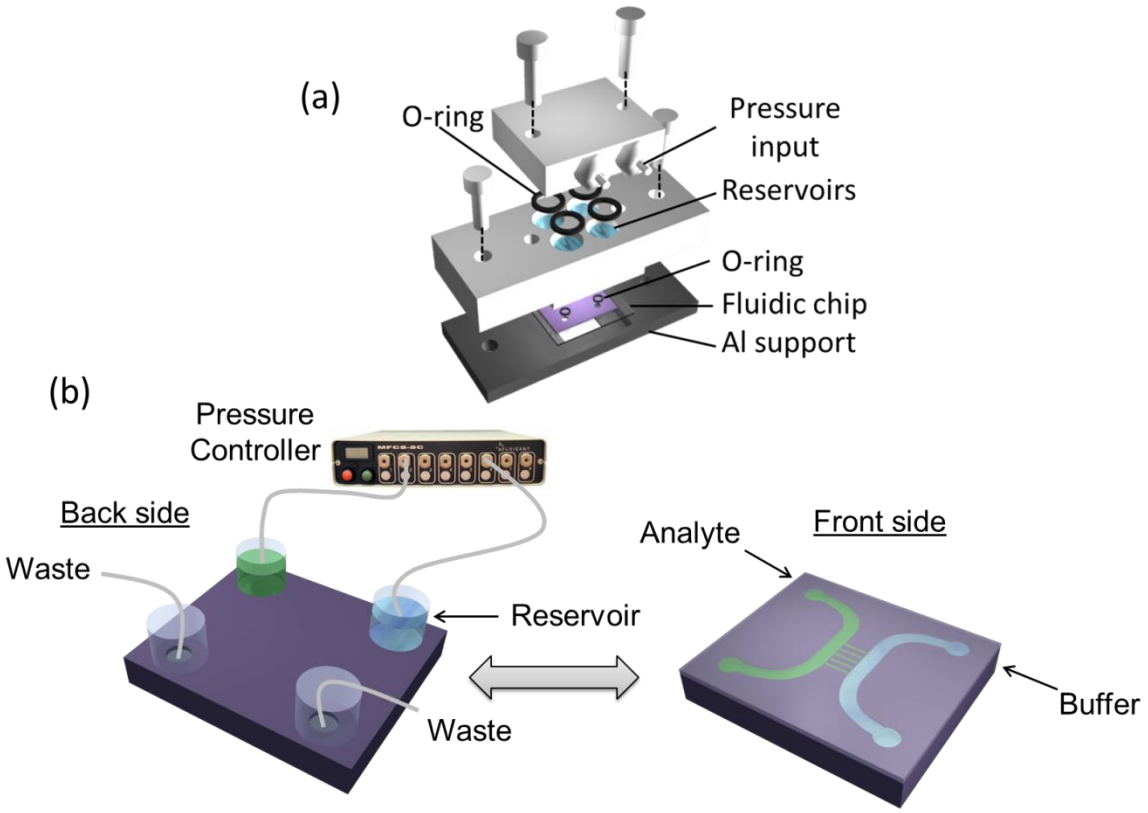

Figure 3.13 (a) Schematic presentation of the chip holder compatible with pressure-induced flow. The fluidic chip is placed upside-down in its emplacement made in aluminum. (b) Diagram of fluidic configuration enabling reverse buffer flow operation in kinetic assay. The pressure controller is employed to induce the flow of biomolecules into nanoslit. The analyte solution is introduced from one inlet while another inlet is used for buffer injection, allowing the study of association and dissociation phases of immunoreactions in one single-experiment.

As far as the fluidic configuration is concerned, the chip included two microchannels used to introduce liquids and connect to the external fluid apparatus (air tubing and pressure generator) while parallel straight nanochannels served to conduct the binding kinetics of protein interactions. There were two inlets and two outlets situated at the end of each microchannel. In kinetic experiments, the sample and the buffer solutions were loaded in two opposite reservoirs. The first inlet empowered the delivery of the target analyte solution for the association phase whereas the buffer solution was injected from the opposite inlet for the complex dissociation (Figure 3.13b).

Based on this configuration, the pressure could be applied to both inlets separately, and as a result the analyte solution could be replaced by the introduction of the fresh buffer solution by simply switching the automated pressure controller from one inlet to another one without having to remove the setup to refill it with the new solution. **This operation is a key feature specific to our device in order to accomplish a full kinetic sensorgram in one single reagent loading, which is commonly impractical in the case of classical microfluidic formats.** Indeed, in the present nanoslit configuration, a thin diffusion layer formed within the channel depth upon probe-target reaction and propagated along the channel length; there was thus a clear boundary between the analyte and the buffer, and so the pressure-driven flow could be conveniently used to switch between the two phases.

3.6 Experimental setup

Once the fluidic chip was assembled in the dedicated chip holder, it was directly placed onto the microscope stage. The experimental setup enabling fluorescence detection of protein binding kinetics inside nanoslits consisted of an inverted fluorescence microscope (IX70, Olympus) equipped with an iXonEM+885 EMCCD (1004×1002 active pixels, 8×8 μm^2 pixel size) from Andor for fluorescence imaging, a white light source (Lumencore SOLA light engine®, USA), and a pressure controller system (MFCS-8C Fluigent, France). This system allowed tunable positive pressure control over a range of 0-1 bar. The chip support containing the fluidic device was connected to the Fluigent using soft tubes (3mm OD, 1mm ID).

Fluorescence images were acquired with a LCPlanF1 20×/0.40 Ph1 objective (Olympus Optical, Japan) and appropriate filter sets (U-MWIB3 from Olympus and U-M41008 from Chroma). The exposure/acquisition time was set to 1 s and illumination of the sample was turned on only during the acquisition time using an external shutter triggered by the camera (Lambda SC, Shutter Instrument) to avoid photobleaching. Time-lapse fluorescence images were recorded using an Andor Solis imaging software. All measurements were carried out at room temperature. The photograph of the experimental setup used for kinetic assay in the nanoslits is demonstrated in Figure 3.14.

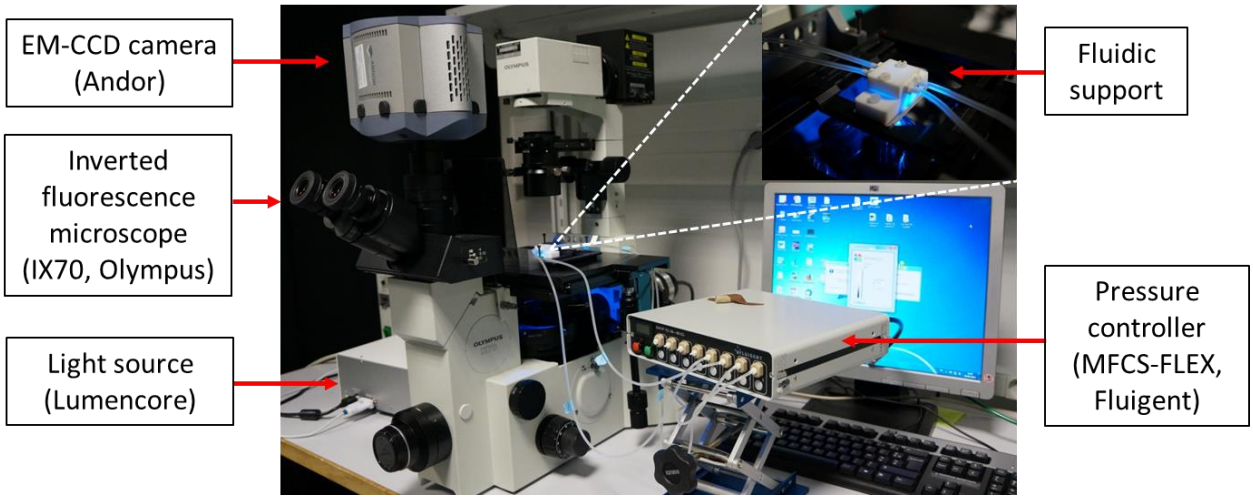

Figure 3.14 Experimental setup for performing kinetic study of protein interactions in nanofluidic devices.

3.7 Flow calibration

The pressure generator system was used in all experiments to induce liquid flow in the nanochannels. Since the reaction kinetics depends on the rate at which the analyte molecules are brought to the sensor, it was essential to know the flow velocity during the experiment. Flow velocity was one of the input parameters desired in the finite element simulation to predict the sensor responses. As a result, its accurate value was required to be able to compare the simulated data with our experimental assay. To this end, it was convenient to be able to relate the applied pressure to the flow velocity associated with the convective flow of surface-based immunoreaction performed in nanoslits.

3.7.1 Materials and methods

Flow calibration within the nanochannels was achieved by measuring the flow velocity of fluorescent beads for applied pressures (P) ranging from 25 to 100 mbar. 100 nm diameter fluorescein conjugated beads were diluted 10^5 times in 10 mM PBS buffer with 0.05% Tween-20. After proper degassing, the solution of beads was introduced into the BSA-passivated nanoslits. Various pressures were then applied at the inlets of the chip following two configurations: (i) using only one inlet where $P_1 = P$; P_2, P_3 and P_4 = 1 atm, and (ii) using two inlets where $P_1 = P_2 = P$; P_3 and P_4 = 1 atm.

The displacement of the beads over time was visualized with the similar experimental setup as described above. Furthermore, a 40X (N.A. 0.6) and a 100X (N.A. 1.3) oil-immersion objective lens from Olympus were employed in this experiment. The minimum exposure time of 31.7 ms was achieved using a frame transfer to obtain a good resolution of bead movement, giving a cycle time of 32.7 ms. For a given applied pressure, the bead movements were captured during 16.4 s, corresponding to 500 video frames. The flow velocity of each bead was then calculated by dividing its traveling distance (x) by the measurement time (s). ImageJ software was used to measure the displacement distance of the beads and the average flow velocity was obtained using 10 different beads.

3.7.2 Results and discussion

The average flow velocities as a function of applied pressures (one and two inlets) are plotted in Figure 3.15 and show a linear relationship in both cases.

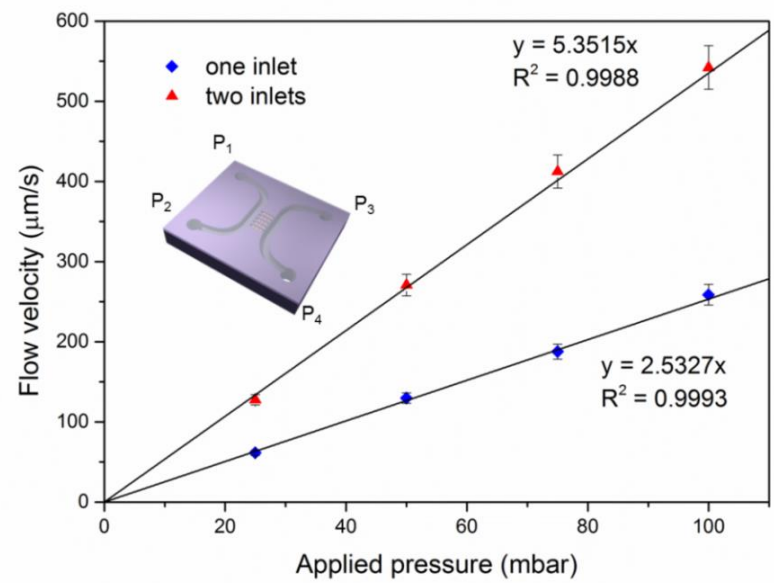

Figure 3.15 The calibration curves showing the relationship between flow velocity in the nanochannels and the applied pressure induced by a pressure controller. The plots show a linear relationship in both cases: one inlet (P_1=P, P_2=P_3=P_4= 1 atm) and two inlets (P_1=P_2, P_3=P_4= 1 atm) connected to the pressure source.

To confirm the flow velocities measured from bead measurement, the experimental values were compared with the theoretical values derived from pressure-driven flow in a rectangular channel (basic theory of mass transport in fluidic device can be seen in Chapter 5). Our device exhibited a rectangular cross section shape where the channel height was much lower than the channel width ($H \ll W$). Hydrodynamic resistance (R_H) is a function of channel geometry and fluid viscosity in the channel. The hydrodynamic resistance of a rectangular channel with a low aspect ratio can be calculated as [39]:

$$R_H = \frac{12\mu L}{WH^3}, \tag{3.1}$$

where W is the width of the channel, H is the height of the channel, L is the channel length and μ is the fluid viscosity (water viscosity is 1.002 mPa.s at 20 ºC).

From Hagen–Poiseuille's law, $\Delta P = QR_H$, the fluid flow rate Q (m^3/s) in a flat rectangular channel can be approximated as:

$$Q = \frac{WH^3}{12\mu L}\Delta P, \tag{3.2}$$

where ΔP is the pressure drop across the channel ($P_{max} = 1$ bar $= 10^5$ Pa). Mean flow velocity, U_m (m/s) can be simply derived by dividing the flow rate with the cross-sectional area as:

$$U_m = \frac{Q}{WH} \tag{3.3}$$

To determine the flow velocity inside the nanochannels, the hydrodynamic resistance of the entire fluidic device was first calculated using equation 3.1 as 0.162 μm^{-3}.Pa.s. Flow rates were then estimated from Hagen-Poiseuille's law at different applied pressures across the channel. Finally, the flow velocity at the entrance of nanochannel can be estimated from equation 3.3. The flow velocities (µm/s) as a function of applied pressures (mbar) were compared between the experimental data obtained from bead analysis and the theoretical values as demonstrated in Figure 3.16.

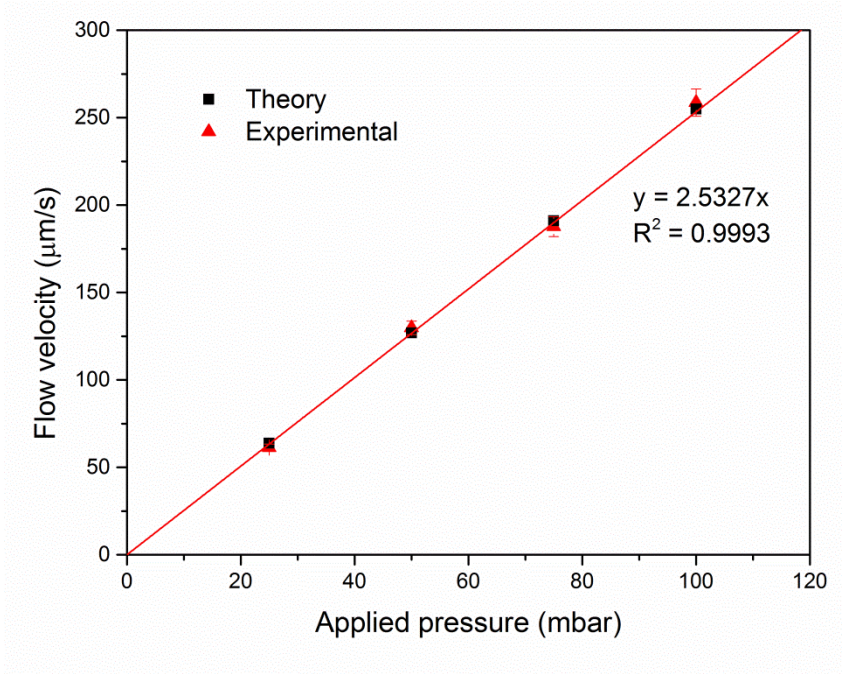

Figure 3.16 The relationship of fluid flow velocity inside the nanochannels and applied pressure obtained from bead displacement analysis. The experimental data are linearly well-fitted with theoretical calculations based on pressure-driven flow in a rectangular cross-section channel.

Although the measured flow velocity is slightly higher than the mean velocity due to size exclusion, the experimental data fitted well with the theoretical calculation (R^2 = 0.9993), exhibiting a linear relationship between the flow velocity and the applied pressure. **It can be concluded that we could rely on the theoretical model to determine the flow velocity in our system and thus used as an input parameter in the finite element model to fit with the experimental data.**

3.8 Conclusion

In this chapter, we have described the design and the microfabrication process of the nanofluidic biosensor devices consisting of 2-D nanoslits connected to microchannels on a silicon substrate. We have chosen a gold surface as the choice of sensing material mainly for comparison purpose between our sensor platform and the SPR technique as well as for easy surface modification via gold-thiol chemistry. We have described the selected biointerface, based on self-assembled monolayers of mixed thiols, used as a generic approach to study protein-protein interactions. Streptavidin-biotin and IgG/anti-IgG interactions have been chosen as the representative biological models to validate our device capability for kinetic constant quantification using a conventional bench-top fluorescence microscope.

The grafting protocol of bio-receptors has been successfully implemented in nanoslits with an open-top modification manner combined with a surface passivation procedure using a well-known effective blocking agent: bovine serum albumin. The fluorescence characterization demonstrated high binding affinity between immobilized biotin probes against streptavidin target analyte in solution with low undesirable non-specific adsorption outside the sensor area, resulting in a high signal-to-noise ratio. This result validated our grafting strategy that was readily applicable for robust kinetic assays in nanofluidic devices (See Chapter 4). Furthermore, the bio-compatible chip encapsulation performed at room temperature environment has been established to preserve the bio-activity of pre-immobilized surface probes by means of oxygen plasma treatment on the h-PDMS coated cover glass.

Concerning the world-to-chip fluid interface for nanofluidic devices, a home-made chip holder and fluidic connections have been realized, allowing low reagent consumption and, more importantly, the generation of a full kinetic sensorgram (association and dissociation assays) with single reagent loading via reversed-buffer flow fashion. We have presented the experimental setup on an inverted fluorescence microscope to visualize bio-recognition events in nanoslits during kinetic analysis. Finally, the flow calibration of the system showed a linear relationship between the applied pressure and the flow velocity inside the nanochannels. Good agreement between the theoretical model and the experimental data has enabled direct correlation of the applied pressure to the flow velocity, giving known hydrodynamic resistances of the fabricated fluidic devices.

Bibliography

1. Duan, C., W. Wang, and Q. Xie, *Review article: Fabrication of nanofluidic devices.* Biomicrofluidics, 2013. **7**(2): p. 026501.
2. Ren, K., J. Zhou, and H. Wu, *Materials for Microfluidic Chip Fabrication.* Accounts of Chemical Research, 2013. **46**(11): p. 2396-2406.
3. Perry, J.M., et al., *Ion Transport in Nanofluidic Funnels.* ACS Nano, 2010. **4**(7): p. 3897-3902.
4. Tegenfeldt, J.O., et al., *Micro- and nanofluidics for DNA analysis.* Anal Bioanal Chem, 2004. **378**(7): p. 1678-92.
5. Peterson, A.W., R.J. Heaton, and R.M. Georgiadis, *The effect of surface probe density on DNA hybridization.* Nucleic Acids Research, 2001. **29**(24): p. 5163-5168.
6. Xu, F., A.M. Pellino, and W. Knoll, *Electrostatic repulsion and steric hindrance effects of surface probe density on deoxyribonucleic acid (DNA)/peptide nucleic acid (PNA) hybridization.* Thin Solid Films, 2008. **516**(23): p. 8634-8639.
7. Göpel, W. and P. Heiduschka, *Interface analysis in biosensor design.* Biosensors and Bioelectronics, 1995. **10**(9–10): p. 853-883.
8. Seokheun, C. and C. Junseok, *Methods of reducing non-specific adsorption in microfluidic biosensors.* Journal of Micromechanics and Microengineering, 2010. **20**(7): p. 075015.
9. Shankaran, D.R. and N. Miura, *Trends in interfacial design for surface plasmon resonance based immunoassays.* Journal of Physics D: Applied Physics, 2007. **40**(23): p. 7187.
10. Holmberg, A., et al., *The biotin-streptavidin interaction can be reversibly broken using water at elevated temperatures.* Electrophoresis, 2005. **26**(3): p. 501-10.
11. Laitinen, O.H., et al., *Genetically engineered avidins and streptavidins.* Cell Mol Life Sci, 2006. **63**(24): p. 2992-3017.
12. Michael Green, N., *[5] Avidin and streptavidin*, in *Methods in Enzymology*, W. Meir and A.B. Edward, Editors. 1990, Academic Press. p. 51-67.
13. Yu, C.-J., et al., *Fiber optic biosensor for monitoring protein binding kinetics.* Proc. SPIE 5591, 2005: p. 200-208.
14. Jacobsen, C. and J. Steensgaard, *Binding properties of monoclonal anti-IgG antibodies: analysis of binding curves in monoclonal antibody systems.* Immunology, 1984. **51**(3): p. 423-430.
15. Karlsson, R. and A. Fält, *Experimental design for kinetic analysis of protein-protein interactions with surface plasmon resonance biosensors.* Journal of Immunological Methods, 1997. **200**(1–2): p. 121-133.
16. Lee, J.W., et al., *Characterization of a self-assembled monolayer of thiol on a gold surface and the fabrication of a biosensor chip based on surface plasmon resonance for detecting anti-GAD antibody.* Biosens Bioelectron, 2005. **20**(7): p. 1422-7.
17. Chaki, N.K. and K. Vijayamohanan, *Self-assembled monolayers as a tunable platform for biosensor applications.* Biosensors and Bioelectronics, 2002. **17**(1–2): p. 1-12.
18. Love, J.C., et al., *Self-Assembled Monolayers of Thiolates on Metals as a Form of Nanotechnology.* Chemical Reviews, 2005. **105**(4): p. 1103-1169.

19. Su, X., et al., *Surface plasmon resonance spectroscopy and quartz crystal microbalance study of streptavidin film structure effects on biotinylated DNA assembly and target DNA hybridization.* Langmuir, 2005. **21**(1): p. 348-53.
20. Spinke, J., et al., *Molecular recognition at self-assembled monolayers: Optimization of surface functionalization.* J. Chem. Phys., 1993. **99**(9): p. 7012-7019.
21. Mir, M., et al., *Comparison of different supramolecular architectures for oligonucleotide biosensing.* Langmuir, 2008. **24**(22): p. 13001-6.
22. Azzaroni, O., M. Mir, and W. Knoll, *Supramolecular Architectures of Streptavidin on Biotinylated Self-Assembled Monolayers. Tracking Biomolecular Reorganization after Bioconjugation.* The Journal of Physical Chemistry B, 2007. **111**(48): p. 13499-13503.
23. Veiseh, M., M.H. Zareie, and M. Zhang, *Highly Selective Protein Patterning on Gold−Silicon Substrates for Biosensor Applications.* Langmuir, 2002. **18**(17): p. 6671-6678.
24. Marie, R., et al., *Use of PLL-g-PEG in micro-fluidic devices for localizing selective and specific protein binding.* Langmuir, 2006. **22**(24): p. 10103-8.
25. Abdallah, B.G. and A. Ros, *2 - Surface coatings for microfluidic-based biomedical devices*, in *Microfluidic Devices for Biomedical Applications*, X. Li and Y. Zhou, Editors. 2013, Woodhead Publishing. p. 63-99.
26. Jeyachandran, Y.L., et al., *Efficiency of blocking of non-specific interaction of different proteins by BSA adsorbed on hydrophobic and hydrophilic surfaces.* Journal of Colloid and Interface Science, 2010. **341**(1): p. 136-142.
27. Cady, N.C., et al., *Real-time PCR detection of Listeria monocytogenes using an integrated microfluidics platform.* Sensors and Actuators B: Chemical, 2005. **107**(1): p. 332-341.
28. Reimhult, K., K. Petersson, and A. Krozer, *QCM-D analysis of the performance of blocking agents on gold and polystyrene surfaces.* Langmuir, 2008. **24**(16): p. 8695-700.
29. Eteshola, E. and D. Leckband, *Development and characterization of an ELISA assay in PDMS microfluidic channels.* Sensors and Actuators B: Chemical, 2001. **72**(2): p. 129-133.
30. Mao, P. and J. Han, *Fabrication and characterization of 20 nm planar nanofluidic channels by glass-glass and glass-silicon bonding.* Lab Chip, 2005. **5**(8): p. 837-44.
31. Zheng, B., L.S. Roach, and R.F. Ismagilov, *Screening of protein crystallization conditions on a microfluidic chip using nanoliter-size droplets.* J Am Chem Soc, 2003. **125**(37): p. 11170-1.
32. Bhattacharya, S., et al., *Studies on surface wettability of poly(dimethyl) siloxane (PDMS) and glass under oxygen-plasma treatment and correlation with bond strength.* Microelectromechanical Systems, Journal of, 2005. **14**(3): p. 590-597.
33. LEE, et al., *PDMS Nanoslits without Roof Collapse.* Vol. 30. 2009, Seoul, COREE, REPUBLIQUE DE: Korean Chemical Society. 5.
34. Odom, T.W., et al., *Improved Pattern Transfer in Soft Lithography Using Composite Stamps.* Langmuir, 2002. **18**(13): p. 5314-5320.
35. Choi, K.M. and J.A. Rogers, *A Photocurable Poly(dimethylsiloxane) Chemistry Designed for Soft Lithographic Molding and Printing in the Nanometer Regime.* Journal of the American Chemical Society, 2003. **125**(14): p. 4060-4061.
36. Viero, Y., et al., *Efficient prototyping of large-scale pdms and silicon nanofluidic devices using pdms-based phase-shift lithography.* Microfluidics and Nanofluidics, 2012. **12**(1-4): p. 465-473.
37. Leichlé, T., et al., *Biosensor-compatible encapsulation for pre-functionalized nanofluidic channels using asymmetric plasma treatment.* Sensors and Actuators B: Chemical, 2012. **161**(1): p. 805-810.
38. Herold, K.E., Rasooly, A., *Biosensors and molecular technologies for cancer diagnostics.* 2012: CRC Press.
39. Bruus, H., *Theoretical Microflidics.* 2007: Oxford Master Series in Physics.

Chapter 4

Real-time fluorescence detection of protein binding kinetics in nanofluidic biosensors

In this chapter, we present an empirical validation of our platform capability for real-time kinetic analysis of protein-protein interactions with two dedicated biological models. The first model deals with high affinity interaction, namely streptavidin-biotin recognition pair. The assessment of bio-functionalization and kinetic assay are demonstrated by means of fluorescence observations. The second binding model involves moderate affinity, mouse IgG/anti-mouse interaction, wherein in-situ functionalization and kinetic measurement with a series of fluorescently labeled IgG concentrations are revealed. We then introduce the different data fitting approaches used along the course of this study to resolve kinetic parameters of bio-specific interactions. They include finite element modeling, analytical approach, and a commercial kinetic evaluation software package. Additionally, our biosensor performances are benchmarked with a mature technology, the SPR-based biosensors, as well as with values found in the literature. Finally, we examine the operational range and detection limit of our system as well as the repeatability of the measurements for mouse IgG detection.

4.1 Real-time kinetic measurement

Real-time biomolecular analysis provides kinetic insight information of protein-ligand pairs of interest and allows the determination of distinct kinetic constants: the association and dissociation rates of the recognition molecules. Herein, real-time measurement of biomolecular interactions was conducted in the fabricated bio-functional nanofluidic devices, based on continuous analyte flow coupled with fluorescence detection, to determine rate constants of two dedicated biological systems. **The underlying investigation aimed to validate our nanofluidic biosensor-based approach for kinetic analysis, similarly to the well-established label-free SPR technique, but offering a simpler and cost-effective analytical tool for wider community use**.

4.1.1 Streptavidin-biotin binding model

4.1.1.1 Assessment of bio-functionalization

Prior to performing the kinetic assays, it was desirable to ensure whether the immobilized biotin probes could preserve their bio-functionality after being subjected to open-top surface modification and asymmetric bonding protocol as described in Chapter 3. To this end, we investigated streptavidin-biotin reactions inside the closed biofunctional nanoslit based on pressure-driven flow.

To elucidate this specific biomolecular interaction, a 100 nM solution of Alexa Fluor 488 conjugated streptavidin (ST-AF 488) diluted in 10 mM PBS buffer + 0.05% Tween-20 was delivered into the 10% biotinylated thiol modified channel loaded with a blocking buffer (1% BSA in 10 mM PBS buffer + 0.02% Tween-20, pH 7.4), at a constant flow velocity of 155 μm/s for 25 min (Figure 4.1).

After rinsing with the buffer (10 mM PBS buffer + 0.05% Tween-20, pH 7.4) to remove excess streptavidin molecules from the channel and any non-specific adsorption on the surface, the fluorescence images were recorded. A significant increase in fluorescence intensity on the gold sensor patches containing pre-immobilized biotin molecules was observed, while the adjacent area on the channel wall (silicon dioxide) remained relatively low in fluorescence intensities (Figure 4.2), indicating minimal non-specific adsorption of analyte on the slit surface.

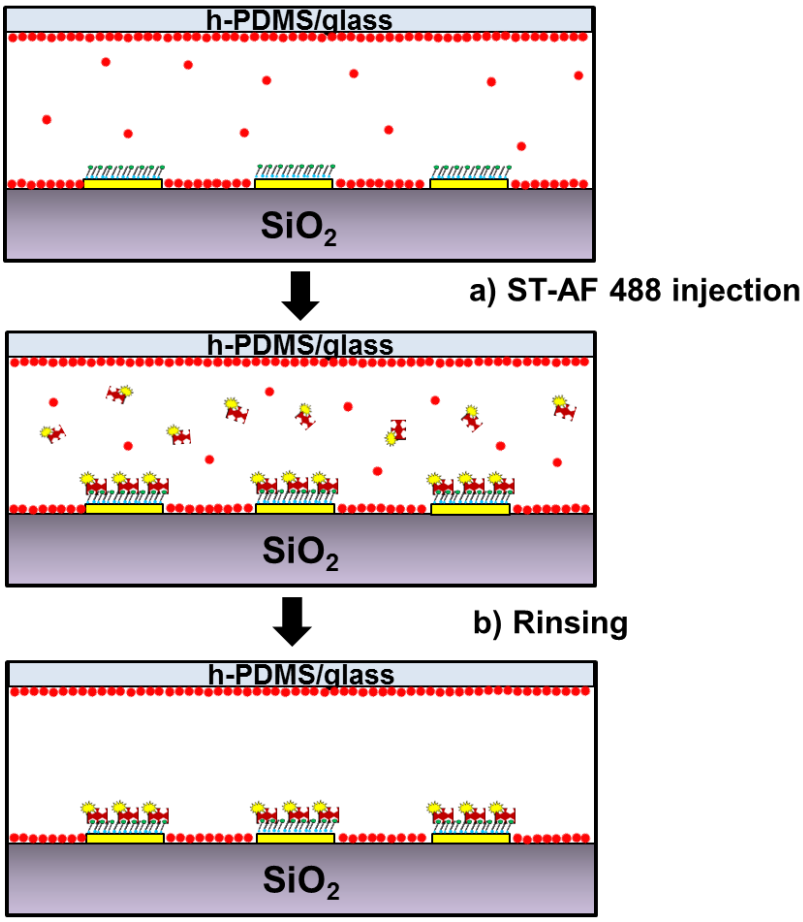

Figure 4.1 Schematic presentation of the in-situ streptavidin functionalization.

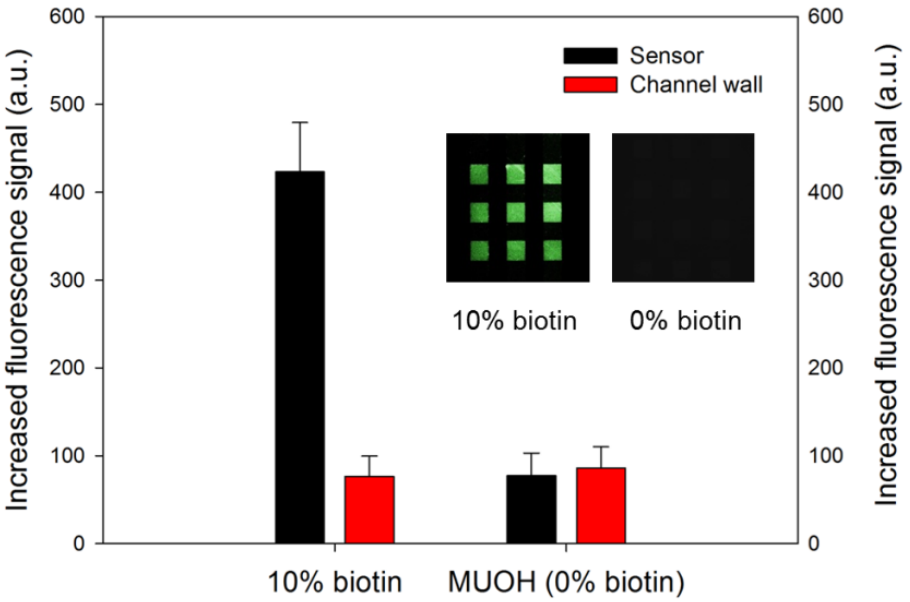

Figure 4.2 A bar plot of fluorescence intensities measured on the gold sensors and channel walls (silicon dioxide) obtained from two different surface-treated nanoslit devices upon streptavidin injection. Fluorescence images of the 10% biotin modified nanoslit and the 0% biotin modified nanoslit (MUOH) after streptavidin introduction are shown in the insets.

A control experiment (no biotin) was also conducted on the hydroxyl-terminated thiol (a spacer) modified sensor surfaces (MUOH). No significant non-specific physical adsorption was observed after the washing step. This indicated the specific recognition between the pre-immobilized biotin and flowing streptavidin target molecules. **The results therefore confirmed that the pre-modified probes maintained their bio-reactivity toward the specific targets after the chip encapsulation, providing a sensing capability with a remarkably high signal-to-noise ratio and diminished non-specific adsorption**.

4.1.1.2 Kinetic assay

In the first experiment, we attempted to study the binding kinetics of flowing fluorescent streptavidin on the surface-immobilized biotin with 10% biotin content inside the nanoslits. Similar to the aforementioned experiment, a 100 nM solution of ST-AF 488 was driven by a positive pressure into the 10% biotinylated thiol modified channels. Using fluorescence time-lapse imaging, streptavidin binding events were now recorded in real-time.

The fluorescence time-lapse imaging of 100 nM ST-AF 488 binding onto the immobilized biotin patches is shown in Figure 4.3. A significant fluorescence signal on the first sensor patch could be distinguished within one minute or even less, and reached equilibrium after around 3 minutes, while the second and the third patches showed relatively dark regions (no or fewer binding events

occurred), noted as **a depletion zone**. When driven streptavidin target molecules were moving extremely close to the surface-immobilized biotin, it literally guaranteed the optimal binding efficiency. As seen from the time-lapse fluorescence images, streptavidin molecules were effectively captured by the sensor patch with a very high signal-to-noise ratio (174 fold) and the binding reaction slowly propagated downstream along the flow direction.

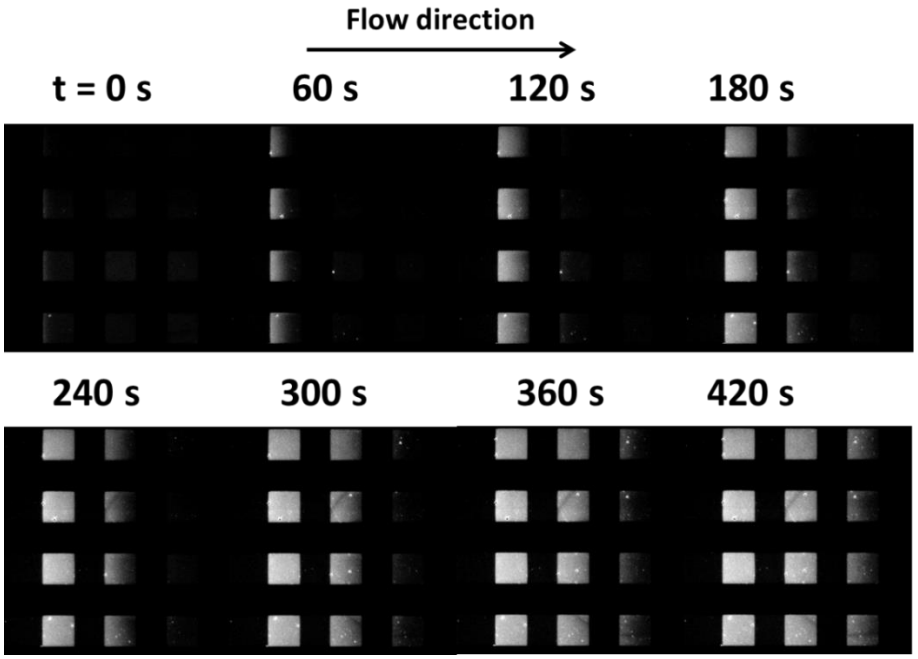

Figure 4.3 Time-lapse fluorescence images taken when a 100 nM solution of Alexa Fluor 488-streptavidin was driven into the biotin-immobilized nanoslit by pressure-driven flow with a flow velocity of 155 μm/s.

This sensing characteristic could be confirmed by the plot of normalized fluorescence signals at different positions on the sensor patch (Figure 4.4), wherein the confronting front edge of the sensor reached the binding equilibrium before the middle and the back edge. The results suggested that all analyte molecules entering the nanochannel were bound to the biotin modified sensor and when the first sensor was saturated, the reaction moved forward to the next sensor patch and the depletion zone progressively disappeared.

Under these experimental conditions, we could observe full collection of the analyte by the sensor, demonstrating the high capturing efficiency of our nanoslit biosensors [1]. Contrary to typical biosensing formats where an excess amount of target analytes flows over the sensor to abolish the diffusion-limited reactions over the entire sensing area, locally immobilized probe layer embedded in the nanoscale-confined slits boosts the analyte-capturing speed without any unnecessary overconsumption of the target sample.

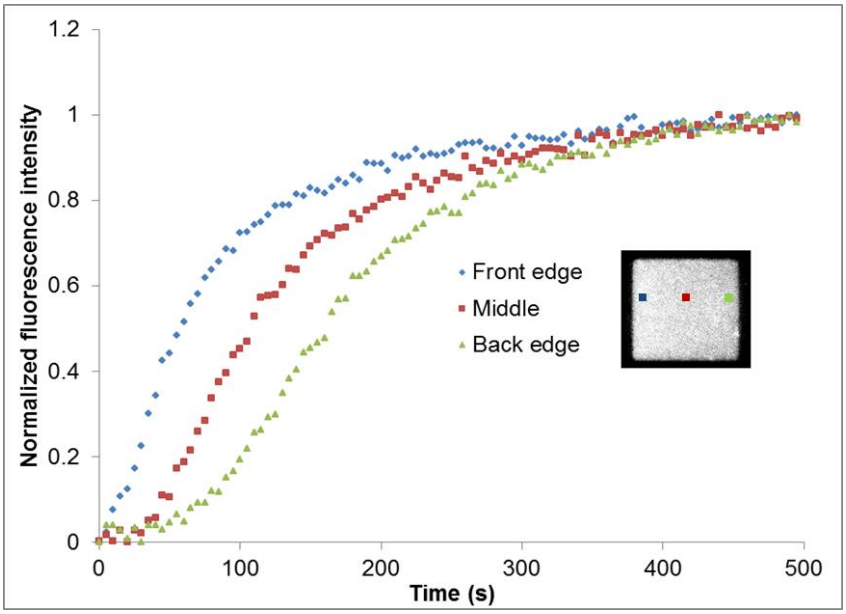

Figure 4.4 Plot of normalized fluorescence intensities as a function of time at different areas on the sensor patch. The data were obtained from 10×10 pixels (4×4 μm total feature size). The reactions that occurred at the front edge of the sensor reached equilibrium earlier than those measured at the middle and the back edge.

This sensor configuration, exhibiting ultimately high adsorption efficiency, is beyond doubt beneficial when a low detection limit is sought, under the constraint of limited-volume of rare sample presented. For a kinetic analysis point of view, however, kinetic data obtained from this experiment could not be correctly interpreted using a simple Langmuir binding model. This was attributed to the fact that the rate at which the analyte was transported to the sensor surface was slower as compared to the rate of the reaction of streptavidin-biotin interaction with an extremely high affinity; fast on-rate. In these conditions, the binding reaction was limited by mass transport of the analyte to the sensor.

Accordingly, we modified the surface probe density of biotin to 1% in order to minimize the mass transport effects and to work under conditions where reaction-limited regime was dominant. Lowering the surface probe density not only reduces steric hindrance effects but also avoids use of a high injection flow rate, which in turn enhances consumption of biological materials.

We then carried out kinetic experiments on the 1% biotin modified nanoslit. To do so, ST-AF 488 solutions ranging in concentration from 10 nM to 100 nM were introduced at a constant flow velocity of 155 μm/s and allowed to bind with the biotin immobilized on sensor surfaces. The fluorescence images were recorded in real-time to monitor the association process of this specific binding event. Due to the very high binding affinity and exceptionally long dissociation time of the

streptavidin-biotin recognition system, four different devices were employed to measure the binding rates of streptavidin at each concentration. The results and the analysis of kinetic data are presented in the kinetic constant quantification section.

4.1.2 Mouse IgG/anti-mouse IgG interaction model

4.1.2.1 Post-sealing surface modification

Following chip bonding, we conducted the in-situ surface functionalization to immobilize receptor molecules on the gold surface embedded in the nanoslits (Figure 4.5). First, we immobilized streptavidin onto the biotinylated SAM layer (10% biotin content) by introducing a 100 nM solution of ST-AF 488 at a constant flow velocity of 200 μm/s for 15-20 min until the saturation was achieved. After rinsing with the buffer, we subsequently immobilized the biotinylated anti-mouse IgG receptor on the sensor via streptavidin-biotin bridges by injecting a 100 nM solution of biotinylated goat anti-mouse IgG for 15-20 min and rinsing with the buffer solution for 10 min.

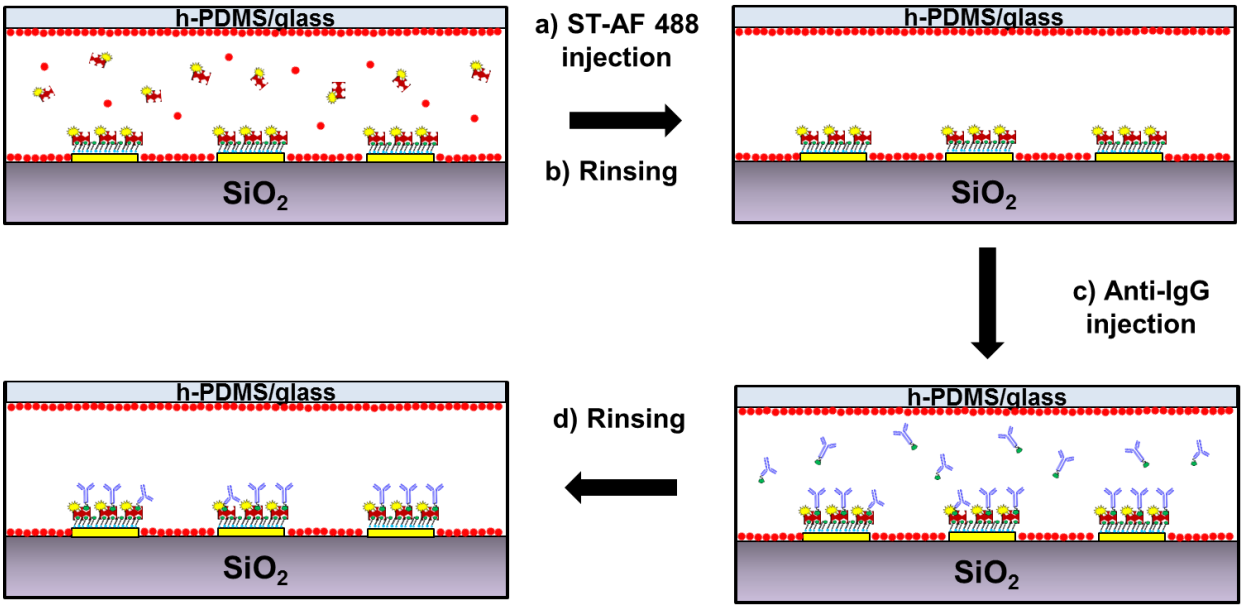

Figure 4.5 Schematic presentation of post-sealing functionalization in the nanofluidic device.

This second step of surface modification after chip encapsulation allowed the kinetic study of mouse IgG/anti-mouse IgG binding model. It should be noted that the immobilization level of the receptor was unknown in the case of the nanoslit experiments since there was no fluorescence detecting point during the receptor functionalization step.

Nevertheless, a high concentration of receptor solution and a long injection time (~15-20 min) were used during the receptor immobilization to ensure its saturation level on the streptavidin modified SAMs. Subsequently, the sensor was exposed to sufficient buffer washing in order to remove any excess receptor molecules.

4.1.2.2 Kinetic assay

After the sensor was functionalized with the desired receptors (anti-mouse IgG), we introduced the fluorescently labeled analyte solutions to the sensor embedded nanoslits in order to perform kinetic assay (Figure 4.6). Briefly, various concentrations of Alexa Fluor-647 conjugated mouse anti-rabbit IgG (mIgG-AF 647) target analyte (diluted in 10 mM PBS buffer + 0.05% Tween-20) ranging from 0.46 to 15 nM were sequentially delivered to the anti-mouse modified sensor chip under continuous flow velocity of 200 μm/s. The bound complex was allowed to dissociate from the surface receptor by injecting pure buffer solution with the same flow velocity by means of reversed flow manner.

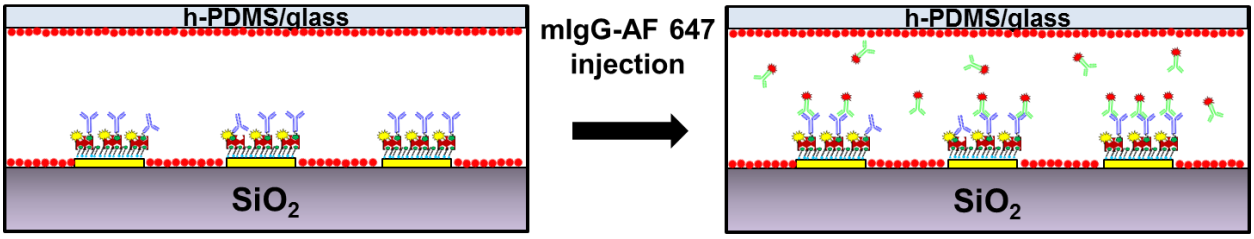

Figure 4.6 Schematic presentation of the labeled target injection into the nanoslit during association phase.

The fluorescence images were recorded in real-time to monitor the association and dissociation processes inside the nanoslit. The association time was set at the same duration for all target concentrations, enabling a global analysis using the BIAevaluation software package (which will be discussed in the following part). The sensor surface was regenerated after each cycle by injecting a solution of 10 mM glycine-HCl pH 2.0 for a short period of time and rinsing thoroughly with buffer solution before the next analyte injection. Additionally, we further examined the non-specific interaction of an irrelevant target analyte (Alexa Fluor-660 goat anti-rabbit IgG) to the anti-mouse immobilized nanoslit. As expected in that case, no significant increase in fluorescence intensity was observed on the gold sensor.

Figure 4.7 depicts real-time fluorescence images during the association and dissociation phases of analyte/immobilized receptor reactions. The fluorescence signal on the gold sensor patch progressively brightened up consequent to the introduction of the target analyte while maintaining fluorescence background in the channels at a relatively low level (high signal-to-noise ratio). Subsequently, the signal on the sensor gradually decreased upon buffer injection due to the dissociation of fluorescently labeled analytes from the sensor surface.

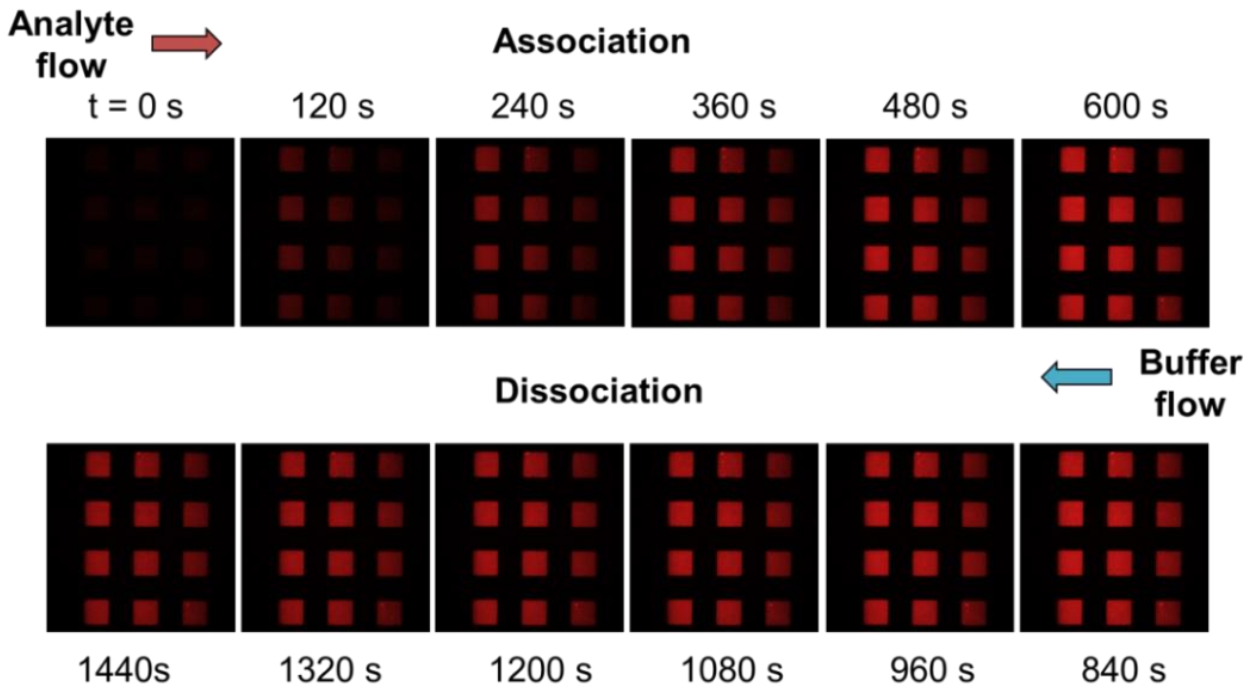

Figure 4.7 Images taken by time-lapse fluorescence microscopy during association and dissociation time courses of 1.87 nM Alexa Fluor-647 mouse anti-rabbit target analyte binding on the anti-mouse IgG modified nanoslit. The dissociation phase was obtained by means of reversed-buffer flow manner.

As a matter of fact, the results showed the feasibility of our nanoslit biosensors for monitoring kinetic reactions (association and dissociation phases) in real-time using a conventional fluorescence microscope and a reversed-buffer flow procedure, without buffer loading and extra washing steps. This capability thus underlined a novel feature of the device. In other words, the full kinetics (binding and dissociation) of IgG/anti-IgG interaction could be assessed without necessity of pause the sample flux to load fresh buffer or to apply an additional washing step in order to discard background fluorescence in the channel.

Such feature specific to nanometer scale channels was literally achieved thanks to the notable reduction of the fluorescence background in nanoslits, caused by the fluorescent molecules flowing above the sensor area and within the channel. Contrary to nanoslits, excessive background noise, arising from a greater observation volume in a micrometer thick channel inherent in ordinary microfluidic based immunoassay formats, often conceals the real binding signal from the sensing element, leading to a comparatively low signal-to-noise ratio.

Moreover, because we operated in full target capture, all upcoming molecules injected onto the sensor were consumed by the reaction and a diffusing layer (depleted layer) formed at the sensor site. This depleted layer constituted a clear boundary between regions where the concentration of analyte dropped from maximum to zero. Thus, the liquid downstream the sensor was virtually analyte free and the dissociation study could be simply implemented after completion of the association phase, by reserving the fluid flow within the nanochannel instead of injecting the new buffer in the inlet. This resulted in a simplified operating protocol and reduced time of analysis.

The unique characteristic of slit-like nanochannels allowed us to directly probe the sensing surface, enabling low-noise real-time kinetic studies without need of using complicated and expensive setups, such as SPR, TIRFM, or QCM. Beyond that, our nanoslit is prominently simple in fluidic design as compared to the typical microfluidic immunoassays, in which individual flow channels and valves are commonly required to induce sequential reagent exchanges for multi-step immunoassays [2, 3].

4.2 Fluorescence data analysis

The fluorescence images were analyzed using ImageJ (NIH Image). Raw SIF ANDOR format images were converted to 16-bit grayscale images. All regions of interest (ROIs) consisted of 10×10 pixels (4×4 μm total feature size) selections within the captured images. The average fluorescence intensity of each ROI was taken as the average pixel value for that region along with the associated standard deviations (variance).

The fluorescence signal from the sensor was background subtracted and normalized to relative fluorescence intensity (see equations below). This normalization provided the means to compare the experimental binding assays with the simulated results from the finite element model. Kinetic sensorgrams were then obtained by plotting the relative fluorescence intensity from the selected regions of interest as a function of time.

$$I \text{ (a.u. fluorescence intensity)} = I_s - I_b \tag{4.1}$$

$$I_{sp} \text{ (a.u. fluorescence intensity)} = I - I_{np} \tag{4.2}$$

$$I_{sp,nor}(0,1) = \frac{I_{sp} - I_{sp,min}}{I_{sp,max} - I_{sp,min}} \tag{4.3}$$

- I is the net fluorescence intensity on the receptor-immobilized sensor (combinations of specific and non-specific binding)
- I_s is the fluorescence intensity on the sensor
- I_b is the fluorescence intensity of the background obtained from adjacent region outside the sensor
- I_{sp} is the fluorescence intensity of specific binding on the sensor
- I_{np} is the fluorescence intensity of non-specific binding on the sensor (without receptor immobilization)
- $I_{sp,nor}$ is the normalized specific binding fluorescence intensity
- $I_{sp,min}$ and $I_{sp,max}$ are the minimum and maximum fluorescence intensity of specific binding on the sensor, respectively.

4.3 Kinetic constant quantification

Here, we present three kinetic constant quantification approaches used throughout this work to deduce kinetic constants of two biological systems from the kinetic data obtained in nanofluidic biosensors. The basic principle of each technique along with governing kinetic equations and the fitted kinetic curves are described. **The aim of using different fitting approaches for kinetic constant determination was to demonstrate the robustness and the utility of our kinetic data acquired in the nanoslits, being applied to a variety of existing fitting methods. The consistency between each model could essentially confirm the reliability of the extracted binding constants.** To demonstrate the feasibility of our approach as the proof of concept for kinetic analysis, we assumed a 1:1 interaction for both protein-receptor pairs for the simplicity of the model.

4.3.1 Finite element method (FEM)

Finite element method (FEM) was primarily utilized to describe the behavior of our biosensor system and to predict the binding kinetics. As nanofluidic-based immunoassays delivered the target analyte onto the receptor surface in a continuous-flowing manner, one should consider the convection-diffusion equations for mass transport of analyte species in combination with the binding reactions between analytes and the surface immobilized receptors in the nanoslits.

4.3.1.1 Model construction

We constructed a 2D model in COMSOL 4.2a Multiphysics software to simulate the heterogeneous immunoreaction in a rectangular nanochannel. The model of a biosensor was built as a two-dimensional geometry due to a reasonable assumption of laminar flow (Reynolds number $\ll 1$) with a parabolic flow profile, expecting a minimum variation in concentration along the channel width (channel width $\gg$ channel height). Furthermore, it was also relevant to consider only a segment of

nanochannel excluding microchannel networks for reaction modeling because the binding was not sensitive to mass transport along the microchannels.

Generally, there were three main coupled physical processes involved in the computational immunoassay: (i) convection or transport of the analytes along the nanochannel, (ii) diffusion of the analytes in all directions, in which the analytes were allowed to diffuse perpendicular to the flow direction and be captured by the probes on the active area, and (iii) surface reactions described by a typical analyte-ligand binding with simple first-order kinetics. Our computational model was relatively similar to previous studies [4, 5].

A schematic of the heterogeneous immunoreaction in a nanofluidic channel is shown in Figure 4.8. The dimensions of nanochannel were 450 nm in depth (H) and 500 μm in length (L). A 50 μm long sensor patch immobilizing capture ligands was located at the bottom center of the nanochannel. The sensor patch was assumed to be a square. Inlet and outlet were defined as the opening of nanochannel on the left boundary and at the end of the geometry on the right boundary, respectively. The analyte with concentration of C_0 was pumped to the channel from the left inlet with a fluid flow velocity (U_m) and they were transported along the channel length in x direction by a convective flow. They diffused freely with diffusion coefficient (D) and were captured by the immobilized probe on the sensor with surface probe density (b_m). Kinetics of biospecific interactions were defined by their association (k_a) and dissociation rate constants (k_d).

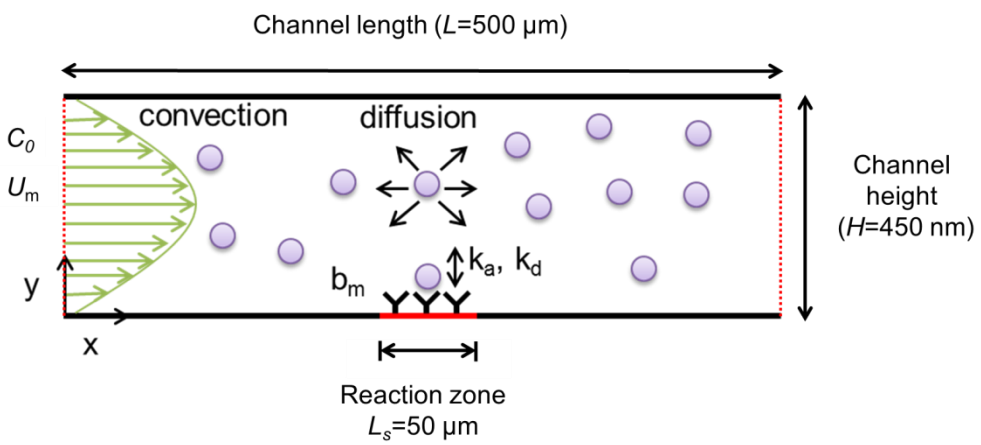

Figure 4.8 A 2-D model used in the finite element simulation of heterogeneous immunoreaction in a nanofluidic channel.

The transport of analyte concentration in the bulk solution was given by the differential equation of convection and diffusion as:

$$\frac{\partial C_0}{\partial t} + \nabla.(-D\nabla C_0 + C_0\vec{u}) = 0, \tag{4.4}$$

where C_0, D and $\vec{u}$ were the bulk concentration, the diffusion coefficient of reacting species, and the flow velocity vector, respectively. The initial condition ($t = 0$) set the bulk concentration $C_0 = 0$. For laminar flow field, the Navier-Stokes equation for an incompressible fluid with no slip boundary conditions was applied. At the surface reaction, the binding between flowing analyte molecules and the immobilized ligand was assumed to follow a simple 1-1 interaction (Langmuir binding model). The reactions were governed by the association and dissociation rate constants of the analyte-ligand recognition as:

$$\frac{\partial C_s}{\partial t} = k_a C_0(b_m - C_s) - k_d C_s, \tag{4.5}$$

where C_s was the surface concentration of bound complex on the sensor. b_m was the total effective surface probe concentration (total number of active binding sites) and the term ($b_m - C_s$) was defined as the free binding sites on the sensor. At the beginning of the reaction ($t = 0$), the concentration of bound analyte was zero ($C_s = 0$). For bulk boundary conditions at the reaction surface, the rate of reaction was balanced with the flux of the analyte as:

$$\vec{n}.(-D\nabla C_0 + C_0\vec{u}) = -k_a C_0(b_m - C_s) + k_d C_s, \tag{4.6}$$

where $\vec{n}$ was the unit normal vector to the surface. The left boundary was defined as an inflow boundary where the concentration at the inlet was set as C_0, which was the initial bulk analyte concentration. The boundary for the outlet was set as the outflow boundary condition where $\vec{n}.(-D\nabla C_0 + C_0\vec{u}) = \vec{n}.C_0\vec{u}$ and all other boundaries (the channel walls), except the reaction boundary at the sensor, was set to no flux boundary conditions where $\vec{n}.(-D\nabla C_0 + C_0\vec{u}) = 0$.

Triangular mesh elements were generated for the non-linear solver calculation with a grid size of 1 μm for the entire domain and a finer mesh of 0.1 μm at the sensor surface (smaller than the pixel size for data analysis), providing an acceptable simulation time with high accuracy. Since the model dealt with a 2D phenomenon (convection-diffusion domain) coupled to another 1D phenomenon occurring only at the sensor surface, the weak form partial differential equation (PDE) module was added.

4.3.1.2 Simulation parameters

The simulation parameters used in the numerical computation of both biological models are summarized in Table 4.1.

Fluid properties (density and viscosity) of water were assumed for both models. The flow velocities were estimated from the theoretical calculation. Due to gold being the sensor surface, the probe grafting density could not be directly investigated from the fluorescence calibration method due to quenching or/and enhancement effects on the metal surface. The effective surface probe densities (b_m) were then obtained from the analogous SPR measurements. These surface densities should reasonably represent what was on our nanoslit surface since the same surface functionalization protocol was performed on the similar sensor surface. Ultimately, regular surfaces such as glass or silicon dioxide can be employed as a sensor surface to enable the characterization of the actual immobilized probe density on our sensor. The ranges of association rate constant k_a and dissociation rate constant k_d were obtained from the values in the literature [6-8].

Table 4.1 Simulation parameters used in COMSOL modeling for streptavidin-biotin and mouse IgG/anti-mouse binding models.

Parameter	Description	Streptavidin-biotin model	Mouse IgG/anti-mouse model
ρ	Fluid density	1000 kg/m^3	1000 kg/m^3
μ	Fluid dynamic viscosity	10^{-3} Pa.s	10^{-3} Pa.s
C_0	Analyte bulk concentration	1.0×10^{-5} to 1.0×10^{-4} mol/m^3 (10-100 nM)	0.46×10^{-6} to 1.5×10^{-5} mol/m^3 (0.46-15 nM)
D	Diffusion coefficient	7.4×10^{-11} m^2/s [9, 10]	1×10^{-11} m^2/s [11, 12]
b_m	Surface probe density	4×10^{-8} mol/m^2	1×10^{-9} mol/m^2
k_a	Association rate constant	1.5×10^2 to 1.4×10^3 m^3/mol.s (1.5×10^5 to 1.4×10^6 M^{-1}s^{-1})	6.0×10^2 to 9.0×10^2 m^3/mol.s (6.0×10^5 to 9.0×10^5 M^{-1}s^{-1})
k_d	Dissociation rate constant	8×10^{-7} to 8×10^{-5} s^{-1}	5.0×10^{-4} to 7.0×10^{-4} s^{-1}
U_m	Flow velocity	155 μm/s	200 μm/s

To obtain a full sensorgram including the association and dissociation phases, the solution containing analyte species was switched to the buffer solution at a user-defined time via a step function module. Figure 4.9 depicts plots of concentration fields above the binding surface inside a nanochannel during the association (a) and dissociation (b) phases of 1.8 nM mouse IgG/anti-IgG interaction. The depletion region was developed above the sensor and it continued across the full channel depth showing a high capturing efficiency of the target analyte in solution by the surface-immobilized probes.

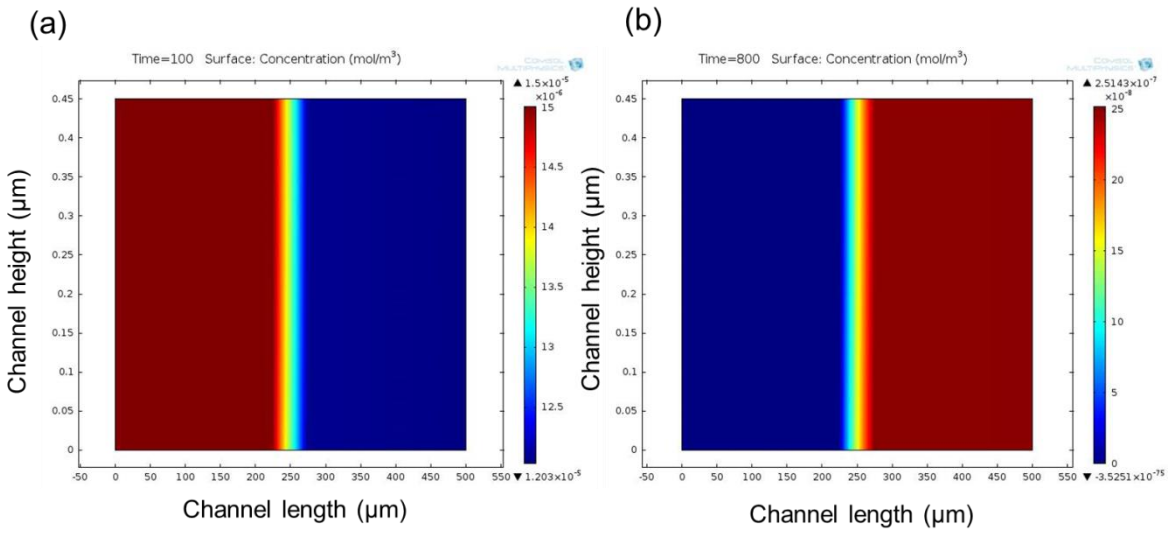

Figure 4.9 The simulated results depicting concentration of target molecules in the channel (color map) upon association (a) and dissociation (b) phases of mouse IgG (1.8 nM)/anti-IgG interaction. The depletion region can be seen across the nanoslit thickness.

The time dependent solver was employed to evaluate the surface concentration of adsorbed species (C_s) as a function of time for different variable parameters. From the simulation results, C_s was calculated by integrating on the sensing length of interest (4 μm) but not the entire sensor length. The simulated kinetic curves at various target concentrations are shown in Figure 4.10.

Conceptually, this finite element-based computational model assumed that the immunoreaction followed a simple Langmuir 1:1 binding model. Moreover, non-specific adsorption on the channel walls and other interfering effects, including heterogeneity of the surface and steric hindrance, were not taken into account.

To minimize time-consuming tasks of the simulation user, we wrote a program in COMSOL 4.2 linked MATLAB software to automatically command COMSOL parametric simulations through MATLAB. Different variable on/off rate parameters were defined and the simulated results were exported to MATLAB for data post-processing.

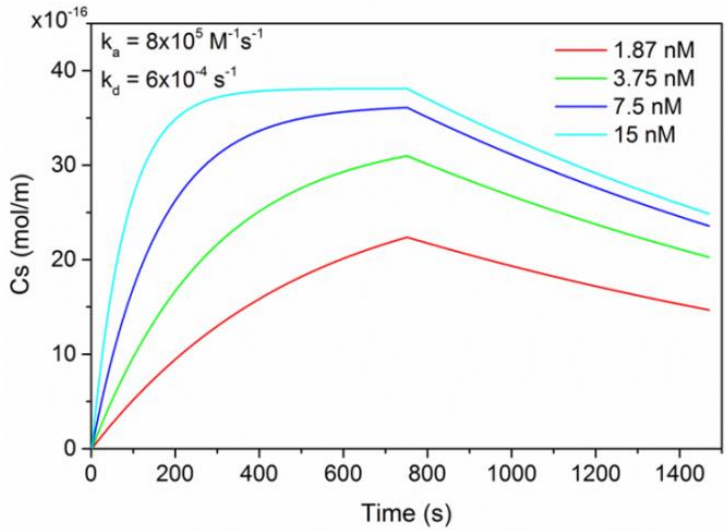

Figure 4.10 A plot of surface concentration of adsorbed species (C_s) as a function of time at different analyte concentrations obtained from the finite element computation model. The association rate of 8×10^5 $M^{-1}s^{-1}$ and the dissociation rate of 6×10^{-4} s^{-1} associated with IgG/anti-IgG interaction were used as input parameters for the simulation.

Surface concentrations of the bound complex (C_s) were normalized and used as a key parameter to correlate predicted sensor responses with relative fluorescence intensities from the experimental immunoassay obtained in nanoslits. Kinetic constants were then determined from the best fit between the experimental kinetic curves and the simulated sensorgrams by means of coefficient of determination (R^2). R^2 is related to the ratio between the residual sum of squares (SS_{res}) and the total sum of squares (SS_{tot}), as defined by $R^2 = 1 - (\frac{SS_{res}}{SS_{tot}})$. The model fits the experimental data well when R^2 is closer to 1.

In order to assess the operation regime of our nanofluidic-embedded biosensor, it was vital to estimate the Peclet number (Pe_H) with respect to the channel height, the sensor size, and the Damköhler number (D_a). As mentioned in Chapter 2, Pe_H relates the rate of convection to the rate of diffusion, $Pe_H = \frac{U_m H}{D}$, where U_m is the mean flow velocity, H is the channel height, and D is the diffusion coefficient. The sensor size is expressed as $\lambda = L_s/H$, where L_s is the sensor length (the whole sensor length or the length of 10 pixels used in data analysis).

The Peclet numbers of 0.9 and 9 were found in the case of streptavidin and mouse IgG, respectively. These numbers being close to the unity suggested that the time for the analyte to diffuse across the entire channel height was comparable to the time for the analyte to be transported over the sensor via convection. Theoretically, all analyte molecules in the channel should have the possibility to interact with probes on the sensor surface, and the system approaches the limit of full

collection when $Pe_H < 0.5$ [13]. This displayed high sensing performances with enhanced analyte binding efficiency and short response time of our nanoslit system.

For both models, the sensor size (λ) can be calculated as 111 for the whole sensor length (50 μm) and 8.9 in the case of 10 pixels data collection (4 μm). These dimensionless numbers again described our sensor falling into a "full collection" regime at sufficiently low Pe_H and large enough sensor (λ) according to the earlier work [14].

On the other hand, the Damköhler number (D_a) is expressed as the ratio between the rate of reaction and the rate of diffusion, $D_a = \frac{k_a b_m H}{D}$, where k_a is the association rate constant (1×10^6 $M^{-1}s^{-1}$ for streptavidin-biotin binding [15] and 4×10^5 $M^{-1}s^{-1}$ for anti-mouse/mouse IgG interaction [16]), and b_m is the immobilized probe density (4×10^{-8} mol/m^2 for streptavidin-biotin model and 1×10^{-9} mol/m^2 for mouse IgG/anti-mouse IgG model). The calculated D_a being smaller than one (0.24 for streptavidin-biotin and 0.018 for anti-mouse/mouse IgG) indicated that the kinetic reactions fell into a reaction-limited regime and were not diffusion-limited.

According to the calculated dimensionless numbers, our pressure-driven flow-based nanoslit biosensor was not limited by mass transport of analyte to the sensor, which could significantly reduce the sensor performances in terms of sensitivity, response time, and kinetic data accuracy. Therefore, a simple analytical solution, namely "well-mixed model", in which the model does not account for analyte mass transfer to the biosensor, can be eventually employed to elaborate the binding constants of the biorecognition pairs.

4.3.2 Analytical solution (well-mixed model)

Based on our sensing configuration in nanofluidic devices, the analyte solution continuously flowed over the sensor surface and as a result the analyte concentration above the binding surface was constantly replenished with the new analyte solution, thus in turn alleviating any mass transfer problems. The kinetics of analyte-surface probe binding can consequently be described by means of a simple analytical solution by solving the kinetic rate equations, called **"well-mixed model"** [17] or **"rapid mixing model"** in some studies [18].

This model assumes that the kinetics is reaction rate-limited. The free analyte concentration being transported to the sensor surface remains uniform in space and constant in time as the binding reaction does not lead to any significant depletion of the analye molecules in solution. Giving a simple biomolecular first-order interaction, the binding of analyte to the sensor surface with the association rate constant k_a and dissociation rate constant k_d is given as:

$$C_s = \frac{k_a b_m C_0 (1 - e^{-(k_a C_0 + k_d)t})}{k_a C_0 + k_d} \tag{4.7}$$

As mentioned in Chapter 1, the apparent time constant is defined by $K_{app} = k_a C_0 + k_d$, which can be derived by fitting the association phase of kinetic curves to equation 4.7. The time course of

the binding reaction during the association process is typically measured for several analyte concentrations. For each concentration, this apparent time constant is determined. The association rate constant can be estimated from a slope of the plot between K_{app} and analyte concentration whereas the dissociation rate constant is separately determined from a single exponential decay.

It is important to note that this analytical model is only valid when the analyte transport does not influence the kinetics of binding and dissociation to and from the surface receptors. Nevertheless, if the mass transport is dominant in kinetic reactions and cannot be neglected, the binding kinetics need to account for transport using a two-compartment model described in a number of studies [19, 20]. However, it is not in the scope of this work.

4.3.3 BIAevaluation software package

BIAevaluation is a stand-alone commercial software package from Biacore AB, developed for the evaluation of the sensorgram collected from kinetic measurements of analte-surface probe interactions. The software supports several means of data evaluation.

The **global analysis** module simultaneously fits an entire set of association and dissociation curves at various target concentrations with one set of rate constants, ideally improving the robustness of the fitting procedure. The software can also fit the association and dissociation phases separately or fit the transient kinetics with equilibrium analysis by means of Scatchard analysis. Another additional module is called **global-local fit** where an individual sensorgram containing association and dissociation phases is separately fit for each analyte concentration. As a result, various sets of on- and off-rates corresponding to each analyte concentration are achieved. In this study, we used global analysis and global-local to fit the experimental kinetic data.

Contrary to the aforementioned fitting approaches, such as FEM and well-mixed models, where 1:1 interaction can solely be assumed for data fitting, different kinetic modules are available in the BIAevaluation software for more complex interactions. Mass transfer limitation can also be included in a 1:1 binding model. Other more complex fit models available in BIAevaluation software include bivalent analyte, heterogeneous analyte (competition reaction), heterogeneous ligand (parallel reaction), and conformation change. More detailed information concerning this software can be found in the handbook [21].

The quality of the fit can be evaluated by various aspects. For example, the residuals are used to visualize the difference between the fitted curves and the experimental data. Practically, the residual values should not exceed 10% of the maximum response of the fitted curve whereas higher values indicate an inaccurate fitting. The chi^2 (χ^2) value is a statistical parameter that measures the closeness of the fit. A good fit should have χ^2 in the same order of the noise magnitude in RU (normally <2). Values of χ^2 below 10 are often acceptable [22]. Standard error (SE) values are considered satisfactory if their values are within one order of magnitude of the rate constants.

The data evaluation using this commercial software strongly requires highly skilled personnel to reliably interpret the kinetic data therefore this exquisite operation was addressed to Martine Pugnière who has expertise in SPR at the Institute de Recherche en Cancérologie de Montpellier (IRCM).

4.3.4 Results and discussion

4.3.4.1 Streptavidin-biotin binding model

The relative sensor responses of streptavidin-biotin binding at various analyte concentrations fitted with the simulation model are shown in Figure 4.11a. It was observed that the experimental data of streptavidin binding at low concentration (10-50 nM) fitted the simulation data well with R^2 in a range of 0.99. Nevertheless, the high concentration of streptavidin (100 nM) showed a relatively poor fit with the simulation results ($R^2 = 0.95$). This might be due to several reasons prominent at high analyte concentration including steric hindrance, heterogeneity of the surface, non-specific binding, and deviation from a 1:1 interaction model. To determine the binding affinity based on computational model, the association and dissociation rate constants at each concentration were extracted from the best fit of the predicted binding curves to the experimental data.

The average association rate constant (k_a) was determined to be 7.1×10^5 $M^{-1}s^{-1}$ and the dissociation rate constant (k_d) of 8.0×10^{-7} s^{-1} was observed from the best fit for all concentrations. Additionally, a lower off-rate was also applied to the simulation model, but there was no change in sensor responses due to an extremely tight bond between streptavidin and biotin. As a result, the dissociation constant (K_D) for streptavidin-biotin interaction can be estimated as $K_D \leq 1.1\times10^{-12}$ M. It should be noted that the dissociation phase was not experimentally studied, thus the dissociation constant of streptavidin-biotin was not determined directly from the experiments but rather its theoretical value found in the literature was used as an input parameter in the simulation to find the best fit for the association data.

The kinetic curves of streptavidin-biotin interaction were also fitted to equation 4.7 in the well-mixed model, obtaining the apparent time constant for each analyte concentration. A replot of apparent time constants as a function of streptavidin concentrations is demonstrated in Figure 4.11b. The apparent time constant increased with increasing analyte concentration. The plot gave a linear fit with a slope of 0.0003 and R^2 of 0.9903. A derived slope of 0.0003 $nM^{-1}s^{-1}$ resulted in the association rate constant k_a of 3.0×10^5 $M^{-1}s^{-1}$. The derived value of k_a was in good agreement with the value extracted from our finite element model.

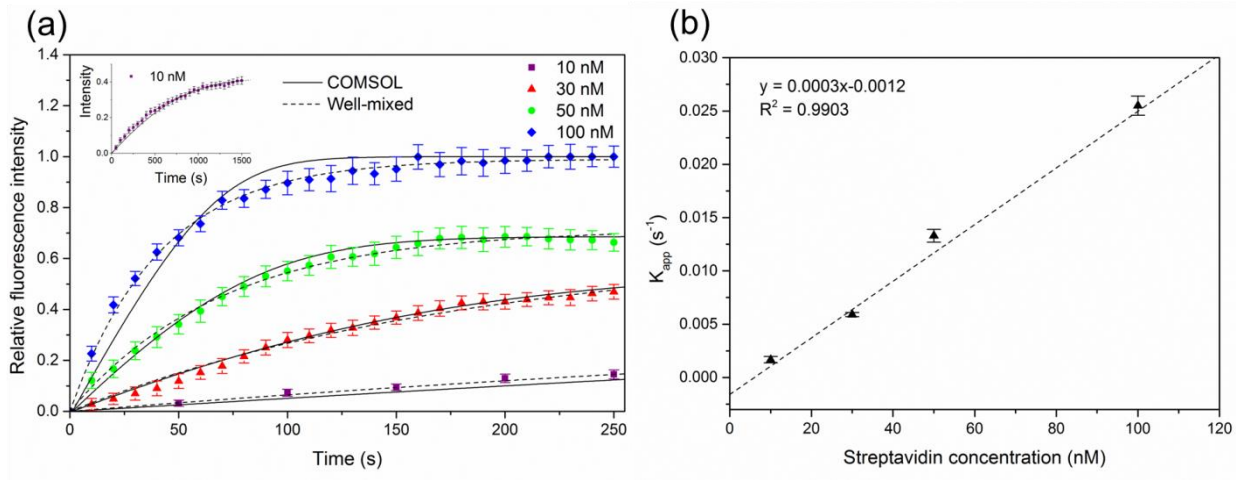

Figure 4.11 (a) Real-time sensor responses of streptavidin-biotin interaction measured in biofunctional nanoslits. Kinetic curves obtained from each concentration were attributed to the measurement from the different nanofluidic device (the error bars: standard errors). The sensor responses were normalized to the relative fluorescence intensity and fitted with the computation model, based on finite element method, and the well-mixed model assuming a simple Langmuir 1:1 interaction. The black (___) and (----) lines represent the predicted curves from the best fit of finite element simulation and the well-mixed model, respectively. Due to a long response time, the binding curve of the lowest concentration of streptavidin (10 nM) is also plotted separately in the inset figure. (b) Plot of apparent rate constants (K_{app}) determined from non-linear least-squares fit as a function of streptavidin concentration. The plot showed a linear trend with R^2 value of 0.9903.

4.3.4.2 Mouse IgG/anti-mouse IgG interaction model

The resulting kinetic data of mouse IgG/anti-mouse IgG interaction obtained in the nanoslits were fitted with three different approaches as described previously: i) our developed finite element model, ii) the well-mixed model, and iii) global-local fitting by BIAevalulation 4.1.1 software.

The simulated kinetic curves at various rate constants were generated in COMSOL Multiphysics software and compared to the experimental kinetic data for each analyte concentration. The other parameters, such as the flow velocity, the channel geometry, and the surface probe density, were kept the same.

For this biological model, the full experimental sensorgram containing association and dissociation phases for each analyte concentration were simultaneously fitted to the simulated curves. It can be observed that our simulated kinetic model described the immunoreaction assay in nanoslits well as each experimental binding curve was fitted accurately (R^2 in a range of 0.99) (Figure 4.12). The average association rate constant (k_a) was determined to be 8.0×10^5 $M^{-1}s^{-1}$ and a

dissociation rate constant (k_d) of 6.2×10^{-4} s^{-1} was achieved, giving an equilibrium dissociation constant K_D of 0.77 nM.

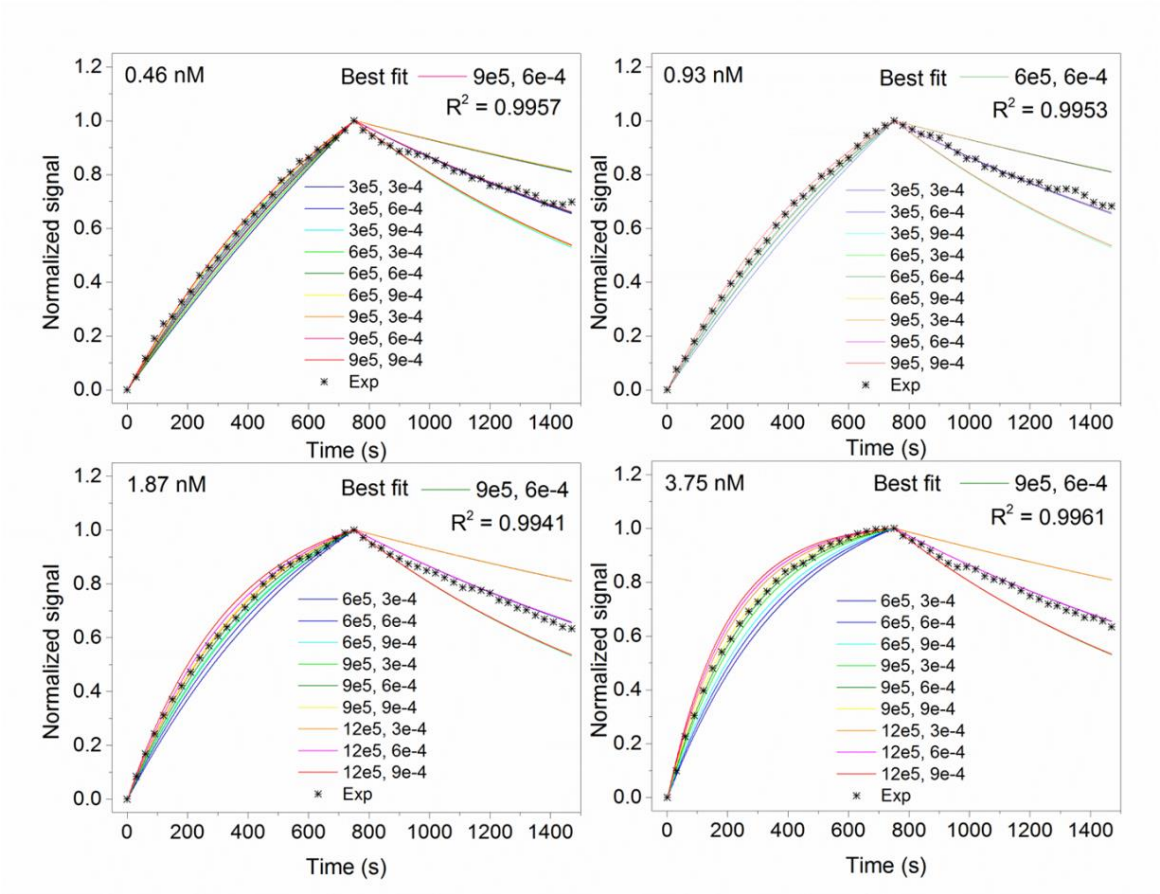

Figure 4.12 Extraction of kinetic constants for mouse IgG/anti-mouse IgG interaction. The experimental data of various mouse IgG concentrations (0.46, 0.93, 1.87 and 3.75 nM) (✱) were plotted with the simulated curves (___) obtained from finite element computation model at different association and dissociation rate constants. The surface probe density and flow velocity were kept the same in all cases. The extracted rate constants were determined from the best fit of the predicted binding curves to the experimental data by means of coefficient of determination.

The effects of various flow velocities ranging from 200 to 600 μm/s (associated with the Pe_H numbers in the range of 9-27) on the binding kinetics were also investigated. However, the sensor responses did not show any significant differences, indicating no mass transport limitation as expected. Consequently, the experimental data were fitted to the 'well-mixed' analytical model using the non-linear least squares method (Figure 4.13a) and the apparent time constant (K_{app}) was plotted as a function of analyte concentration, giving a good fit with R^2 of 0.9959 (Figure 4.13b). Desorption of bound analyte molecules from the surface receptor was estimated using a first-order

exponential decay. This resulted in the association and dissociation rate constants of 6.0×10^{5} $M^{-1}s^{-1}$ and 5.5×10^{-4} s^{-1}, respectively with K_D being 0.92 nM.

Finally, the kinetic data were examined using a global-local analysis from BIAevaluation software. Comparable to our simulation, the best fit was found using a Langmuir 1:1 binding model giving residual versus time plots lower than 0.1 (Figure 4.13a). The average values of k_a and k_d were determined to be 12×10^{5} $M^{-1}s^{-1}$ with SE of 2.0×10^{4} and 5.0×10^{-4} s^{-1} with SE of 1.8×10^{-5}, respectively. The value of K_D can be calculated to be 0.42 nM.

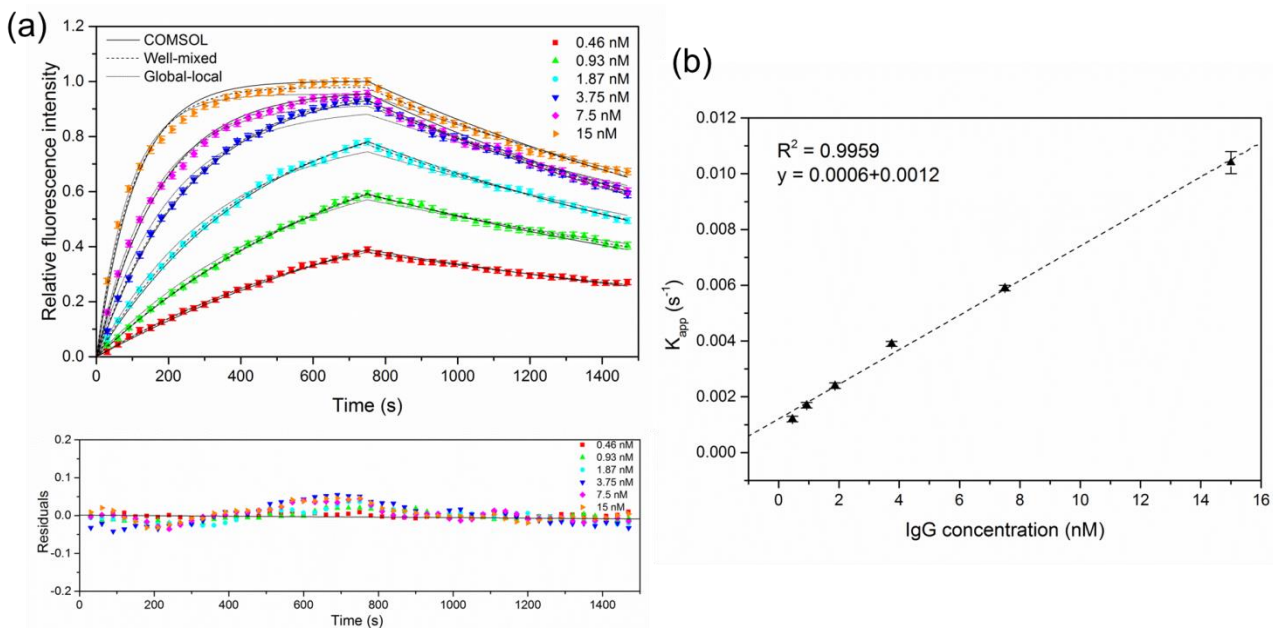

Figure 4.13 (a) Real-time sensor responses of mouse IgG/anti-mouse IgG interaction measured in the biofunctional nanoslit at various analyte concentrations ranging from 0.46 nM to 15 nM (the error bars: standard errors). The data were normalized to relative fluorescence intensity and fitted with three different models: (1) finite element simulation, (2) well-mixed model, and (3) global-local fitting by BIAevaluation software package with associated residual plots, assuming a simple Langmuir 1:1 interaction. The black (___), (----) and (……) lines represent the predicted curves from the best fit of finite element simulation, the well-mixed model, and global-local fitting, respectively. (b) Plot of apparent rate constants (K_{app}) as a function of mouse IgG concentrations, showing a linear trend with R^2 value of 0.9959.

To summarize, the extracted binding constants measured from three different fitting approaches were shown to be in good agreement, supporting the validity of our finite element model for good quantitative description of the kinetic data and, more importantly, demonstrating that our kinetic data obtained in nanoslit biosensors could readily applied to various fitting methodologies.

4.4 SPR benchmarking

To further evaluate the feasibility of our platform for use in kinetic studies of biomolecular interactions, using the same preparation coated-gold surface as nanoslits, an analogous real-time kinetic measurement of mouse IgG/anti-mouse IgG interaction was conducted using a surface plasmon resonance (SPR) setup. BIACORE was used to study the binding kinetics of only mouse IgG/anti-mouse IgG interaction. The streptavidin-biotin interaction was not addressed because of the limitation of the apparatus. All SPR measurements and kinetic curve fitting were performed by our colleagues, Martine Pugnière and Corinne Henriquet, at IRCM.

4.4.1 SPR principle

The surface plasmon resonance (SPR) biosensor is a surface-based analytical tool used in qualitative and quantitative characterization of reversible interactions between flowing reactant and its binding partner immobilized on the sensor surface. The optical detection principle of SPR relies on the excitation of surface plasmons in the metal film with a beam of p-polarized light, based on the total internal reflection (TIR) at a well-defined angle of incidence, called the **resonance angle**. This process occurs at a glass/thin metal film/dielectric interface. The evanescent wave generated by plasmons is useful for the measurement within ~ 300 nm (distance of one wavelength) from the sensor surface as it decays exponentially with distance from the interface [23].

The resonance angle is sensitive to the change in refractive index (RI) of the sample adjacent to the metal film (within the evanescent field above the sensor surface). Any adsorption or desorption of macromolecules on the sensor surface induces changes in refractive index, leading to a measurable shift in the resonance angle (Figure 4.14). Reviews of SPR biosensor including fundamental theory, different SPR configurations and its applications can be found in the literature [24, 25].

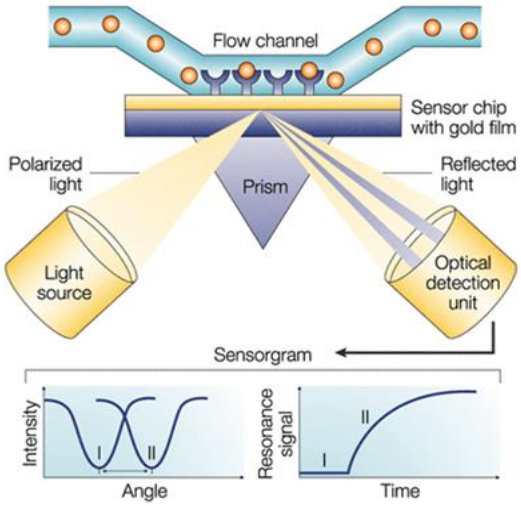

Figure 4.14 A typical Kretschmann SPR biosensor setup. The sensor chip containing receptors immobilized on the thin gold film is placed onto the prism. The sample solution is supplied to the sensor through the flow channel via an integrated microfluidic system. SPR detects the change in refractive index occurring adjacent to the surface from the reflected light. This change is dependent on the mass of biomolecules bound to the surface. The angle shift can be monitored in real-time upon binding progress as a plot of time-course of resonance signals (from [26]).

SPR can detect changes in refractive index in the vicinity of the surface upon biomolecule binding in real-time and these changes are typically measured in resonance units (RU), in which 1 RU corresponds to ~ 1 pg protein/mm^2 [27]. The sensorgram (a plot of sensor responses or resonance units versus time) contains an abundant variety of information on the investigated biomolecular interactions including affinity, kinetics, and binding thermodynamics.

4.4.2 Kinetic measurement

The pre-surface functionalization protocol analogous to nanoslits was performed on specific gold substrates manufactured by GE Healthcare (SIA Kit-Au) and the experiments were conducted on a BIACORE 3000 instrument (Figure 4.15). Experimental details of the sensor preparation and receptor immobilization can be found in the **Appendix E**.

In this kinetic experiment, we optimized the level of immobilized ligand (260 RU) in order to obtain binding data that fitted well with the 1:1 interaction model. At high probe density, the surface heterogeneity problem induced by steric crowding was more pronounced and there was a high degree of bivalent binding due to the nature of the used polyclonal anti-mouse receptors (VH+VL), mixtures of antibodies in which each of them could recognize various parts of the same analyte

molecule. By reducing the grafting density of the receptors on the sensor, we could alleviate these problems leading to more binding with 1:1 Langmuir behaviors.

Figure 4.15 A BIACORE 3000 SPR biosensor apparatus used in kinetic studies (from [28]).

Despite the use of polyclonal antibodies due to several constraints in finding the compatible protocol for both SPR and nanoslits, biotinylated anti-mouse Fc gamma specific could be ideally exploited in future work to avoid bivalent binding. This receptor only recognizes the Fc part of an antibody.

To conduct kinetic measurements, a continuous flow of 50 μL/min was applied throughout the experiments. The association and dissociation time were 180 s and 400 s, respectively. Five different concentrations of Alexa Fluor-647 conjugated monoclonal mouse anti-rabbit IgG (mIgG-AF 647) ranging from 1.6 to 26 nM were exploited to obtain kinetic sensorgrams. The regeneration steps were performed with a solution of 25 mM HCl for 36 s at each cycle. Furthermore, a 32 μg/ml solution of Alexa Fluor-660 conjugated goat anti-rabbit IgG (irrelevant analyte) was injected at a flow rate of 50 μL/min to verify non-specific binding. However, no significant binding signal was observed. The kinetic curves were finally evaluated and fitted using the BIAevaluation 4.1.1 software.

The binding data was complemented by two types of reference experiments [29]. A blank-surface reference was primarily used to correct the bulk effect or artifacts of refractive index change from the sample solution and non-specific binding. A blank-buffer reference was performed on a ligand surface with a buffer injection prior to analyte injection in order to correct for baseline drift. Unwanted parts of the sensorgrams, such as regeneration step, were removed, the baseline of sensor responses was adjusted to zero, and all spikes induced by buffer change were deleted. Global analysis was utilized to identify the binding model and quantify kinetic parameters.

Figure 4.16 depicts the sensorgrams containing kinetic information of protein binding events at various target concentrations ranging from 1.6 nM to 26 nM. The best fit for the entire data was found with a 1:1 Langmuir binding model without influence of mass transport, giving k_a and k_d of 7.3×10^5 $M^{-1}s^{-1}$ with SE of 3.0×10^3 and 1.9×10^{-4} s^{-1} with SE of 8.0×10^{-6}, respectively, with K_D being 0.26 nM.

It is important to mention that the kinetic sensorgrams measured at higher analyte concentrations (> 26 nM) tended to deviate from the 1:1 interaction, due to the heterogeneity of our model (use of polyclonal antibody as surface receptors). In general, analyte concentrations for kinetic experiments should be in the range of the affinity constants (K_D) of the interaction pairs to estimate the accurate results. In this SPR experiment, high analyte concentrations were included and a 1:1 interaction was utilized in the model fit for demonstration purpose only.

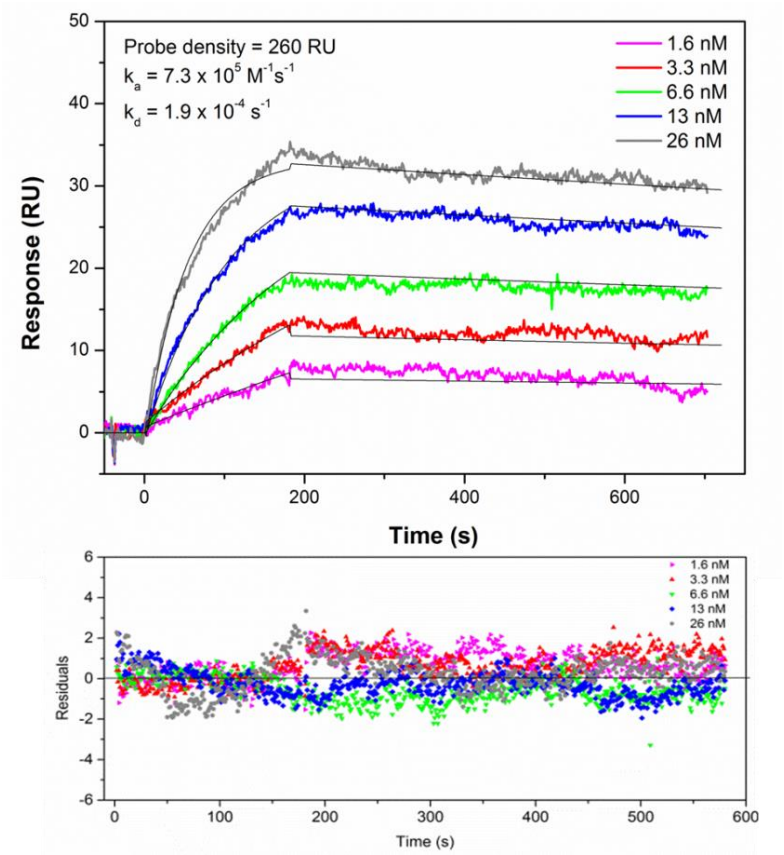

Figure 4.16 Sensorgrams of Alexa Fluor-647 conjugated mouse IgG/anti-mouse IgG binding kinetics obtained from analogous SPR measurements with the corresponding residual plot. Kinetic curves were fitted with a 1:1 global analysis model from BIAevaluation software package (black line).

4.4.3 Binding kinetics at varying probe grafting density

Optimal density of the immobilized probes on the sensor surface is critical to obtaining high quality kinetic data. **A low surface density of ligand is preferable for accurate measurement of the binding kinetics of an interaction.** An excess of ligand density can result in the data artifacts due to crowding effects, steric hindrance or aggregation on the surface [30]. Moreover, extensive amount of ligand density promotes weak non-specific interactions at high analyte concentration, impacting the observed binding kinetics and the resulting binding rates [29]. Yet, not enough ligand density inherently reduces the sensitivity of the measurement.

A high dependence of the binding kinetics of DNA-protein interaction and DNA hybridization on the probe surface density has previously been reported [31, 32], wherein the high probe density film resulted in slow kinetics of the target capture. For kinetic assay, it is usually recommended to use the minimum amount of surface immobilized ligand that generates an acceptable measurable response. This probe loading level could be as high as 300RU [33].

One way to assess the reliability and the accuracy of the measured binding rate constants is to conduct kinetic experiments with varying surface receptor densities. In this way, one could reveal obscuring effects such as heterogeneity and mass transfer on the binding kinetics. With this aim, the binding kinetics of mIgG-AF 647/anti-mouse IgG on the SPR setup with different immobilized probe densities (80RU and 800 RU) was performed. The experimental conditions (analyte concentration ranges, flow rate, etc.) were similar to the one described in the **Appendix E** except the exposure time of the gold sensor surface to the receptor (biotin-anti-mouse) solution. The estimated binding constants were compared with those obtained with the medium surface loading density (260 RU) in the foregoing experiment.

The kinetic sensorgrams of mIgG-AF 647/anti-mouse IgG for various surface probe densities are demonstrated in Figure 4.17. The data were globally fitted with 1:1 binding interaction without influence of mass transport. In spite of the fact that the kinetic curves of the immobilized sensor at low probe density exhibited higher noise level (lower signal-to-noise ratio), both kinetic curves were fitted well to a Langmuir model.

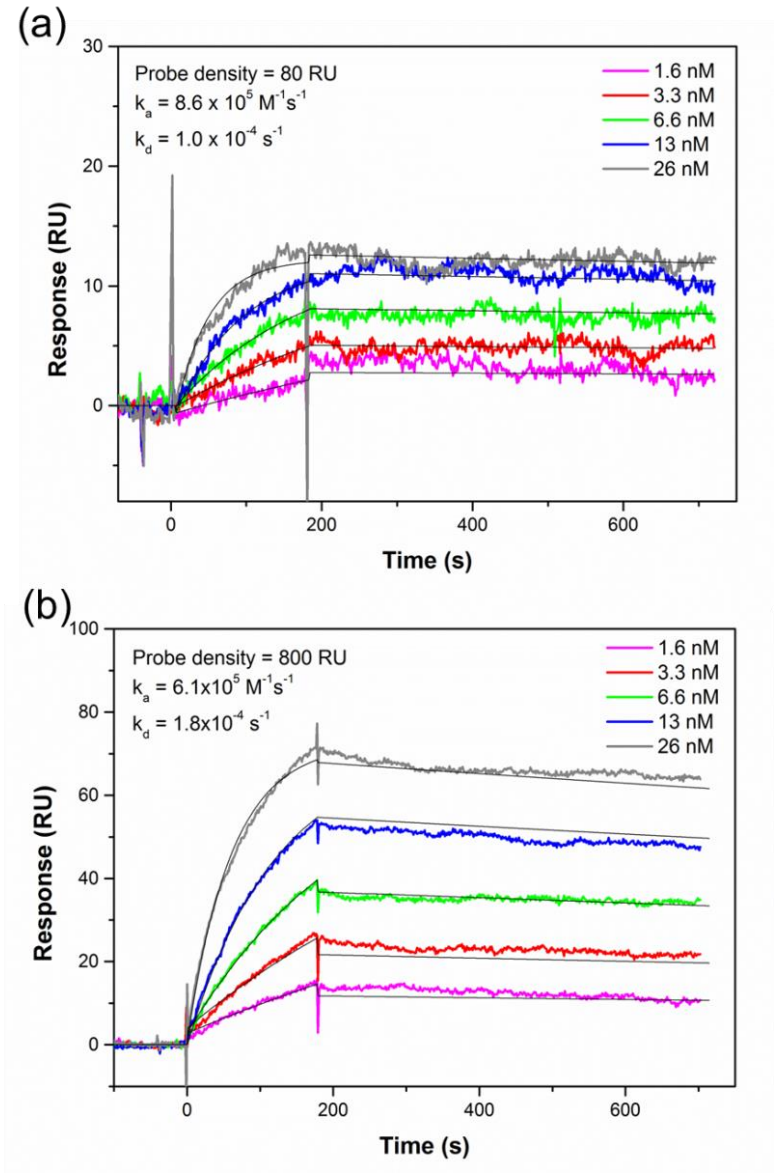

Figure 4.17 Kinetic sensorgrams of Alexa Fluor-647 conjugated mouse IgG/anti-mouse IgG interaction obtained from the SPR experiments at different immobilized surface probe densities (a) 80 RU and (b) 800 RU. The data were both fitted to a simple Langmuir 1:1 interaction using global analysis. The experiment with a probe density of 80 RU yielded k_a of 8.6×10^5 $M^{-1}s^{-1}$ and k_d of 1.0×10^{-4} s^{-1} while k_a of 6.1×10^5 $M^{-1}s^{-1}$ and k_d of 1.8×10^{-4} s^{-1} were obtained from the measurement with a probe density of 800 RU.

The kinetic constants and χ^2 values of mouse IgG/anti-mouse IgG interaction obtained at varying surface probe densities are summarized in Table 4.2. The estimated maximum response (R_{max}) decreased which was proportional to the reduced ligand densities. The extracted kinetic constants and the affinity constants were shown to be consistent for all three measurements.

Based on these results, kinetic experiments were not dependent on the variation of the surface ligand density under our investigated experimental conditions. As a result, there were no involved experimental artifacts associated with mass transport limitation and steric hindrance. It is important to mention that when the surface grafting level of anti-mouse receptors increased up to 1520 RU, the kinetic data did not fit well with a simple 1:1 binding but rather fitted a bivalent model.

Good consistency of kinetic constants between different kinetic experiments at various probe grafting densities confirmed the accuracy of the determined rate constants of the investigated mouse IgG/anti-mouse binding model.

Table 4.2 Summary of kinetic parameters of Alexa Fluor-647 conjugated mouse IgG/anti-mouse IgG interaction obtained from SPR experiments at varying surface probe densities.

Probe density (RU)	k_a ($M^{-1}s^{-1}$)	k_d (s^{-1})	R_{max} (RU)	K_D (nM)	χ^2
80	$8.6\pm0.1\times10^5$	$1.1\pm0.1\times10^{-4}$	12.9	0.122	0.393
260	$7.3\pm0.1\times10^5$	$1.9\pm0.1\times10^{-4}$	34.1	0.262	0.790
800	$6.1\pm0.1\times10^5$	$1.8\pm0.1\times10^{-4}$	72.6	0.297	2.82

4.4.4 Effect of fluorescence labeling on protein binding kinetics

To be able to compare the performance of our fluorescence-based nanofluidic biosensors with the label-free SPR technique, it was desirable to investigate the influence of fluorescence labeling on kinetic behaviors of biorecognition events.

How the presence of the fluorescent label alters the protein binding kinetics is a golden question that needs to answer to biosensor communities prior to applying our new platform for biomolecular interaction analysis. Sun Y.S. *et al.* reported that the equilibrium dissociation constants of the streptavidin-peptide reaction and antibody-antigen reaction changed significantly when the analytes were labeled with a Cy3 dye [34]. Fluorescent labeling may alter the binding behavior of the biomolecules of interest to some extent; this effect arising from the charge of the fluorescent labels could be minimized by a proper design of fluorescence tags [35].

The influence of labeling on the binding affinity and kinetics could be negligible in some applications, considering that kinetic measuring of protein-ligand interactions by means of fluorescence detection has been demonstrated by numerous studies [36-38]. **When working with fluorescently tagged biomolecules, care must be taken to validate their use in any specific application.**

Here, the binding kinetics of unconjugated mouse IgG and fluorescently labeled mouse IgG (mIgG-AF 647) with the anti-mouse receptor immobilized surfaces were investigated using SPR apparatus. Both experiments were carried out under similar conditions, providing the same surface probe density of 800 RU and the same range of analyte concentrations varying from 1.6 nM to 26 nM.

Figure 4.18 demonstrates the sensorgrams globally fitted with a 1:1 interaction without influence of mass transport. Both kinetic curve profiles appeared similar. However, the estimated maximum response (R_{max}) was decreased 17% in the case of labeled analytes. The extracted kinetic parameters are summarized in Table 4.3. The equilibrium dissociation constant (K_D) of mouse IgG with the anti-mouse IgG immobilized surface decreased by a factor of 2 when mouse IgG was labeled, primarily from a decrease in the association rate constant (k_a). On the other hand, labeling had a minor consequence on the dissociation constant (k_d).

Even though fluorescence labeling was shown to have an impact on the protein binding kinetics to a small extent, this influence could be considered negligible as the binding affinity of both experiments was still in the same order of magnitude. **This experiment was essential to demonstrate that our nanofluidic biosensor platform exploiting fluorescence detection for protein binding kinetics studies combined with attentive experimental designs was valid to produce reliable kinetic data, enabling accurate determination of rate constants.**

Furthermore, the competitive assay format [39], where a non-labeled analyte (cold analyte) and a labeled analogue analyte (hot analyte) compete for the same binding site on the sensor surface, is another possibility to completely remove any ambiguity raised from labeling. According to this format, indirect kinetic information of unlabeled analytes can be acquired and the interactions remain label-free. Nevertheless, the compatibility of this competitive assay format with our nanofluidic biosensor system needs to be verified.

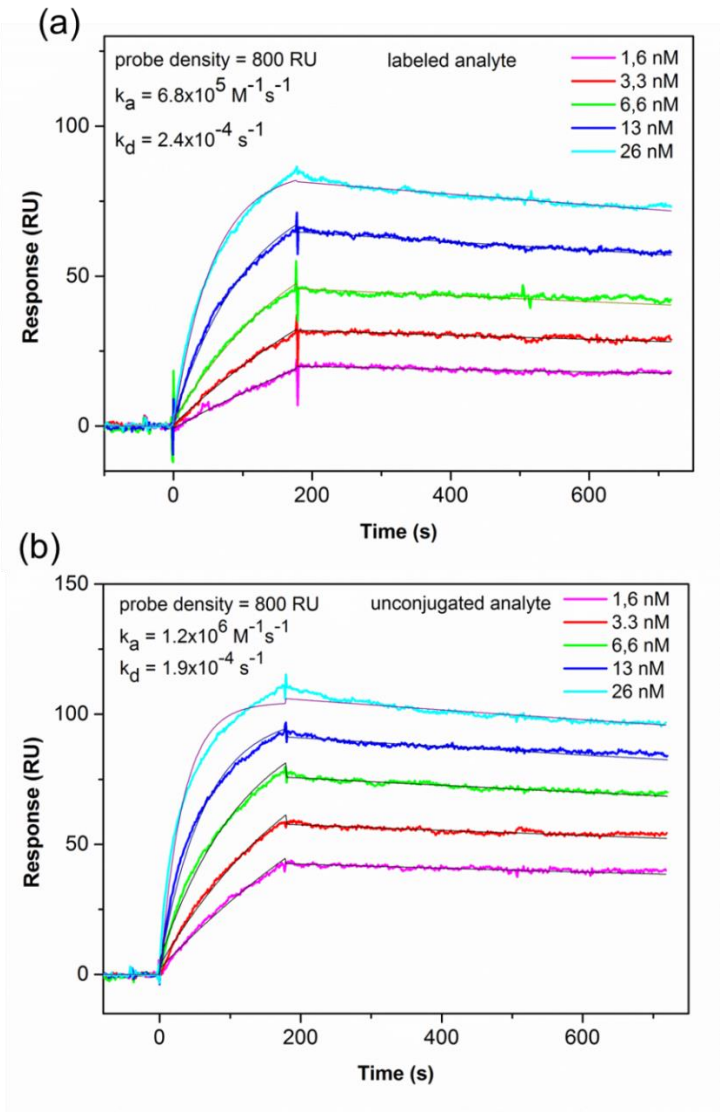

Figure 4.18 Association and dissociation curves of Alexa Fluor-647 conjugated mouse IgG (a) and unconjugated mouse IgG (b) against anti-mouse IgG immobilized surface at different mouse IgG concentrations obtained from SPR experiments.

Table 4.3 Summary of kinetic parameters of unlabeled and labeled mouse IgG/anti-mouse IgG interactions obtained from SPR experiments.

Target analyte	k_a ($M^{-1}s^{-1}$)	k_d (s^{-1})	R_{max} (RU)	K_D (nM)	χ^2
unlabeled mouse IgG	$12\pm0.1\times10^5$	$1.9\pm0.1\times10^{-4}$	112	0.157	2.69
Alexa Fluor 647-labeled mouse IgG	$6.8\pm0.1\times10^5$	$2.4\pm0.1\times10^{-4}$	92.9	0.347	0.766

4.5 Comparison of our sensor performances with the literature and SPR setup

To shed light on the validity of our nanoslit biosensor platform for accurate quantification of binding kinetics of biomolecular interactions, the estimated binding rate constants of the two selected biological models were compared with those obtained from SPR measurement or/and with the values available in the literature. Since the kinetic measurement of streptavidin-biotin interaction was not possible to perform in the SPR-based instrument, the comparison of kinetic constants was accomplished merely between our platform and the literature. From Table 4.4, our nanoslit-based biosensor platform yielded kinetic constants of the streptavidin-biotin interaction that were within the range of values reported in the literature which primarily are solution-based assays.

Table 4.4 Comparison of kinetic constants for streptavidin-biotin binding between our biofunctional nanofluidic platform and the literature.

Biosensor platform Streptavidin-biotin binding	Association rate k_a ($M^{-1}s^{-1}$)	Dissociation rate k_d (s^{-1})	Equilibrium dissociation constant K_D (M)
Nanoslit biosensor			
- FEM model	$7.1\pm2.5\times10^5$	$8.0\pm1.2\times10^{-7}$	$\leq1.1\times10^{-12}$
- Well-mixed model	$3.0\pm0.3\times10^5$	N/A	
Literature [8, 15, 40, 41]	$4.4\times10^5 – 4.5\times10^7$	2.4×10^{-6}	$\sim 10^{-13}$

Generally, the extracted kinetic parameters (K_D) from surface-based biosensors should reflect the one in solution. However, these constants derived from immobilized ligand-based sensors are strongly affected by the state of the ligand on the sensor surface [42]. This causes the determined kinetic parameters to deviate from the assay in solution. In addition, the on-rate for biotin-

streptavidin binding reported in the literature can be used as approximate values only. The on-rate of 7×10^{7} $M^{-1}s^{-1}$ reported by Green N.M., et al. [43] is actually based on avidin-biotin interaction rather than streptavidin-biotin interaction.

It has been reported by Srisa-Art *et al.* [40] that the binding rate constants could be slightly different depending on the applied conditions of streptavidin-biotin system. Interestingly, the results obtained from X-ray crystallography data also showed that not every collision between streptavidin and biotin gave a productive binding because the exposed surface area of the four biotin binding sites on a tetrameric streptavidin represented only 2% of the total exposed area of a tetrameric streptavidin. All these factors could lessen the association rate into the range of 10^{6} $M^{-1}s^{-1}$ and it was likely that the binding rate could be varied by 1 order of magnitude.

The very low equilibrium dissociation constant ($K_D \sim 10^{-14}$ M) of streptavidin-biotin binding is actually attributed to the extremely low k_d due to its very strong non-covalent interaction; although the association rate constant can be in the same range as that of other analyte-ligand couples. **Based on a simple concept of our work to demonstrate the ability of our platform, the theoretical value of dissociation rate constant was considered sufficient for being used in the kinetic model fitting of the streptavidin-biotin association reaction using a simple 1:1 interaction.**

Table 4.5 summarizes the extracted kinetic parameters of mouse IgG/anti-mouse IgG interaction obtained from our biofunctional nanofluidic platform with different fitting approaches compared with those obtained from SPR and the literature. For this model, our nanofluidic-based biosensor was able to perform the association and dissociation phases consecutively, and as a result both on- and off-rate constants were experimentally derived. However, the values from the literature could be used as a rough guide to advocate our platform due to dissimilar experimental factors among various techniques: for instance, surface immobilization chemistry, sensor surface, and detection schemes. The analogue SPR experiment seemed to be the most well-suited comparison in which the experimental conditions were the most matching to those performed in our nanofluidic biosensor platform.

The resulting kinetic parameters determined from our platform were in good agreement with the SPR measurement and within the range of values in the literature, thus extending the validity of our platform for effective quantification of kinetic constants of protein-protein interactions. Our platform therefore displayed advantageous characteristic for bio-sensing and related applications.

Table 4.5 Comparison of kinetic constants for IgG/anti-IgG binding obtained from our biofunctional nanofluidic platform, SPR, and the literature.

Biosensor platform Mouse IgG/anti-mouse binding	Association rate k_a ($M^{-1}s^{-1}$)	Dissociation rate k_d (s^{-1})	Equilibrium dissociation constant K_D (M)
Nanoslit biosensor			
- FEM model	$8.0\pm1.2\times10^5$	$6.2\pm0.3\times10^{-4}$	7.7×10^{-10}
- Well-mixed	$6.0\pm0.3\times10^5$	$5.5\pm0.4\times10^{-4}$	9.2×10^{-10}
- Global local fit	$12\pm0.2\times10^5$	$5.0\pm0.2\times10^{-4}$	4.2×10^{-10}
SPR (Global analysis)	$7.3\pm0.1\times10^5$	$1.9\pm0.1\times10^{-4}$	2.6×10^{-10}
Literature [16, 44, 45]	$2.5\times10^5 – 1.3\times10^6$	3.0×10^{-4}	1.5×10^{-10}-1.2×10^{-9}

4.6 Range of operation and detection limit

The accurate determination of association and dissociation constants for the two couples of ligands presented here (streptavidin/biotin and mouse IgG/anti-mouse IgG) illustrated the various affinity strengths that could be studied with our system. Affinity studies usually require kinetic plots for several analyte concentrations ranging from 1/10 to 10 K_D in order to adequately extract kinetics constants.

Limitation of our technique in terms of working concentrations is given by the fluorescence signal to noise ratio, *e.g.*, the fluorescence emitted by the analytes specifically interacting at the sensor surface *vs.* the fluorescence due to the molecules flowing in the fluidic channel. In reaction-limited regime at equilibrium, for concentrated ($C_0 \gg K_D$) and diluted solutions ($C_0 \ll K_D$), where analyte molecules bind all or a fraction of the receptor molecules, we respectively have:

$$\frac{S}{N} = \frac{b_m}{H \times C_0} \tag{4.8}$$

$$\frac{S}{N} = \frac{b_m}{H \times K_D} \tag{4.9}$$

Thus, the sampling volume reduction during observation translates into a decreased background with a signal to noise ratio inversely proportional to the channel height. Using the grafted probe density, b_m, obtained with the presented surface functionalization protocol for IgG grafting, the previous equations demonstrate that high enough S/N can be obtained with sub-micrometer channels (H <1μm) even for low affinity molecules, *e.g.*, we can expect S/N of ~100 in 100 nm deep channels for K_D of 0.1 μM. In fact, the pM to the sub-μM range of K_D can be addressed with the presented technique, which concerns most molecules of interests regardless of the analyte size.

Furthermore, to ensure that our device can be employed not only for investigating binding kinetics of protein-ligand interactions but also as a highly sensitive and rapid on-chip immunosensor, limit of detection (LOD) is another performance characteristic for validation. **LOD is defined as the lowest concentration of an analyte in a sample that can be reliably detected by an analytical method, but not necessarily quantified** [46].

It was demonstrated recently that the detection limit of surface-based sensors depended on the true affinity of the probe to its target when working under concentration-limited regime (low affinity probe), whereas it was rather dependent on the effective surface probe density and the sample volume under interrogation under ligand-depletion regime (high affinity probe) [47]. **In our experiment, we simply employed the visual evaluation to experimentally determine the detection limit of our biosensor system.** The basic concept of such evaluation is to analyze the samples with known concentrations and the detection limit is determined by establishing the minimum concentration at which the analyte can be reliably detected [46].

To this end, different concentrations of Alexa Fluor-647 mouse IgG target solutions were introduced to the anti-mouse-modified nanoslits and the fluorescence intensities were recorded. Fluorescence time-lapse images were acquired with a 40 (N.A. 0.6) objective, an exposure time of 0.5 s, and a gain of 150. Each image was recorded with an accumulation of 10 and binning factor 2×2. It should be noted that the obtained LOD strongly depended on the sensitivity of the camera in which the imaging parameters were adjusted, which in our case was to optimize this LOD. The changes in fluorescence intensity on the sensor associated with their standard errors upon the introduction of different target analyte concentrations are plotted as a function of time in Figure 4.19.

No significant increase in fluorescence intensity was observed when an analyte-free buffer solution was injected, while an introduction of 1 pM resulted in a significant increase in fluorescence intensity after 30 min (S/N ~3). **With a sample volume of 10.5 nL, a mole detection limit can be determined as 10 zeptomole.** Notably, increasing the analyte concentration to 10 pM, our sensor could easily detect the binding response signal within 5 min.

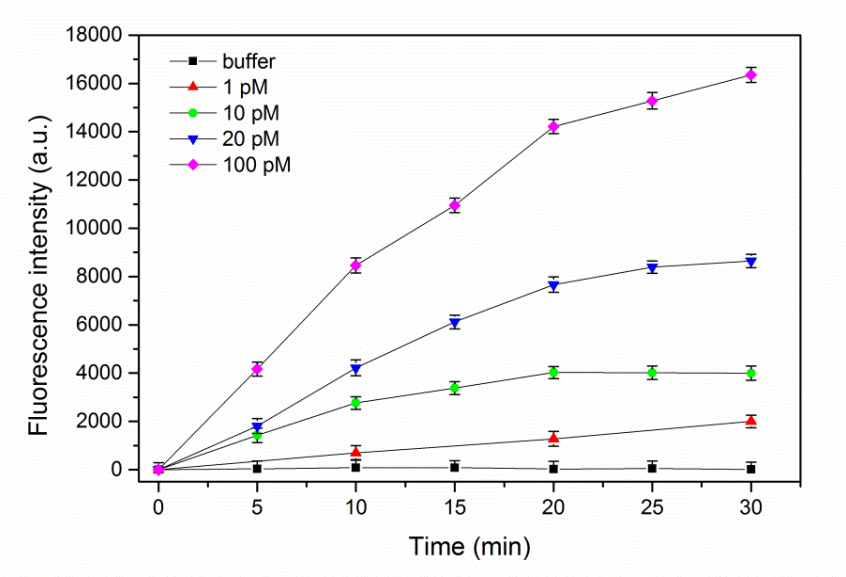

Figure 4.19 Fluorescence intensity changes with time upon the introduction of different concentrations of Alexa Fluor-647 mouse anti-rabbit IgG (mIgG-AF 647) target ranging from 0 pM (analyte-free buffer) to 100 pM on the anti-mouse IgG immobilized nanoslit (the error bars: standard errors).

The value of the detection limit obtained from our system for mouse IgG sensing is significantly better (~100 times) than, or comparable to, existing microfluidic immunosensing formats [48-50]. Furthermore, the total immunoassay time (including injection, immobilization and detection steps) required for mouse IgG detection, based on streptavidin-biotin linkage for anti-mouse IgG grafting, was found to be approximately 40 min in our study while the traditional enzyme-linked immunosorbent assay (ELISA) takes hours to days to complete the whole assay. Therefore, our approach also demonstrated a fast and sensitive immunosensing platform for protein detection with low reagent consumption (~1000 times less than SPR setup), indicating a great potential in clinical diagnosis.

4.7 Repeatability assay

Repeatability is defined as the capability of a single sensor used repeatedly for a series of measurements under the same circumstances and the same analyte concentration to produce an identical result. In this study, the repeatability of the sensor responses was assessed by measuring the association and dissociation phases of mouse IgG/anti-mouse IgG for three consecutive experiments carried out on the same device under similar working conditions.

Each cycle of the measurement consisted of the injection of a 5 nM solution of mIgG-AF 647 for 720 s during the association phase, followed by the introduction of a pure buffer solution for 750 s to dissociate the surface bound analyte under an applied flow velocity of 200 μm/s. The

sensor surface was subsequently regenerated by a short injection (10 s) of 10 mM solution of glycine-HCl, pH 2 and rinsed with the buffer solution prior to performing the next measurement cycle.

The fluorescence data of three measurements were obtained from the same sensor area (10×10 pixels) on the gold patch and the normalized signals were plotted as a function of time as demonstrated in Figure 4.20. According to the time-course, association and dissociation of mouse IgG/anti-mouse interaction, **our sensor exhibited an outstanding repeatability with the relative standard deviation (RSD) of the response being 2.28% (*n* =3)**, RSD = 100×standard deviation/average. Likewise, the results essentially revealed the reversibility and the stability of the surface-immobilized probe for multiple detection of its target analyte after being subjected to several regeneration cycles, which was a crucial characteristic of the biosensing elements for repeated use in kinetic applications. In this case, small deviation of the fluorescence signal results from measurement errors between experiments. The reported standard errors which originate from noise sources and fitting errors are still within the reproducibility of the data.

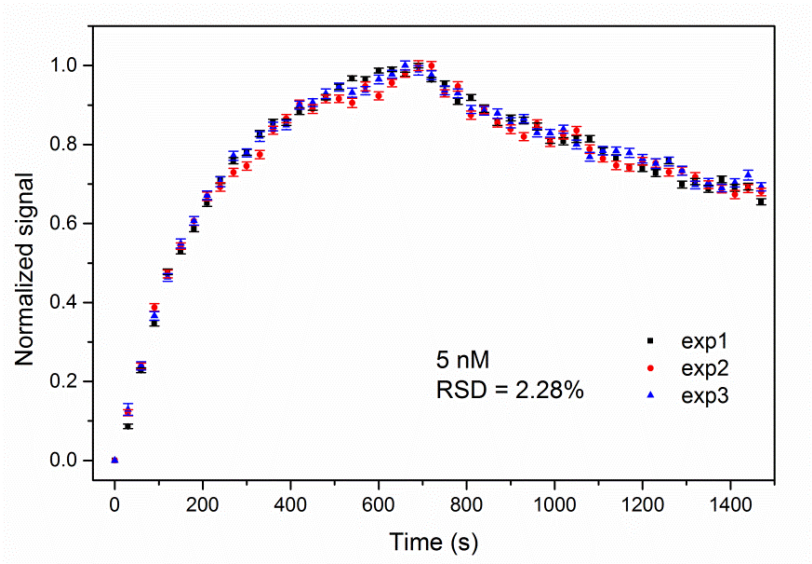

Figure 4.20 Repeatability of the nanoslit biosensor for multiple sensing of 5 nM Alexa Fluor-647 mouse anti-rabbit IgG (mIgG-AF 647). The plots represent the normalized fluorescence intensity as a function of time for three repeated experiments during kinetic assays on the same device (the error bars: standard errors).

4.8 Conclusion

In this chapter, we have presented the experimental validation of our nanofluidic biosensor platform for real-time monitoring of binding kinetics of two biological systems with different affinity ranges (streptavidin-biotin and IgG/anti-IgG interactions) as well as the effective determination of the binding constants using different fitting methodologies.

To this end, special attention has been paid in the first part to assess the bio-functionality of the biotin receptor-immobilized in the closed-fluidic chip, initially performed by open-top immobilization combined with the biocompatible bonding procedure. Based on the results obtained from fluorescence imaging under pressure driven flow scheme, we were able to confirm that the pre-immobilized probe molecules retained their bio-reactivity toward their streptavidin target, providing a high signal-to-noise ratio suitable for further kinetic assay. By conducting the first kinetic experiment of streptavidin-biotin binding, the importance of surface probe density on the binding kinetics has been revealed, in which a low surface density was required to produce more accurate kinetic data while a high surface density showed the eminent capturing efficiency of our nanoslit biosensors.

Remarkably, we have established for the first time the reversed-buffer flow technique to generate the full kinetic sensorgrams (association and dissociation curves), which was demonstrated by mouse IgG/anti-mouse interaction in the nanoslit. This has been a golden feature of our device since this method has been typically impractical for the classical microfluidic immunoassay formats. Additionally, a model based on finite element method coupled with MATLAB has been developed for data fitting and eventually extracting on-and off-rates of the investigated biorecognition pairs.

The dimensionless numbers (Peclet and Damköhler numbers) have been central to examine the operating conditions of our system. Using these calculated numbers and the experimental verification with varying flow velocities, we have confirmed that the kinetic reactions occurring in nanoslits were free of mass transport limitation. Moreover, the kinetic data were successfully fitted to the analytical model (well-mixed model) and local-fit from the commercial software (BIAevaluation). The results showed a good consistency of estimated binding constants among each method, thus giving great possibility in applying our kinetic data obtained in nanoslits to various fitting approaches.

To further validate our biosensor platform, we have carried out the analogous kinetic assay using the SPR apparatus and the extracted binding constants were compared with those obtained from nanoslit biosensors. Additionally, kinetic assays performed with varying surface probe densities and the evaluations of labeling on the binding kinetics have ensured the accuracy of the determined kinetic parameters. The extracted values from our system were in good agreement with SPR measurement and previously reported values in the literature. Hence, it has extended the validity of nanoslit biosensors in quantifying kinetics of biomolecular interactions along with a noteworthy detection limit of 1 pM or 10 zeptomole, and a good repeatability of the sensor response (RSD = 2.28%) at analyte concentration of 5 nM.

Bibliography

1. Leïchlé, T. and C.-F. Chou, *Biofunctionalized nanoslits for wash-free and spatially resolved real-time sensing with full target capture.* Biomicrofluidics, 2015. **9**(3): p. 034103.
2. Lee, K.-H., et al., *Microfluidic systems integrated with two-dimensional surface plasmon resonance phase imaging systems for microarray immunoassay.* Biosensors and Bioelectronics, 2007. **23**(4): p. 466-472.
3. Luo, Y., F. Yu, and R.N. Zare, *Microfluidic device for immunoassays based on surface plasmon resonance imaging.* Lab on a Chip, 2008. **8**(5): p. 694-700.
4. Zimmermann, M., et al., *Modeling and optimization of high-sensitivity, low-volume microfluidic-based surface immunoassays.* Biomed Microdevices, 2005. **7**(2): p. 99-110.
5. Choi, C.J., et al., *Comparison of label-free biosensing in microplate, microfluidic, and spot-based affinity capture assays.* Anal. Biochem., 2010. **405**(1): p. 1-10.
6. Lu, H., et al., *Optical fiber immunosensor for the real-time analysis of ligand-receptor binding kinetics.* Proc. SPIE 1999. **3863**: p. 143.
7. Ivnitski, D., et al., *An amperometric biosensor for real-time analysis of molecular recognition.* Bioelectrochemistry and Bioenergetics, 1998. **45**(1): p. 27-32.
8. Coltro, W.K.T., et al., *Microfluidic devices with integrated dual-capacitively coupled contactless conductivity detection to monitor binding events in real time.* Sensor. Actuat. B-Chem., 2014. **192**(0): p. 239-246.
9. Spinke, J., et al., *Molecular recognition at self-assembled monolayers: Optimization of surface functionalization.* The Journal of Chemical Physics, 1993. **99**(9): p. 7012-7019.
10. Foley, J.O., et al., *Experimental and model investigation of the time-dependent 2-dimensional distribution of binding in a herringbone microchannel.* Lab Chip, 2008. **8**(4): p. 557-64.
11. Hu, G., Y. Gao, and D. Li, *Modeling micropatterned antigen–antibody binding kinetics in a microfluidic chip.* Biosensors and Bioelectronics, 2007. **22**(7): p. 1403-1409.
12. Didar, T.F., A.M. Foudeh, and M. Tabrizian, *Patterning Multiplex Protein Microarrays in a Single Microfluidic Channel.* Analytical Chemistry, 2012. **84**(2): p. 1012-1018.
13. Sjoelander, S. and C. Urbaniczky, *Integrated fluid handling system for biomolecular interaction analysis.* Anal. Chem., 1991. **63**(20): p. 2338-2345.
14. Squires, T.M., R.J. Messinger, and S.R. Manalis, *Making it stick: convection, reaction and diffusion in surface-based biosensors.* Nature Biotechnol., 2008. **26**(4): p. 417-26.
15. Roberta, D.A., G. Giuseppe, and S. Giuseppe, *Real-Time Binding Kinetics Monitored with Surface Plasmon Resonance Imaging in a Diffusion-Free Environment.* Open. Spectro. J., 2008. **2**(1): p. 1-9.
16. Sapsford, K.E., et al., *Kinetics of Antigen Binding to Arrays of Antibodies in Different Sized Spots.* Anal. Chem., 2001. **73**(22): p. 5518-5524.
17. Vijayendran, R.A., F.S. Ligler, and D.E. Leckband, *A Computational Reaction−Diffusion Model for the Analysis of Transport-Limited Kinetics.* Analytical Chemistry, 1999. **71**(23): p. 5405-5412.
18. Karlsson, R., A. Michaelsson, and L. Mattsson, *Kinetic analysis of monoclonal antibody-antigen interactions with a new biosensor based analytical system.* Journal of Immunological Methods, 1991. **145**(1–2): p. 229-240.
19. Myszka, D.G., et al., *Extending the range of rate constants available from BIACORE: interpreting mass transport-influenced binding data.* Biophys J, 1998. **75**(2): p. 583-94.

20. Goldstein, B., et al., *The influence of transport on the kinetics of binding to surface receptors: application to cells and BIAcore*. J Mol Recognit, 1999. **12**(5): p. 293-9.
21. *BIAevaluation software handbook*, G.H.B.-S. AB, Editor. 2008.
22. Ritzefeld, M. and N. Sewald, *Real-Time Analysis of Specific Protein-DNA Interactions with Surface Plasmon Resonance*. Journal of Amino Acids, 2012. **2012**: p. 19.
23. Hutchinson, A.M., *Evanescent wave biosensors. Real-time analysis of biomolecular interactions*. Mol Biotechnol, 1995. **3**(1): p. 47-54.
24. Homola, J., S.S. Yee, and G. Gauglitz, *Surface plasmon resonance sensors: review*. Sensors and Actuators B: Chemical, 1999. **54**(1–2): p. 3-15.
25. Campbell, C.T. and G. Kim, *SPR microscopy and its applications to high-throughput analyses of biomolecular binding events and their kinetics*. Biomaterials, 2007. **28**(15): p. 2380-2392.
26. Cooper, M.A., *Optical biosensors in drug discovery*. Nat Rev Drug Discov, 2002. **1**(7): p. 515-28.
27. Karlsson, R., et al., *Kinetic and Concentration Analysis Using BIA Technology*. Methods, 1994. **6**(2): p. 99-110.
28. *Biacore 3000* [cited 2015 May]; Available from: http://www.gelifesciences.com/webapp/wcs/stores/servlet/catalog/en/GELifeSciences-us/products/AlternativeProductStructure_11932/14110045.
29. Myszka, D.G., *Improving biosensor analysis*. J Mol Recognit, 1999. **12**(5): p. 279-84.
30. Rich, R.L. and D.G. Myszka, *Advances in surface plasmon resonance biosensor analysis*. Current Opinion in Biotechnology, 2000. **11**(1): p. 54-61.
31. Spuhler, P.S., et al., *Platform for in situ real-time measurement of protein-induced conformational changes of DNA*. Proceedings of the National Academy of Sciences of the United States of America, 2010. **107**(4): p. 1397-1401.
32. Peterson, A.W., R.J. Heaton, and R.M. Georgiadis, *The effect of surface probe density on DNA hybridization*. Nucleic Acids Research, 2001. **29**(24): p. 5163-5168.
33. Brogioni, B. and F. Berti, *Surface plasmon resonance for the characterization of bacterial polysaccharide antigens: a review*. MedChemComm, 2014. **5**(8): p. 1058-1066.
34. Sun, Y.S., et al., *Effect of fluorescently labeling protein probes on kinetics of protein-ligand reactions*. Langmuir, 2008. **24**(23): p. 13399-405.
35. Yin, L., et al., *How does fluorescent labeling affect the binding kinetics of proteins with intact cells?* Biosens Bioelectron, 2015. **66**: p. 412-6.
36. Cheow, L.F., et al., *Multiplexed Analysis of Protein–Ligand Interactions by Fluorescence Anisotropy in a Microfluidic Platform*. Analytical Chemistry, 2014. **86**(19): p. 9901-9908.
37. Yan, Y. and G. Marriott, *Analysis of protein interactions using fluorescence technologies*. Curr Opin Chem Biol, 2003. **7**(5): p. 635-40.
38. Gunnarsson, A., et al., *Kinetics of Ligand Binding to Membrane Receptors from Equilibrium Fluctuation Analysis of Single Binding Events*. J. Am. Chem. Soc., 2011. **133**(38): p. 14852-14855.
39. Karlsson, R., *Real-time competitive kinetic analysis of interactions between low-molecular-weight ligands in solution and surface-immobilized receptors*. Anal Biochem, 1994. **221**(1): p. 142-51.
40. Srisa-Art, M., et al., *Monitoring of Real-Time Streptavidin−Biotin Binding Kinetics Using Droplet Microfluidics*. Anal. Chem., 2008. **80**(18): p. 7063-7067.
41. Piran, U. and W.J. Riordan, *Dissociation rate constant of the biotin-streptavidin complex*. J. Immunol. Methods, 1990. **133**(1): p. 141-3.
42. Schasfoort, R.B.M., et al., *Method for estimating the single molecular affinity*. Analytical Biochemistry, 2012. **421**(2): p. 794-796.
43. Michael Green, N., *[5] Avidin and streptavidin*, in *Methods in Enzymology*, W. Meir and A.B. Edward, Editors. 1990, Academic Press. p. 51-67.

44. Yu, C.-J., et al., *Fiber optic biosensor for monitoring protein binding kinetics.* Proc. SPIE 5591, 2005: p. 200-208.
45. Ivnitski, D., et al., *An amperometric biosensor for real-time analysis of molecular recognition.* Bioelectroch. Bioener., 1998. **45**(1): p. 27-32.
46. Chandran, S. and R.S. Singh, *Comparison of various international guidelines for analytical method validation.* Pharmazie, 2007. **62**(1): p. 4-14.
47. Esteban Fernández de Ávila, B., et al., *Determinants of the Detection Limit and Specificity of Surface-Based Biosensors.* Analytical Chemistry, 2013. **85**(14): p. 6593-6597.
48. Hosokawa, K., et al., *Power-free sequential injection for microchip immunoassay toward point-of-care testing.* Lab Chip, 2006. **6**(2): p. 236-41.
49. Lee, K.-H., et al., *Microfluidic systems integrated with two-dimensional surface plasmon resonance phase imaging systems for microarray immunoassay.* Biosens. Bioelectron., 2007. **23**(4): p. 466-472.
50. Pereira, A.T., et al., *Heterogeneous immunoassays in microfluidic format using fluorescence detection with integrated amorphous silicon photodiodes.* Biomicrofluidics, 2011. **5**(1): p. 014102-13.

Chapter 5

One-shot kinetic assay in nanofluidic sensors with integrated concentration gradient generator

In this chapter, we propose a new generation of our cost-effective micro-/nanofluidic system with an on-chip gradient-generating system, which enables a one-shot parallel kinetic analysis. The basic concept is to exploit the real-time sensing function of our previously validated nanoslit platform for high-throughput kinetic measurements by simply embedding a microfluidic gradient generator into the device. To provide a basic comprehension of the concentration gradient generator, the underlying theoretical background regarding the transport phenomena in fluids and a literature survey of on-chip diluter systems are presented. The design and the fabrication process of the proposed device are discussed. Furthermore, we experimentally validate the gradient-generating device through fluorescence observations. Lastly, we carry out one-shot kinetic assays of mouse IgG/anti-mouse IgG interactions to demonstrate the effectiveness of our device.

5.1 Introduction

The need for cost-benefit and high-throughput kinetic measurements with rapid determination of the affinity and kinetics is essential in numerous biochemical applications. This is particularly paramount in an early stage of the drug discovery process, where large libraries of therapeutically relevant compounds are screened to select a new drug candidate against a particular disease, based on their interaction affinity and stability [1].

In traditional kinetic studies employing affinity-based biosensors, a single analyte concentration is introduced over the ligand surface and the signal response is measured in real-time. The sensor surface is then regenerated to prepare a free ligand surface for the next cycle of measurement. These processes are generally repeated until a full series of analyte concentrations is measured, which are termed as '**multi-cycle kinetics**" [2]. The kinetic constants can be determined by fitting the binding curves to an appropriate model. The classical kinetic approach has several drawbacks. In order to achieve robust kinetic data with meaningful kinetic information, 4-6 analyte concentrations are typically required. As a result the total analysis time associated with multiple reagent exchanges can reach hours to days and the materials consumed in the process is increased.

Furthermore, the surface regeneration practically becomes a profound bottleneck for high-throughput analyses [3]. The core objective of the surface regeneration is to completely remove the remaining bound analytes from the surface and to ensure that the same ligand binding sites are available for analyte binding in the next cycle. Various regeneration buffers or cocktails (usually involving harsh basic or acid solutions) are available to accomplish effective regenerated surfaces [4], however, extensive fine-tuning work is required to select a proper regeneration buffer without damaging the immobilized ligand. The regeneration step commonly succeeds when the ligand surfaces are easy to regenerate but it is not always the case for high affinity small molecule/protein interactions. In addition, the multiple regeneration cycles, resulting from non-optimized regeneration cocktails, could lead to the denaturation of the immobilized ligand and eventually cause a progressive loss in surface binding capacity. This ligand loss may induce a vast impact on the measured kinetic data due to a run-to-run variability.

In the case where it is unfeasible or impractical to regenerate the surface ligand, the "**kinetic titration series**" procedure has been established to obtain sufficient kinetic information without the need of surface regeneration between each analyte binding cycle [5], thus saving resources and increasing throughput. This approach generates a "saw-tooth" binding profile (Figure 5.1a) because of the remaining analyte molecules bound to the sensor at reaction equilibrium after each injection with increasing concentration. Despites these advantages, the kinetic titration method demands sequential injections of a series of analyte concentrations with precise timing, therefore, it cannot totally eliminate time-extensive processes as well as tedious and error-prone manual dilution tasks.

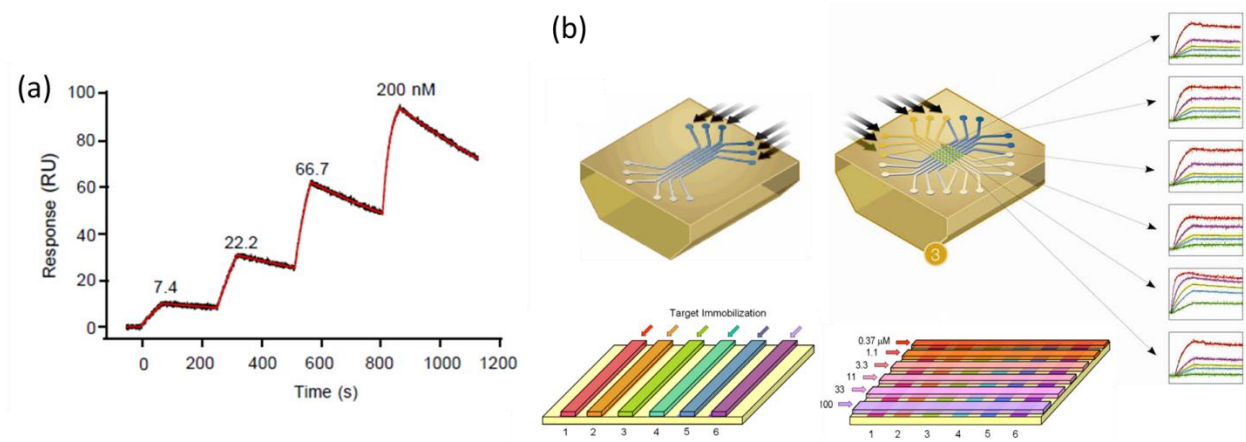

Figure 5.1 (a) A saw-tooth binding profile obtained from the kinetic titration series (from [5]). (b) Flow cell configurations of the ProteOn's crisscrossing flow path system used for one-shot kinetics (adapted from [3, 6]). After the ligand immobilization, the chip is rotated 90º for analyte injection.

Alternative to kinetic titration series, the **"parallel titration"** can be performed to measure kinetics on multiple ligand surfaces with no requirements for regeneration, as demonstrated in a flow-through ProteOn XPR36 assay system [6] (Figure 5.1b). This parallel-processing biosensor offers the benefits for rapid kinetic screening in drug discovery as well as real-time protein interaction monitoring in arrays. While this technology permits a one-shot parallel kinetic analysis, it is limited by the complexity of the orthogonal orientation of the chip and sophisticated instrumentation relying on the SPR apparatus.

Miniaturized nano-/microfluidic systems have addressed some of the challenges associated with the present bioanalytical approaches because they enable rapid biochemical assays in a highly parallel manner. This is particularly true when the number of sensors can be easily scaled up without making the system more complex. This technology offers great promise for multiplexing analysis to study the biological functions and cellular behaviors with reduced reagent consumptions and assay costs [7]. Microfluidic dilutors, allowing stable and tunable concentration gradient generations of biomolecular species at cellular length scales with spatial and temporal control, could potentially be used in applications ranging from rapid screening assays [8] to cell-based experiments [9].

As compared to the traditional macroscopic formats, microfluidic gradient generators offer higher gradient resolutions and lower time scale to transport specific dose gradients to the cells due to miniaturization of the geometrical dimensions. They also enable cell monitoring in a real-time fashion. While most studies have utilized microfluidic gradient generators to elucidate cellular signaling pathways induced by chemical stimuli gradients, chemotaxis [10, 11], and cell culture [12], **there have been a few efforts to implement this technology for one-shot parallel kinetic assays.**

In this chapter, we developed a simple and effective micro-/nanofluidic device, exploiting an outstanding capability of the microfluidic gradient generators combined with the distinctive characteristic of the nanoslits for parallel kinetic measurements. Our system enables a one-shot kinetic operation where concurrent interrogations of the biomolecular interactions with a full titration series of analyte can be handled in one single experiment using a single-analyte injection. Basically, different concentrations of analyte solutions generated from the microfluidic gradient dilutors can be injected over the sensors located on independent nanochannels, and the concentration-dependent binding can be gathered at once using a bench-top fluorescence microscope and a CCD camera.

The well-designed gradient generator offers a means to automatically generate reproducible, simply-quantified concentration gradients that are stable in space and time for biological studies. Furthermore, the gradient dilutors require only a small amount of the input solutions and avoid the use of macroscopic tools, *e.g.*, human-operated pipettes, to perform the dilutions outside the device, thus eliminating inaccuracy from manual operation. Notably, avoiding the need of surface regeneration substantially shrinks the analysis time and abolishes labor intensive tasks. High-throughput and low material consumption features make this technology very appealing for therapeutic and diagnostic applications.

To employ the microfluidic gradient generation as a tool for biological studies, one should envisage the underlying transport phenomena allowing the generation of chemical gradients across the microfluidic networks (which will be discussed in the following section). This fundamental understanding surely reaps the benefit to design and realize an effective micro-/nanofluidic system for biomolecular analysis.

5.2 Principle of transport phenomena in microfluidic gradient dilutors

Due to small dimensions of most microchannels and associated relatively low flow rates, the Reynolds number (Re) is often less than 100, and thus the fluid transport exhibits laminar flow [13]. This leverages the ability to control the fluid flow precisely and to quantify the gradients in a high accuracy manner. As a consequence of this laminar regime and because of the absence of turbulences, different fluids flowing side-by-side do not mix unlike what is observed at the macroscale, *e.g.*, in the case where we stir a cup of water added with sugar crystals to attain a homogeneous solution. Molecular mixing in a microchannel rather occurs purely through diffusion.

5.2.1 Navier-Stokes equation

Fluid flows within a microfluidic device are governed by the **Navier-Stokes equation** assuming incompressible and Newtonian fluids. This equation balances the rate of momentum change with the convective, pressure and viscous forces, and also other externally applied forces (electrical or gravitational forces) as:

$$\rho \frac{\partial \vec{u}}{\partial t} = -\rho \vec{u}.\nabla \vec{u} - \nabla P + \mu \nabla^2 \vec{u} + \vec{F} \tag{5.1}$$

$\vec{u}$ (m.s^{-1}) is the velocity field which is defined as the velocity of the fluid at a given point in space and time, ρ is the fluid density (kg/m^3), μ is the fluid viscosity (Pa.s), ∇P is the pressure gradient (Pa), and $\vec{F}$ is the external force. In the case of our gradient dilutor solely based on pressure-driven flow, the term $\vec{F}$ can be omitted from the equation. The equation can be further simplified by considering the microfluidic device with a low Re and a steady-state flow system, $\partial \vec{u}/\partial t = 0$, and the Navier-Stokes equation now becomes the **Steady Stokes equation** as:

$$\nabla P = \mu \nabla^2 \vec{u} \tag{5.2}$$

With a simplified version of the Stokes equation, we can correlate the fluid flow velocity with the pressure gradients across the channel lengths (pressure differences between the channel inlet and outlet), by solving mass transport problems by means of numerical computation or even analytical solution with given appropriate assumptions.

5.2.2 Hydraulic analogy of Ohm's law

An analytical solution of the mass transport equation, assuming an unidirectional pressure-driven flow with no-slip boundary conditions and applying a finite Fourier transformation, results in a linear relationship between the pressure difference (ΔP, Pa) and the volumetric flow rate (Q, $m^3.s^{-1}$), which is termed as the **Hagen-Poiseuille's law**.

$$\Delta P = Q R_H \tag{5.3}$$

R_H is the hydraulic resistance of a rectangular microchannel [14] ($Pa.s.m^{-3}$). In the case of a high aspect ratio channel (*i.e.*, $H/W \ll 1$), the hydraulic resistance can be approximated as:

$$R_H = \frac{12\mu L}{wH^3}, \tag{5.4}$$

where L is the channel length, W is the channel width, and H is the channel height. The hydraulic resistance and the Hagen-Poiseuille's equation are analogous to the electric resistance and the Ohm's law ($V = IR$), wherein V is the voltage (V) across the conducting material, I is the flowing current (A), and R is the resistance of the resistor (Ω). This analogy is valid when the flow is incompressible, viscous and laminar. **The analogy of the electric and the hydraulic circuits allows us to design predictive pressure-driven microfluidic networks**, particularly in the complete-mixing gradient generating devices (*e.g.*, Christmas trees), prior to fabrication without using a specialized computational fluid dynamic (CFD) model [15].

5.2.3 Convective-diffusive transport

The propagation of concentration gradients inside a rectangular microfluidic channel occurs through mass convection and/or diffusion given as:

$$\frac{\partial C_0}{\partial t} + \nabla.(\vec{u}C_0) = D\nabla^2 C_0 + R, \tag{5.5}$$

where C_0 is the concentration of a solute, D is the diffusion coefficient of that solute within a solvent, and R is the local reaction term. According to the conservation of mass, the convection-diffusion equation for solute species balances the mass accumulation rate and the convective flux $(\nabla.(\vec{u}C_0))$ with the diffusive flux $(D\nabla^2 C_0)$ and the rate of species generation (R).

The velocity vector, $\vec{u}$, from the convective term is deduced from the abovementioned Navier-Stokes equation. The net rate of specie reaction, R, is omitted from the mass transport equation of gradient generators since the chemical reactivity between the solute and the solvent is considered negligible. This is true when the biological solutes (*e.g.*, stimuli, organic compounds, and fluorescent dye) have no chemical reaction with their diluents (mostly aqueous based solutions) in a gradient formation.

For laminar flow in a straight microchannel with rectangular cross-section (Figure 5.2), the only inherent mixing mechanism is due to molecular diffusion.

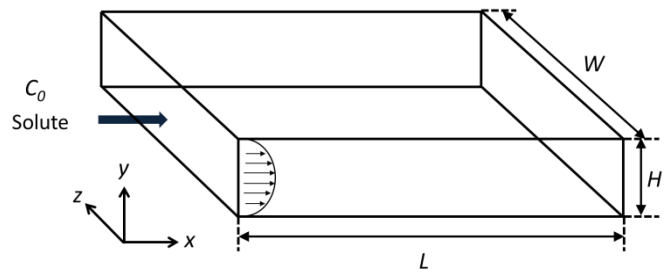

Figure 5.2 Schematic diagram of a rectangular channel with fluid flow along the channel length.

The fluid transport can be driven by the gradient of concentrations from a high concentration region to a lower concentration region as described by the Fick's first law. In a steady state, the diffusion of molecular species is characterized by the diffusion coefficient (D) as:

$$J = -D\frac{\partial C_0}{\partial x}, \tag{5.6}$$

where J is the diffusive flux or the rate of transfer per unit area of a section, and $\frac{\partial C_0}{\partial x}$ is the concentration gradient with respect to x direction. On the other hand, **Fick's second law predicts how mass transport via diffusion changes with time in a non-steady state process.** After an infinite time ($t \to \infty$), the solute molecules tend to move leading to homogenization of the concentration in a domain.

$$\frac{\partial C_0}{\partial t} = D\frac{\partial^2 C_0}{\partial x^2} \tag{5.7}$$

The solution of the Fick's second law depends on the initial and boundary conditions. In the case of a semi-infinite planar diffusion, where two semi-infinite media (*i.e.*, a solution with concentration of C_0 and pure water ($C_0 = 0$)) are brought into contact either from removing a separation wall or from a parallel injection, the solution of this diffusion problem is written in the form of the error function as [16]:

$$C(x,t) = \frac{1}{2}C_0 erfc\frac{x}{2\sqrt{Dt}}, \tag{5.8}$$

where erfc is the complementary error function, erfc z= 1-erf z. This form relates the concentration (C) at any position (x) and time (t) to the initial concentration (C_0), and the diffusion coefficient.

To describe the mass transport characteristic in a gradient generator, the Peclet number (Pe_H) is primarily employed as an indication of the relative importance of convection to diffusion. It simplifies the convection-diffusion equation in the case of the pure convective-based or pure diffusive-based transport in which the problems can be simply solved analytically [17]. Nevertheless, in the complex problems where convective and diffusive transports are comparable, the numerical methods are applied to predict the velocity and the concentration gradient formed within microfluidic dilutors [18].

5.2.4 Mixing length in gradient generators

The simplest case of fluid mixing in a microfluidic gradient generator is a **T-sensor**, wherein two streams with different specie concentrations flow alongside each other down a channel. In the T-sensor, both convective and diffusive transports take place in the microfluidic channel, however, the convective mixing (axial diffusion) is normally considered negligible as compared to the traverse diffusive mixing. This is usually true for practical concentration gradient generators that exhibit a Peclet number greater than 1. In other words, the molecular species are transported along the channel length via convection whereas the molecular diffusion occurs across the channel width (Figure 5.3).

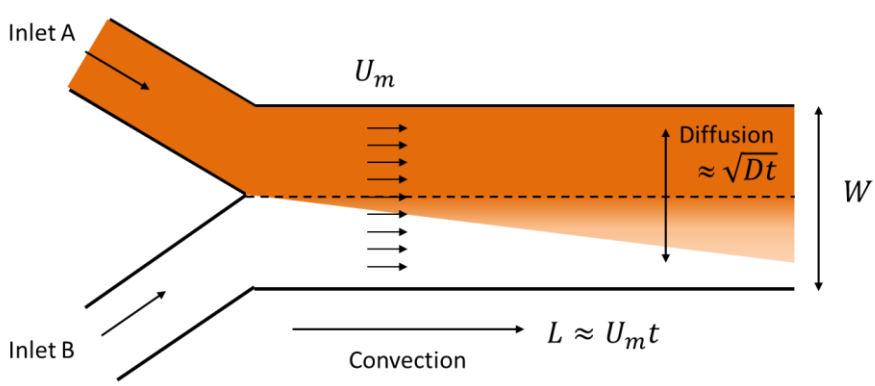

Figure 5.3 Schematic diagram of a T-sensor microfluidic channel where the diffusion of molecules between two streams flowing side by side occurs across the channel width.

Based on the relationship between the random walk distance, diffusivity and residence time, $x = \sqrt{Dt}$ [19], the mixing time required for a fully diffusive mixing (**the characteristic diffusion time**) can be written as $t = \frac{W^2}{D}$, giving that the diffusion distance is about the same as the channel width ($x \approx W$) [13]. **The minimum length (L_m) of a mixing channel required to achieve a complete mixing via diffusion**, producing a fully homogenous solution can thus be estimated as:

$$L_m = U_m t = \frac{U_m W^2}{D}, \tag{5.9}$$

where U_m is the area-averaged velocity in the mixing channel. The mixing length thus depends on the average flow velocity in the channel, the channel width, and the diffusivity of molecular species. In other words, the Peclet number dictates the length of the mixing channel needed for the complete mixing. At a high Pe_H number, a longer channel length is required to homogenize two fluid streams due to a low degree of diffusive mixing.

The estimation of this mixing length is necessary to have an idea of the microchannel length that is suitable for the gradient generation with desired concentration profiles. In our case, we used this length as an indicative limit number, particularly, because we took advantage of the **laminar diffusion-based partial mixing** to generate traverse concentration gradients. This means that the length of our microfluidic channel should not exceed the minimum length required for the complete diffusional mixing (L_m) or else there would be no concentration gradients at the output.

5.3 Gradient generator achievements up-to-date

Microfluidic concentration gradient generators offer a great promise in the study of cell biology including observation of the cell migration and proliferation responses to chemical gradients and cancer metastasis. The traditional *in vitro* techniques (Figure 5.4) including pipetting-format [20], Boyden chamber [21], and gel [22], restrict the generation of user-defined gradients with spatiotemporal distribution control, thus do not necessary elicit effective cell responses. Furthermore, these conventional assays suffer from the gradient instability arising from the accumulation/depletion in the reservoirs.

Till now, numerous configurations of microfluidic devices have been developed for generating chemical gradients that are predictable and reproducible with the ability to directly visualize the biological behaviors within cellular-mimic gradient environments. These appealing characteristics of the microfluidic devices enhance quantitative elucidation and reproducibility of biological experiments. In general, the microfluidic gradient generators can be classified into two main categories: **diffusive-based and laminar flow-based devices**.

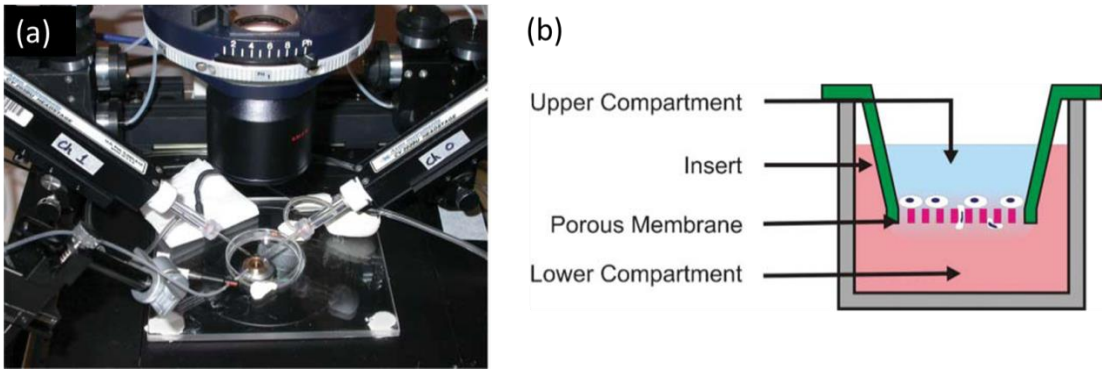

Figure 5.4 (a) Micropipette gradient generation where the signaling molecules are loaded inside a micropipette and are pneumatically injected to the cell creating a gradient. (b) Boyden chamber used to form a gradient across the membrane where cells are seeded (from [23]).

Diffusive-based generators create a static concentration gradient environment relying solely on the **molecular diffusion**. This type of system is amenable for the cellular behavior analysis because there is no sheer stress induced by the presence of the flow field to the biological cells situated at the bottom of the channels [24]. Diffusion-based gradient generators are inexpensive due to no continuous fluid replenishment. This could be beneficial for certain experiments where expensive reagents or limited reagent volume are involved. The limitations of this system include the difficulty to control the shape of the generated concentration gradients as well as a long establishing time and complicated fabrication processes [25].

On the other end of the spectrum, **laminar flow-based gradient generators** allow a rapid dynamic control of more complex concentration gradient profiles by tuning the flow rates and the geometry of the flow channels [26]. They exploit the partial molecular diffusion in the presence of a laminar flow to generate spatially and temporally stable concentration gradients over time. Despite all these attractive features, the continuous flow is not suitable for the free-moving cell experiments because cells exposed to the shear flow tend to change their motility [27].

In the following part, the state-of-the-art microfluidic gradient generators, based on diffusive- and convective-based devices, will be reviewed together with their applications for kinetic assays**. In our work, we chose the laminar flow-based gradient generator to integrate into the nanofluidic biosensors** as it was easy to implement and fabricate. Furthermore, it also allowed a better control of the gradient profiles.

5.3.1 Diffusion-based gradient generators

The concentration gradients produced by this approach are built-up by purely molecular diffusion between a high concentration source and a low concentration sink (Figure 5.5). The underlying principle is to prevent the convective fluid flow, by employing microchannels with a high fluidic resistance, porous membranes, or hydrogels, while permitting solely diffusion phenomenon to establish the gradient of chemical concentrations.

Saadi *et al.* [28] have designed a one-dimensional diffusion-based gradient generator in a ladder-like microchannel to leverage on the cell migration in flow-free channels. This device was composed of two parallel microchannels acting as the source and the sink which were connected by an array of microgrooves (shallower channels). Due to a high resistance of the microgrooves, the bulk fluid flow was restrained in the main channels while the diffusion was the prevalent transport in the microgrooves where the gradients were formed. In this configuration, a symmetric design of the ladder chamber was indispensable to provide sustained chemical gradients by a pressure balance.

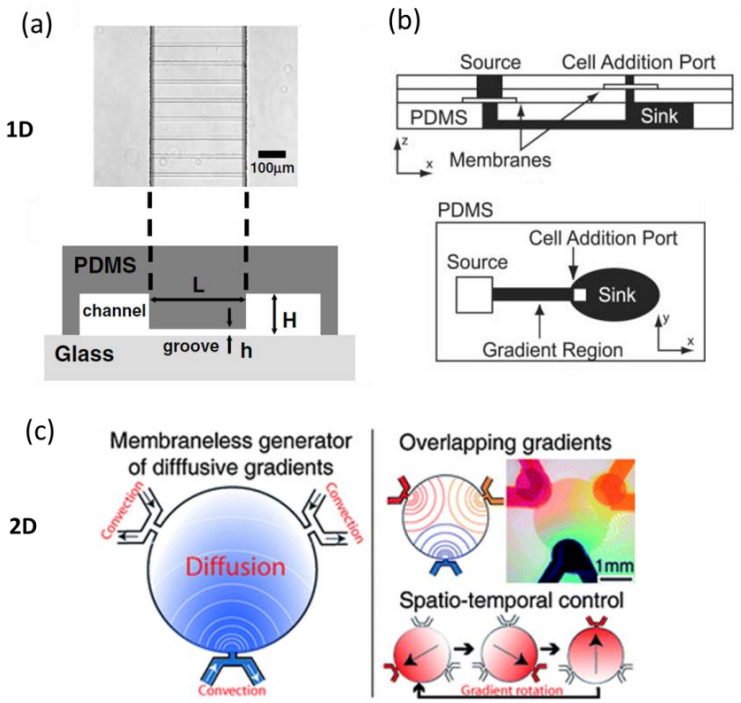

Figure 5.5 (a) A ladder-like microchannel, employing a high fluidic resistance of microgrooves to establish the concentration gradients via pure diffusion, used for neutrophil chemotaxis studies (from [28]). (b) A simple flow-free gradient generator composed of reservoirs of a source and a sink isolated from the gradient region by high fluidic resistance porous membranes (from [29]). (c) A 2D circular chamber generating the gradients by the pressure balance among three access source and sink ports (from [30]).

Atencia and co-workers [30] have developed a more rapid means to generate concentration gradients on a 2D circular chamber through a balance of the pressure between three access ports, serving as sources and sinks. By periodic switching of these access ports, the concentration gradient in the chamber was formed and established in a time scale of 15 min. Furthermore, hydrogels acting as a convective flow barrier can be incorporated into the microchannel to generate gradient hydrogels. Hydrogel scaffolds containing extracellular matrix (ECM) proteins recreate real tissues-like environments *in vitro* and they are ideal for investigation of the cell migration and cell culture in response to specific chemical gradients, such as growth factors [31] (Figure 5.6).

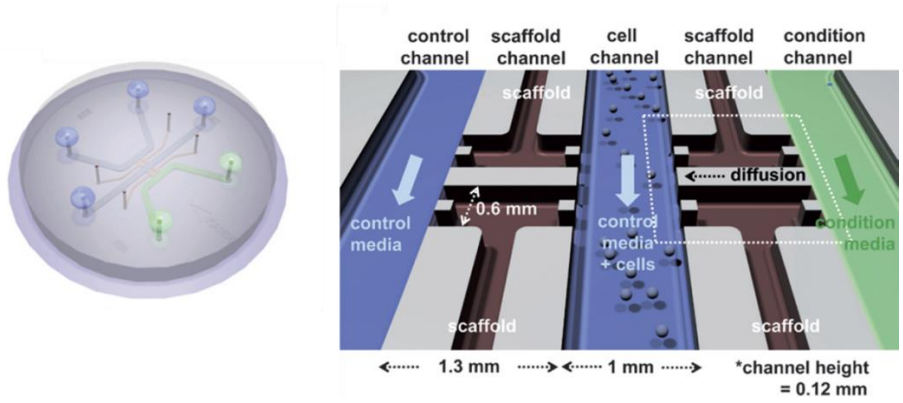

Figure 5.6 A schematic of a microfluidic device used in cell migration assays under a gradient of growth factor. This microfluidic cell composed of three flow microchannels separated by collagen hydrogel scaffolds between each other. The cells were cultured in the center and the stimuli agents in the condition channels diffused toward the cell channel, forming a gradient (adapted from [31]).

The major drawback of the flow-free gradient generation techniques is the lack of a dynamic control of concentration profiles. To unravel this problem, many attempts to integrate active valves into diffusion-based gradient devices have been done, enabling more precise manipulation of the chemical gradient distribution [32, 33]. This approach also includes "**microfluidic multi-injector**", exploiting the on-chip valves for pulsatile solution release with an exact time and volume into the chamber for a temporal control of the gradient distributions.

5.3.2 Laminar flow-based gradient generators

Unlike diffusion-based devices, flow-based gradient generators provide more tunable and wider ranges of concentration profiles including linear, logarithm and superimposed profiles. The desirable gradients stabilize faster as compared to the diffusion-based systems and they can be maintained over long assay periods as soon as the convective flow is constantly preserved. The flow-based gradient generators rely on fluid streams, composed of different chemical species or concentrations that are brought into contact in a laminar flow fashion within a microchannel. The chemical species are allowed to diffuse across the interface as they flow downstream. The laminar flow-based devices can be divided into two sub-categories: **a complete-mixing and a partial mixing**.

The most common design of the **complete-mixing gradient generators** with a pre-mixer microchannel network was first introduced as the "**Christmas tree**" by Jeon *et al.* [34]. Different solutions are introduced at the inlet streams on top of a pyramid network and the fluid streams are repeatedly split and mixed through serpentine networks. They are then recombined to produce multiple streams of concentrations with different portions of the chemical species from the input. At the end of the network, theses streams are merged into a single wide microchannel to yield the desired gradient distributions.

Based on this basic Christmas tree design, several gradient generators were developed to realize more complex concentration shapes ranging from linear [35], polynomial [34], and periodic [36] (Figure 5.7a). This was done by tuning the configuration of the input ports and varying the input flow rates. These types of microfluidic devices have been widely used in cellular studies including chemotaxis [37, 38], drug screening [39], and on-chip sensors such as immunoassays [40]. Campbell and Groisman [41] have improved the aforementioned splitting-and mixing architectures by modifying the length of the vertical serpentine channels (hence the flow resistances) to make more well-controlled mixing ratios and reduce the network stages (Figure 5.7b). This allowed the generation of monotonic concentration profiles with diverse shapes such as exponential and double-parabolic profiles while keeping the network relatively compact.

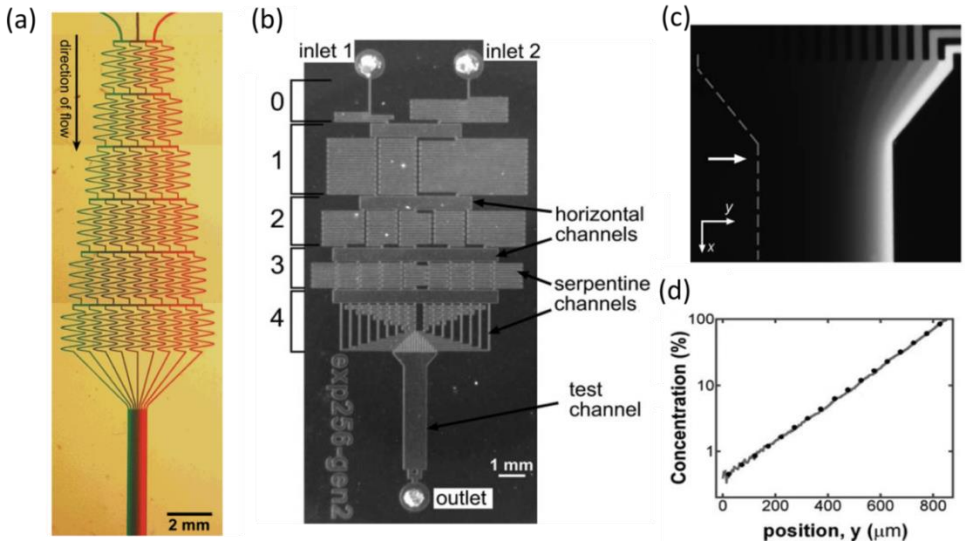

Figure 5.7 (a) A photograph of the microfluidic device used for gradient generations, based on splitting-mixing networks [36]. (b) A micrograph of the microfluidic platform for the generation of an exponential concentration gradient profile. (c) A fluorescence image showing FITC distributions in the test channel. (d) A plot of the concentration of FITC as a function of the position across the test channel showing a concentration exponential profile (adapted from [41]).

Another attractive microfluidic gradient generator involves an on-chip serial dilution, employing stepwise dilutions to reduce the concentration of the sample through successive dilutions in the *N* cascaded-mixing stages (Figure 5.8a). In this manner, stepwise linear, 2-fold, and Gaussian concentration profiles can be achieved [42]. This method is capable of generating arbitrary output flow rate gradients, which is conceivably appropriate for some specific applications such as flow rate dependent assays. However, this network requires long diffusive mixing channels for the complete mixing within a low flow rate scheme, thus limiting miniaturization of the operative devices.

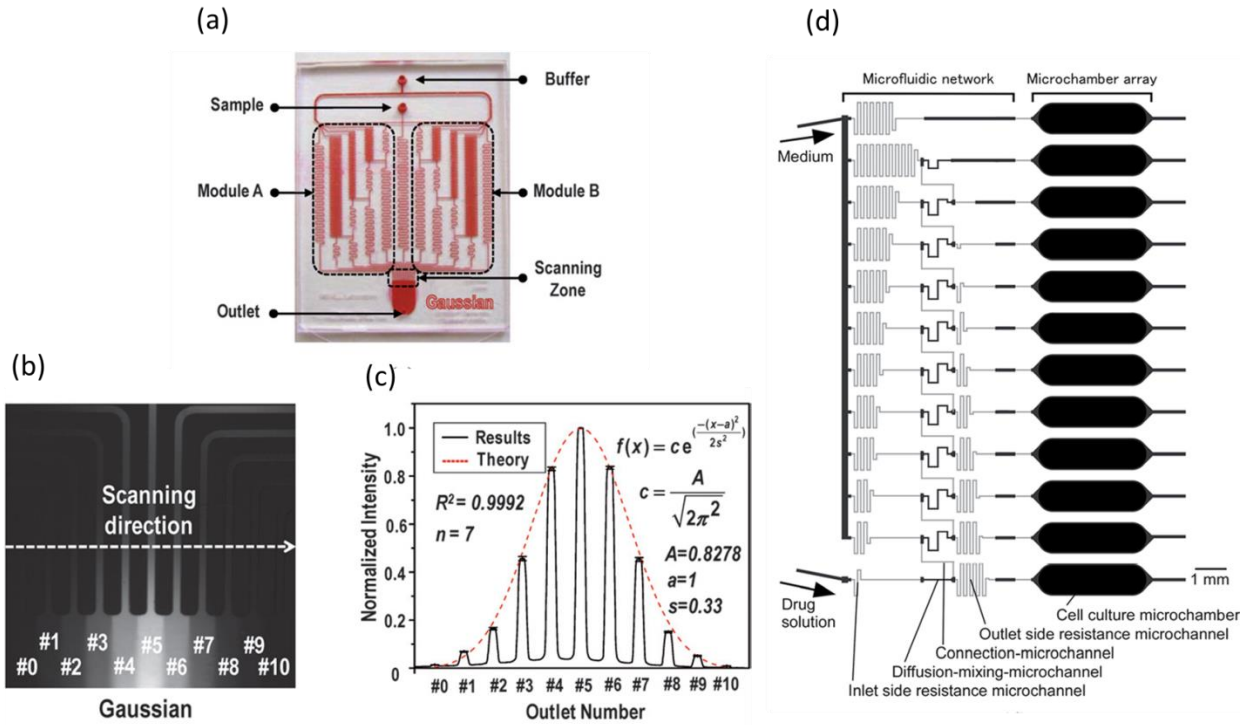

Figure 5.8 (a) An image of the fabricated serial dilution device comprised of N cascaded mixing stages for monotonic and arbitrary gradient generations. (b) A fluorescence image of the FITC distribution. (c) The intensity profiles for a Gaussian concentration profile (from [42]). (d) The serial network comprised of different cross-sectional channels (from [43]).

An alternative and more compact on-chip serial dilution was demonstrated by Sugiura *et al.* [43] (Figure 5.8d). The thin resistance microchannels and thick diffusion-mixing microchannels, allowing a long residence time for sufficient mixing, were utilized in their configurations. This method provided a wide range of concentrations spanning up to 6 orders of magnitude, which could be beneficial for dose-response evaluations as well as high-throughput drug screening and optimization. The applications of the serial microfluidic networks are prevalent ranging from SERS-based immunoassays [44] to cell perfusion experiments [45].

The above complete-mixing based microfluidic generators are often bulky and prone to leakage and clogging with a large accumulated dilution error from their previous dilution stages. Furthermore, the performances of gradient generators are dictated by a highly precise flow control from the external pumps as the desired concentration profiles are extremely sensitive to the volumetric flow rate ratio between buffer and sample solutions at the inlets.

While the complete-mixing is desirable for most bio-related applications, **partial-mixing based gradient generators** such as **Y-type** or **T-type** networks are simpler in design and fabrication, enabling a steady-state concentration gradient formation perpendicular to the flow field (Figure 5.9). The parallel-flow T-shape configuration consists of two input channels that merge into a single main mixing channel and multiple outputs, depending on the user-defined applications. The diffusion magnitude is strongly dependent on the residence time between the adjacent input streams, which is controlled by regulating the input flow rates and the geometry of the mixing channel. On the other hand, the shape of the gradient can be dynamically modulated by the choice of branch flow rates and the solution concentrations.

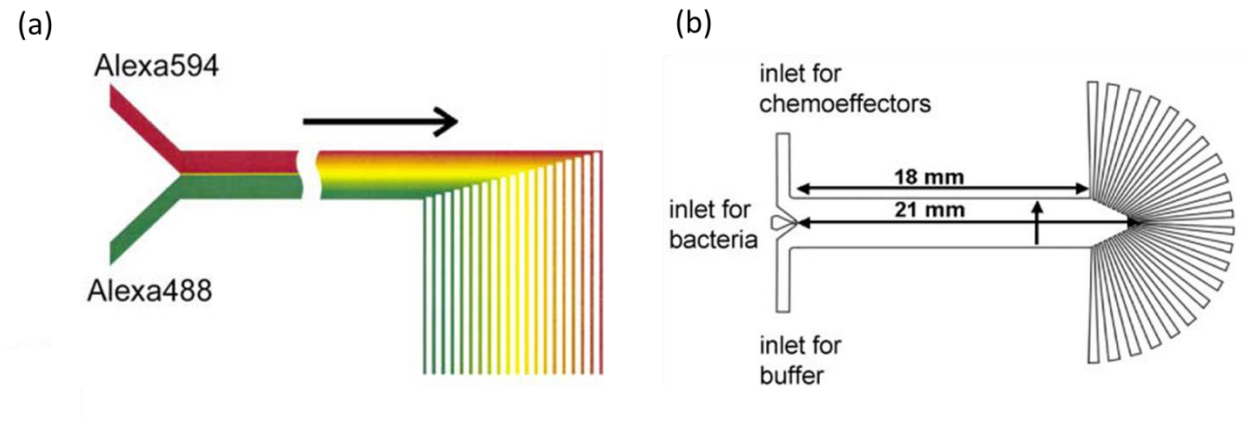

Figure 5.9 (a) A Y-shape laminar microfluidic diffusion dilutor comprising of two analyte inputs splits into an array of parallel channels (from [46]). (b) A T-type microfluidic network used in the chemotaxis assays (from [47]).

Despite the simplicity of the T-shape dilutor, the obtained concentration profile across the channel only exhibits a characteristic sigmoidal shape whose steepness depends on the flow speed and the position along the channel. The T-type microfluidic networks (more commonly known as T-sensor) have been previously utilized to perform biological assays such as enzyme kinetics [48] as well as to determine the chemical concentration and the molecular diffusion coefficient of bimolecular species [49].

5.3.3 Gradient generators for kinetic analysis

The most advanced optical biosensor technologies, such as SPR, can only interrogate a single analyte stream in a single experiment, thus limiting the number of binding interactions being studied. To address this limitation, Ouellet *et al.* [50] have developed a SPR imaging format, combining 264 element-addressable chambers (10 μm deep) with a microfluidic dilution network, in order to simultaneously probe multiple binding events with up to 6 different analyte concentrations in one single experiment (Figure 5.10). The developed dilution network accommodated the chaotic advection micromixers which were adapted from the previous work [51], leading to the generation of the concentration gradients with a dynamic concentration range of 32. They demonstrated the utility of this device to acquire the kinetic information of an anti-IgG/thrombin binding in a parallel fashion.

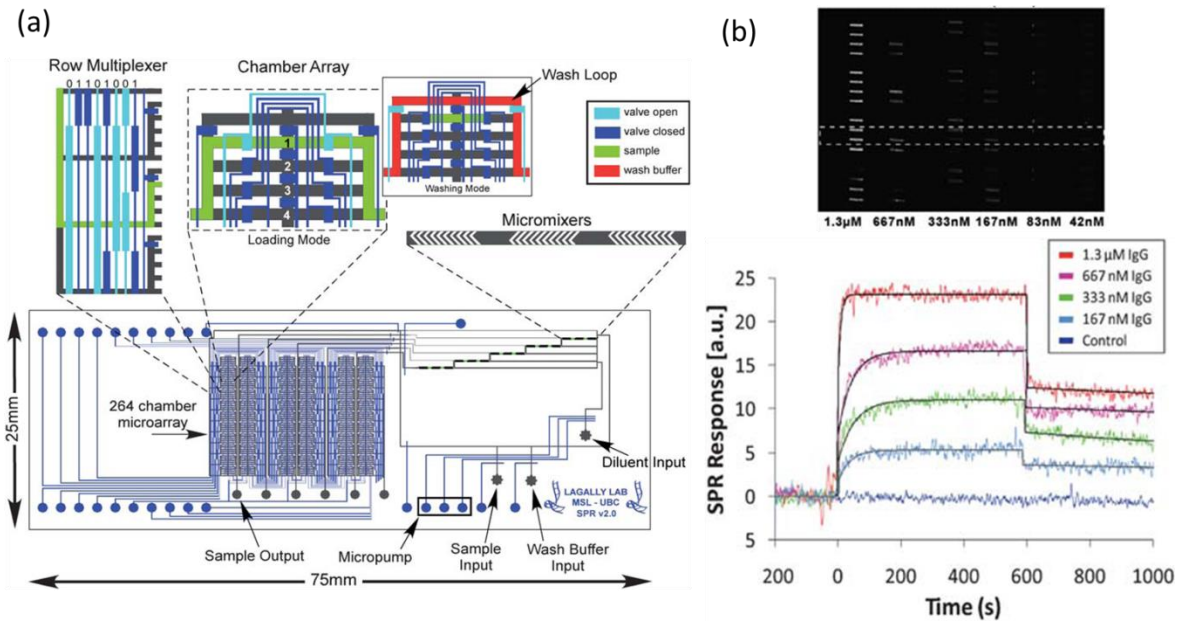

Figure 5.10 (a) A design of the microfluidic device consisting of 264 separate addressable chambers isolated by microvalves and combined with a dilution network. (b) SPRi sensorgrams at varying analyte concentrations created by the dilution network (from [50]).

While this technology facilitates high-throughput and parallel binding kinetic measurements in a single-experiment, the use of chaotic advection micromixers is laborious in layout and fabrication. In addition, it necessitates a high level of washing loops, microvalve and pump systems, which in turn renders the operation protocol expensive and complicated to be implemented. Another example of a microfluidic device exploiting concentration gradient generations and based on droplet formation and laminar diffusive mixing, was reported by Bui *et al.* [52]. Despite its application for in-situ enzyme kinetic measurements, this device merely allowed the generation of a linear concentration profile, thus limiting its usage for relevant kinetic studies.

From latest achievements of microfluidic gradient generators for kinetic analysis stated above, there is still plenty of room for improvement and eventually development of a more simple and effective device that allows reaction kinetics of multiple binding events to be probed in a parallel fashion. In this framework, we propose to incorporate a concentration gradient generator to the biofunctional nanoslits for one-shot parallel kinetic studies. The imperative requirements needed for the device to generate meaningful kinetic data and the concept of our approach will be presented in the following section.

5.4 Requirement of microfluidic gradient generator-incorporated nanoslit system for kinetic study

The main requirements of an on-chip dilutor nanoslit platform for studies of protein binding kinetics can be listed as follows:

- The gradient generation system should produce a concentration range of approximately 2 orders of magnitude ($0.1K_D$ -$10K_D$), a typical range for kinetic studies.
- The time required to establish a stable gradient should be as short as possible to enable the observation of the initial association phase of the kinetic reactions.
- The gradient has to be stable and controllable during a time span of kinetic experiments (typically in a range of 5-15 min). This is particularly important to achieve robust and accurate kinetic information of the observed protein interactions.
- The flow velocity at each output should be the same and constant to permit accurate quantification of kinetic parameters within the gradient. It is necessary that all sensors situated at each nanoslit are exposed to an identical flow speed of the target solutions.
- The dilution network integrated to the nanoslit system should allow an in-situ functionalization and a reversed-buffer flow operation.

All abovementioned concentration gradient generators are often suitable for end-point biological assays because they usually require some time to establish a stable concentration gradient. Here, **we employed a simple Y-shape dilutor to generate partial-mixing concentration gradients resulting in a suitable concentration range for protein kinetic studies.** Using a well-tuned flow velocity and an optimized characteristic length, this method provided reasonably rapid gradient establishment which allowed kinetic reactions to be measured in real-time, particularly, at the beginning of the binding reaction. This time scale was important as the sensor response should be monitored under a constant analyte concentration, which was a prerequisite for accurate determination of the kinetic parameters by means of an analytical model.

5.5 Device concept and design validation

In this present work, we incorporate a Y-type microfluidic dilutor with the previously validated nanoslit platform, enabling rapid generation of stable concentration gradients and allowing kinetic assays for different target concentrations to be carried out simultaneously. To this end, we designed the device with respect to those requirements stated earlier and we validated this design by means of finite element simulations.

5.5.1 Chip design

The chip dimensions were 16×16 mm^2 resulting in 16 individual chips on a 100 mm silicon wafer (Figure 5.11). Each chip composed of three main components: (1) a Y-shaped microfluidic gradient network, referred as a main microchannel for the generation of sample concentration gradients, (2) nanoslits used for kinetic studies, and (3) a microchannel used for in-situ functionalization and reversed-buffer flow operation. In principle, we introduced a buffer solution in one inlet of the Y-shaped microchannel and a sample solution with the maximum concentration for kinetic studies in another inlet. The Y-shape microchannel allowed two confluent streams of liquid to be combined at the junction and diffusively mixed in the main channel as they flowed downstream side by side. The geometry of the main microchannel was designed according to the desired concentration gradient profiles with respect to applied pressures or flow velocities (which we wanted similar to the ones used in the previous kinetic experiments presented in Chapter 4). The dimensions of the main microchannel were 10 μm in height, 2.8 mm in length, and 750 μm in width. This 10 μm deep microchannel was previously employed in a typical T-sensor to diminish the artifacts due to the parabolic velocity profile, inducing the non-uniformity of diffusing analytes across the channel height (known as the "**butterfly effect**") [53].

To obtain the concentration gradients at the output, we needed to ensure that the designed channel length of the main microchannel did not exceed the minimum length (L_m) needed for two liquid streams to completely mix via diffusion. L_m required for complete mixing across the channel width (750 μm) for molecules with a diffusion coefficient $D = 1\times10^{-11}$ m^2/s (for a 150 kDa protein) and a fluid flow velocity U_m = 7 μm/s, can be estimated to be 394 mm ($L_m = U_m W^2/D$). With our designed channel length (2.8 mm), the two solutions streams do not completely mix to a homogeneous solution and the concentration profile of the diffusive species still meets our requirements in terms of the concentration range at the output (see the simulation results in the following section).

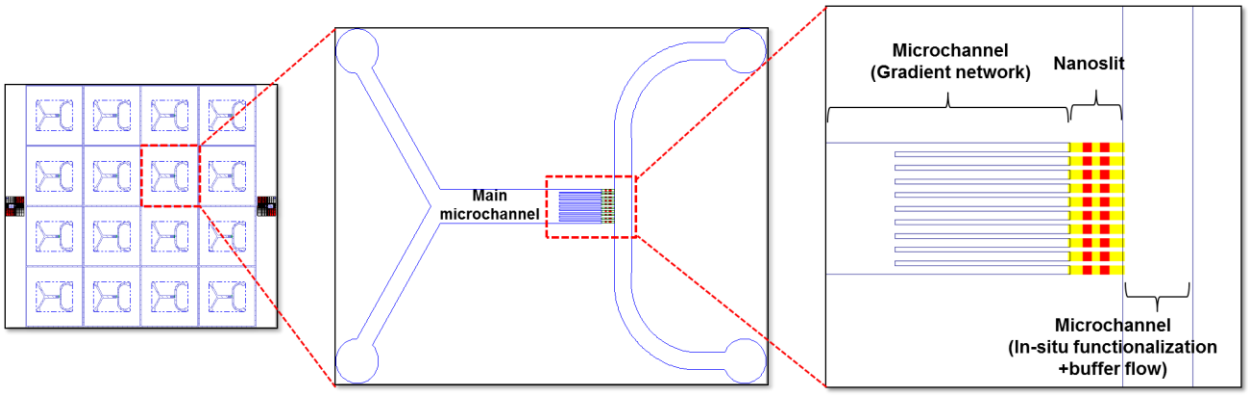

Figure 5.11 Design of the gradient devices. A sketch of the 100 mm silicon wafer pattern contains 16 individual chips whose dimensions are 16 × 16 mm^2. Each device consists of a main Y-shape microchannel network with 10 separated outputs wherein each of them is linked to a nanoslit. Two sensor patches are situated on the bottom of each nanoslit. The output microchannel on the right side of the design serves as the input channel for nanoslits functionalization and it is also used during the reversed buffer flow operation.

After a fixed distance of 2.8 mm downstream, the main microchannel was partitioned into a series of 10 parallel narrow microchannels to permanently separate distinct sample concentrations that emanated from the main flow stream before entering the nanoslits. The width of these narrow microchannels was designed to be the same as that of the nanochannels (50 μm) and as a result the length was set to induce homogeneous sample concentrations at their outputs. This length scale was vital because the sample solutions that flowed in the output microchannels were not homogenous along the 50 μm width and thus a sufficient distance was needed to completely mix the sample streams in order to produce homogeneous solutions. This distance was strongly dependent on the applied flow velocity. The importance of this narrow microchannel length to generate separate homogenized sample solutions at the outputs is shown in the following section (design validation with finite element simulations). Furthermore, we designed the Y-shaped microfluidic gradient network to be symmetrical in order to guarantee the same flow velocity at all outputs, which was indispensable for parallel kinetic measurements.

For the kinetic study aim, each microchannel conveying different concentrations of target solutions was linked to a nanoslit embedding two square gold patches. The dimensions of the nanoslits and the gold sensors were similar to those of the fabricated device presented in Chapter 3, except that the nanochannel length was reduced to 300 μm. Another 400 μm wide microchannel was joined to all nanochannels to serve as the outlet as well as to enable the in-situ surface functionalization and the reversed-buffer operation during the dissociation phase. The total area of

10 nanochannels covered about 750 × 350 μm^2. As a consequence a 10X microscope objective was utilized to conveniently observe kinetic reactions in all channels within the same field of view.

5.5.2 Design validation with finite element simulations

To optimize and validate the design of our gradient device prior to fabrication, we directly exported the gradient dilutor geometry drawn in AutoCAD to COMSOL Multiphysics in order to predict the gradient of concentrations generated at the output channels.

We built a 2D model of the Y-shape microchannel structure only (excluding nanochannels) using a Creeping flow physical module (Stokes flow) with incompressible flow by neglecting the inertial term from the laminar flow equation. We also assumed a shallow channel approximation by taking the effect of the boundaries that are usually excluded in a simple 2D laminar flow model. This gave rise to a flat velocity profile in the middle of the channel (with velocity variations very close to the channel walls) covering a region of 10 μm, *i.e.*, approximately the channel thickness (Figure 5.12). This flat velocity profile is commonly observed in rectangular cross-section channels with low aspect ratios ($H/W < 1$).

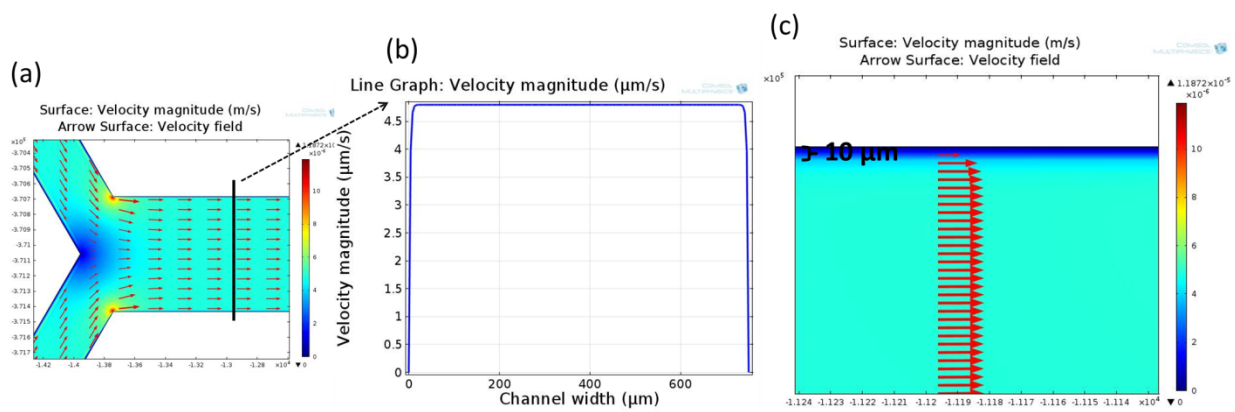

Figure 5.12 (a) A 2D flow velocity field obtained from the COMSOL modeling. (b) A flow velocity plot across the channel width. (c) A zoom-in 2D velocity field close to the channel wall. A color map indicates the local velocity magnitude.

The calculated velocity field was then used as an input for obtaining the output concentration gradient using the transport of diluted species interface. The input concentrations at the Y-junction inlets were 0 mol/m^3 (for the buffer solution) and 12 mol/m^3 (for the concentrated sample solution), and the diffusion coefficient of an IgG (1×10^{-11} m^2/s) was directly applied to precisely envisage the real conditions of the kinetic experiments.

The applied pressure was calculated using the total resistance of the fluidic device comprising the microchannel and nanochannel network in order to obtain the actual flow rate in the final device. We varied the applied pressures in the two inlets while keeping the pressure at the outlet to 0 to investigate spatial concentration profiles at the outputs. A triangular mesh size of 20 μm was employed for all domains except at the channel walls where a finer mesh size of 5 μm was created to obtain more accurate results (Figure 5.13). The numerical solution was obtained using the stationary model.

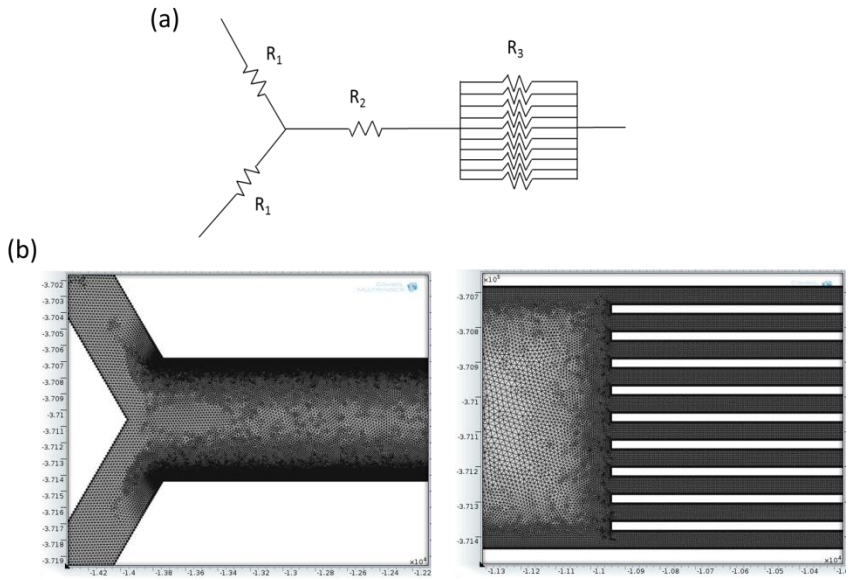

Figure 5.13 (a) A simplified electrical circuit of our gradient generator network used for hydrodynamic resistance calculation. (b) 2D mesh geometries built in the simulation model.

The concentration profiles obtained from the 2D model (Figure 5.14) show that the chemical species diffuse across the channel width. The numerical computation resulted in the generation of a concentration gradient at the output channels in the range of 0.013 – 12 mol/m^3 for an applied pressure of 4.6 Pa at each inlet. The plot of concentration across the channel width at a fixed distance downstream (black lines in the main channel) shows a characteristic sigmoidal diffusion curve which typically can be solved using an analytical model based on the diffusion of semi-infinite media as described earlier (equation 5.8).

On the other hand, the plot of the concentration profiles within distinct parallel narrow microchannels (red lines in the narrow channels) shows that the concentration of the sample solutions is not uniform across the 50 μm width near the entrance of these separated microchannels. However, once the liquid moves toward the outlets (with a given distance of 1 mm), the solutions are completely mixed and stabilized, resulting in flat concentration profiles for all channel outputs.

This device validation thus underlines the importance of an adequate length of the narrow microchannel needed to achieve well isolated homogenized concentrations suitable for kinetic studies downstream.

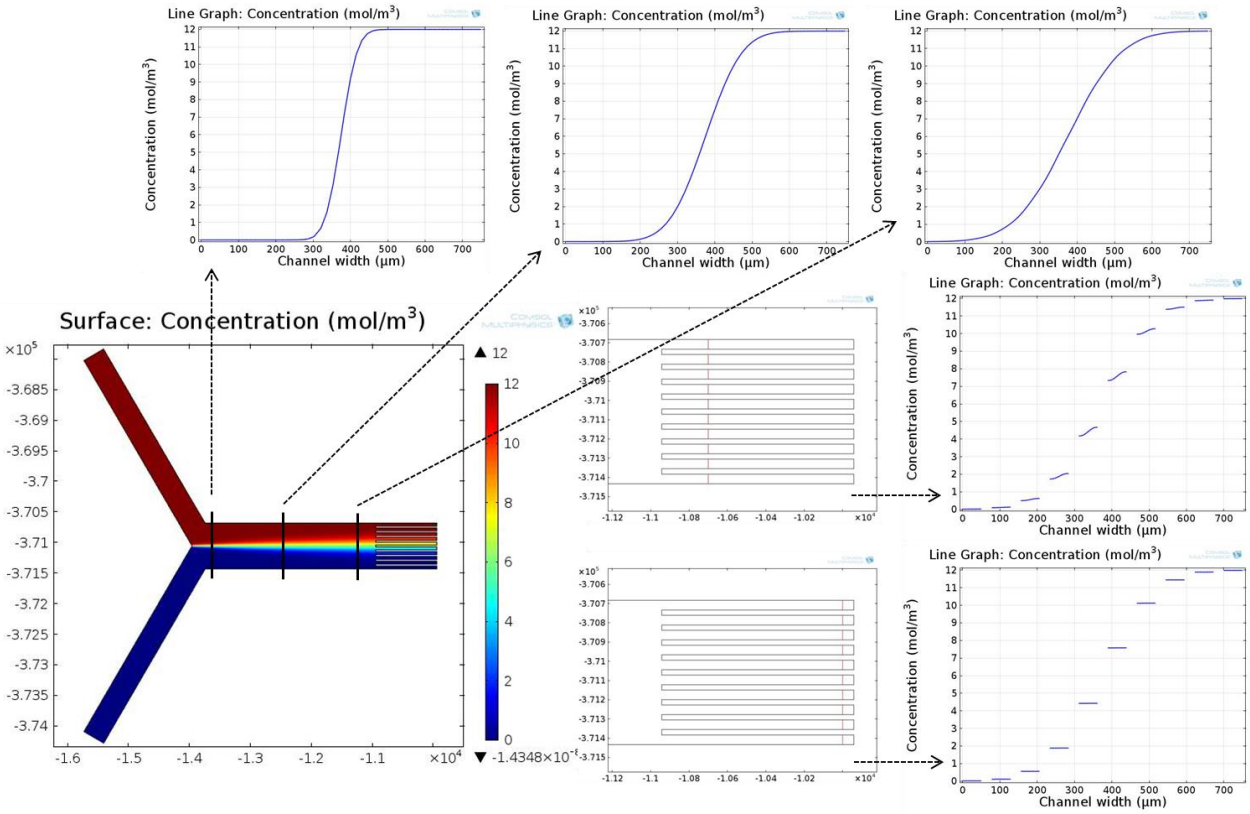

Figure 5.14 Concentration profiles inside a gradient microfluidic device at different positions downstream obtained from a stationary study in the 2D modeling. A color map indicates the local concentration of the sample.

From Figure 5.15, the flow velocity across the channel width is minimized at the stagnation point (Y-junction), where the two inlet channels encounter due to the corner effect, and it increases rapidly until the flow is fully developed when the fluid moves downstream. A normal flat velocity profile is observed in the main microchannel as expected for a thin and wide rectangular channel. Close to the entrance of 10 narrow microchannels, the velocity profile is again distorted due to the corner effect at the interface between the main and narrow channels. The velocity profile is finally stabilized in each narrow channel having the same velocity magnitude (7.0 μm/s), except for the first and the last channels whose velocity are slightly lower (6.9 μm/s).

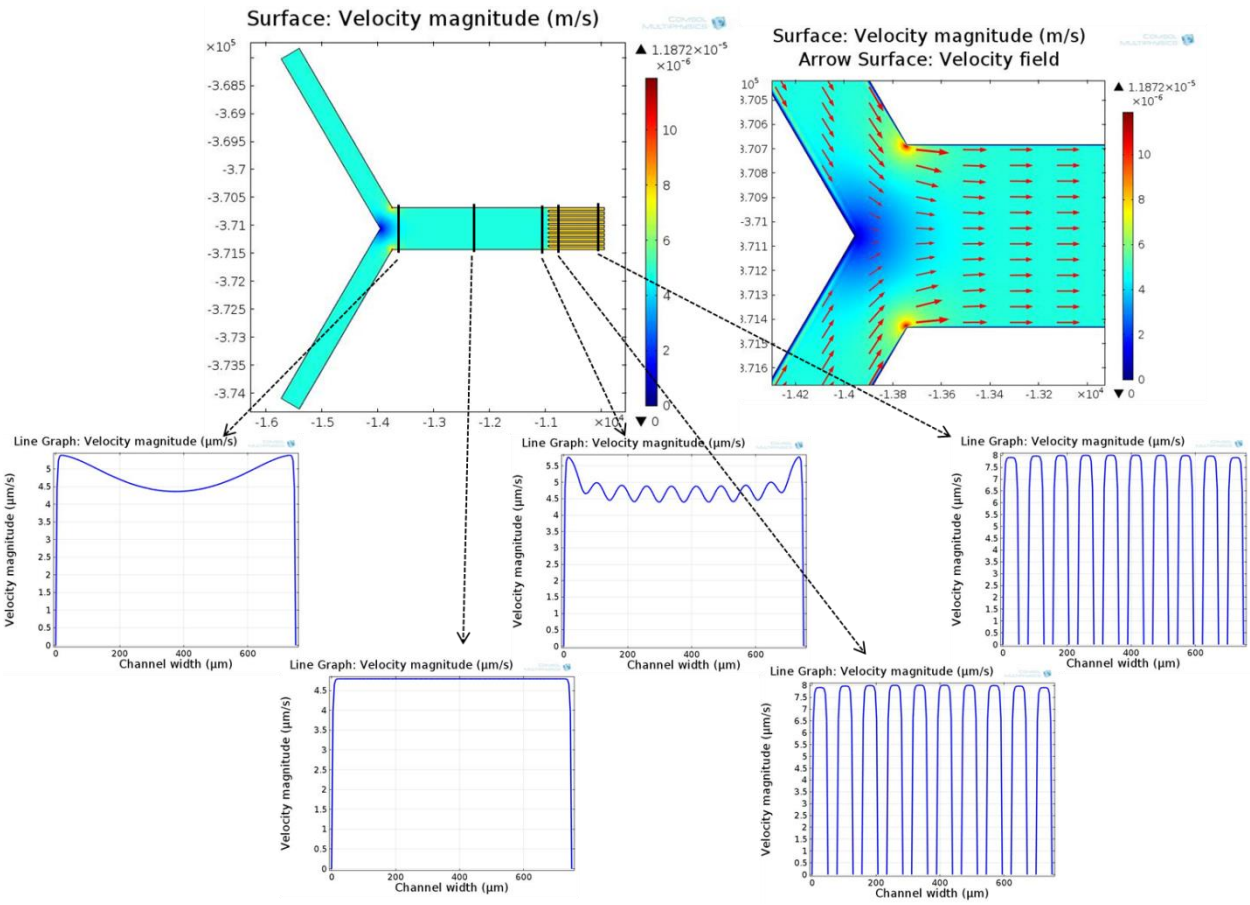

Figure 5.15 Velocity profiles inside a gradient microfluidic device at different positions along the channel length obtained from stationary study in the 2D modeling.

The flow velocity has a major influence on the steepness of the output concentration gradient profile wherein a wide sigmoidal concentration profile is obtained at a low flow velocity. Nevertheless, too high a flow velocity can lead to non-homogeneity of the sample solutions at the exit as they do not experience enough residence time to mix while flowing along the narrow microchannels. Hence, **there is a tradeoff between the concentration range generated from the gradient device and the homogeneity of the sample solution.**

Still, the simulation results showed that with the selected geometry and inlet pressure, our Y-shape microfluidic dilution network enabled gradient generation with a range of concentrations spanning approximately two orders of magnitude, and all channel outputs possessed virtually identical flow velocities, thus partially validating our microfluidic gradient design.

5.6 Device fabrication

The concentration gradient generator-integrated nanoslit devices were fabricated using standard photolithography and dry etching techniques as described in Chapter 3. The schematic diagram of the device fabrication and associated SEM images are shown in Figure 5.16 and Figure 5.17, respectively. The chip packaging and device bonding were also similar to those described in Chapter 3.

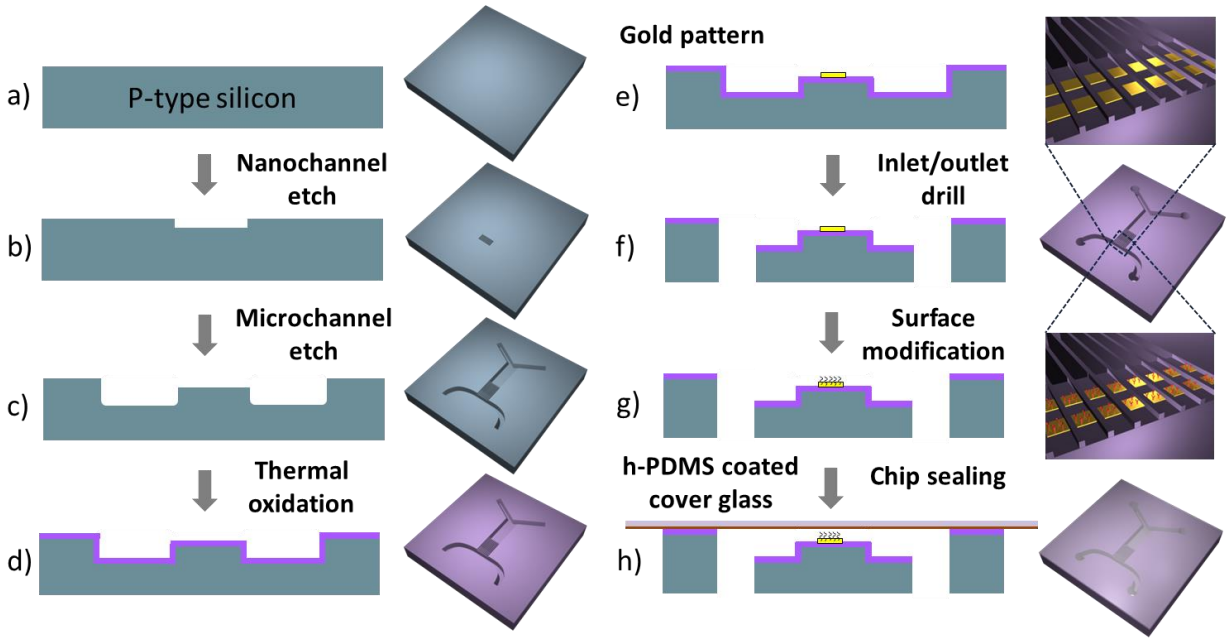

Figure 5.16 A schematic diagram of the fabrication procedures for gradient generator-integrated nanoslit devices.

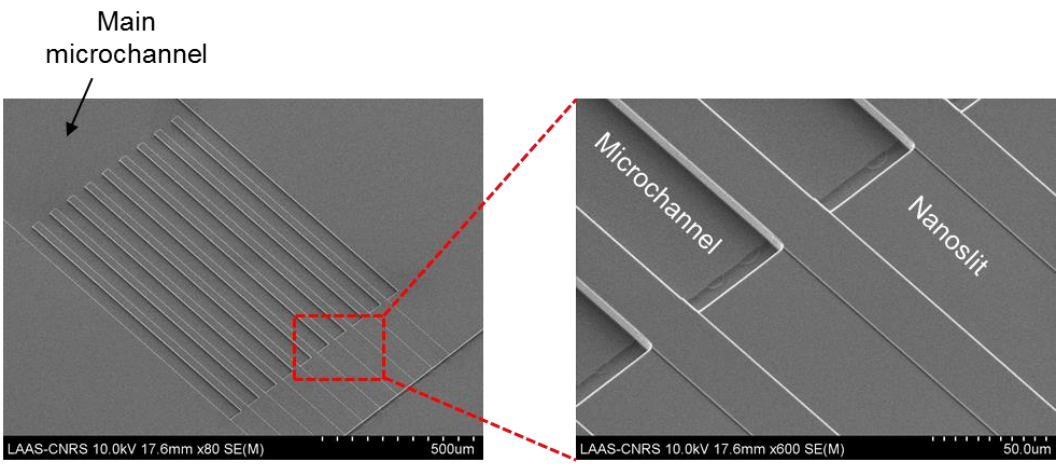

Figure 5.17 SEM pictures of the etched channels.

5.7 Experimental validation of the concentration gradient generator

To validate the efficiency of the dilutor for generating accurate concentrations of a target solution in the gradient channels, we utilized fluorescent molecules to visualize the local concentration by means of fluorescence microscopy.

5.7.1 Fluorescence calibration

Prior to conducting the experiment with the fabricated on-chip dilutor, we should know how the measured fluorescence intensity correlates with the fluorescently labeled analyte concentration (Alexa Fluor-647 conjugated mouse anti-rabbit IgG, mIgG-AF 647). This would allow an accurate quantification of the target concentration within the gradients. To this end, we sequentially injected different solutions of mIgG-AF 647 ranging from 0 to 20 nM to the same fluidic chip. This concentration range corresponded to the one used in kinetic assays of the anti-IgG/IgG interaction. The fluorescence signals of microchannel areas filled with various analyte concentrations were recorded using an inverted fluorescence microscope and a CCD camera.

The average fluorescence intensities of 10 different regions of interest located in the main microchannel (35 μm × 35 μm) were obtained with associated standard deviations, and they were subtracted with the background fluorescence (a microchannel filled with the buffer solution). A standard curve correlating the measured fluorescence intensity with the fluorescently labeled IgG concentration was plotted (Figure 5.18), showing a linear relationship (R^2 = 0.9975) within the investigated concentration range (0-20 nM).

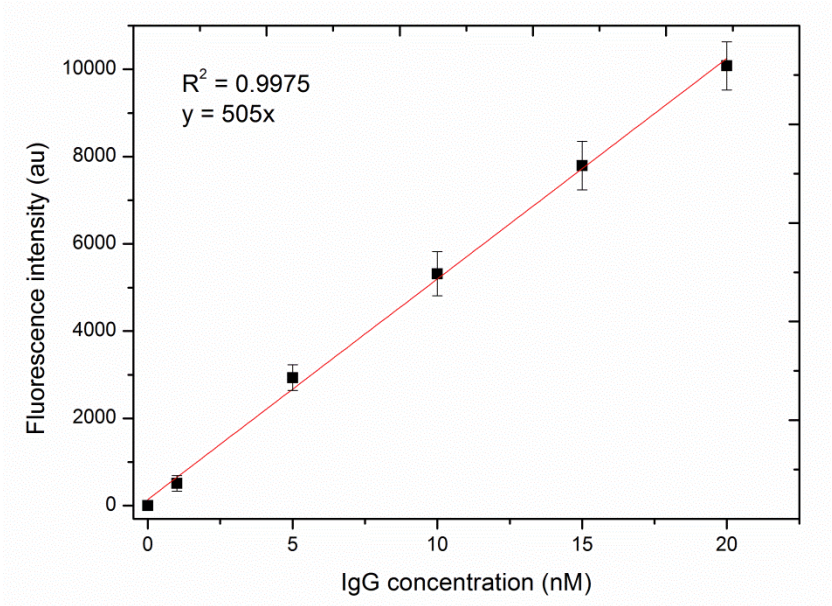

Figure 5.18 A calibration curve correlating the fluorescence intensity of fluorescently labeled IgG with the concentration ranging from 0-20 nM, showing a linear relationship.

It is worth to mention that we did not use this calibration curve to directly determine the target concentration for each experiment because there could be any intensity variations arising from day-to-day experimental conditions. Instead we exploited this linear relationship to correlate the fluorescence intensity measured from the gradient outputs with that of the known target concentration close to the inlet of the chip.

5.7.2 Concentration gradient visualization

Once completing the fluorescence intensity calibration, we experimentally validated the on-chip generation of concentration gradients through fluorescence observations. The schematic diagram of the experimental setup is shown in Figure 5.19. **The key prerequisite for creating a stable concentration gradient using the Y-type gradient network was to maintain the pressure equilibrium between two feeding streams (sample and buffer) at the inputs.**

As the nanochannels displayed an extremely high fluid resistance (~1000 times) with respect to the Y-shape microchannel network, the fluids tended to undergo a backflow which pushed the liquid back into one of the inlet reservoirs. Therefore, it was compulsory to equilibrate the flow pressure at the two entrances by using a single pressure source to feed both inlets by means of a Y-barbed connector. In this manner, two fluid streams were mainly forced to enter and flow along the Y-shape network, thus improving the flow stability in the main microchannel.

On top of that, we needed to ensure that equal amounts of liquid were fed on each reservoir by a pipette. The imbalance of pressures or reservoir levels would result in an asymmetric sigmoidal concentration gradient profile because two sample streams introduced from the inlets would not encounter at the center of the stagnation point (Y-intersection). In practice, the pressure imbalance was difficult to circumvent which in turn had an influence on the stability and the reproducibility of generated concentration gradients.

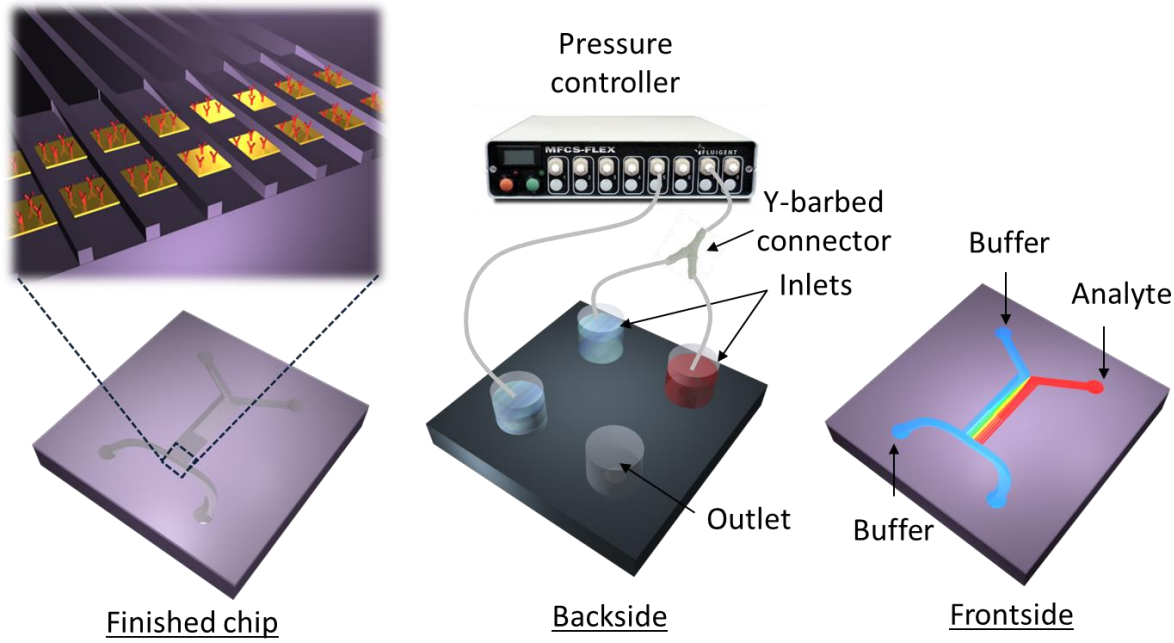

Figure 5.19 Schematic diagram of the experimental setup used to create the concentration gradients.

To visualize the generated gradient, a 20 nM solution of mIgG-AF 647 was introduced on the right inlet whereas a buffer solution was injected from the left one. An analyte-buffer interface was observed virtually at the center of the Y-junction (Figure 5.20a). Two solutions flowed adjacently and mixed via diffusion as they moved downstream. As a result, a broader fluorescence region was observed. The diffusion profile exhibited a characteristic sigmoidal shape as expected (Figure 5.20b). The normalized fluorescence intensities at different positions along the main microchannel also fitted well with an analytical model based on diffusion equations.

The fluorescence signals inside the small microchannel outputs were recorded. A gradient of concentration was observed as the fluorescence intensity varied across all outputs. To determine the analyte concentrations at different microchannel outputs, the average fluorescence intensity of each microchannel measured from ten different regions of interest (8 μm × 8 μm) was first subtracted with the background fluorescence corresponding to each microchannel filled with the buffer solution.

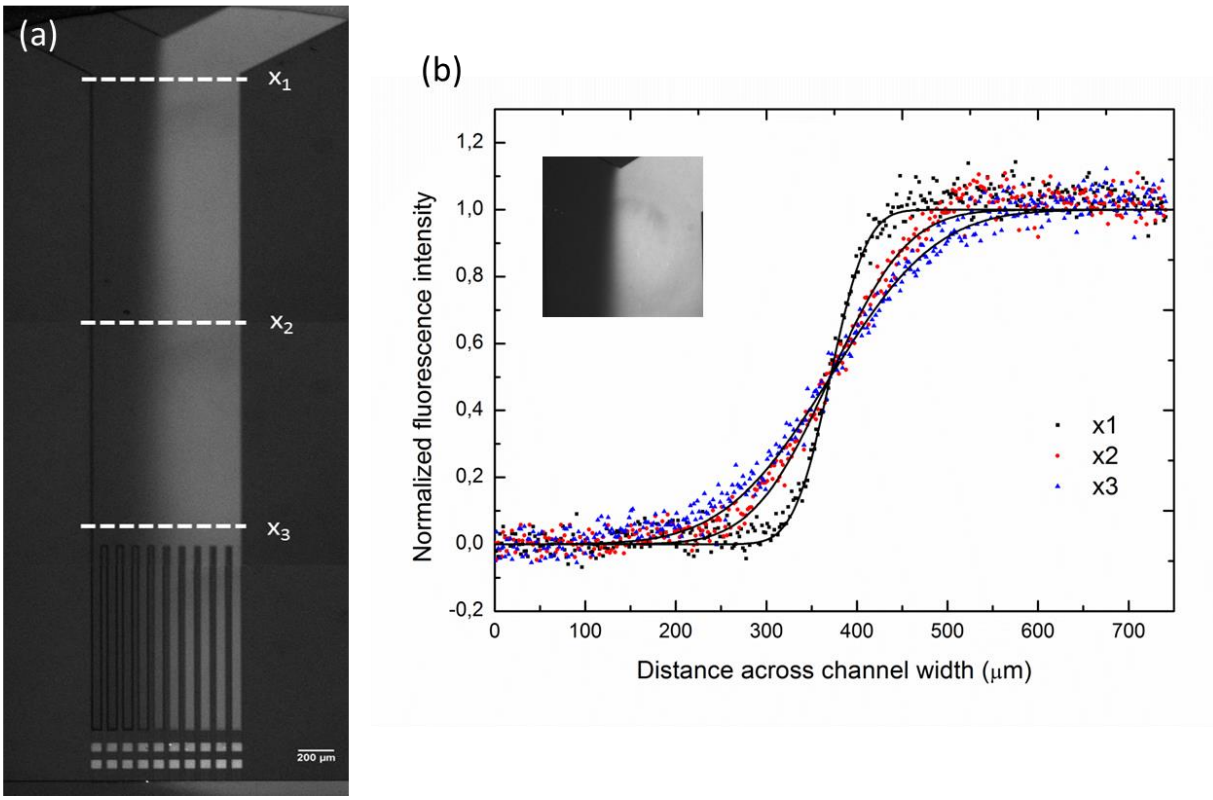

Figure 5.20 (a) A fluorescence image of the device injected with a buffer solution on the left inlet and a fluorescent IgG solution (20 nM) on the right inlet. (b) A plot of normalized fluorescence intensities across the channel width at different distances downstream, 0 µm (x_1), 1450 µm (x_2), and 2650 µm (x_3), showing the analyte-buffer interface at the stagnation point (inset). The black lines are the intensity profiles obtained from an analytical model.

The average intensities at different outputs were then normalized to the intensity of the fully concentrated analyte solution (channel with maximum fluorescence intensity), which was the same intensity level as the region close to the inlet (Figure 5.21). Knowing a linear relationship between the fluorescence intensity and the analyte concentration, we could estimate the analyte concentration at different microchannel outputs as summarized in Table 5.1. **Although the Y-shape dilutor generated merely a sigmoidal shape of concentrations, the generated gradient profile offered us a sufficient number of different analyte concentrations (5-6 data points) within a suitable range for kinetic analysis.**

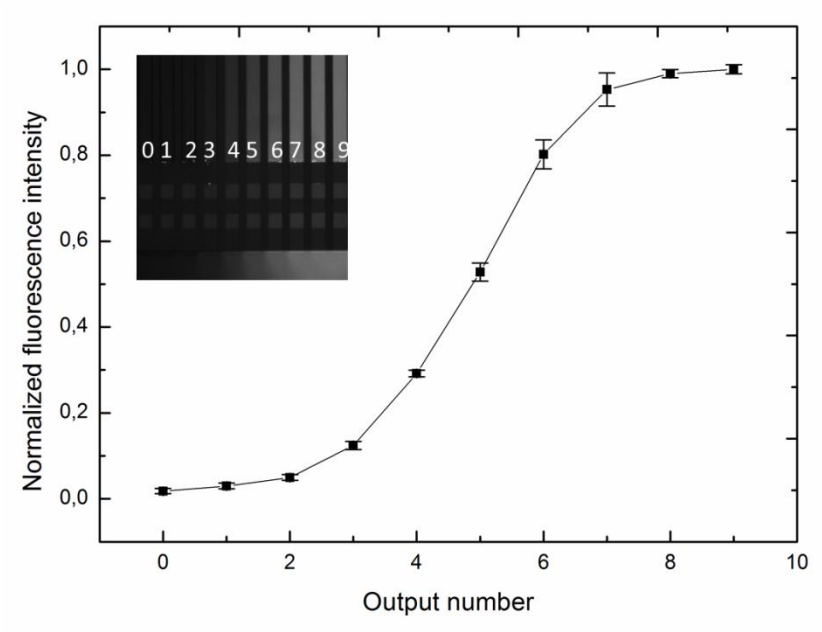

Figure 5.21 A plot of normalized fluorescence intensity at the different microchannel outputs (inset) generated by the on-chip dilutor, exhibiting a sigmoid diffusion curve. The error bars represent the fluorescence variations from 10 different regions of interest.

Table 5.1 Summary of normalized fluorescence intensities and output analyte concentrations obtained from the on-chip dilutor.

Output number	Normalized signal	Analyte concentration (nM)
0	0.018	0.36
1	0.030	0.60
2	0.050	0.99
3	0.12	2.5
4	0.29	5.8
5	0.53	10
6	0.80	16
7	0.95	19
8	0.99	20
9	1.0	20

With an optimized flow velocity of the injected solutions at the inlet reservoirs, our device was capable of producing the gradients with a concentration range of **approximately 2 orders of magnitude and with an adequate number of different analyte concentration values required for kinetic studies**. The concentration ratio between the last channel (the fully concentrated solution) and the first channel (the most diluted solution) was found to be approximately **55**. Therefore, **this experiment validated the effectiveness of our simple on-chip dilutor as a concentration gradient generating-device for being used in kinetic assays of biomolecular interactions** (which will be discussed in the following section).

5.8 One-shot parallel kinetic measurements

Here, we demonstrated the performance of our on-chip dilutor-integrated nanoslit biosensor system to simultaneously interrogate protein binding kinetics of a full analyte concentration series in a single experiment. **We chose to study the kinetics of the anti-IgG/IgG interaction model for the demonstration purpose.**

Since the kinetic data of each analyte concentration was procured from different sensor surfaces located in different nanoslits, we assumed that each sensor exhibited an equal sensing performance in terms of binding efficiency, hence the same surface probe density, giving that an identical functionalization protocol was applied.

The chip preparation and in-situ surface functionalization protocol used to immobilize the receptors on the sensor surface were similar to the ones used in the experiment detailed in Chapter 4. For the kinetic study, a 20 nM solution of mIgG-AF 647 was used as a sample input concentration. During the association phase, the interaction of the analyte at various concentrations, generated from the concentration gradient dilutor, with the receptor immobilized sensor surfaces located on 10 separate nanochannels were monitored simultaneously under the fluorescence microscope.

In order to monitor the dissociation phase, we stopped the fluid flow at the Y-junction input and simultaneously applied a reverse flow, thus introducing a fresh buffer solution from the outlet channel. In this way, the capability of our device to generate both association and dissociation curves without additional buffer loading step were still preserved while creating concurrent possibility of a one-shot parallel kinetic measurement thanks to the incorporated gradient dilution feature.

The fluorescence intensities at different microchannel outputs were also measured in real-time during the association phase (Figure 5.22). It can be observed that the fluorescence intensities were stabilized within 2 min, which was way shorter than the association time used in the experiment. Furthermore, fairly uniform analyte concentrations were achieved during the time period of the association process. This permitted us to extract the kinetic parameters using an analytical well-mixed model, assuming a constant and uniform analyte concentration above the sensor.

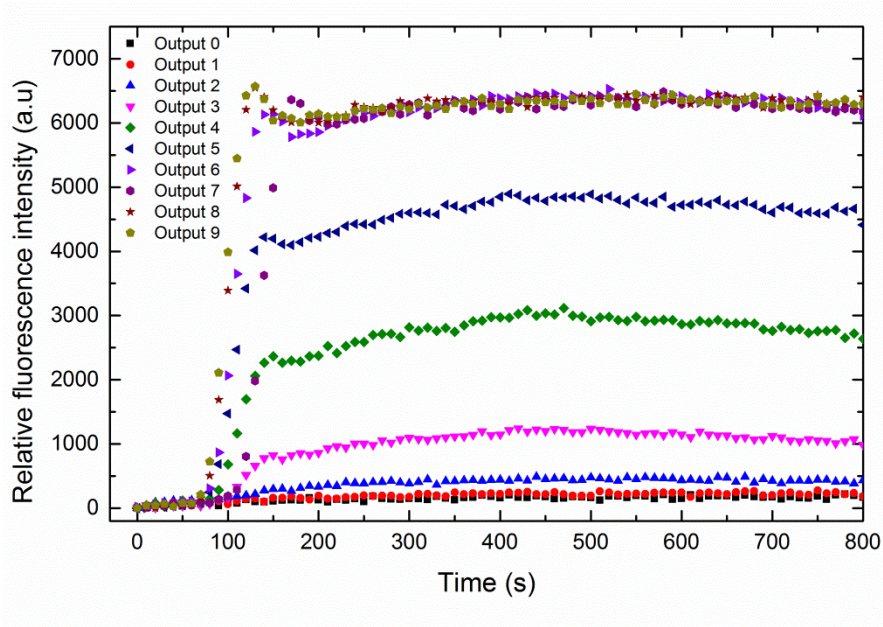

Figure 5.22 Transient fluorescence profiles as a function of time at various microchannel outputs during the association phase.

The analyte concentrations at various outputs were determined to be 0.57 nM to 20 nM (Figure 5.23). From the fluorescence image of the device (inset), the fluorescence signals on the sensor patches gradually increase from the left channel to the right one, corresponding to the lowest to the highest target concentrations. As the analyte concentrations in the last four outputs (output 6-9) were nearly identical, only the output 1-6 were selected for kinetic constant determination, giving adequate concentration ranges for curve fitting.

Figure 5.24 depicts the kinetic sensorgrams of anti-IgG/IgG reaction at various analyte concentrations obtained from the on-chip gradient generator-integrated nanoslit device. To determine the binding constants of this interaction, the data were fitted with a well-mixed model, assuming a simple 1:1 interaction. The plot of the apparent time constant as a function of the analyte concentration yielded a linear fit with a slope of 0.00053 and R^2 of 0.9909 (Figure 5.25). A derived slope of 0.00053 $nM^{-1}s^{-1}$ resulted in an on-rate of 5.3×10^5 $M^{-1}s^{-1}$.

The dissociation constant was extracted by fitting the dissociation curves with a first-order exponential decay. The average off-rate constant was calculated to be $7.8\times10^{-4}s^{-1}$. Therefore, the equilibrium dissociation constant (K_D) which is the ratio between k_d and k_a can be estimated to be 1.5 nM. **These values were shown to be in a good agreement with the extracted rate constants obtained from the previous nanoslit device using the conventional kinetic assay (Chapter 4).**

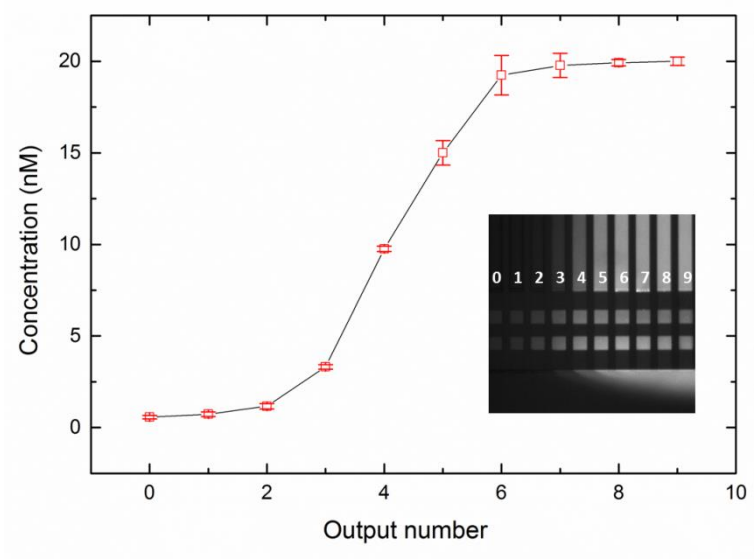

Figure 5.23 The concentration at various microchannel outputs (inset) obtained from the gradient chip. The error bars were obtained from ten different regions of interest.

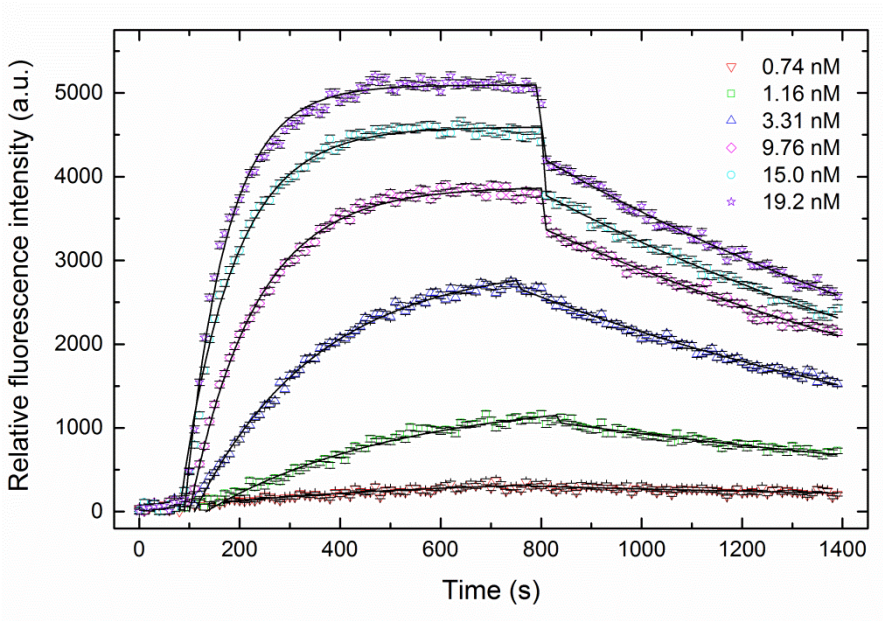

Figure 5.24 Kinetic curves of the analyte-immobilized receptor interactions at various analyte concentrations using the gradient integrated-nanofluidic chip. The curves were fitted with a well-mixed model for the association phase and an exponential decay for the dissociation phase. The error bars represent the standard errors.

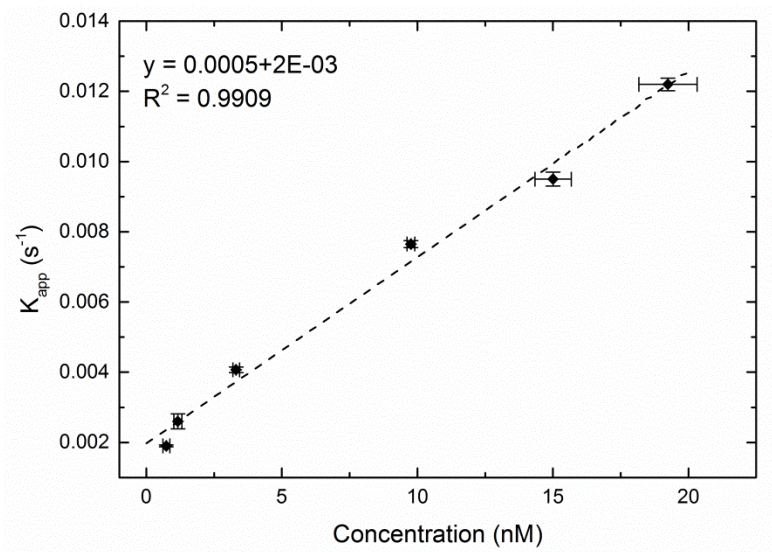

Figure 5.25 A plot of the apparent time constants as a function of the analyte concentrations.

In addition, we conducted two additional kinetic measurements on the different gradient dilutor devices. The extracted kinetic parameters and experimental conditions for all kinetic assays are summarized in Table 5.2. **The consistency among different kinetic experiments confirmed the robustness of our kinetic data performed in the developed gradient chips.** Furthermore, our device operated in a reaction-limited regime but not a mass transport-limited because varying the flow velocity did not contribute a significant change in the estimated kinetic constants.

Table 5.2 Summary of kinetic parameters obtained from 3 experimental conditions with 3 different gradient chips.

Experiment	Concentration ranges (nM)	Flow velocity in a nanochannel (μm/s)	k_a ($M^{-1}s^{-1}$)	k_d (s^{-1})	K_D (nM)
1	0.41-19	445	$6.0\pm0.3\times10^5$	$9.3\pm0.5\times10^{-4}$	1.6
2	0.74-19	667	$5.3\pm0.3\times10^5$	$7.8\pm0.9\times10^{-4}$	1.5
3	0.40-13	489	$6.6\pm0.4\times10^5$	$8.7\pm0.9\times10^{-4}$	1.3

5.9 Conclusion

We have established for the first time a simple and effective on-chip gradient generator-based nanoslit biosensors by combining a Y-type microfluidic feature for concentration gradient generation via laminar diffusive mixing and the nanoslit biosensor platform. The newly developed device has enabled one-shot parallel kinetic assays by monitoring interactions between multiple analyte concentrations and surface-immobilized probes simultaneously in a single experiment without time-extensive surface regeneration.

We have designed the device according to the desired concentration ranges and operational flow velocities. Numerical simulations showed that the device enabled a stable gradient generation with the concentration range of 2 orders of magnitude and the equal flow velocity for all outputs, thus confirming the functionality of the device. To validate the effectiveness of the gradient generation, we have visualized the gradient formation in the enclosed-dilution device using a fluorescence microscope. The results confirmed that the generated concentration was stable and could be maintained downstream. The desired concentration ranges have been achieved by tuning the applied pressure at the inlets although it was burdensome to achieve a precise pressure balance between the two inlets. This is due to a high resistance of the existing nanoslit network as well as the inevitable variations in the amount of sample loaded into each reservoir and the way we assembled the fluidic chip.

Future improvement allowing more user-oriented operation is to include a pressure balancing fluidic circuit with a high flow resistance network, which can potentially reduce the pressure difference between two fluid streams coming from two reservoirs and two individual pressure tubing. This would definitely improve the reproducibility of the generated concentration gradients.

The ability of this device to accommodate parallel kinetic measurements at multiple analyte concentrations has been investigated by monitoring the binding of fluorescently labeled mouse IgG and the surface-immobilized anti-IgG. The results obtained from kinetic analysis and good agreement of the extracted kinetic parameters with the previous work and the SPR setup further validated the utility of this device to provide accurate and robust kinetic information across parallel experiments. Furthermore, this approach offered time-saving assays (20 min instead of hours) and substantially reduction of reagent consumption per assay as compared to the traditional kinetic experiments (*e.g.*, in SPR setup)

Our compact device is operated using one pressure controller and a conventional bench-top fluorescence microscope. Therefore it is highly desirable for everyday practice of experimental biologists. This simple and inexpensive platform with reduced material and equipment resources brings us a step closer toward real-world applications, such as high-throughput drug-screening and clinical diagnostics.

Bibliography

1. Seethala, R., Zhang, L., *Handbook of drug screening, second edition*. 2009: CRC Press.
2. GE-Healthcare, *Biacore T200 Software Handbook*. 2010: GE Healthcare Bio-Schiences AB. 161 p.
3. Bravman, T., et al., *Exploring "one-shot" kinetics and small molecule analysis using the ProteOn XPR36 array biosensor*. Anal Biochem, 2006. **358**(2): p. 281-8.
4. Andersson, K., M. Hamalainen, and M. Malmqvist, *Identification and optimization of regeneration conditions for affinity-based biosensor assays. A multivariate cocktail approach*. Anal Chem, 1999. **71**(13): p. 2475-81.
5. Karlsson, R., et al., *Analyzing a kinetic titration series using affinity biosensors*. Analytical Biochemistry, 2006. **349**(1): p. 136-147.
6. Nahshol, O., et al., *Parallel kinetic analysis and affinity determination of hundreds of monoclonal antibodies using the ProteOn XPR36*. Analytical Biochemistry, 2008. **383**(1): p. 52-60.
7. Marcus, J.S., W.F. Anderson, and S.R. Quake, *Parallel picoliter rt-PCR assays using microfluidics*. Anal Chem, 2006. **78**(3): p. 956-8.
8. Yang, J., et al., *A microfluidic device for rapid screening of chemotaxis-defective Caenorhabditis elegans mutants*. Biomed Microdevices, 2013. **15**(2): p. 211-20.
9. Ye, N., et al., *Cell-based high content screening using an integrated microfluidic device*. Lab on a Chip, 2007. **7**(12): p. 1696-1704.
10. Ahmed, T., T.S. Shimizu, and R. Stocker, *Bacterial Chemotaxis in Linear and Nonlinear Steady Microfluidic Gradients*. Nano Letters, 2010. **10**(9): p. 3379-3385.
11. Kim, S., H.J. Kim, and N.L. Jeon, *Biological applications of microfluidic gradient devices*. Integrative Biology, 2010. **2**(11-12): p. 584-603.
12. Ziolkowska, K., et al., *PDMS/glass microfluidic cell culture system for cytotoxicity tests and cells passage*. Sensors and Actuators B: Chemical, 2010. **145**(1): p. 533-542.
13. Squires, T.M. and S.R. Quake, *Microfluidics: Fluid physics at the nanoliter scale*. Reviews of Modern Physics, 2005. **77**(3): p. 977-1026.
14. Cornish, R.J., *Flow in a Pipe of Rectangular Cross-Section*. Proceedings of the Royal Society of London A: Mathematical, Physical and Engineering Sciences, 1928. **120**(786): p. 691-700.
15. Oh, K.W., et al., *Design of pressure-driven microfluidic networks using electric circuit analogy*. Lab on a Chip, 2012. **12**(3): p. 515-545.
16. Crank, J., *The mathematics of diffusion*. 1975, London: Oxford University Press, Ely House.
17. Deen, W.M., *Analysis of transport phenomena*. 1998, New York: Oxford University Press.
18. Boy, D.A., Gibou, F. , *Simulation tools for lab on a chip research: advantages, challenges, and thoughts for the future*. Lab on a Chip, 2008. **8**(9): p. 1424-1431.
19. Einstein, A., *Investigations of the theory of brownian movement*. Dover, 1956.
20. Weiner, O.D., et al., *Spatial control of actin polymerization during neutrophil chemotaxis*. Nat Cell Biol, 1999. **1**(2): p. 75-81.
21. Boyden, S., *The chemotactic effect of mixtures of antibody and antigen on polymorphonuclear leucocytes*. J Exp Med, 1962. **115**: p. 453-66.

22. Wilkinson, P.C. and J.M. Lackie, *The influence of contact guidance on chemotaxis of human neutrophil leukocytes*. Exp Cell Res, 1983. **145**(2): p. 255-64.
23. Keenan, T.M. and A. Folch, *Biomolecular gradients in cell culture systems*. Lab Chip, 2008. **8**(1): p. 34-57.
24. Decave, E., et al., *Shear flow-induced motility of Dictyostelium discoideum cells on solid substrate*. J Cell Sci, 2003. **116**(Pt 21): p. 4331-43.
25. Nguyen, N.-T., *Chapter 5 - Micromixers based on molecular diffusion*, in *Micromixers (Second Edition)*, N.-T. Nguyen, Editor. 2012, William Andrew Publishing: Oxford. p. 163-194.
26. Zhou, B., et al., *Generation of tunable and pulsatile concentration gradients via microfluidic network*. Microfluidics and Nanofluidics, 2015. **18**(2): p. 175-184.
27. Walker, G.M., et al., *Effects of flow and diffusion on chemotaxis studies in a microfabricated gradient generator*. Lab on a Chip, 2005. **5**(6): p. 611-618.
28. Saadi, W., et al., *Generation of stable concentration gradients in 2D and 3D environments using a microfluidic ladder chamber*. Biomed Microdevices, 2007. **9**(5): p. 627-35.
29. Abhyankar, V.V., et al., *Characterization of a membrane-based gradient generator for use in cell-signaling studies*. Lab Chip, 2006. **6**(3): p. 389-93.
30. Atencia, J., J. Morrow, and L.E. Locascio, *The microfluidic palette: A diffusive gradient generator with spatio-temporal control*. Lab on a Chip, 2009. **9**(18): p. 2707-2714.
31. Chung, S., et al., *Cell migration into scaffolds under co-culture conditions in a microfluidic platform*. Lab Chip, 2009. **9**(2): p. 269-75.
32. Keenan, T.M., C.-H. Hsu, and A. Folch, *Microfluidic "jets" for generating steady-state gradients of soluble molecules on open surfaces*. Applied Physics Letters, 2006. **89**(11): p. 114103.
33. Bhattacharjee, N., et al., *A Neuron-Benign Microfluidic Gradient Generator for Studying the Response of Mammalian Neurons towards Axon Guidance Factors*. Integrative biology : quantitative biosciences from nano to macro, 2010. **2**(0): p. 669-679.
34. Jeon, N.L., et al., *Generation of Solution and Surface Gradients Using Microfluidic Systems*. Langmuir, 2000. **16**(22): p. 8311-8316.
35. Lin, F., et al., *Generation of dynamic temporal and spatial concentration gradients using microfluidic devices*. Lab Chip, 2004. **4**(3): p. 164-7.
36. Dertinger, S.K.W., et al., *Generation of Gradients Having Complex Shapes Using Microfluidic Networks*. Analytical Chemistry, 2001. **73**(6): p. 1240-1246.
37. Vozzi, G., et al., *Finite element modelling and design of a concentration gradient generating bioreactor: application to biological pattern formation and toxicology*. Toxicol In Vitro, 2010. **24**(6): p. 1828-37.
38. Tirella, A., et al., *A microfluidic gradient maker for toxicity testing of bupivacaine and lidocaine*. Toxicology in Vitro, 2008. **22**(8): p. 1957-1964.
39. Yeh, C.-H., C.-H. Chen, and Y.-C. Lin, *Use of a gradient-generating microfluidic device to rapidly determine a suitable glucose concentration for cell viability test*. Microfluidics and Nanofluidics, 2011. **10**(5): p. 1011-1018.
40. Chon, H., et al., *On-Chip Immunoassay Using Surface-Enhanced Raman Scattering of Hollow Gold Nanospheres*. Analytical Chemistry, 2010. **82**(12): p. 5290-5295.
41. Campbell, K. and A. Groisman, *Generation of complex concentration profiles in microchannels in a logarithmically small number of steps*. Lab Chip, 2007. **7**(2): p. 264-72.
42. Lee, K., et al., *Generalized serial dilution module for monotonic and arbitrary microfluidic gradient generators*. Lab Chip, 2009. **9**(5): p. 709-17.
43. Sugiura, S., K. Hattori, and T. Kanamori, *Microfluidic Serial Dilution Cell-Based Assay for Analyzing Drug Dose Response over a Wide Concentration Range*. Analytical Chemistry, 2010. **82**(19): p. 8278-8282.

44. Lee, M., et al., *SERS-based immunoassay using a gold array-embedded gradient microfluidic chip*. Lab on a Chip, 2012. **12**(19): p. 3720-3727.
45. Greve, F., et al., *A hybrid microsystem for parallel perfusion experiments on living cells*. Journal of Micromechanics and Microengineering, 2007. **17**(8): p. 1721.
46. Holden, M.A., et al., *Generating fixed concentration arrays in a microfluidic device*. Sensors and Actuators B: Chemical, 2003. **92**(1–2): p. 199-207.
47. Mao, H., P.S. Cremer, and M.D. Manson, *A sensitive, versatile microfluidic assay for bacterial chemotaxis*. Proc Natl Acad Sci U S A, 2003. **100**(9): p. 5449-54.
48. Mao, H., T. Yang, and P.S. Cremer, *Design and characterization of immobilized enzymes in microfluidic systems*. Anal Chem, 2002. **74**(2): p. 379-85.
49. Kamholz, A.E., et al., *Quantitative analysis of molecular interaction in a microfluidic channel: the T-sensor*. Anal Chem, 1999. **71**(23): p. 5340-7.
50. Ouellet, E., et al., *Parallel microfluidic surface plasmon resonance imaging arrays*. Lab Chip, 2010. **10**(5): p. 581-8.
51. Jiang, X., et al., *A miniaturized, parallel, serially diluted immunoassay for analyzing multiple antigens*. J Am Chem Soc, 2003. **125**(18): p. 5294-5.
52. Bui, M.-P.N., et al., *Enzyme Kinetic Measurements Using a Droplet-Based Microfluidic System with a Concentration Gradient*. Analytical Chemistry, 2011. **83**(5): p. 1603-1608.
53. Kamholz, A.E. and P. Yager, *Molecular diffusive scaling laws in pressure-driven microfluidic channels: deviation from one-dimensional Einstein approximations*. Sensors and Actuators B: Chemical, 2002. **82**(1): p. 117-121.

General conclusion

Real-time kinetic studies of protein-protein interactions are of particular importance in understanding biological functions at the cellular level, facilitating the discovery of novel therapeutic drugs and the improvement of medical remedy to cure human diseases. A variety of affinity-based biosensors have been employed to elucidate protein binding kinetics in real-time, which enable the quantification of distinct kinetic constants, on-and off-rates. Each technique has its own advantages and inconveniences, depending on the requirements of a particular application. During the past years, nanofluidics has been extensively exploited for biophysical studies, molecular separation and pre-concentration, as well as single-molecule analysis, owing to its unique features at the nanoscale. Surprisingly, little effort has been placed on developing nanofluidics-based biosensor, and in particular for real-time kinetic studies. This is attributed to several technological and biological challenges (*e.g.*, preservation of biological entities during device assembly).

In the frame of this PhD work, we have developed a cost-effective nanofluidic biosensor platform for real-time monitoring of protein binding kinetics in physiological media. Our approach exploited biofunctionalized planar extended-nanochannels or nanoslits in combination with a conventional fluorescence microscope, enabling the quantification of kinetic parameters of protein-protein interactions. The nanoslits exhibit several unique characteristics which cannot be attained in typical microfluidic formats. A considerable reduction of the fluorescence background signal within the nanoconfined-analytical space permits real-time monitoring of protein association and dissociation processes without the need of reagent wash and without using sophisticated techniques, such as SPR or TIRF. Furthermore thanks to the molecular confinement between the analytes in solution and the immobilized-probes on the surface, the binding reactions in the nanoslits can be dramatically enhanced, leading to a maximized target capture efficiency and optimized response times. In this framework, we have fabricated nanofluidic devices and conducted kinetic studies of protein interactions. In order to validate our platform, our sensor performances were compared with the existing technology, such as SPR. The outcomes of this study bridging technological and biological aspects are summarized below.

In the first part, we have focused our efforts on the conception and implementation of nanofluidic biosensor devices, including the fabrication process, the nanochannel bio-functionalization, as well as the chip packaging. The devices, consisting of 2-D nanoslits connected to microchannels, were fabricated using silicon microfabrication technology. We have decided to pattern a gold sensing layer at the bottom of the nanoslits for two main purposes. Firstly, elucidation of protein interactions on a gold surface has empowered us to compare our biosensor performances with the established SPR technique, providing that the similar grafting protocol was used. Secondly, local selective grafting of receptor biomolecules in the nanochannel was possible through gold-thiol surface chemistry. We have selected two representative biological interaction models with different

binding affinities: streptavidin/biotin and IgG/anti-IgG pairs, to demonstrate our platform effectiveness. Furthermore, we have successfully implemented a bio-functionalization protocol and a room-temperature sealing procedure that ensured the preservation of bioactivity of the immobilized receptors and allowed the optical visualization of kinetic reactions through a hybrid silicon/h-PDMS coated glass fluidic chip. Customized chip assembly/packaging was also constructed for world-to-chip interface. Since our platform employed a pressure-driven flow system as a liquid pumping mechanism, we have carried out the flow calibration to correlate the applied pressure to the flow velocity in the nanoslits. The exact values of the applied flow velocity were important to identify the operational regimes of our biosensor system, and more importantly to allow the comparison of our experimental assays with the simulated data (because the flow velocity was used as an input parameter in the simulation model to predict the sensor responses).

In the second part of this study, special emphasis was placed on the validation of our platform for kinetic constant quantification of two dedicated protein-protein interaction pairs. Prior to conducting kinetic assays, we have evaluated the bio-functionality of the pre-immobilized receptors in an enclosed fluidic chip by means of fluorescence observations. We have confirmed that the preceding grafted receptors maintained their bio-functionality toward the target analytes and the sensor exhibited a high signal-to-noise ratio. Rigorous kinetic studies of two dedicated biological systems were then carried out. For streptavidin-biotin binding, we have confirmed that the grafting density of the receptors on the sensor surface played a crucial role in kinetic reactions and the accuracy of the estimated kinetic parameters. In addition, we have also implemented a simplified protocol in order to achieve full kinetics (association and dissociation curves) of IgG/anti-IgG interaction in one single experiment without extra washing steps via a reversed-buffer flow manner. This achievement was attributed to the unique features of our system which involved a drastically reduced fluorescence background and high capture efficiency. We have demonstrated that the kinetic data obtained from the nanoslits could be readily employed with different fitting methodologies, including finite element method, analytical model, and a commercialized software package, to quantify the kinetic parameters. The extracted kinetic parameters obtained from the nanoslits were in accordance with those obtained from the SPR and the values found in the literature. These results thus validated our biosensor platform to be used as an alternative tool for real-time kinetic studies of biomolecule interactions with the detection limit of 1 pM or 10 zeptomole for IgG detection.

Finally, we have proposed a new generation of our nanoslit biosensor which enabled a one-shot parallel kinetic measurement in a time-saving manner. We have exploited real-time sensing performance of our validated biofunctionalized nanoslits for high-throughput kinetic assays by integrating a Y-type microfluidic gradient generator into the final device. This integrated device has allowed stable concentration gradients to be automatically created and consequently enabled simultaneous interrogation of multiple binding reactions of different target concentrations in a single experiment without the need of surface regeneration. We have validated the device design for gradient generation using both finite element simulation and experimental verification. With an optimized flow velocity, our device generated a gradient of concentration in a range of

approximately 2 orders of magnitude and provided us a sufficient number of different analyte concentrations (5-6 concentration points) for accurate quantification of kinetic parameters. Furthermore, one-shot parallel kinetic assays were investigated through the IgG/anti-IgG interaction model and the estimated kinetic parameters were found to be in good agreement with those obtained from the previously presented kinetic assays in our nanoslit biosensors using multiple association and dissociation cycles. Therefore, our proposed device offered the possibility to produce robust kinetic data, with significantly reduced overall assay time (~10 times) and lower reagent consumption (~1000 times) relative to the traditional kinetic experiments, such as in SPR setup. We believe that this innovative technology will drive future advancements not only in the discipline of biomedical and personalized medicine, but also in basic chemical/biological research.

Abbreviations

Aβ	Amyloid Beta
AMP	Adenosine Monophosphate
AR	Aspect Ratio
ATP	Adenosine Triphosphate
BAT	Biotinylated Thiol
BSA	Bovine Serum Albumin
CCD	Charge-Coupled Device
CDRs	Complementary-Determining Regions
CFD	Computational Fluid Dynamic
CNTs	Carbon Nanotubes
CRP	C-Reactive Protein
DEP	Dielectrophoresis
DLP	Diffusion-Limited Patterning
DNA	Deoxyribonucleic Acid
DRIE	Deep Reactive Ion Etching
EBL	Electron Beam Lithography
ECM	Extracellular Matrix
EDL	Electrical Double Layer
ELISA	Enzyme-Linked Immunosorbent Assay
EMCCD	Electron Multiplying Charge-Coupled Device
EPR	Electron Paramagnetic Resonance
FCS	Fluorescence Correlation Spectroscopy
FEM	Finite Element Method
FET	Field-Effect Transistor
FIB	Focused Ion Beam
FITC	Fluorescein Isothiocyanate
FP	Fluorescence Polarization
FRET	Förster Resonance Energy Transfer
GOx	Glucose Oxidase
HAR	High Aspect Ratio
HMDS	Hexamethyldisilazane
h-PDMS	Hard-Polydimethylsiloxane
ICP	Ion Concentration Polarization
ID	Internal Diameter
IgG	Immunoglobulin G
IR	Infrared
IRIS	Interferometric Reflectance Imaging Sensor
IS-FET	Ion-Selective Field-Effect Transistor
ITC	Isothermal Titration Calorimetry
QCM	Quartz Crystal Microbalance
QCM-D	Quartz Crystal Microbalance with Dissipation monitoring
LED	Light-Emitting Diode
LIF	Laser-Induced Fluorescence
LOD	Limit of Detection
LPSR	Localized Surface Plasmon Resonance
mAB	Monoclonal Antibody
MEMS	MicroElectroMechanical System
mIgG-AF	Alexa-Fluor conjugated mouse anti-rabbit immunoglobulin
NA	Numerical Aperture
NMR	Nuclear Magnetic Resonance
NW-FET	Nanowire Field-Effect Transistor
OD	Outer Diameter
OEG	Olio (Ethylene Glycol)
OWLS	Optical Waveguide Lightmode Spectroscopy
PBS	Phosphate Buffer Saline
PCR	Polymerase Chain Reaction
PDE	Partial Differential Equation
PDMS	Polydimethylsiloxane
PEG	Poly (Ethylene Glycol)
PSA	Prostate-Specific Antigen
PSQ	Polysilsesquioxane
RI	Refractive Index
RIE	Reactive Ion Etching
ROI	Region of Interest
RSD	Relative Standard Deviation
RU	Resonance Unit
SAM	Self-Assembled Monolayer
SE	Standard Error

SEM	Scanning Electron Microscope
SERS	Surface-Enhanced Raman Spectroscopy
SiN	Silicon Nitride
SNARE	Soluble N-ethylmaleimide-sensitive factor Attachment Receptor
SPFS	Surface Plasmon-enhanced Fluorescence Spectroscopy
SPR	Surface Plasmon Resonance
SPRi	Surface Plasmon Resonance Imaging
ssDNA	Single-Stranded Deoxyribonucleic Acid
ST-AF	Alexa-Fluor conjugated streptavidin
TIRFM	Total-Internal-Reflection Fluorescence Microscopy
μTAS	Micro-Total-Analysis-Systems
UV	Ultraviolet
VUV	Vacuum Ultraviolet

Appendix A

Device fabrication process

1. Substrate	100 mm p-type silicon wafer, thickness = 525 μm
2. Substrate cleaning	▪ Piranha solution (H_2SO_4/H_2O_2; 1:1 v/v) 2 min ▪ 5% HF buffer solution 30 s ▪ Piranha solution (H_2SO_4/H_2O_2; 1:1 v/v) 2 min ▪ Dehydration 10 min at 200 ºC
Nanochannel etching	
4. Define nanochannel dimension (first mask)	▪ HMDS deposition ▪ Spin-coating ECI 3012 photoresist (EVG 120), soft-baking, 2.6 μm thick ▪ UV exposure (MA 150, Karl Suss Inc.) 12.5 s at 20 mW/cm^2, vacuum contact ▪ Post-baking and development ▪ Post-baking 60 s at 115 ºC
5. Nanochannel etching	▪ RIE (Alcatel) ▪ Resist dissolution in acetone and/or oxygen plasma (800W, 10 min) ▪ Nanochannel depth = 550 ± 20 nm
6. Substrate cleaning	▪ Oxygen plasma (800W, 5 min)
Microchannel etching	
7. Define microchannel dimension (second mask)	▪ HMDS deposition ▪ Spin-coating ECI 3012 photoresist (EVG 120), soft-baking, 2.6 μm thick ▪ UV exposure (MA 150, Karl Suss Inc.) 12.5 s at 20 mW/cm^2, vacuum contact ▪ Post-baking and development ▪ Post-baking 60 s at 115 ºC
8. Microchannel etching	▪ DRIE (Alcatel) ▪ Resist dissolution in acetone and/or oxygen plasma (800W, 10 min) ▪ Microchannel depth = 5 ± 0.4 μm
9. Thermal oxidation	▪ Piranha cleaning (2 min) + 5% HF (30 s) ▪ Thermal oxidation, oxide thickness 200 nm
10. Substrate cleaning	▪ Oxygen plasma (800 W, 5 min)

Metal deposition	
11. Define gold patch dimension (third mask)	▪ HMDS deposition ▪ Spin-coating AZ-NLOF 2035 photoresist (EVG 120), soft-baking, 5 µm thick ▪ UV exposure (MA 150, Karl Suss Inc.) 7.5 s at 20 mW/cm^2, vacuum contact ▪ Post-baking and development
12. Gold deposition	▪ Gold evaporation Cr/Au (5/100 nm)
13. Lift-off process	▪ Acetone bath
14. Annealing	▪ 20 min at 250 ºC under N_2H_2
15. Substrate lamination	▪ Dry photoresist PH2050 ▪ Shipley laminator (RT + 110 ºC)
16. Hole drilling	▪ Sandblasting machine (aluminum oxide particles), hole diameter 1 mm ▪ Resist dissolution (acetone bath with ultrasonics + oxygen plasma (800 W, 5 min) with a faraday cage
17. Dicing	▪ Spin-coating of photoresist (wafer protection), soft-baking ▪ Dicing 16 individual chips (dimensions: 16×16 mm^2)

Appendix B

Materials and reagents

Biotinylated tri(ethylene glycol) undecane thiol (BAT) (HS-(CH)n-OEG-biotin) was purchased from Nanoscience Instruments (USA). 11-mercapto-1-undecanol (MUD) (HS-(CH2)11-OH), bovine serum albumin (BSA) were purchased from Sigma-Aldrich (France). Tween-20 was purchased from ACROS Organics (France). Biotinylated anti-mouse IgG (Ref. No. 115-065-003) and Alexa Fluor 647 conjugated monoclonal mouse anti-rabbit IgG (Ref. No. 211-602-171) were purchased from Jackson ImmuoResearch (UK). Alexa Fluor 488 conjugated streptavidin and Alexa Fluor 660 conjugated goat anti-rabbit were purchased from Invitrogen, Inc. All proteins were diluted in phosphate buffer saline (PBS) (10 mM PBS, 0.138 M NaCl, 0.0027 M KCl, pH 7.4) purchased from Sigma-Aldrich (France).

Appendix C

Validation of the full functionalization protocol using quartz crystal microbalance (QCM) apparatus

QCM-D (E1, Q-sense instrument) was used to perform all QCM-D measurements (Figure A-1). AT-cut 5 MHz quartz crystal sputtered coated with a 100 nm thick Au layer were obtained from Q-sense AB. All measurements were performed at a controlled temperature of 20 ºC, using degassed solutions.

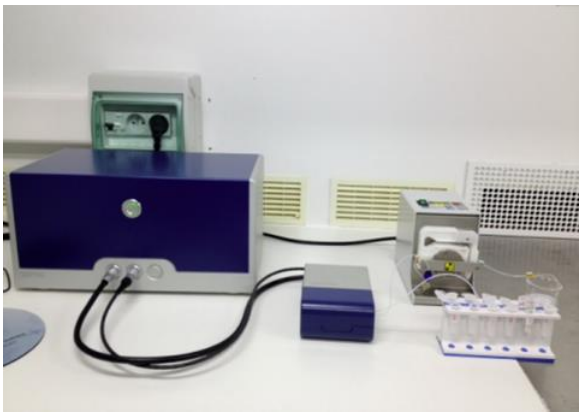

Figure A-1 QCM-D experimental setup used to verify the functionalization protocol.

For off-line sensor modification, the gold crystal sensors were cleaned in a piranha solution (H_2SO_4:H_2O_2, 70:30 % v/v) for 2 min. After rinsing the surface with DI water, the sensors were dried gently under nitrogen flow. The quartz crystals were immediately incubated in a 0.5 mM ethanolic solution of biotin terminated thiol and 11-mercapto-1-undecanol in 1:9 mole ratio for the sensor for > 12 h, protected from the light, at room temperature to form SAMs. After incubation, the sensors were rinsed with ethanol once and DI water twice to remove any non-covalently bound thiol molecules.

For online measurement, the applied flow rate for the buffer and biomolecules were 100 µl/min and 50 µl/min, respectively. First, a phosphate buffer saline (PBS) solution (1X, pH 7) was injected until the baseline signal was stabilized. A 500 nM (26.5 µg/ml) streptavidin solution prepared in PBS buffer (1X) was introduced for 20 min, followed by rinsing with buffer solution. Similarly, streptavidin sensors were exposed to biotinylated anti-mouse (166.7 nM, 25 µg/ml in PBS), until the saturation was reached. The simplified schematic illustration of the assay procedures used in this QCM-D measurement and the plot of the frequency and the dissipation changes for streptavidin and biotin-anti-mouse adsorption on monolayers with 10% biotin content are shown in Figure A-2.

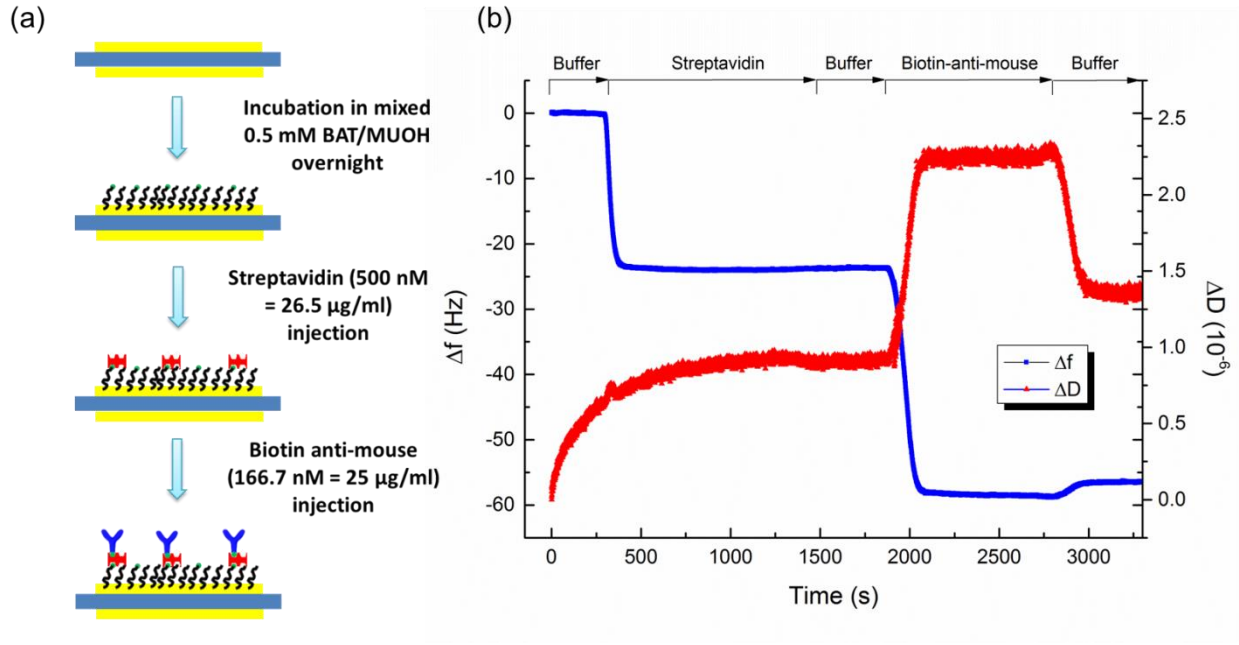

Figure A-2 (a) Schematic illustration describing the conjugation of streptavidin onto self-assembled monolayer containing 10% biotin and subsequent molecular recognition of biotin-anti-mouse onto streptavidin-modified surface. (b) QCM-D responses (frequency and dissipation shifts) corresponding to the immobilization of streptavidin and biotin-anti-mouse to the biotinylated monolayer surface.

To validate the full functionalization protocol, biotin-anti-mouse immobilized sensor surface (receptor immobilized surface) was exposed to non-targeted analyte solution (50 nM, Alexa Fluor 660 goat anti-rabbit in PBS buffer, pH 7) and specific analyte (50nM, Alexa Fluor 647 mouse anti-rabbit in PBS buffer, pH 7). The resonance frequency shifts were recorded in real-time as shown in Figure A-3. It was observed that there was no noticeable change in resonance frequency ($\Delta f = 0.00 \pm 0.20$ Hz) upon irrelevant analyte injection while introduction of specific analyte exhibited a relatively significant change in resonance frequency (-10.4 Hz), corresponding to mass adsorption with coupled water mass of 184 ng/cm^2 (7.32×10^3 molecules/μm^2).

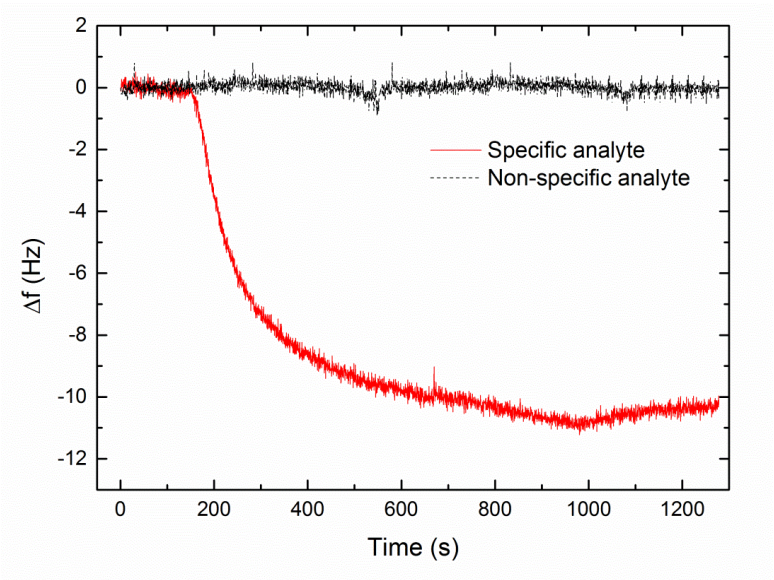

Figure A-3 Resonance frequency shifts upon exposure of specific analyte (mouse anti-rabbit IgG) and non-specific analyte (goat anti-rabbit IgG) onto anti-mouse immobilized sensor surface.

To summarize, the full surface functionalization protocol was successfully validated using QCM-D measurements. Streptavidin was specifically bound to biotinylated SAMs forming a rigid organized monolayer on the gold surface due to high affinity of these protein-ligand pairs. Additionally, streptavidin-biotin linkage is a robust model that can be used for further functionalization of biotin-tagged antibody receptor of interest. Importantly, immobilized anti-mouse receptor could specifically recognize specific target analytes while minimizing undesirable interference adsorption of non-targeted protein molecules. Therefore, this surface modification procedure was valid for implementation of sensing layer construction on our nanofluidic biosensor platform.

Appendix D

Compositions and preparation of h-PDMS mixtures

Five product compositions for hard-PDMS preparation, vinyl PDMS copolymer, vinyl modified silica Q resin, platinum-divinyltetramethyldisiloxane, hydrosilane prepolymer and 2,4,6,8-tetramethyl-tetravinylcyclotetrasiloxane, were purchased from abcr GmbH & Co. Kg (Germany) and Sigma-Aldrich (France).

Compositions and preparation

Compounds	Quantity
1) VDT 731 (7-8% vinylmethylsiloxane dimethylsiloxane cop.)	6.8 g
2) VQM 135 (vinyl Q-resin dispersion)	1 g
3) Modulator (tetramethyl-tetravinyl cyclotetrasiloxane)	50 μL
4) SIP6831.1 catalyst (platinum cyclovinylmethylsiloxane complex in xylene 2.1~2.4% Pt)	10 μL
Slowly mix the mixture in an ice bath to prevent overheating of the mixture which induces undesirable polymerization	
5) HMS 301 (methylhydrosiloxane dimethylsiloxane cop.)	2 g
Slowly mix the products in an ice bath until obtaining a homogenous mixture	
Store the mixture at -20 ºC until use (maximum 2-week storage)	

Appendix E

Sensor preparation and receptor immobilization with BIACORE setup

Sensor preparation

The piranha cleaned gold chip was immersed in a 0.5 mM mixture solution of biotin-terminated thiol and 11-mercapto-1-undecanol overnight, in the dark at room temperature. The modified gold surface was then washed twice with absolute ethanol (gentle stirring) to remove excess thiol compounds and washed several times with deionized water. The biotin modified gold surface was assembled according to the manufacturer's instructions and the user-modified sensor chip was docked in the BIACORE 3000.

Receptor immobilization

Running buffer of 10 mM PBS, pH 7.4, 0.138 M NaCl, 0.0027 M KCl, and 0.05% Tween-20 was injected at a constant flow rate of 5 μL/min for 20 min to stabilize the system. For streptavidin immobilization, a 165 μg/ml solution of Alexa Fluor 488 conjugated streptavidin (ST-AF 488) in PBS buffer was injected at 10 μL/min for 7 min to achieve a saturation level. After successful immobilization of streptavidin on two separate flow channels, the receptor was subsequently immobilized only on the second flow cell by injecting a 14 μg/ml solution of biotin anti-mouse in PBS buffer at a flow rate of 10 μL/min. The first flow cell was used as a control without anti-mouse receptor immobilization.

Author: Pattamon TEERAPANICH

Title: Fluorescence-based nanofluidic biosensor platform for real-time measurement of protein binding kinetics

Thesis director: Thierry LEICHLE

Date and place of the defense: LAAS-CNRS, 10th November 2015

Summary

Kinetic monitoring of protein-protein interactions offers fundamental insights of their cellular functions and is a vital key for the improvement of diagnostic tests as well as the discovery of novel therapeutic drugs. Surface plasmon resonance (SPR) is an established biosensor technology routinely used for kinetic studies of biomolecular interactions. While SPR offers the benefits of real-time and label-free detection, it requires expensive and sophisticated optical apparatus and highly trained personnel, thus limiting the accessibility of standard laboratories. In this PhD project, we have developed an alternative and cost-effective biosensor platform exploiting biofunctionalized nanofluidic slits, or nanoslits, combined with a bench-top fluorescence microscope. Our approach enables the visualization of protein interactions in real-time with the possibility to determine associated kinetic parameters along with optimized response times and enhanced binding efficiency. We have demonstrated the effectiveness of our devices through kinetic studies of two representative protein-receptor pairs with different binding affinities: streptavidin-biotin and mouse IgG/anti-mouse IgG interactions. Good agreement of extracted kinetic parameters between our device, SPR measurements and literature values indicated that this approach could be readily applicable to study kinetics of protein interactions with sensitivity down to 1 pM on a large scale of dissociation constants. In addition, we have incorporated a microfluidic gradient generator to our validated nanoslit device, which has allowed one-shot parallel kinetic measurements to be realized in a single-experiment. This integrated system provides advantages of diminished material consumption and analysis time over the conventional kinetic assays. We believe that this innovative technology will drive future advancements not only in the discipline of biomedical and personalized medicine, but also in basic chemical/biological research.

Keywords: kinetic studies, protein-protein interactions, biosensors, fluorescence microscopy, nanofluidics, concentration gradient

---

Discipline: Micro and nanosystems

Auteur: Pattamon TEERAPANICH

Titre: Développement d'une plateforme nanofluidique de biodétection en fluorescence pour la mesure de cinétiques d'interaction de protéines en temps-réel

Directeur de thèse: Thierry LEICHLE

Lieu et date de soutenance: LAAS-CNRS le 10 novembre 2015

Résumé

L'analyse cinétique d'interactions de protéines offre une multitude d'informations sur les fonctions physiologiques de ces molécules au sein de l'activité cellulaire, et peut donc contribuer à l'amélioration des diagnostics médicaux ainsi qu'à la découverte de nouveaux traitements thérapeutiques. La résonance plasmonique de surface (SPR) est la technique de biodétection optique de référence pour les études cinétiques d'interaction de molécules biologiques. Si la SPR offre une détection en temps réel et sans marquage, elle nécessite en revanche des équipements coûteux et sophistiqués ainsi que du personnel qualifié, limitant ainsi son utilisation au sein de laboratoires de recherche académiques. Dans ces travaux de thèse, nous avons développé une plateforme de biodétection basée sur l'utilisation de nanofentes biofonctionnalisées combinées avec une détection par microscopie à fluorescence. Ce système permet l'observation en temps réel d'interactions protéines-protéines et la détermination des constantes cinétiques associées, avec des temps de réponse optimisés et une excellente efficacité de capture. La fonctionnalité du système a été démontrée par l'étude des cinétiques d'interaction de deux couples modèles de différentes affinités : le couple streptavidine/biotine et le couple IgG de souris/anti-IgG de souris. Une très bonne cohérence entre les constantes cinétiques extraites, celles obtenues par des expériences similaires réalisées en SPR et les valeurs rapportées dans la littérature montre que notre approche pourrait être facilement applicable pour l'étude cinétique d'interactions de protéines avec une sensibilité allant jusqu'au pM, sur une large gamme de constantes de dissociation. De plus, nous avons intégré un générateur de gradient de concentrations microfluidique en amont de nos nanofentes, permettant ainsi des mesures simultanées de cinétiques d'interactions à différentes concentrations d'analyte en une seule expérience. Ce système intégré offre de nombreux avantages, tels qu'une réduction de la consommation des réactifs et des temps d'analyse par rapport aux approches séquentielles classiques. Cette technologie innovante pourrait ainsi être un outil précieux non seulement pour les domaines du biomédical et de la médecine personnalisée mais aussi pour la recherche fondamentale en chimie et biologie.

Mots-clés: études cinétiques, interactions protéine-protéine, biocapteurs, microscopie à fluorescence, nanofluidique, gradient de concentration

---

Discipline: Micro et nano systèmes